UNIVERSITY OF SOUTHAMPTON

WEAR AND IMPACT PROPERTIES OF POLYMERIC COATINGS USED IN THE OFF-SHORE INDUSTRY

Yanmeng Xu

Doctor of Philosophy

Faculty of Engineering, Science and Mathematics
Surface Engineering and Tribology Group

July 2003

UNIVERSITY OF SOUTHAMPTON

ABSTRACT

SCHOOL OF ENGINEERING, SCIENCE AND MATHEMATICS
SURFACE ENGINEERING AND TRIBOLOGY GROUP

Doctor of Philosophy

WEAR AND IMPACT PROPERTIES OF POLYMERIC COATINGS USED IN THE OFF-SHORE INDUSTRY

by Yanmeng Xu

The steel tubulars for water injection in the oil industry are internally coated primarily for corrosion resistance. Various polymeric materials have been used for these coatings which are sprayed or deposited on to the bore of the downhole tubulars. However in service it has been found that the polymeric coatings can be damaged by the tools that are periodically lowered at speed down the well. This damage takes the form of wear of the coatings by the wire to which the tool is attached (wireline wear) and impact damage when the tool impacts the bore of the tube.

The polymeric materials used in these coatings are composites consisting of a polymeric matrix which normally contains a filler. The mechanism by which the addition of a filler improves wear resistance is still not fully understood and detailed wear testing and microscopy on wear tracks are needed to elucidate the mechanism. In particular, the effect of the nature, amount, size and distribution of the filler on the wear resistance requires further study. This information is essential if a model is to be developed to predict the wear resistance of a particle filled polymeric coating.

Similarly, the influence of the nature, amount, size and distribution of filler on the impact resistance is still lacking. This information is also necessary if a model of the impact strength of filled polymeric coatings is to be developed. In addition, the bond strength between the coating and steel substrate is important in determining the behaviour of the polymeric coating under both wear and impact conditions. The bond strength of the coating is unknown, therefore, this investigation will assess the adhesive strength by using four-point bending and acoustic emission (AE) tests. This will lead to an improved understanding of the relation between the mechanisms of wear and impact resistance and the microstructure of the polymeric coatings.

Experiments on the wireline wear and impact of different polymeric coatings will be undertaken by simulating the in-situ working conditions of downhole tubulars to investigate the mechanism of wireline wear and impact damage to polymeric coatings caused by the inspection tools. The emphasis of this study will be to correlate the microstructural factors and the wear and impact resistance of polymeric coatings.

Acknowledgements

I should like to thank my research supervisor, Dr. Brian Mellor, for his guidance, helpful advice and enthusiasm. Special thanks to my research advisor, Dr. Robert Wood, for his invaluable advice.

Financial support for this work was provided by BP Amoco. I should like to thank Dr. Steve Groves of BP Amoco for this support and for the provision of specimens.

Yanmeng Xu

July 2003

CHAPTER 7 APPLICATION OF ACOUSTIC EMISSION TO DETECT DAMAGE MECHANISMS IN POLYMERIC COATINGS

CHAPTER 8 CONCLUSIONS AND FUTURE WORK

LIST OF FIGURES:

LIST OF TABLES:

CHAPTER 1 INTRODUCTION

1.1 Background Associated with the Use of Downhole Tubulars within the Petroleum Industry

During the process of oil production, the fluids in the reservoir are set into motion as oil is produced from the well [1]. This creates a fluid potential gradient towards the well and a drop in pressure of the reservoir around the well; the drop in pressure results in the reduction of oil producing efficiency. Pressure maintenance programmes are carried out for reasons of economy and efficiency. This is achieved by the injection of water around the reservoir through the injection wells called water injectors. Water is injected under pressure into the reservoir rocks and so drives the oil through the rocks towards the production wells. This water is either the produced water generated from the oil producing process after separation of oil and gas, or sea water.

The steel tubulars for water injection in the oil industry are internally coated primarily for corrosion resistance. Various polymeric materials have been used for these coatings which are sprayed or deposited on to the bore of the downhole tubulars. However in service it has been found that the polymeric coatings can be damaged by the tools that are periodically lowered at speed down the well. This damage takes the form of wear of the coatings by the wire to which the tool is attached (wireline wear) and impact damage when the tool impacts the bore of the tube.

The polymeric materials used in these coatings are composites consisting of a polymeric matrix which normally contains a filler. This is a low cost material such as mineral silicates etc. The filler component has not been optimised in contrast to Metal Matrix Composites where the filler, which in this case is more aptly named the reinforcement phase, is carefully tailored as regards its proportion, size and surface properties, in order to provide optimum properties to the composite [1, 2]. This investigation will thus address the role of the detailed microstructure of the polymeric coating, in particular that of the filler or reinforcement, and its subsequent effect on the overall performance of the

coating under impact and wireline wear conditions. The project is sponsored by BP Amoco in conjunction with major international suppliers of internally polymeric coated tubulars.

1.2 Wireline Wear and Impact Damage of Polymeric Coatings

Wireline damage to internally coated tubing is of major concern because nearly all producing wells are subject to periodic wireline work. NACE PR0291 [3] outlines procedures for minimizing wireline damage to internally coated tubing. However, these guidelines are not always followed. From the preceding introduction of what happens to the polymeric coatings being used in downhole tubulars in oil wells, it is known that the damage takes the form of wear of the coatings by the wire to which the inspection tool is attached and impact damage when the tool impacts the bore of the tube. The inspection tool is lowered into the well periodically to measure the temperature, pressure etc. which affects the production of oil very much. Rock formation and the positioning of the oil deposits impose restrictions on the drilling direction of wells, resulting in a well with bends and an overall slope. This situation causes wear of the polymeric coating since the wireline slides against the surface of the coating and impact damage to the coating as well. The schematic representation of wireline wear and impact damage is shown in Figure 1.1.

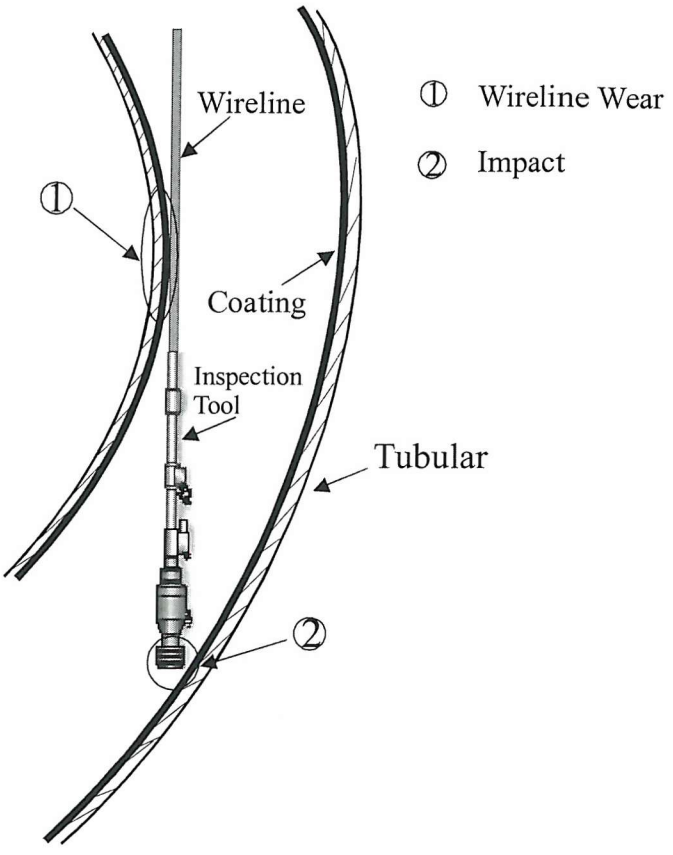

Fig. 1.1 Schematic diagram of wireline wear and impact (not to scale).

1.3 Scope and Objective of the Research Work

The wear resistance of polymeric coatings can be improved by adding fillers which are harder than the polymeric matrix material. However, the fillers can act as stress raisers and impair the impact resistance. The wear resistance and impact strength of polymeric coatings have been the object of a recent thesis by Symonds [1], where the work was mostly concerned with thermosetting polymers, although a limited amount of work was also carried out on a number of thermoplastic materials. A conclusion from this work was that the thermoplastic matrix could be used to enhance both the wear and impact resistance of polymeric coatings. The present investigation will concentrate on using thermoplastic materials which are not at present widely used as coatings on water injectors.

The mechanism by which the addition of a filler improves wear resistance is still not fully understood and detailed wear testing and microscopy on wear tracks are needed to elucidate the mechanism. In particular, the effect of the nature, amount, size and distribution of the filler on the wear resistance requires further study. This information is essential if a model is to be developed to predict the wear resistance of a particle filled polymeric coating.

Similarly, the influence of the nature, amount, size and distribution of filler on the impact resistance is still lacking. This information is also necessary if a model of the impact strength of filled polymeric coatings is to be developed. In addition, the bond strength between the coating and steel substrate is important in determining the behaviour of the polymeric coating under both wear and impact conditions. The bond strength of the coating is unknown, therefore, this investigation will assess the adhesive strength by using four-point bending and acoustic emission (AE) tests. This will lead to an improved understanding of the relation between the mechanisms of wear and impact resistance and the microstructure of the polymeric coatings.

Experiments on the wireline wear and impact of different polymeric coatings will be undertaken by simulating the in-situ working conditions of downhole tubulars to investigate the mechanism of wireline wear and impact damage to polymeric coatings caused by the inspection tools. The emphasis of this study will be to correlate the microstructural factors and the wear and impact resistance of polymeric coatings.

REFERENCES:

[1] N. Symonds, Polymer Coatings for Wireline Wear and Impact Resistance, PhD Thesis (2001), University of Southampton.

[2] N. Symonds, B. G. Mellor, Polymeric Coatings for Impact and Wear Resistance I: Wear, Wear 225-229 (1999), pp 111-118.

[3] NACE Standard RP0291-91, Care, Handling, and Installation of Internally Plastic Coated Oilfield Tubular Goods and Accessories, Section 7: Operation, Houston, TX: NACE (1991).

CHAPTER 2 LITERATURE REVIEW

2.1 Polymers

Polymers which include such diverse materials as plastics, rubbers, and adhesives – are giant organic, chain-like molecules that have molecular weights from 10,000 to more than 1,000,000 $g.mol^{-1}$. Polymers are used in a large number of applications, including toys, home appliances, structural and decorative items, coatings, paints, adhesives, automobile tyres, foams, and packaging. Polymers are often used in composites, both as fibres and as a matrix [1].

As polymers improve and as designers learn the advantages of polymers, the friction and wear properties of polymers, therefore, become of greater interest and importance, which in turn encourages research and development efforts in this field. The understanding of the mechanisms of friction and wear of polymers has progressed very slowly, undoubtedly because of the great range of compositions of polymers and because of the wide range environments to which these polymers are subjected [2].

2.1.1 Classification of polymers

Polymers are classified in several ways [1]: by how the molecules are synthesized, by their molecular structure, or by their chemical family. However, the most commonly used method to describe polymers is in terms of their mechanical and thermal behaviour. Table 2.1 lists a number of polymers [3], fillers and reinforcements of interest for tribological application and which have a close relation to this research work.

Thermoplastic polymers are composed of long chains produced by joining together small molecules, or monomers; they typically behave in a plastic, flexible manner. These polymers soften and are formed by viscous flow when heated to elevated temperatures. Thermoplastic polymers may be recycled. The majority of the thermoplastics listed in Table 2.1 are crystalline. Of these, the polyamides, polyacetals, and polyethylenes are

well-established engineering polymers. Polytetrafluoroethylene (PTFE) is of major importance in tribology, as a suitably reinforced matrix material, an additive to other polymers to reduce friction, a thin film solid lubricant, or as a grease additive.

Table 2.1 Polymers, fillers, and reinforcements of interest for tribological applications

Thermoplastics	Polyethylenes	High density polyethylene (HDPE), ultra-high-molecular-weight polyethylene (UHMWPE)
	Polyamides	Nylon 6, 6.6, 6.10, 11, 12
	Polyacetals	Homopolymer, copolymer
	Fluorocarbons	Polytetrafluoroethylene (PTFE) Copolymers of TFE with: hexafluoropropylene (FEP), ethylene (E-TFE), vinylidene fluoride (VF_2-TFE), Fluorinated propylvinylether (PFA), Poly(vinylidene fluoride) (PVDF)
	High-temperature polymers	Poly(phenylene sulphide) (PPS), poly(ether sulphone) (PES), poly(pe-hydroxy benzoic acid (HBA)
Thermosetting		Phenolic (PF), cresylic, polyester, epoxy (EP), silicone, polyimide
Elastomeric		Natural rubber, styrene-butadiene (SBR), butadiene-acrylonitride (nitrile), polyacrylate, fluorocarbons
Fillers and reinforcements	To improve mechanical properties	Asbestos, carbon, glass, textile, aromatic polyamide fibres, mica, metal oxides, carbon black, silica
	To reduce friction	Graphite, MoS_2, PTFE, mineral oils, silicones, fatty acids/amides
	To improve thermal conductivity	Bronze, carbon, silver

Thermosetting polymers are composed of long chains of molecules that are strongly cross-linked to one another to form three-dimensional network structures. These polymers are generally more rigid, stronger, but more brittle, than thermoplastics. Thermosets do not have a fixed melting temperature and cannot easily be reprocessed after the cross-linking reactions have occurred. Of the materials listed in Table 2.1, phenolic and cresylic resins are of most general application and are invariably filled or reinforced.

Elastomers, including rubbers, have an intermediate structure in which some cross-linking of the chain is allowed to occur. Elastomers have the ability to elastically deform by enormous amounts without being permanently changed in shape. Elastomers will not be used in this research, so their characteristics and applications will not be discussed in detail.

Polymerization of all three polymer types normally begins with the production of long chains in which the atoms are strongly joined by covalent bonding. The amount and strength of cross-linking gives each type its special properties. It should be noted that the distinctions between these three types often become blurred. For example, there is a continuum of change between the simple structure of polyethylene (a thermoplastic) and the more complex structure of epoxy (a thermoset).

2.1.2 Reinforced polymer composites

A polymer itself is seldom used alone because the major problem in the application of polymers in engineering is their low stiffness and strength when compared to metals [4, 5]. Usually, in order to overcome these deficiencies and improve the mechanical properties of the polymers, reinforcing particles or fibres are added to the resin to form a composite material. A good reinforcing additive has the following attributes:

(i) it is stiffer and stronger than the polymer matrix;
(ii) its particle size, shape, and surface character give effective mechanical coupling to the matrix;
(iii) it preserves the desirable qualities of the polymer matrix.

Many reinforced polymer composites are based on thermoset polymers, and for many years the most popular has been the family of polymers known as polyesters [4]. These are versatile, inexpensive polymers, used extensively with glass-fibre reinforcement, often in substantial plastic components (such as storage tanks, pipes, boat hulls, and

seating for public places). Another thermoset polymer which is increasingly being utilised is the epoxy, i.e. in repair, coating and construction projects.

Thermoset polymers have some important properties when used as matrices in reinforced polymers [4]:

(i) the low viscosity of the precursor liquids, prior to cross-linking, facilitates thorough wetting of reinforcing particles by the polymer;
(ii) economical forming is possible for large components;
(iii) high softening points can be achieved in materials of only moderate cost.

Recently, there has been a rapid growth in the use of reinforced thermoplastic polymers [4]. The semi-crystalline polymers polypropylene and nylon are especially popular as matrices. A major advantage of a thermoplastic matrix is that forming is possible by normal injection moulding or extrusion techniques. These are the most economical processes when cost effective and precise manufacture of very large quantities of components are required. Allowance must be made for the effect of reinforced particles on the flow of molten plastic during forming; for example, the viscosity is significantly increased. Consequently, some modifications to tooling and process parameters are usually necessary.

Generally, the polymer composites may be classified as follows by the various forms of reinforcement in a polymer matrix [4, 6, 7]:

2.1.2.1 Fibrous reinforced polymers

Fibrous reinforced polymers have continuous or discontinuous filaments or whiskers in a matrix. Three types of reinforcing fibre dominate the reinforced polymers. These are: glass fibres, carbon fibres, and oriented polymeric fibres [4]. The other major constituent in fibrous reinforced polymer composites, the matrix, serves two very important functions:

(i) it holds the fibrous phase in place;

(ii) and under an applied force it deforms and distributes the stress to the high-modulus fibrous constituent.

2.1.2.2 Particulate reinforced polymers

Particulate reinforced polymers have particles in a matrix. In its simplest form, a particulate filled polymer composite consists of a continuous three-dimensional structural matrix infiltrated or impregnated with a second-phase filler material. In effect, both the matrix and the filler exist as two separate constituents that do not alloy (except for a bonding action) and do not combine chemically to any significant extent. In most particulate filled polymer composites the matrix provides the framework and the filler provides the desired engineering or functional properties. Although the polymer matrix usually makes up the bulk of the composite, the filler material is often used to such a large extent that it becomes the dominant material and makes a significant contribution to the overall strength and structure of the composite. In order to obtain the optimum properties in filled composites the two materials must be compatible and not react in a way that would degrade or destroy their inherent properties. Thus, it is important for the matrix and filler materials to exist as two separate constituents.

A subset of particulate reinforced composites is a flake or platelet reinforced composite. Embedded in a matrix and made parallel in a plane, flakes provide equal properties in all directions in the plane. The flake reinforcements in common use are all minerals, two in particular are of notable success: talc and mica. Talc is a magnesium silicate, while mica is an aluminium silicate (talc: $3MgO \cdot 4SiO_2 \cdot H_2O$; Mica: $K_2O \cdot 3Al_2O_3 \cdot 6SiO_2 \cdot 2H_2O$ (muscovite form)). Talc and mica are both crystalline, with similar structures of a layered type. The SiO_2 groups are firmly linked together in layers, sandwiching other oxides, but with only weaker bonding between the layers [4]. The success of mineral flake reinforcement is due to their desirable combination of cost and properties:

(i) low price — price per unit mass is typically less than one-fifth that of the common polymer materials; and

(ii) stiffness and strength are greater than those of polymers.

As a result, when they are used to reinforce polymers, significant increases in modulus or strength can be obtained at little or no increase in cost. There are also further advantages over fibres: when flakes are aligned parallel to each other they provide reinforcement in all directions in their plane, not merely in one direction as with uniaxially aligned fibres; flake reinforced polymers also have a higher theoretical modulus than fibre reinforced polymers and can be packed closer with fewer voids.

In this study, wear and impact resistant properties of particulate filled polymeric coatings will be investigated. The influence of fillers on the wear and impact resistance of polymeric coatings will be discussed in Sections 2.3.4 and 2.4.3.

2.1.3 Polymeric coatings

The range of application of polymeric materials as coatings is vast: almost all the major types of the thermoplastics, thermosets and elastomers find use as coatings in some form [3]. Polymeric coatings are used for a number of purposes, e.g., decorative, protective, functional (as dielectrics or insulators), etc [8].

In offshore well conditions, internal polymeric coatings have been used to effectively prevent corrosion attack and reduce the frequency of leaks in tubulars for almost fifty years [9]. Polymeric coatings prevent corrosion primarily by acting as a barrier material, restricting water, oxygen, and ionic materials to the metallic surface underneath. Past field history has shown the effectiveness of internal polymeric coatings as a primary tool for corrosion control in secondary and tertiary recovery programs [10]. In recent times, new coating materials have been developed that enhance the overall coating performance by providing materials with greater flexibility and impact resistance.

Historically, internal polymeric coatings have been primarily based on phenolic resin, a high-bake thermosetting plastic. The phenolic resin was desired because of its temperature stability up to 400°F (204°C) and its chemical resistance to most acid gases and corrosives found in oil and gas production [10].

More recently, epoxy and nylon materials have been selected in order to develop new coating systems with improved flexibility and durability. These resins, when properly formulated, offer excellent corrosion resistance to water, oxygen, CO_2, and trace levels of hydrogen sulfide (H_2S) up to temperatures in excess of 200°F (93°C), depending on the well conditions [9].

2.1.4 Performance of polymeric coatings in downhole conditions [9]

Thermosetting and thermoplastic coatings, regardless of their formulation, have many common application properties. The coating may be applied as either a liquid or powder depending on the resin system and local environmental regulations.

Numerous coating formulations are required to meet the various demands of downhole pipe coatings. *Phenolic coatings* were chosen as the first thermoset internal coatings because of their broad range of chemical resistance and ability to withstand temperatures up to 400°F (204°C). Phenolics also have adequate impact, bending, and abrasion resistance. *Modified phenolic coatings* were designed to resist depressurization damage; therefore, they are commonly used in high pressure gas wells. The physical properties of modified phenolic coatings are similar to phenolic coatings. *High bake epoxy coatings* are used in lower temperature environments that do not require the chemical resistance of phenolics. Epoxy coatings also offer a substantial increase in flexibility over phenolic coatings. *Epoxy-phenolic coatings* offer an acceptable compromise in flexibility and chemical resistance in service environments to 250°F (121°C). Epoxy-phenolics are formulated by copolymerizing an epoxy and a specifically designed phenolic resin. *Epoxy novolac coatings* are powder coatings that offer performance similar to epoxy phenolics at temperatures up to 300°F (149°C). *Urethane coatings* offer enhanced abrasion resistance, a glass smooth surface and flexibility in environments below 225°F (107°C) with primary applications for control of scale and paraffin deposition. All of these coatings are thermoset materials and only the epoxies and epoxy novolacs are applied as thick film powder coatings. Recently, a specific nylon thermoplastic powder was formulated utilizing a proprietary primer system for downhole environments. *This Nylon*

powder coating is limited to service below 225°F (107°C) and has limited resistance to concentrated stimulation acids such as hydrochloric acid (HCl), hydrofluoric acid (HF), acetic acid or their blends; yet nylon has the resilience and flexibility that makes it much more resistant to handling and installation damage than the traditional thermoset coatings.

2.2 Wear of Polymers

2.2.1 Introduction

During the past decade there has been a continuous increase in the utilization of polymers and polymer-based composites in a wide variety of tribological applications. These include such diverse components as piston rings, seals, brakes, prosthetic joints, gears, tires, and dry bearings, and the materials involved cover a wide spectrum of mechanical properties from elastomers to hard reinforced thermosetting resins. This literature review is intended to describe the different types of wear behaviour exhibited by this range of materials in different conditions of sliding, but with particular emphasis on the more rigid thermoplastic and thermosetting materials.

There have been many attempts to classify the wear of polymeric materials, based either on the phenomena observed or on the causative agents believed to be responsible [11]. The most widely accepted is that which seeks to identify the main causative factors involved, and it is most convenient to divide the wear processes for polymers into three main groups — adhesion, abrasion and fatigue. Definitions of these processes are given elsewhere [12].

Various parameters have been used to quantify wear of polymers. Ravikiran [13] summarised the parameters which are used for wear quantification.

(i) Wear (V): volume loss — m^3 (seldom used).

(ii) Wear rate (W): volume loss (m^3) per unit sliding distance (m) — m^3/m (the most frequently used one).

(iii) Specific wear rate (W_{sp}): volume loss (m^3) per unit sliding distance (m) per unit applied load (N) — m^3 / Nm (frequently used).

(iv) Wear coefficient (k): this is similar to specific wear rate except that it is multiplied by room temperature hardness (H_0) — $W_{sp}H_0$ – a non-dimensional number (frequently used).

(v) Normalized wear rate (W_n): wear rate (W) divided by apparent contact area (A) — W / A – a non-dimensional number (seldom used).

In some cases 'mass loss' is used instead of 'volume loss' as in i and ii.

2.2.2 Adhesive wear of polymers

The primary consequence of adhesion is the transfer of polymer from one surface to the other, and this has been demonstrated several times for polymers sliding against themselves and against other materials [14, 15, 16]. Adhesive interactions are likely to play their most significant role during sliding of polymers against metals when the surfaces are relatively smooth and there is repetitive sliding over the same wear track on the metal.

During repetitive sliding of polymers on metals, a small piece of the polymer is plucked from the bulk material to form a loose wear particle or to be attached to the counterface to contribute to the transfer film, as illustrated in Figure 2.1. The formation of the transfer film changes the type of contact occurring from the initial polymer/metal to polymer/polymer, and also changes the surface topography. These factors influence the magnitude of the localized stresses and in turn will affect wear occurring as a result of fatigue. With relatively rigid and brittle polymers (e.g. some epoxies, polyester or polystyrene), the film transferred to smooth metals is present as irregular lumps and the wear rate tends to increase with time as the transfer film develops [17]. However, with the more ductile thermoplastics (e.g. acetals, polyamides and polyethylene), the transferred fragments can readily be deformed during repeated contacts leading to a

topography which may be smoother than that of the original metal; the localized stresses, and hence the wear rate, thus decrease with time as the transfer film develops.

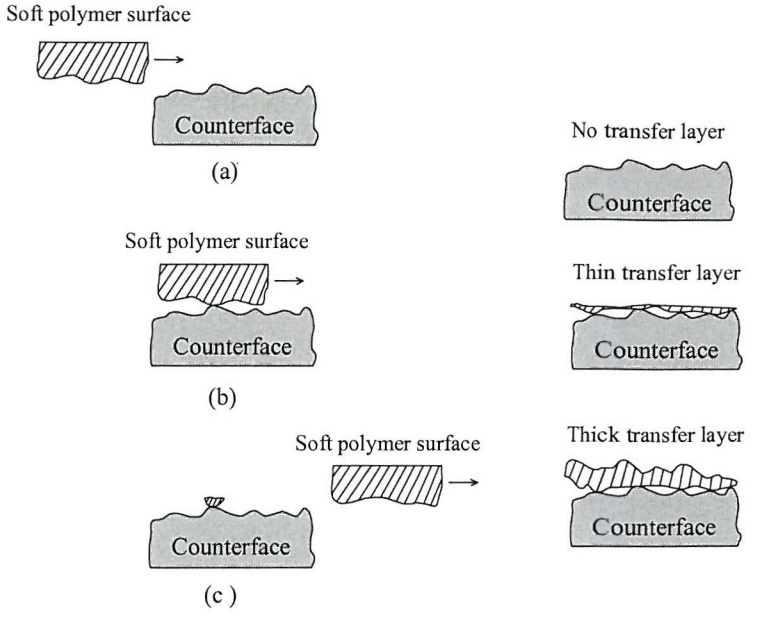

Fig. 2.1 Diagrammatic representation of adhesive wear mechanism for polymers.

(a) Effects of load, speed, and temperature on the adhesive wear rate of polymers

Simple theories of wear, based on adhesion by Archard published in 1953 [18], predict a direct proportionality between wear rate and load. This is frequently observed experimentally, as in Figure 2.2(a), but it should be emphasized that proportionality will be observed only when changes in load do not induce changes in any other variable affecting wear, such as temperature or the topography of the polymer and its counterface. The rapid rise in specific wear rate, shown in Figure 2.2(a) for polyethylene and poly(ethyl methacrylate) above a critical load, is associated with thermal softening of the polymer. It should also be mentioned that the relevant variable is, in fact, the absolute load and not the nominal pressure. In general, the wear rates of polymers are largely independent of the apparent area of contact, although again the precondition must be made that changes in the apparent contact area do not introduce additional factors into the wear process.

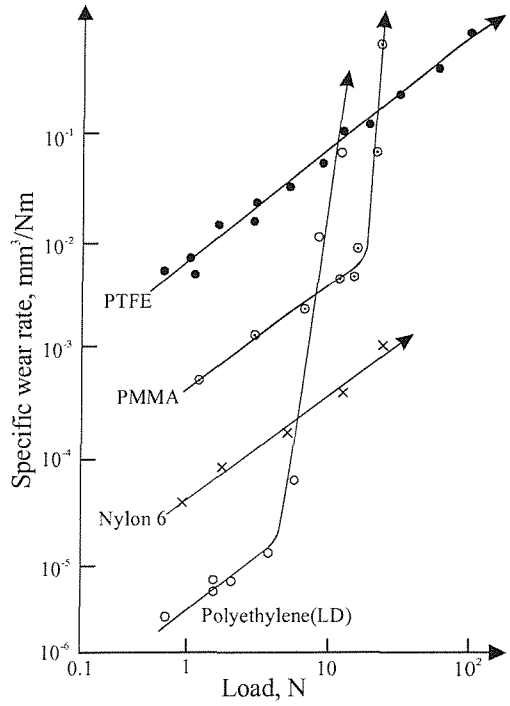

Fig. 2.2(a) Variation of steady-state specific wear rate with load for polymers sliding on mild steel (from Lancaster, Plastic & Polymers Dec. 1973, 297-306).

The influence of temperature on the steady-state specific wear rate of polymers against metals is more complex than that of load, and typical variations are shown in Figure 2.2(b). The main reason for the decrease in wear rate with increasing temperature is the associated change in the mode of deformation. As the temperature increases the elastic modulus decreases, leading either to an increase in the number of cycles to failure (fatigue wear) or to a smaller component of abrasive wear (cutting) compared to fatigue wear. The rapid rise in wear rate at high temperatures is associated with thermal softening. Finally, the influence of sliding speed on the wear of some thermoplastics is shown in Figure 2.2(c). The maxima occurring at relatively low speeds are qualitatively consistent with viscoelastic (rate of strain) effects, and the subsequent minima and rapid increases in wear again result from temperature increases associated with high speed.

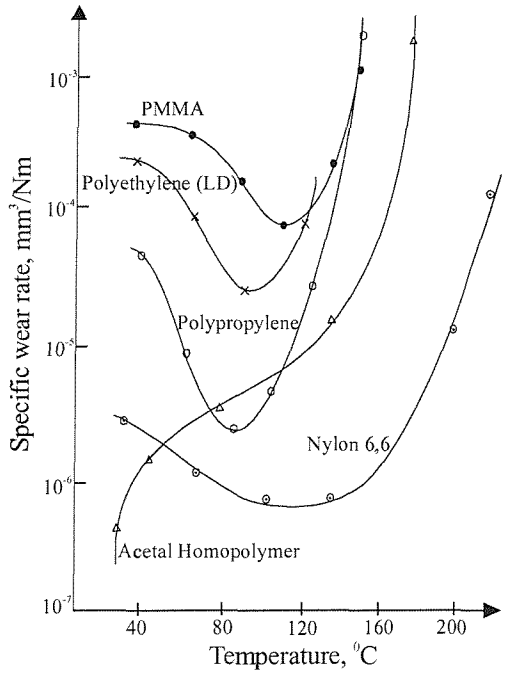

Fig. 2.2(b) Variation of steady-state specific wear rate with temperature for various polymers sliding on mild steel (from Lancaster, Plastic & Polymers Dec. 1973, 297-306).

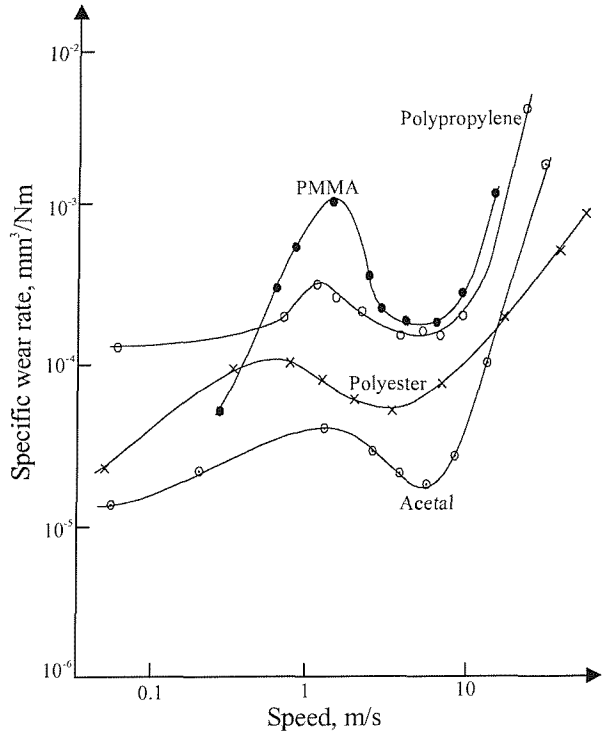

Fig. 2.2(c) Variation of steady-state specific wear rate with speed for various polymers sliding on mild steel (from Lancaster, Plastic & Polymers Dec. 1973, 297-306).

2.2.3 Abrasive wear of polymers

Abrasive wear happens when material is removed or displaced from a surface by hard particles, or sometimes by hard protuberances on a counterface, forced against and sliding along the surface [19]. Several qualifying terms are often used in describing abrasion. A distinction is often made between two-body abrasive wear and three-body abrasive wear. The main difference between these two types of abrasive wear is that two-body wear is caused by hard protuberances on the counterface, while in three-body wear hard particles are free to roll and slide between the two. Rabinowicz [20] has proposed a simple equation for the volume of material removed during two-body abrasion by a conical abrasive particle:

$$\frac{W_V}{s} = \frac{2\tan\alpha}{\pi}\frac{F_N}{H} \qquad (2.1)$$

where W_V is the volume loss due to wear, s is the sliding distance, F_N is the normal load on the conical particle, H is the yield pressure or hardness of the wearing surface and α the attack angle of the abrasive particle. A precondition for the validity of Eqn. 2.1 is that all the material produced from the wear groove is detached in a single pass from the surface of the wearing material. Wear is about one to two orders of magnitude smaller in three-body abrasion than in two-body abrasion. In three-body abrasion only a small proportion of the abrasive particles cause wear, due to variation in the angle of attack [21]. Three-body abrasion is often of considerable practical importance but appears to have received much less attention than the two-body problem. In some situations, wear is caused by hard particles striking the surface, either carried by a gas stream or entrained in a flowing liquid. This type of wear is called erosion, or slurry erosion. Figure 2.3 schematically illustrates the different mechanisms of these three kinds of wear associated with abrasive particles. As the wear mechanism of erosion is not applicable to the present research work, erosion wear will therefore not be discussed further.

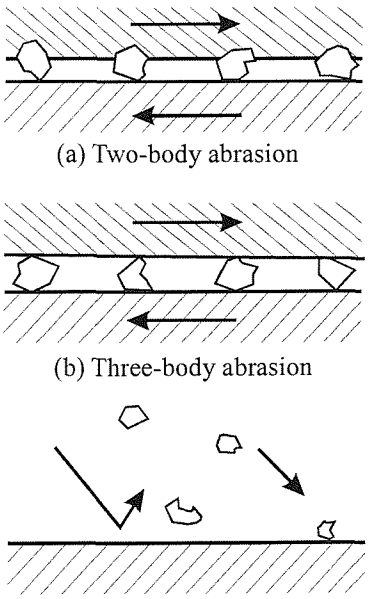

Fig. 2.3 Illustration of the differences between (a) two-body abrasion; (b) three-body abrasion; and (c) erosion.

Several mechanisms have been proposed to explain the processes that are possible when a single abrasive tip traverses a surface of a material. This study has adopted the mechanisms defined by Zum Gahr [22] as microploughing, microcutting, microfatigue, and microcracking. Because of the complexity of abrasion, no one mechanism completely accounts for all the loss of material. These mechanisms of abrasive wear are shown schematically in Figure 2.4.

In the ideal case, microploughing due to a single pass of one abrasive particle does not result in any detachment of material from a wearing surface. A prow is formed ahead of the abrading particle and material is continually displaced sideways to form ridges adjacent to the groove produced. Volume loss can however occur owing to the action of many abrasive particles or the repeated action of a single particle. Material may be ploughed aside repeatedly by passing particles and may break off by low cycle fatigue, which is called microfatigue. Pure microcutting results in a volume loss by chips equal to the volume of the wear groove. Microcracking occurs when highly concentrated stresses are imposed by abrasive particles, particularly on the surface of brittle materials. In this

case, large wear debris are detached from the wearing surface owing to crack formation and propagation. Microploughing and microcutting are the dominant processes on ductile materials while microcracking becomes important on brittle materials.

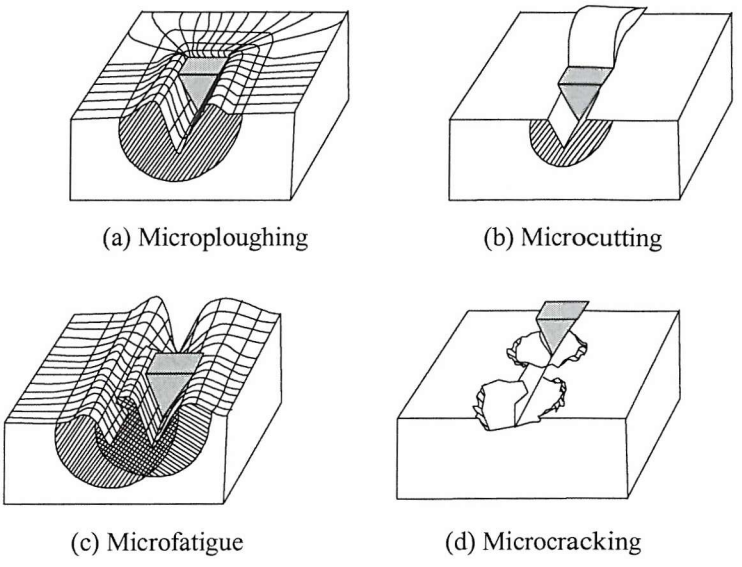

Fig. 2.4 Physical interactions between abrasive particles and the surfaces of materials in abrasive wear [21].

A simple theory of abrasive wear of polymers given by Lancaster [23] assumes a model in which hard irregularities, cones or ridges, penetrate a softer material and remove material by shear or cutting. This model leads to the relation:

$$V = \frac{KWd \tan\theta}{H} \qquad (2.2)$$

where V is the volume removed, W is the load, d is the distance of sliding, H is the indentation hardness of the material being worn, and θ is the angle of slope of the irregularities. The constant K partly expresses the fact that not all the material involved in the deformation process is removed as debris; an appreciable proportion is merely displaced plastically. It is easy to see that the Eqns. 2.1 and 2.2 are basically the same. Both of these models show the abrasive wear rate of polymers should be proportional to

the normal load and the surface roughness (computer analysis of the topography of these surfaces shows that $\tan\theta$ is approximately proportional to the square of the center-line-average roughness [23]), and inversely proportional to the hardness. However, researchers such as Hutchings and Lancaster [24, 25] point out that this conclusion is always obeyed for the soft metals rather than for the polymers. The question thus arises as to which particular mechanical properties of polymers are, in fact, relevant to this type of wear process. Ratner [26] considers that the most important parameter is the work required to rupture material during sliding, which is equivalent to the area under the stress/strain curve and approximately equal to the product of the breaking stress, s, and the elongation to break, e. Figure 2.5 shows the relationship between the specific wear rates of a number of polymers, during single traversals over rough mild steel and confirms that a significant correlation does exist between the wear rate and $1/se$. Despite the fact that the abrasive wear rates of polymers do not correlate with hardness, it is nevertheless possible to use hardness as a very general criterion in order to put the wear rates of polymers into perspective with those of metals [25].

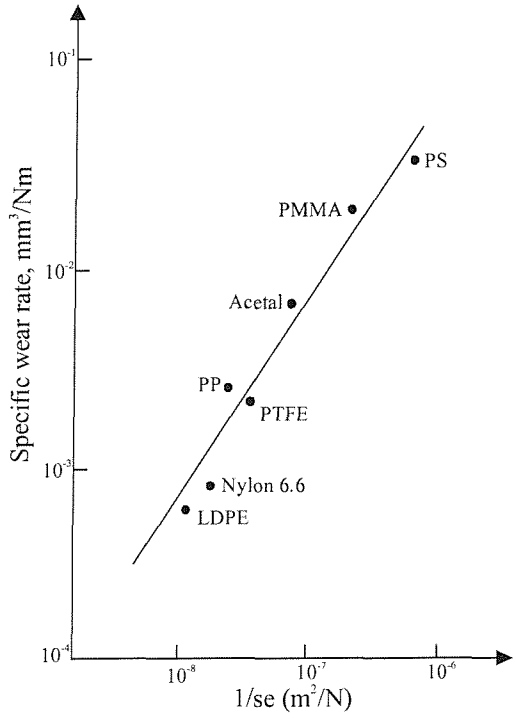

Fig. 2.5 Correlation between specific wear rates and $1/se$ during single traversals of polymer over rough mild steel (from Lancaster, Plastic & Polymers Dec. 1973, 297-306).

2.2.4 Fatigue wear of polymers

Fatigue wear has long been recognized as an important process in some rolling and sliding combinations involving metals, but evidence of a similar effect in polymers has recently been presented by Dowson et al. [27]. Surface fatigue wear in polymers probably results from repeated stress cycles applied to the material associated with asperity interactions. It has been observed after a substantial period of rubbing and hence might not be detected in short-term tests. The following simplified treatment given by Lancaster [25] will suffice to illustrate the main ideas involved in the wear process of polymers. The fatigue properties of a material can be characterized approximately by the relation $n \propto (\sigma_0 / \sigma)^t$ where n is the number of cycles to failure, σ_0 is the failure stress corresponding to a single application of stress, σ is the applied cyclic stress and t is a material constant. The rate of wear will be inversely proportional to n, and hence wear rate is proportional to $\sigma_0^{-t}\sigma^t$, i.e. to the product of a parameter involving the material properties and one involving the asperity stresses and, in turn, the topography of the surfaces. In the simplest case of a hard, spherical asperity of radius r penetrating a softer polymer plane, elasticity theory gives $\sigma \propto r^{-2/3}$, and hence wear rate is proportional to $\sigma_0^{-t} r^{-2t/3}$.

It is not always very easy to decide the point at which conventional abrasive wear, involving plastic deformation and cutting, changes to fatigue wear as the topography of the surfaces alters, particularly that of the counterface. For a particular topography, the type of deformation may range from wholly elastic, with elastomers, to entirely plastic, with the most rigid thermosetting resins. In any given situation, therefore, it is probable that the wear process of a polymer will comprise a mixture of abrasion (cutting) and fatigue. The relative proportion of wear attributable to each of these processes is shown schematically in Figure 2.6 for different types of polymers.

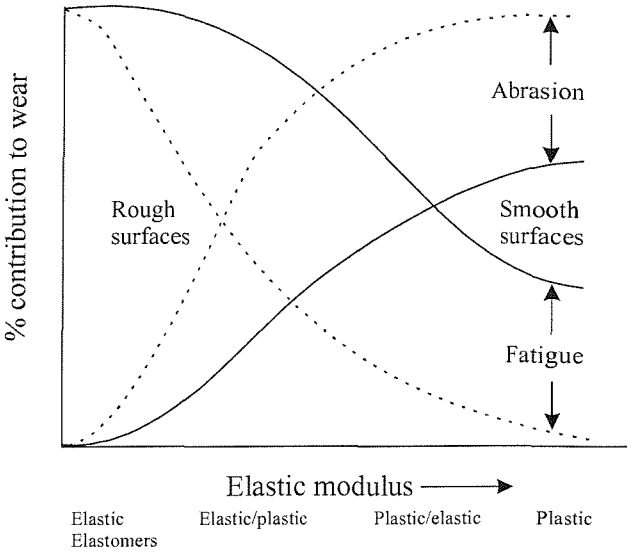

Fig. 2.6 Schematic variation of abrasive wear and fatigue wear with elastic modulus of polymers and the roughness of the counterface (from Lancaster, Plastic & Polymers Dec. 1973, 297-306).

2.2.5 Laboratory wear testing methods

Considerable research efforts have been made in recent years into the study and measurement of the wear of a range of polymer-based materials in the laboratory [24]. This has resulted in the publication of numerous papers that describe in detail the wear mechanisms pertaining to restricted test conditions and specific materials. However, each laboratory has its own test conditions and machines, controls and variables, which lead to case specific results.

A number of relatively simple wear testing machines have been developed to assess the wear properties of polymers. These tests attempt, as far as possible, to reproduce the sliding conditions encountered in practice. A common simulation technique that is widely used to evaluate the wear of polymers is to slide the polymer, usually in the form of a pin, over the surface of a rotating disc. There are two basic configurations; the pin may be loaded, along its major axis, in a direction either normal to or parallel with the axis of rotation. Hence the contact area is produced on the edge, or the face of the disc, see Figure 2.7.

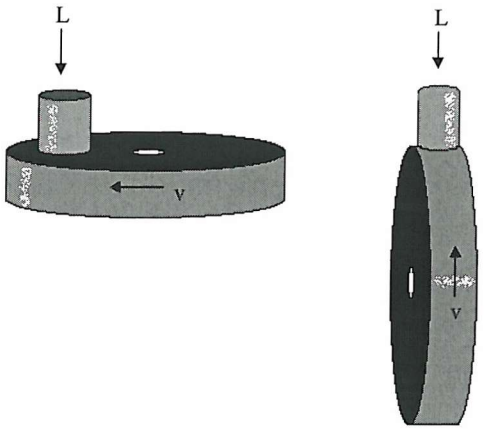

Fig. 2.7 Face and edge loading versions of the pin-on-disc rig.

These rigs are described as 'pin-on-disc'. The method of testing is similar to that reported in ASTM-D-2716 [28]. A pin-on-disc machine is one in which the point of contact is stationary with respect to one of the specimens and subject to constant speed uni-directional sliding. Other examples of this type include: Block-on-Ring, Ring-on-Ring, Pin-on-Plate, Crossed cylinder, Journal bearing, Sliding four ball, Ball-on-disk [29].

The pin-on-disc rig and similar rigs are used widely for wear research. The main reason is their simplicity; the variables can be controlled with a suitable degree of accuracy; wear mapping and parametric studies are readily performed. Adaptations can be made to suit individual research needs with minimal effort.

An essential objective in the design of the laboratory test is a desire to change dependent variables of the real process into independent or non-interacting and hence controllable variables in the test. It is common to choose specific combinations of load, speed, contact geometry (point, line or area), motion (continuous rotation, oscillation, reciprocation or fretting), counterface materials and surface finish, ambient temperature and the presence or absence of lubricant or abrasive. The number of possible test combinations is vast, and yet it is vitally important for the correct choice to be made, or the test loses validity. Alliston-Greiner [24] described in a recent presentation the framework offered by

Hogmark and Jacobson for the selection of test machine and test conditions. They suggested three possible classes of test, the higher the level the more "authentic" the test. (1) Complete tribocouple: using the actual components. (2) Semi-tribocouple: one true component and one model. (3) Model test: using two model components. The model tests are simplest with a high degree of control and accessibility, but a complete tribocouple has the potential to offer the truest result.

Further information and descriptions of experimental methods involved in adhesive and abrasive wear tests for polymer materials can be found in Symonds' thesis [30].

2.2.6 Summary of wear of polymers

The wear of polymers is a complex process involving one or more of the three mechanisms described in Sections 2.2.1 to 2.2.3. The relative importance of each process will depend upon the load, speed and environment, and might even change with time in a given situation. When a polymer slides over a hard counterface some abrasive action can be expected in the initial stages. Adhesive processes generally assume increasing importance and in due course dominate the wear behaviour of the polymer. If the sliding points persist for a long period, fatigue wear might supplement the adhesive action and increase the total rate of wear. However, if the counterface is relatively rough, the rate of removal of polymer by abrasive and adhesive actions might be so great that the surface does not have time to develop surface distress associated with fatigue [25, 27].

2.3 Wear of Polymer Composites

2.3.1 Introduction

The wear mechanisms and the wear rate of a polymer composite are different from those of the bulk polymer material. The wear of a polymer composite depends on the following factors: wear of bulk polymer material, wear of filler material, fracture or pull out of fillers and synergic effect of reinforced phases.

It is known that although fillers and reinforcing fibres significantly improve many physical and mechanical properties of polymers, it is not valid to assume that they also improve their wear properties [31]. For example, in abrasive conditions, i.e., wear against rough surfaces, the wear rates of filled or reinforced polymers can sometimes be greater than those of the matrix polymer alone [32]. The reason for this is that although the fillers generally increase the breaking strength s, they almost invariably reduce the elongation to break e; hence the product se can therefore be lower than for the unfilled polymer, and as discussed in Section 2.2.2 wear resistance tends to decrease with decrease in se. However, in conditions of steady-state wear during sliding against relatively smooth metals, the effects of fillers on wear are usually beneficial and often dramatic.

In this section (2.3), the adhesive wear and abrasive wear of polymer composites will be discussed, with particular emphasis on the effect of fillers on the wear of polymer composites.

2.3.2 Adhesive wear of polymer composites

Generally, in the absence of chemical degradation the strength of adhesive junctions appears to be relatively low for pure polymers. The transferred films may often be stripped off with pressure sensitive tape and by immersion in aqueous surfactant solutions. This relatively poor adhesion has been suggested as an important rate controlling factor in the overall rate of adhesive wear [33]. This belief emerges from studies on the influence of filler particles on the rate of adhesive wear of certain polymeric composites. Studies by Seward [34] indicated that effective fillers substantially increase the adhesion of the transferred layer to the counterface and hence reduce the rate of wear. Briscoe et al. observed that a good composite material may provide a rate of wear of perhaps three orders of magnitude less than that of the virgin polymer and at the same time maintain approximately the same level of frictional work [35].

In order to study the influence of the transferred film and counterface interactions in adhesive wear, a wide range of filled polymers have been investigated. The important

fillers were of the following types: carbon or graphite, inorganic glasses, transition metals and a number of high temperature polymers such as polyphenylene sulphide (PPS) and polyimides [31, 36]. Examination of sliding contacts provides a number of interesting general results. The surface of the matrix often appears to have an excess concentration of filler [37, 38] and the filler itself suffers appreciable wear or deformation and stands proud of the surface and thus supports a significant fraction of load [31]. The counterface is coated with a transferred layer of a type similar to that formed by the whole polymer. The most efficient matrices in terms of wear resistance produce the more strongly attached transferred layers and at the same time the most pronounced changes in surface topography. Transfer layers formed by filled composites do adhere more strongly to the counterface and such a layer will also maintain a low rate of wear when an unfilled polymer is slid over its surface [39].

Composites based on PTFE are more widely used and have received more attention than any other group of materials [40]. The wear rate of unfilled PTFE is extremely high, but additions of almost any inorganic, and some organic, fillers can reduce wear by a factor of 100 or more [31]. Carbon and graphite fillers are of particular interest because these materials are not only capable of exhibiting low friction and wear in their own right but also reduce expansion coefficients and increase strength and thermal conductivity [41]. In view of the extreme sensitivity of the friction and wear properties of carbon and graphite to environmental conditions, there have been a number of investigations into environment effects on carbon-PTFE composites. Sometimes, the results are conflicting. Hart [42] claimed that carbon-filled PTFE shows a tenfold increase in wear in dry gases, but Fuchsluger and Taber [43] claimed that the wear rate of a similar material is lower in dry nitrogen than in wet air. A collection of data extracted from the literature by Arkles [40] showed that the relative rankings of different PTFE composites for wear change significantly in different environments and there was no discernible pattern of behaviour.

In general, most filled or reinforced polymers other than PTFE and related fluorocarbons require solid lubricant additions to reduce friction and heat generation to an acceptable level for most dry sliding applications. PTFE itself is a very common additive, and the

wear properties of a range of glass-fibre-reinforced thermoplastics containing PTFE powder have been evaluated by Theberge and Arkles [44]. It was concluded that friction, wear and composite strength all tended to decrease with increasing PTFE content. It is generally recognized that the presence of thin films of transferred PTFE on a metal counterface significantly affects both friction and wear, and usually leads to a reduction in both [31]. The mechanisms by which these films reduce wear appear to be twofold. First, the effective surface roughness of the counterface is reduced after a period of wear test, which can lead to considerable reductions in wear. Second, sliding now occurs between oriented molecular chains of PTFE on both surfaces, the friction is reduced, the localized contact stresses are reduced, and thus the wear rate. The other common solid lubricant additions to polymer composites to reduce friction are graphite and MoS_2. In general they seem to be less effective than PTFE at concentrations below about 15 vol %, but graphite has the merit that it provides some degree of mechanical reinforcement as well as reducing friction. Giltrow et al. showed that a greater degree of reinforcement is possible by using graphite, or carbon in fibre form, and such reinforcements can lead to very low wear with both thermoplastic and thermosetting polymers [45].

However, many fillers are abrasive to a metal counterface and can either prevent transfer film formation or cause wear of the metal itself. The degree of surface damage to the counterface by the filler will depend on the relative hardness [46] and on the shape of the filler particles [47]. The influence of embedded fillers on the wear of polymer composites will be discussed in Section 2.3.4.

2.3.3 Abrasive wear of polymer composites

As discussed previously, many engineering polymer composites consist of a reinforcing phase of high strength and/or high modulus of elasticity embedded in a weak polymer matrix. The volume fraction of the reinforcing phase may reach about 80% in fibre-reinforced composites. The influence of the structure of composites on abrasive wear is a complex function of the properties and interactions of the matrix, the reinforcing constituent, and the interface between them [21]. Most of the abrasive wear problems

which arise in agricultural and industrial equipment involve three-body wear, while two-body abrasion occurs primarily in material removal operations. Despite the importance of three-body abrasion, the majority of abrasive wear studies have dealt with the two-body problem.

There are many references that illustrate the influence of fillers and fibre reinforcement on the abrasive wear resistance of polymeric composites [48, 49, 50]. Under controlled testing a given phase shows a specific wear mode and wear rate which is defined by its individual properties. Consequently, when the various phases are combined forming a multiphase material, it is expected that the overall behaviour will be a function of the respective contribution of each phase [51]. Based on this approach the wear resistance of a polymer composite has been mathematically described by Khruschov [52] as a linear function of the volume fraction of the phases present. Khruschov conducted a number of abrasive wear tests of plastic / metallic materials and showed that the constituents had additive wear resistance. The wear resistance of structurally heterogeneous materials was equal to the sum of the products of the volumetric share of the two separate constituents multiplied by their relative wear resistance. The 'linear rule of mixtures'(LROM) may be analytically expressed as:

$$R_C = \sum_{i=1}^{n} R_i V_i \qquad \text{where } \sum V_i = 1 \qquad (2.3)$$

R_c = wear resistance of a general multiphase material

R_i = relative wear resistance of an individual constituent

V_i = volume fraction of each of the n constituents

The conditions applied by Khruschov to Eqn. 2.3 were that all the magnitudes of wear resistance must be expressed in relation to a single standard material, and that the hardness of the abrasive used must be considerably higher than the hardness of the structural constituents. For the polymeric coating composites studied in this thesis, the additive phases such as silica, glass and aluminium oxide are much harder than the abrasive 'slickline wire' ($450HV_{30}$), therefore the LROM is not applicable to this study.

Fillers in the form of particulates and fibres are often embedded into a polymeric matrix to improve its mechanical properties. Fillers whose hardness and elastic modulus are greater than those of the polymer will increase the strength and initial elastic modulus of the mixture, at least in the case of good adhesion [53, 54] and hence are effective in reducing wear in dry sliding conditions involving adhesive transfer and fatigue. However, embedded fillers can either enhance or degrade other properties because performance depends strongly on the type of test, on the type of reinforcement, and upon the nature of the interface and the strength of the adhesion between the phases. In the case of polymer composites, the effect of fillers on abrasive wear is not, by any means, predictable [55]. Friedrich [56] has reported that the wear rate of thermoplastics is not improved by adding short fibres if the wear mechanism is highly abrasive in nature. In contrast, in the case of continuous fibre reinforcement, an increased wear resistance has been reported [57, 58]. Lancaster [59] has studied the effect of short carbon fibres (30%) in 13 polymers and reported that in six of them abrasive wear increased due to fibre reinforcement while in the remaining seven polymers a decrease in wear occurred. Bijwe et al. [48] tested polyamide (nylon 6), PTFE and their various composites in abrasive wear under dry and multipass conditions against silicon carbide (SiC) paper on a pin-on-disc device. Particulate fillers (except a bronze powder in PTFE) were observed to be detrimental to wear performance and polymers without fillers had better abrasive wear resistance than their composites. The abrasive wear rate of quartz and glass particle-reinforced PMMA polymer composites has been investigated by Prasad and Calvert [60]. Their experimental results revealed that the increased wear rate of these PMMA composites was due to enhanced chipping of the filler at the filler/matrix interface. When filled PMMA was abraded by soft abrasives, filler removal was mainly by particle pull-out which was very dependent on the filler/matrix interfacial strength. All the above indicates that the effect of fillers on the abrasive wear of polymers and their composites is determined by the properties of the matrix materials, the nature of the fillers, the amount and distribution of the embedded particles, and the interfacial bonding between the matrix and filler particles [61-64].

2.3.4 Effects of fillers on wear of polymer composites

The model shown in Figure 2.8 shows different cases for a hard protuberance causing two-body abrasive wear in a reinforced polymer composite. Reinforcing fillers affect wear by supporting the applied load with less deformation than the pure matrix, due to their greater strength and elastic modulus. Fillers always carry a proportionately greater part of the load than their volume fraction would imply, and can impede plastic deformation of the polymers. This effect of fillers on wear of polymer composites depends on the size, shape, orientation, abrasiveness and volume fraction etc. of the reinforcing phase.

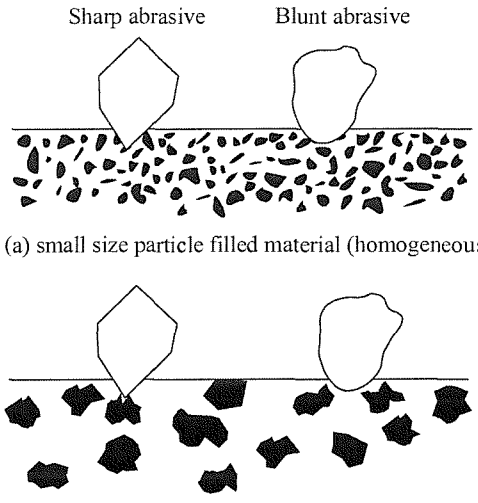

Fig. 2.8 Schematic diagram of hard abrasive penetrating into particle filled composite materials in two-body abrasive wear [65].

(a) Effect of the size of fillers

Fillers of medium size are more effective in reducing wear loss than very small or very large fillers [66]. The load carrying capacity should increase with the size of spherical fillers in dispersion structures. Reinforcing fillers of a size smaller than the indentation depth of the abrasive particles are easily dug out as shown in Figure 2.8 (a). Hence, the abrasive wear loss may increase with decreasing size of reinforcing fillers.

Tanaka and Kawakami [67] studied the effect of different fillers on PTFE based composites. They recommended a filler size ranging from several micrometres to about 30 μm as the most suitable for PTFE based composites. Small fillers within PTFE result in poor wear resistance of the PTFE; this is due to the fact that small fillers on the frictional surfaces cannot prevent large scale destruction of the banded structure of the PTFE matrix and thus very small fillers were easily removed from the wearing surface together with the PTFE film transferred onto the counterface. Krushchov and Babichev [68] stated that when incoherent fillers are smaller than abrasive grits and wear chips, they could be cut out with the matrix, adding little to the abrasion resistance of the material; however, when incoherent fillers are somewhat larger than the abrasive grits abrading the surface, they are generally effective in decreasing the total material wear. An optimum filler size can be expected, depending on the structure of a composite and operating conditions.

(b) Effect of the shape of fillers

The shape of the filler particles is one of the important factors that affect wear [48]. Irregular shaped particles of aluminium oxide in PTFE increased the rate of wear by a factor of several times over that found with spherical particles in the same polymer [69]. Figure 2.8 (b) shows a reinforced filler in the matrix being broken by the sharp abrasive, thus it loses its ability to support the load.

The influence of dispersed paint particles on the mechanical properties of rubber toughened polypropylene (PP) was investigated by Quazi et al. [69]. They revealed that the strain at break decreased more drastically with paint particles than glass beads. This demonstrated that irregularly shaped particles offered greater stress concentrations. Krushchov and Babichev [68] proved that hard, tough and blocky fillers can offer the best wear protection for the matrix material, since blocky fillers versus those that are plate- or rod-shaped fillers can effectively reduce crack propagation and breakage.

(c) Effect of volume fraction of fillers

The general rule that a high volume fraction of hard second phase particles is desirable for abrasion resistance is not, however, universally true [24]. The polymer matrix must also possess adequate toughness. In some polymers where the matrix itself is brittle and the particle-matrix interface is weak, hard particles can act as internal stress-concentrators; cracks initiate at the particle/matrix interface and then propagate through the matrix. A high volume fraction of the second phase in such a material then leads to enhanced wear by fracture mechanisms.

The wear behavior of mineral filler reinforced polypropylene (PP) was assessed by Sole and Ball [70] against a coarse (260 μm) and a fine (30 μm) abrasive belt. The mineral fillers investigated were talc, $CaCO_3$, $BaSO_4$ and fly ash. They measured a decreasing wear resistance with increase of filler contents wt%. The result was that an increasing volume of brittle constituents may substantially decrease the ductility of the composite. Reduced ductility, i.e. elongation to fracture, favours microcracking during abrasion and results in lower abrasive wear resistance.

Speerschneider [71] studied the abrasive wear of thermoplastics reinforced by short glass fibres and glass spheres against rough and fine Al_2O_3 paper. The abrasive wear loss of both polyethylene and polyamide increased with increasing weight fraction of fillers, independently of the filler shape.

(d) Effect of mean free path of the fillers

The volume fraction of a reinforcing phase is not sufficient for describing the abrasive wear resistance. The distribution of the reinforcing phase, represented by the mean free path, has to be considered as an additional factor. At a given volume fraction, a varying filler size leads to a varying mean free path between the reinforcing fillers. Decreasing the mean free path was found to be particularly effective in reducing the wear loss due to a coarse abrasive grit [58]. Figures 2.8 (a) and (b) schematically show the relationship of mean free path with the size of fillers. Assuming these two cases have the same fraction of reinforced fillers, then smaller fillers shown in (a) provide shorter mean free path than

that large fillers provide in (b). Therefore, the shorter mean free path shown in case (a) might provide better wear resistance to the matrix material. Generally, hard fillers which are relatively larger than the abrasive grits always offer better wear protection to the matrix material, however, in the case where abrasive grits are smaller than the gaps between fillers, then the grits are able to undermine the hard fillers, allowing them to detach out and their protecting ability towards the matrix material is lost [58].

(e) Effect of bonding

The filler/matrix bond is an additional factor which may influence abrasive wear loss. This has been demonstrated by Prasad and Calvert [60]. They studied three-body abrasion on PMMA reinforced by quartz and glass beads. SiC, SiO_2 or $CaCO_3$ abrasive slurries in water were used in the wear tests. A silane treatment of the fillers was carried out to improve the interfacial bond to the polymer matrix. The silane treatment resulted in stronger interfacial bonds compared with untreated samples. The improved filler-to-matrix bond due to the silane treatment resulted in markedly reduced wear loss. Non-silanated fillers were more easily pulled out from the matrix. Using soft abrasives such as $CaCO_3$, the fillers stood proud of the worn polymer matrix after wear testing. The wear loss from the fillers was very small, and wear loss was caused mainly by matrix loss and filler pull-out. Debonding of the filler from the matrix promotes wear processes such as pull out or fracture of the filler. Hence, the interfacial bond between matrix and filler plays an important role in the wear process.

PTFE and PEI (Polyethylenimine) proved to be good wear-resistant materials in a study by Bellow and Viswanath [72]. However, when combined with fillers, this showed a performance inferior to both parent polymers. SEM analysis of the pin surface revealed that there were a number of deep cracks propagating in the direction normal to the abrasion furrows. Poor adhesion of the filler gave rise to the initiation of the cracks and hence increased the wear rate.

In the study of the tensile behaviour of calcium carbonate-filled polystyrene [73], Godard et al. pointed out that the level of the matrix-filler adhesion could be defined as the stress

to be applied to the interface for dewetting. Their investigation showed that for low interfacial adhesion, crazes or shear bands are initiated at points located between the poles of fillers and the equatorial plane. In this case, a partial dewetting of the matrix surrounding the fillers has to be observed due to the applied load. The importance of this 'dewetting effect' depends directly on the level of the matrix-filler adhesion.

An enhanced crack resistance is often observed when impenetrable particles are effectively bonded into a brittle matrix [74]. According to the crack-pinning mechanism proposed by Lange [75], when a crack meets an array of such obstacles it becomes pinned and tends to bow out between the fillers, thus more energy is needed if new fracture surfaces are formed.

(f) Effect of abrasiveness of fillers

The abrasiveness of fillers affects the surface finish of the counterface substantially as well as when detached contributing to wear of the polymer itself [58]. Abrasiveness or hardness of the fillers can influence the coefficient of friction. Soft fillers such as graphite reduce, but the hard fillers such as SiO_2 can increase the coefficient of friction compared with the unfilled material.

Five kinds of polytetrafluoroethylene (PTFE) based composites, pure PTFE, PTFE + 30(v)% MoS_2, PTFE + 30(v)% PbS, PTFE+ 30(v)% CuS, and PTFE + 30(v)% graphite composites were investigated by Zhang et al. [76]. Experimental results under dry friction conditions show that graphite reduces the friction coefficient of the PTFE composite, but metal sulfides MoS_2, PbS, and CuS increase the friction coefficient of the PTFE composite. As for MoS_2, PbS or CuS-filled composites under dry friction conditions, the friction property of MoS_2-filled PTFE composite is the best, while that of CuS filled PTFE composite is the worst.

Saito and Takahashi [77] studied the wear and friction of particle filled polymers. Three polymer materials, polyoxymethylene (POM), high density polyethylene (HDPE) and polytetrafluoroethylene (PTFE), and bronze powder with shape indices (ratio of the major

axis to minor axis) of 1.1, 1.4 and 1.8 were tested under unlubricated conditions using a thrust washer type testing apparatus. The inclusion of bronze powder in POM, HDPE and PTFE increased the coefficient of friction. This is because the transfer film existing in the interface between the bronze powder particle and the slider is partially broken and the bronze powder particle contacts directly with the slider. It was also observed that a larger filler shape index in POM resulted in an increase of coefficient of friction.

Gong et al. [78] studied the wear of PTFE based composites, filled by incorporating a metallic net with inorganic fillers, by rubbing composite pins against a mild steel block on a reciprocating tester. It was found that the wear rate of the composites filled with a stainless steel net incorporating graphite is more than 300 times lower than that of pure PTFE. Similarly, Bahadur and Tabor [79] reported that when PTFE filled with polar graphite rubbing against flat counterfaces of mild steel and glass, graphite as a filler reduced the wear rate of PTFE by about factor of 100.

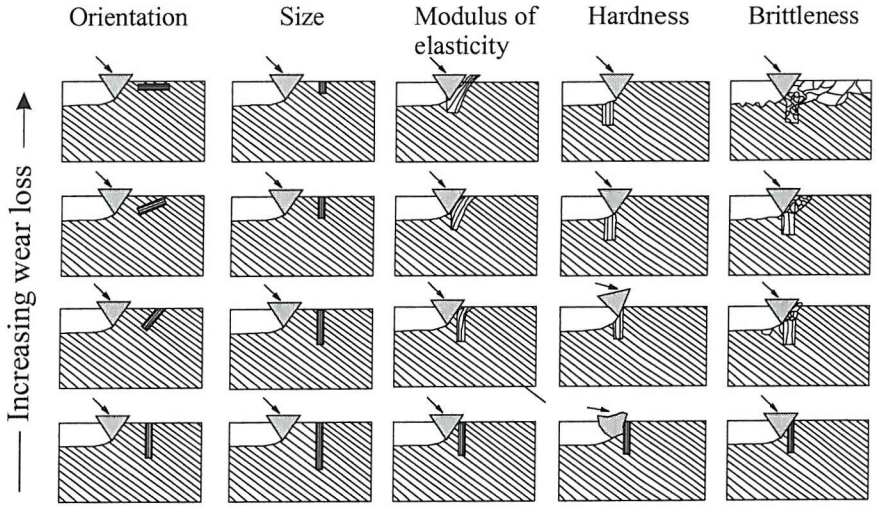

Fig. 2.9 The effect of orientation, size, modulus of elasticity, hardness, and brittleness of reinforcing constituents and / or matrix on the abrasive wear of composites [58].

(g) Effect of orientation of the fillers

As shown in Figure 2.9 [58], if the inclination of a filler in the polymer composite is close to the direction of movement of abrasive grits it will be easily pulled out providing less capability of preventing loss of matrix material and supporting less load.

Mcgee et al. [50] measured two-body abrasive wear of graphite fibre-reinforced polyimide against SiC abrasive paper. The unidirectional graphite fibre-reinforced polyimide is an oriented material. In the wear tests, the wear rates for this material were measured as a function of the fibre orientation relative to the wear direction and the abrasive plane. Normal orientation (N) is defined as the orientation in which the fibres are perpendicular to the abrasive plane. In the transverse orientation (T), the fibres are parallel to the abrasive plane and perpendicular to the wear direction, while in the longitudinal orientation (L) the fibres are parallel to the abrasive plane and parallel to the wear direction. The lowest wear rate was obtained for the N-oriented specimens. The abraded surface is relatively smooth with less evidence of fibre fragmentation as compared with the abraded surfaces in the L and T orientations. In the L orientation, the abraded surface shows evidence of debonding at the fibre-matrix interface; however, the amount of debonding at each fibre is not sufficient to result in the removal of the fibre, thus, the wear rate is low. Wear in the T orientation is probably governed by the degree of fibre-matrix debonding resulting in the highest wear rate. As debonding progresses, fibre failure probably occurs by column buckling of the partially debonded fibre. The fibres, abraded in the transverse direction, are subjected to transverse shear, bending and torsion loading by the SiC abrasive grains, resulting in fragments of fibres torn from the matrix.

The friction and wear properties of unfilled and filled liquid crystal polymers (LCPs) were examined by Uchiyama and Uezi [80] in the longitudinal (L), transverse (T) and normal (N) directions of the polymer molecules. When rubbed against emery paper at room temperature, the maximum abrasive wear rates tended to be observed in the T direction, because of easy cutting and detachment of the LCP molecules. The wear rates in the N direction were half the value of those in the T direction wear. The wear rates in the L direction were slightly lower than those in the T direction.

(h) Effect of ratio of the hardness of the abrasive grits to the hardness of fillers

Fillers harder than the abrasive grits act as strong barriers against grooving and reduce wear loss effectively, see Figure 2.9. Abrasive wear loss increases when the hardness of the abrasive grits increases relatively to the hardness of the reinforcing fillers. Prasad and

Calvert [60] pointed out in their study that the abrasive wear loss increased with increasing hardness ratio. Using a soft abrasive grit, i.e. hardness ratio smaller than or equal to unity, the wear loss decreased with increasing volume fraction of filler. In contrast, wear loss against a hard abrasive increased with increasing filler volume.

The hardness of the abrasive grits is important to the rate of abrasion of the wearing material. As the hardness of the abrasive exceeds that of the wear material, abrasive wear typically becomes much worse [65], as shown in Figure 2.10. As the abrasive hardness exceeds the hardness of the material, it is able to penetrate the surface and cut/remove material without having its cutting edges broken or rounded.

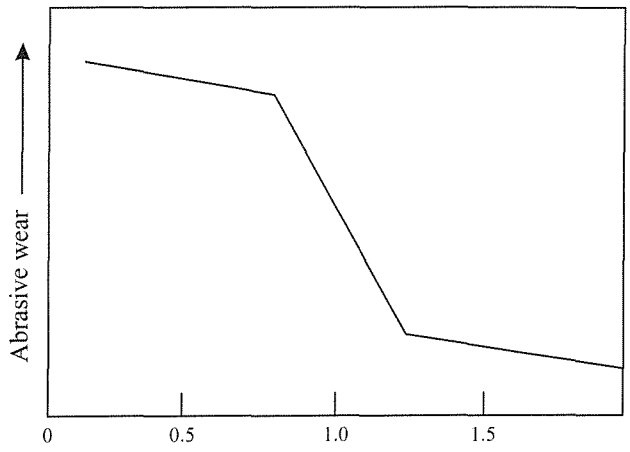

Fig. 2.10 Ratio of material hardness to abrasive hardness.

(i) Effect of modulus of elasticity and brittleness of the fillers

High modulus of elasticity and low brittleness of reinforced fillers are helpful to the wear resistance of polymer composites as they are not easily broken or dug out by the abrasive grits. Fillers having a low modulus of elasticity or hardness are easily deformed or broken by the abrasive grits and hence do not protect the matrix material.

Yu and Bahadur et al. [81] investigated the friction and wear behaviors of ceramic particle filled polyphenylene sulfide (PPS) composites. It has been reported that the wear resistance of PPS increased with the addition of ceramic fillers Si_3N_4, SiC and Cr_3C_2.

Visconti et al. [82] investigated the wear behavior of polymer composite materials with epoxy matrix filled with harder powder, sliding under dry conditions against a smooth steel counterface. The composite materials consisted of glass woven fabric reinforcing three different systems of matrix: epoxy resin, epoxy resin filled with SiO_2 and epoxy resin filled with WC powders. For all the materials examined the wear rate increases as the normal load increases, but not linearly. At low values of the sliding velocity and normal load, the composite materials with the unfilled matrix present values of the wear rate lower than the values of the composites with the filled matrix. This is due to the adhesive wear mechanisms that, for the unfilled matrix and under that test conditions, result relevant with respect to the abrasive wear mechanisms. At high values of the sliding velocity and normal load, the abrasive wear mechanisms could govern the interaction between the surfaces in contact; in these conditions the wear resistance of composite materials could be increased filling the matrix with harder powders. In particular, the composite with the matrix filled with WC powders was observed to present the highest value of wear resistance in more severe wear conditions.

(j) Conclusion

In conclusion, the wear of polymeric composites is influenced by the properties of the filler, of the matrix and of the interface, by the relative hardness of the filler to that of the abrasive grit or a counterface, by content, shape, size, distribution and orientation of filler, by the abrasiveness of filler against the matrix and last but not least by the loading conditions during abrasive wear.

2.4 Impact Resistance of Polymers

In a downhole work situation, when an inspection tool is lowered at speed it invariably strikes the coated inner surface of the water injector, as discussed in Section 1.2. Accompanying wireline wear, impact damage to the coating surface of downhole tubulars is caused by the inspection tool head at the same time. Figure 1.1 schematically shows how impact damage occurs in downhole tubulars. The impact energies are transferred to the protection system applied to the coating surface of the tubulars. Failure occurs if the

impact energies exceed the impact strength of the coating and expose the substrate, carbon steel, to corrosive attack. The subject of impact is therefore of interest.

Little work has been published on the subject of impact testing of polymeric coatings. The majority of the literature was found to reflect the interest in bulk polymer or sheet polymer testing where sample penetration was achieved by use of annular specimen clamps. This is unsuitable for polymer coating testing. This lack of directly relevant work highlights the need for research into this area.

2.4.1 Nature of impact tests

Impact tests are supposed to measure the toughness or the resistance to breakage of materials under high velocity impact conditions. The characteristics measured by most impact tests are complex quantities difficult to define in scientific terms, but they have great practical importance. Impact tests attempt to rank materials in terms of their resistance to breakage; this ranking is generally done by measuring the energy required to break a standard plastic object of the material under certain specified conditions [83-85]. The impact strength (or energy to break) of a ductile polymer may be much greater than the impact strength of a brittle polymer [86].

The field of impact testing is very complex for a number of reasons. First, there are a large number of impact tests. These tests all measure somewhat different quantities, some of which are not clearly defined or understood. Secondly, tests are made on specimens of various size and shapes. The specimens are broken under different kinds of stress distributions and under different speeds of impact. Finally, variations in the specimens themselves make it difficult to obtain reproducible results. Specimens may have surfaces which differ in behaviour from their interiors, or they may have varying degrees of molecular orientation which may be parallel or perpendicular to the stresses encountered during the impact test. As a result, many of the values of impact strengths published in the literature are practically useless [86]. It is not realistic to highly orient a material and

then test it in its strongest direction when in nearly all practical situations, the object will break in the direction in which it is weakest [87].

2.4.2 Standard impact test methods

Many impact testing methods have been devised for measuring the impact strength but there is little correlation among them. After many years of investigation several methods have found their way into recognized national and international specifications, those are discussed here as Standard Tests. These test methods may be divided broadly into three classes. First, there are methods based on pendulum-type machines, using either notched or unnotched specimens which may be of different sizes and supported as a cantilever (Izod), or as a bar supported at its ends (Charpy). Second, there are the falling-weight methods usually using sheet specimens with three point supports. The weight may be gradually increased in mass or dropped from increasing heights on the same specimen or onto a series of specimens. Third, there is the high-speed impact test.

2.4.2.1 Pendulum-type impact tests

Izod Impact Test. This test is based on an old, established metallurgical test in which a notched bar specimen is tested in cantilever fashion with an excess energy pendulum machine. The Izod test is used largely in the United States (ASTM D256-56) [28] and in the United Kingdom (BS 2782, Method 306A). A pendulum striker of 1/8-in. (3.2 mm) radius, falling from a height of 2 ft (610 mm) (ASTM) or 1 ft (310 mm) (BS), hits the specimen horizontally at a point above the notch. After the specimen has been fractured, the pendulum continues on its arc and the energy remaining is measured by the extent of the excess swing. Factors contributing to the total breaking energy as measured by the Izod test are: (a) energy to initiate fracture of the specimen; (b) energy to propagate fracture across the specimen; (c) energy for plastic deformation of the specimen; (d) energy to throw the broken end of the test piece; and (e) energy lost through vibration of the apparatus and its base and through friction [88]. For most materials (a) and (b) are the major factors, the first being dependent in a high degree upon the geometry of the notch. Factor (c) is important in materials that, even when notched, break by ductile failure.

Factor (d) is important in tests of materials of low impact strength and high density, i.e. a mineral-filled phenolic resin; in such cases, it is advisable to apply a correction for this effect.

Charpy Impact Test. The essential feature of the Charpy method of impact testing is that the test piece is mounted on a span support and struck centrally. In this case, also, the most common way of breaking the test piece and measuring the energy required is with a swinging pendulum. In a different version of the test, the results are expressed either in terms of energy to break per unit cross section at the point of break, or as energy to break per unit volume of test piece. In the Charpy test the sample is notched and is supported horizontally against the stops at either end. The pendulum striker hits the sample centrally behind the notch and the excess energy of the pendulum is then measured by the angle of the swing. A large number of samples are necessary to give an average value for the impact strength. The Charpy-type test used in the United Staes is ASTM D256-56, Method B; in Great Britain, it is BS 2782, Methods 306 D and E. Different Charpy test results can be caused by the conditions of the impact machine, the methods of machining and finishing the specimens and techniques of testing specimens [89].

Telfair and Nason [88] have analysed the pendulum type of tester. Such tests use a standard specimen which gives results that cannot be compared with specimens of other dimensions, therefore, the data have no absolute physical significance. These tests do not measure the true energy required to fracture the specimen. In addition to the energy to initiate a crack and the energy to propagate the crack through the specimen, these tests also measure the energy to permanently deform the material and the energy to throw the broken ends of the specimen. The energy used in throwing the pieces of the broken specimen contributes nothing to the toughness of the material, but this factor may represent a large fraction of the total energy measured by the test.

2.4.2.2 Falling-Weight impact test

The Falling-Weight Test has been actively developed in the United Kingdom (BS 2782, Method 306B). This is a test for assessing the impact resistance of material by subjecting

specimens, ordinarily in the form of sheet, to a direct blow from a falling weight. The Falling-Weight Test uses a spherical ball striker, 12.7 mm in diameter, attached to a load-carrying device to which weights can be attached. The striker slides freely in vertical guides and is released from a predetermined height to strike centrally on a specimen, which is supported on the base of the equipment. One recognized procedure for carrying out these tests is the "staircase" method in which the load is increased on successive specimens, each stuck once, until a specimen fails. The weight is then reduced until a specimen withstands the impact, after which it is increased again by fixed increments until a specimen fails again. This procedure is repeated using at least twenty samples, to determine the energy level at which 50% of the specimens break; the result is quoted as the impact strength for 50% failure (F_{50}).

The cause of failure of sheet material in practice is more likely to be closely simulated by a falling-weight impact test than by an Izod or Charpy test [90]; falling-weight tests thus give a more reliable guide to practical behavior. Vincent [91] summarized four advantages of the falling weight technique over the pendulum technique: (a) The falling-weight impact apparatus is comparatively cheap and easy to construct. There is no need for elaborate precautions to avoid energy absorption in the apparatus; (b) A pendulum machine cannot easily be used to study the effect of speed, because the velocity of impact is fixed. With a falling weight apparatus, the striking velocity can be varied by changing the height of drop; (c) The comment has been made that it is a disadvantage of the falling weight technique that the straining rate is not constant; the weight is slowed down as the specimen extends. However, in a way this is an advantage because it is more realistic; in practice, a limited energy is applied to the object by dropping or striking it. In the pendulum test, more than enough energy is used to break the specimen; (d) Pendulum tests can be seriously inaccurate. As discussed in section 2.4.2 (a), the energy lost by the pendulum may include, in addition to the energy needed to break the specimen, that wasted in distorting the apparatus and the kinetic energy of the moving clamp.

In the present research, a falling-weight type of impact rig will be used which was designed and built at the University of Southampton. This falling-weight impact rig

correlates much better with downhole working conditions and practical experience than does the pendulum type rigs, because in practical applications, the polymer coatings can be considered as having failed as soon as the first crack forms. Therefore, the falling-weight impact test is more suitable for current research because it can measure just the energy to form a crack rather than the energy to completely fracture the specimen [86].

2.4.3 Impact strength of polymer composites

Polymer toughness, in the form of impact resistance, is a measure of the ability of a material to withstand the application of a sudden load without "failure" [92]. Impact resistance is therefore a complex function of geometry, mode of loading, load application rate, environment (thermal and chemical), material properties such as chain length, packing, tacticity, alignment and bonding forces, and, of course, the definition of what constitutes failure. The measured impact strength of a polymer must be the result of the sum of the contributions of all processes that dissipate any of the energy of the impact blow, and is probably the most critical mechanical property of plastics, because it relates to the service life of the part, and involves the increasingly important matters of product safety and liability. Impact resistant polymer materials can be divided into three groups [93]. First, there is the group of materials, which, because of their inherent chemical structure, are tough even with no modification at all. This type of polymers includes acetal resin, phenoxy resin and polycarbonate etc. Second, there is the type of polymer material modified by another polymeric additive such as rubber. Mechanical blends of styrene-butadiene rubber with polystyrene (toughened polystyrene), acrylonitrile-butadiene-styrene copolymers (ABS), and toughened rigid poly(vinyl chloride) (PVC) fall into the this class. Third, there is the type which is modified by an inert material such as filler or reinforcement to give it greater toughness than the basic material possesses.

Since this study will concentrate on the impact resistance of filled polymeric coatings, only the third type of polymer materials (filled polymers) modified by filler or reinforcement will be discussed in this thesis.

2.4.3.1 Factors affecting the impact strength of polymer composites

Notch effect

A notch in a test specimen may drastically lower the measured impact strength of a material. A notch concentrates the stress in a small region during the impact test; the smaller the radius of curvature at the base of the notch the greater the stress concentration [94]. A notch has an effect similar to increasing the speed of testing by increasing the stressing rate in the neighborhood of the notch. By concentrating the stress in a small volume, a notch tends to decrease the apparent ductility of a material. Thus, a notch often has a greater apparent effect on ductile materials than on brittle ones [95]. However, even with a brittle, thermosetting, asbestos-filled phenolic, a notch decreases the Izod impact strength by a factor of eight.

Temperature and environmental effects

The impact strength of thermosetting polymers varies little with temperature over a very wide range. Between –80 and 200 °C the impact strength may be nearly constant [86]. The impact strength of thermoplastic material is generally strongly temperature dependent [96]. Near the glass temperature the impact strength dramatically increases with temperature. However, at temperatures well below the glass transition two rigid polymers can differ greatly in impact strength. For instance, cellulose nitrate and polycarbonates have much higher impact strengths than polystyrene or polymethyl methacrylate. The differences between these polymers is due primarily to secondary transitions. A polymer with a low temperature secondary glass transition is nearly always much tougher than a polymer which has no such transition [97]. Therefore, one of the main reasons for making polymer composites is to increase the impact strength of a brittle material by adding a rubber to it so that the material will have a low temperature transition in addition to its normal glass transition [98, 99].

The effects of temperature on impact properties of injection-molded glass nylon-6 composites were investigated by Takeda et al. [100] Impact fractured specimen surfaces showed the following observations: (1) At room temperatures the nylon-6 matrix exhibits

much ductility and extensive plastic deformation, in addition, much resin remains on many fibre surfaces under the impact tests, which demonstrates high fibre/matrix interfacial strength; (2) Less plastic deformation was observed at low temperatures than at room temperatures for nylon-6 matrix. Moreover, less resin exists on fibre surfaces and fibre pull-out length is much longer. Larger residual stresses are shown near fibre/resin interfaces at low temperatures due to the difference in the fabrication and test temperatures. Thus, it is easy for interfacial fractures or debondings to occur at low temperatures and plastic deformation capability is not fully utilised.

Ho and Fong studied the temperature dependence of high strain-rate impact fracture behavior in highly filled polymeric composite and plasticised thermoplastic propellants [101] The effect of temperature on the fracture behavior during high strain-rate (~ 10^3 sec^{-1}) impact of two highly filled polymeric composite propellants (containing segmented polyurethanes based on hydroxy-terminated polybutadiene (HTPB) or glycidyl azide polymer (GAP) filled with ammonium perchlorate (AP) particles) and a plasticised thermoplastic (cast double base (CDB) nitrocellulose-nitroglycerine) propellant has been examined over a wide temperature range encompassing the "brittle-ductile" transition. It was found that in the "elastic" region of the load-displacement curve the yield stress and fracture toughness is highest for GAP/AP and lowest for HTPB/AP. In the "elastic" and post-yield "ductile" regions CBD is more fracture-resistant than GAP/AP and HTPB/AP over the temperature range – 20 to 50 °C, but below – 40 °C, where both CDB and GAP/AP are brittle, GAP/AP is more fracture-resistant than CDB (as observed in the "elastic" region).

Fillers effect

Many polymeric materials in their unreinforced state are not satisfactory in applications for which good mechanical properties are essential. If improved stiffness or toughness of these materials can be obtained, their field of use can be considerably widened [102]. In order to obtain the greatest improvements in toughness by reinforcement, it is necessary for fibrous fillers or reinforcements to be used [103].

Fillers, especially fibrous ones, increase the impact strength of thermosetting phenolics and other brittle polymers [95, 104]. Fibres, distribute the stress over a large volume at the base of the notch; they can also stop the propagation of a crack by carrying a large portion of the loads in the neighborhood of a crack. Conversely, large quantities of nonfibrous fillers such as ground calcium carbonate in brittle polymers such as polystyrene decrease the impact strength. The filler particles act as stress concentrators in these cases.

The details of filler reinforced polymeric materials and the effects of fillers on the impact behavior of filled polymer materials are introduced in the following sections.

2.4.3.2 Fibre reinforced polymeric materials

Polyester resins have a number of properties which make them very satisfactory as a matrix for binding reinforcements to make articles of various types [85]. Reinforced with glass fibre in the form of either chopped-strand mat or of woven cloth, polyester resins have particularly good strength-to-weight ratios, impact resistance and even chemical resistance. Dough-molding compounds or premix made from polyester resins combined with glass fibres and other inert fillers are used in the preparation of moldings with exceptional toughness and rigidity. Molding materials containing glass-fibre reinforcement have also been made from melamine-formaldehyde resins, phenolic resins, alkyd resins, and epoxy resins with similar enhancement of properties [103].

The main factors affecting the impact strength of these glass-fibre reinforcement thermosetting molding materials is the length of the glass fibre [99]. Glass fibres of less than 3.2 mm, have little or no toughness effect. As the length of the fibre increases up to about 20 mm, the toughness increases accordingly. However, fabrication and manipulation of the materials become difficult with fibres above 12.7 mm length, and the usual range of fibre length is between 6.35 mm and 12.7 mm.

It is now possible to obtain commercially almost any thermoplastic resin reinforced with glass fibre [98]. In some cases toughness is enhanced but in others where tougher resins are used, impact strength can be reduced, especially with the shorter glass fibres. As is the case with thermosetting materials, little improvement in impact strength occurs with short glass fibres in any material. However, much higher stiffness, and better heat resistance, tensile strength, and creep resistance are obtained in all cases; this can lead to a widening field of use as well as to a greater range of available materials [98, 99]

Since thermoplastic polymers are ordinarily used in the form of granules of the order of 3.2 × 25.4 mm., rather than the dough or premix of thermosetting materials, the length of glass fibres is limited [98]. This has led to the use of larger pellets or strands, but these are much more difficult to fabricate and tend to degrade by the shortening of the fibres during processing. Difficulties in molding, leading to poor welds and other defects, can destroy the advantages of improved strength and toughness inherent in the materials [102]. New materials, therefore, have tended to be more of the short-fibre type; these are easier to manufacture and fabricate to give better dispersion and better joining of material where it flows together in the mould [102]. If glass-reinforced thermoplastic polymers are to give satisfactory improvement of properties, it is essential that the coupling or binding between the resin and the glass should be of high strength; in this connection the nature of any coupling agent is critical [103].

2.4.3.3 Particulate reinforced polymeric materials

The addition of mineral fillers to commercial thermoplastic or thermoset polymers reduces the overall cost of the composite and offers an important means of achieving new combinations of properties. The stiffness of polymers is generally enhanced by the incorporation of high modulus fillers. The effect of mineral fillers on the elastic modulus of polymers has been widely studied and there are many theoretical models available predicting the behavior of composites in the elastic zone [105-109]. The tensile and impact behavior of filled polymers at high strain levels is more complex and depends on non-elastic deformation mechanisms. The effect of particulate fillers on the tensile and

impact strength of polymers has been studied by many authors [110-112]. Some theories and models have been proposed [113-115]. The elaboration of theoretical models is a very difficult task because of the great number of parameters affecting the tensile and impact strength of particulate composites. The main parameters are: the filler weight or volume fraction, the particle shape, the particle size, the nature of the matrix and its adhesion to the filler particles. The effects of these parameters on the impact behavior of filled polymeric materials will be discussed in detail.

(a) Effect of interfacial agents on the impact behavior of filled polymer composites

In the case of poor interfacial adhesion between the fillers and the polymer matrix, the impact strength generally decreases with increasing filler loading [116]. It produces a situation in which the filler cannot sustain much load and the matrix may be considered as filled with voids. Moreover, when there is poor interfacial adhesion, the filler acts as a stress concentrator in a more effective manner. This effect also contributes to the reduction in tensile and impact strength of the material. Tensile and impact strength is generally enhanced when interfacial adhesion is improved. This can be ascribed to better stress transfer at the interface between the matrix and the filler. The improvement of interfacial adhesion can prevent dewetting (i.e. loss of contact) at the matrix-filler interface during tensile deformation. Therefore, well adhering filler particles can bear part of the load applied to the matrix and contribute to the tensile or impact strength of the composite. The addition of filler combined with an efficient coupling agent has proved to be a way to enhance the tensile and impact strength of polymers [117, 118]. However, the increase in adhesion may produce local changes in the micromorphology and the mechanical properties of the polymer chains bonded to the filler particles. That may result in the formation of a rigid polymer layer surrounding the filler particles. This rigid interphase may have mechanical properties rather closer to the filler than to the matrix. It increases the apparent volume fraction of filler and leads to a stiffer but more brittle composite [119].

Sahnoune et al. [116] investigated the effect of elastomer interfacial agents on the tensile and impact properties of $CaCO_3$ filled HDPE. Interfacial adhesion may be improved by

the addition of an elastomer which creates entanglements with the matrix and interacts with the filler surface. In order to increase both impact properties and the tensile strength of filled polymers, it appears interesting to create an adhesive elastomer interphase. When the amount of elastomer interfacial agent increases, the tensile yield stress is gradually enhanced until a maximum value corresponding to the maximum contribution of the filler. The tensile yield stress seems to be an interesting macroscopic property to follow the adsorption of the interfacial agent on the filler particles surface and the gradual modifications of the interface (i.e. surface coverage, degree of adhesion). It was observed that the extent of the increase in yield stress (i.e. filler contribution) with increasing amount of interfacial agent depends on both the interfacial area and the volume of filler. To obtain the highest potential contribution of fillers to the tensile strength, it is preferable to use fine particles and high filler loading. In this case, the amount of elastomer interfacial agent necessary to reach the maximum contribution of filler will also be high.

The impact behavior of epoxy specimens containing 10% by volume of fly-ash particles with their surface treated for improving or decreasing adhesion was studied by Kishore et al. [120]. The results showed that treatment of particulate fillers to improve their adhesion characteristics to the matrix improves the overall properties of the polymer composite system, especially strength and load bearing capacities. Among the various treatments, the silane treatment was found to be quite effective. Acetone-cleaned fly-ash particulate also yielded comparable results. Treatment with paraffin oil reduced adhesion and thus also the energy and load-bearing capacities during impact. Ductility index, however, showed a reversed trend with adhesion-reducing treatment yielding the highest value.

Levering and Nijenhuis [121] studied the influence of the interphase on impact properties of zirconium silicate filled high-density polyethylene. It was found that it is possible to incorporate a mineral filler in polyethylene without significant loss of impact strength of the polymer. To achieve this it is necessary to create a thick rubbery interphase that is bonded covalently to both filler and matrix polymer. A combination of covalent bonding and the formation of a flexible network at the interphase improves the impact strength to

that of the virgin polymer. The flexible rubbery network is capable of resisting the high forces during impact strength measurements, failure is transferred from adhesive (at the interphase) to cohesive (in the matrix). Hence, the creation of this type of interphase is a good method of incorporating a mineral filler in a polymer without loss of impact resistance.

(b) Effect of filler content, size and shape on the impact behavior of filled polymer composites

Filler content, size and shape are the important parameters for a particulate filled polymer material and correlate with the impact behavior of the material [92], and the complicity between various parameters of the filled polymer materials and the impact behavior has been investigated by many researchers [122-126].

A study of the influence of calcium carbonate on the impact energy of $CaCO_3$/high-density polyethylene composites was conducted by Suwanprateeb [127]. The impact resistance of composites was found to decrease as the volume fraction of calcium carbonate increased with the ductile-brittle transition at 20% filler volume fraction. This can be attributed to the effect of fillers on the initiation and propagation stages in the impact event. The impact crack initiation process of unfilled polyethylene was generated by craze formation. The addition of calcium carbonate changed the mechanism of initiation from crazing to microvoid nucleation, regardless of filler level. The propagation of cracks was observed to depend on the filler volume content or the proportion of ductile matrix remaining after filling. The propagation energy decreased with an increase in filler volume fraction (decrease in matrix effective cross section).

The effect of a titanate coupling agent (KR-11) modified talc on the impact behavior of PP/LDPE blends has been studied by Arroyo-Ramos and Lopez-Manchado [128] It was found that the impact strength mainly depends on matrix composition and hardly varies with the talc content. Only at high filler percentages (above 37%) was a significant decrease observed. In comparison with the unmodified talc filled composites, it can be deduced that, in general, the impact strength does not increase with the filler

organophilisation except in the case of composites with PP/LDPE ratio above 3 in the matrix composition and talc contents between 20~35% in the composite.

Liang et al. [129, 130] studied the effects of filler content and size on the impact fracture behavior of filled polypropylene binary composites. Three sizes of A-glass beads, 6000 (4 μm), 3000 (35 μm) and 1922 (219 μm), were chosen to identify the effects of filler content and size on the drop-weight dart impact fracture of filled polypropylene (PP) composites at room temperature. At higher filler concentration, the values of the maximum impact load and the crack initiation energy for the PP filled with smaller glass beads were higher than those of the unfilled PP and the systems filled with larger glass beads. However, the crack propagation energy of the former was lower than that of the latter. The influence of the filler content and size on the impact fracture energy of these composites was significant. Comparatively, the drop-weight dart impact resistance of the system filled with smaller glass beads was somewhat improved. Furthermore, microstructural observations indicated that the small rigid particles were more beneficial in initiating microcracks of the matrix interlayer around the inclusions than the larger ones, leading to an improvement of the impact resistance of the composites at high filler concentration.

Fong and Warren [131] studied the effect of particle shape and orientation on the inherent fracture toughness of a filled plasticized polymeric material Nitroguanidien (NQ). The crystalline NQ was used in the "as-received" form of needles and in a "ground" state. The material containing as-received NQ consistently had a higher fracture toughness than the material with ground NQ, and the toughness was a maximum when the fillers were aligned perpendicularly to the fracture surface.

Five different mineral fillers with different shapes (solid glass beads, hollow glass microspheres, quartz, alumina trihydrate and mica) were selected by Pritchard and Yang [132] to study the low-energy impact damage of particulate-filled glass-epoxy laminates by means of a falling weight device. Approximately 8.5 mm thick laminates, with and without fillers, were impacted at various energies up to 43 J. The tests indicated that the

unfilled glass-epoxy laminates showed the best resistance to impact damage, and had the smallest damage zone in all cases. This can be attributed to their having lower stress concentrations and fewer weak interfaces than the filled ones. The hardest filler, quartz, induced a larger damage area and more severe damage at higher impact energies. Mica and hollow glass spheres caused the most significant reduction in impact damage resistance of laminates. Mica particles have an easily delaminated structure and irregular shape. The first feature produces relatively weak interfaces between laminates, easily broken by impact-induced shear stress. The second feature induces stress concentrations at which cracks are initiated. Among the five fillers, glass beads gave the least damage at all impact energies. The chief reason is believed to be their intrinsic strength, but minor contributions may be made by their favorable spherical shape and the resistance they provide to delamination. From this study, it is concluded that particle shape had a small, but noticeable effect on impact damage. Spherical particles required increased impact energy to generate the stress concentrations required to initiate delamination in laminates.

2.4.4. Impact damage of polymeric composite coatings

Compared to bulk polymers, there is very little literature on impact tests on polymer coatings, which gives all the more importance to the present work.

Hocking [133] pointed out problems with coatings, many of which can be applied to polymeric coatings: porosity, adhesion, substrate compatibility, cost, possibility of renewal or repair, inter-diffusion, effect of thermal cycling and corrosion. Another problem is that of internal stress. Internal stress is present in many types of polymeric surface coating to a greater or lesser extent. It effectively reduces the adhesion between the coating and substrate or between binder and filler. The internal stress energy stored in a coating increases with thickness [134]. Polymeric coatings tend to shrink as they dry due to chemical changes or physical changes, for example solvent evaporation. However, the area of coating is constrained to remain at its original wet size by adhesion to a normally rigid substrate. After the coating has solidified and can no longer flow, further

chemical change or solvent loss produces a residual internal tensile stress in the plane of the coating as it proceeds to its final dry state [134].

A novel testing technique, micro-impact testing, has been recently developed by Beake et al. [135], and has been evaluated on materials ranging from soft polymers to hard TiN films [136, 137]. The primary objective of the development was to produce quantifiable techniques that closely simulate the conditions that thin films experience in service. Variations of the technique allow measurements related to: impact wear and adhesion failure, erosive wear resistance, fracture toughness, work hardening, and dynamic hardness. This technique for thin films can be used to carry out single or repeated impacts for measurement of impact wear. The impact energy can be controlled and either single impacts or multiple impacts can be produced. For single impacts, the energy delivered to the contact point can be quantified, allowing calculation of a dynamic hardness number. In the micro-impact technique, the sample is oscillated at high frequency by a piezoelectric oscillator connected to a signal generator, whilst subjected to a static load. Depending on the oscillation amplitude and frequency (and therefore the energy supplied to the contact point) either impact or contact fatigue behavior can be observed. During the impact test, the probe 'bounces' on the surface, which can lead to impact wear (high frequency repetitive contact testing). In contrast, during the contact fatigue test, the amplitude of oscillation is lower and the probe stays in contact with the sample. The surface is then subjected to a fatigue process by a repetitive flexing and relaxing of the contact point. The evolution of surface damage is followed by continuously monitoring the probe position. Coating failure, such as coalescence of small cracks leading to brittle fracture, is revealed by abrupt changes in probe depth. After testing a wide range of specimen, from diamond like carbon (DLC) films and titanium nitride (TiN) coatings to soft polymeric films, by the micro-impact testing technique, the results showed: the new technique provides a new approach to the investigation of fracture toughness; time to failure and the overall change in probe depth during a test are measures of the resistance of the coating to fracture [137].

Taylor et al. [138] measured the hypervelocity impact response of the silicon wafers coated with metal and polymeric coatings. The metal and polymeric coatings produced diverse damage morphologies, with delamination zones being up to twice the diameter (diameter approximately 1 mm) of the damage area (diameter approximately 0.5 mm). The results indicate that impact on silicon wafers will define a large damage area and the fracture-based failure modes suggest that further post-impact crack growth may occur.

Kim and Mai [139] pointed out that one of the most effective methods in controlling the interface to enhance the fracture toughness of fibre composites is the application of polymer coatings, either fully or intermittently along the fibre length. The enhancement of transverse fracture toughness of unidirectional Kevlar and carbon fibre reinforced epoxy rein composites (KFRP and CFRP) has been studied using polymer coating on the fibres. The results showed a substantial improvement in the impact fracture toughness of both KFRP and CFRP with a polyvinyl alcohol (PVAL) coating, the improvement being by about 100%, without any loss of flexural strength; but there was only a moderate increase in impact toughness with other types of coatings (i.e. carboxyl-terminated butadiene acrylonitrile (CTBN) copolymer and polyvinyl acetate (PVA)) with some reduction in flexural strength.

Past field history has shown the effectiveness of internal plastic coatings as a primary tool for corrosion control in secondary and tertiary recovery programs. In recent times, new coating materials have been developed by coating manufacturers that enhance the previous coating performance by providing materials with greater flexibility and impact resistance [140]. Comparative laboratory test results for seven internal plastic coatings, evaluated for use in sweet oil well service, were provided by Lewis and Barbin [141]. These plastic coatings are: epoxy ceramic, modified epoxy/phenolic, phenolic, nylon powder, novolac powder, modified epoxy and phenolic. The coating evaluation program included autoclave, rocker arm, acid resistance, wireline abrasion, and impact resistance tests. Tests were designed to compare coating performance under harsh conditions such as high water production, temperature up to 150 °C, and high carbon dioxide (CO_2) gas concentration. The evaluation of the seven coatings showed that all the products do not

perform equally well in each test; there were substantial performance differences between the internal coatings and no single coating performed best in all tests. Most of the coatings had strengths under some test conditions while exhibiting weakness in other test environments. For example, the nylon powder coating clearly dominated the wireline abrasion and external deformation tests but performed poorly in the acid resistance and impact resistance tests. The test program was judged to be particularly useful for identifying and quantifying the performance strengths and weakness of all coatings tested.

Symonds [30] extensively investigated the impact damage mechanisms of particulate filled thermoplastic and thermoset polymeric coatings. Through analyses of high-speed video film, she was able to identify the salient features of the impact damage process, and to reconstruct the order of impact events. Some useful results were deduced from Symonds' study, which are relevant to the present experimental work: the tough, elastic, nylon coatings deformed plastically upon impact; the coatings were identified as suited for the application of water injectors, if they were made thicker; the thermoset coatings, when impacted, failed by cracking which was a result of the impact induced buckling forces; the damage to modified epoxy coatings could be reduced by decreasing the coating thickness and limiting the filler content to less than 30%. However, cracking remained the dominant damage mechanism, making the coatings unsuitable for downhole applications.

Further information and descriptions of experimental methods and analyses of damage mechanisms involved in impact tests for polymer coatings can be found in Symonds' thesis [30].

REFERENCES:

[1] Donald R. Askeland, The Science and Engineering of Materials, Stanley Thornes Publishers Ltd (1998).

[2] G.M. Bartenev and V.V. Lavrentev, Friction and Wear of Polymers, Elsevier (1981).

[3] Christopher Hall, Polymer Materials-2nd ed., Macmillan Education Ltd (1989).

[4] N. G. McCrum, C. P. Buckley, and C.B. Bucknall, Principles of Polymer Engineering, Oxford University Press (1988).

[5] Stephen L. Rosen, Fundamental Principles of Polymeric Materials, A Wiley-Interscience Publication, John Wiley & Sons, pp 303-311.

[6] M. M. Schwartz, Composite Materials Handbook, McGraw-Hill Book Company (1983).

[7] A. G. Atkins, Elastic and Plastic Fracture, Ellis Horwood Limited (1985).

[8] K. L. Mittal, Adhesion Aspects of Polymeric Coatings, Plenum Press, (1983).

[9] Rober H. Davis, The Use of Internal Plastic Coatings to Mitigate CO_2 Corrosion in Downhole Tubulars, NACE, Corrosion 94, Paper No. 23.

[10] John M. Nelson, New Advancements in the Use of Internal Plastic Coating for Enhanced Oil Recovery, Materials Performance, Vol. 30, No. 12 (1991), pp 27-30.

[11] J. F. Archard and W. Hirst, The Wear of Metals under Unlubricated Conditions, Proceeding of the Royal Society of London A. 236 (1956), pp 397-412.

[12] OCED, Friction, Wear and Lubrication — Terms and Definitions, Res. Group on Wear of Engineering Materials, Paris (1969).

[13] A. Ravikiran, Wear Quantification, Journal of Tribology, 122 (2000).

[14] K. C. Ludema and D. Tabor, The Friction and Viscoelastic Properties of Polymeric Solids, Wear 9 (1966), pp 329-348.

[15] R. F. King and D. Tabor, The Effect of Temperature on the Mechanical Properties and the Friction of Plastics, Proceeding of Physics Society B. Vol. B66 (1953), pp 728-736.

[16] C. M. Pooley and D. Tabor, Friction and Molecular Structure: the Behaviour of Some Thermoplastics, Proceeding of the Royal Society of London A. 329 (1972), pp 251-274.

[17] J. K. Lancaster, Relationships Between the Wear of Polymers and Their Mechanical Properties, Proceeding of the Institution of Mechanical Engineerings, Vol. 183 (1968), pp 98-114.

[18] J. F. Archard, Contact and Rubbing of Flat Surfaces, Journal of Applied Physics, 24 (1953), pp 981-988.

[19] Standard Terminology Relating to Wear and Erosion, Annual Book of Standards, Vol. 03.02, ASTM (1987), pp 243-250.

[20] E. Rabinowicz, Friction and Wear of Materials, Wiley, New York (1965).

[21] K. H. Zum Gahr, Microstructure and Wear of Materials, Elsevier (1987), pp 513-524.

[22] K. H. Zum Gahr, Formation of Wear Debris by the Abrasion of Ductile Metals, Wear 74 (1981), pp 353-373.

[23] J. K. Lancaster, Abrasive Wear of Polymers, Wear 14 (1969), pp 223-239.

[24] A. Alliston-Greiner, Guidelines for Laboratory Wear Testing, The 1996 Donald Julius Groen Prize Lecture (1996), Organised by Tribology Group of the IMechE.

[25] J. K. Lancaster, Basic Mechanisms of Friction and Wear of Polymers, Plastics & Polymers (1973), pp 297-306.

[26] S. B. Ratner and I. I. Farberova., Connection Between Wear Resistance of Plastics and Other Mechanical Properties, Abrasion of Rubber, MacLaren & Sons, London (1967), pp 145-152.

[27] D. Dowson, J. R. Atkinson, and K. Brown, The Wear of High Molecular Weight Polyethylene with Particular Reference to Its Use in Artificial Human Joints, Advances in Polymer Friction and Wear, Vol. 5B, Plenum Press (1975), pp 533-548.

[28] ASTM D256-56, Standard Methods of Test for Impact Resistance of Plastics and Electrical Insulating Materials, ASTM Standards, Part 9 (1958), Philadelphia, pp 284-291.

[29] A. I. Sviridyonok and Y. E. Kirpichenko, Standardisation of Laboratory Methods to Evaluate Friction Behaviour of Polymer-Based Materials (1984), pp 332-387.

[30] N. Symonds, Polymer Coatings for Wireline Wear and Impact Resistance, PhD Thesis, University of Southampton (2001).

[31] D. C. Evans and J. K. Lancaster, The Wear of Polymers, Treatise on Materials Science and Technology, Vol. 13 (1979), pp 85-139.

[32] J. K. Lancaster, Polymer-based Bearing Materials-The Role of Fillers and Fibre Reinforcement, Tribology 5 (1972), pp 249-255.

[33] B. Briscoe, Wear of Polymers: An Essay on Fundamental Aspects, Tribology International (1981), pp 231-243.

[34] M. P. Steward, Friction and Wear of PTFE Composites, PhD Thesis, University of Cambridge (1978).

[35] B. J. Briscoe, M. D. Steward and A. Groszek, The Effect of Carbon Aspect Ratio on the Friction and Wear of PTFE, Wear, 42 (1977), pp 99-108.

[36] B. Arkles, J. Theberge and M. Schireson, Wear of Thermoplastic Filler PTFE Composites, J. American Soc., Lubrication Engineering 33 (1977), pp 33-38.

[37] B. Arkles, S. Gerakaris and R. Goodhue, Wear Characteristics of Fluoropolymer Composites, pp 663-668.

[38] K. Tanaka, Friction and Wear of Glass and Carbon-Filled Thermoplastic Polymers, pp 510-517.

[39] B. J. Briscoe, A Pogosian and D. Tabor, The Friction and Wear of High Density Polythene: The Action of Lead Oxide and Copper Oxide Fillers, Wear 27 (1974), pp19-34.

[40] B. C. Arkles and M. J. Schireson, The Molecular of PTFE Wear Debris, Wear 39 (1976), pp 177-180.

[41] N. P. Istomin and M. M. Krushchov, The Effect of the Cleavage Plane Orientation of Graphite on the Friction and Wear of Its Compositions with PTFE-4, Mechanical Science, Vol. 1 (1973), pp 97-101.

[42] R. R. Hart, Performance of PTFE Based Piston Rings in an Unlubricated Reciprocating Compressor, Proceeding of the Institution of Mechanical Engineerings, Vol. 181 (1966), pp 13-17.

[43] J. H. Fuchsluger and R. D. Tabor, The Effect of Atmospheric Environment on the Wear Properties of Filled TFE Materials, Journal of Lubrication Technology, Vol. 93 (1971), pp 423-429.

[44] J. E. Teberge, B. C. Arkles and P. Cloud, Mechanical Design (1974), pp 60-76.

[45] J. P. Giltrow and J. K. Lancaster, The Role of the Counterface in the Friction and Wear of Carbon Fibre Reinforced Thermosetting Resins, Wear 16 (1970), pp 359-374.

[46] J. K. Lancaster, Polymer-based Bearing Materials-The Role of Fillers and Fibre Reinforcement, Tribology 5 (1972), pp 249-255.

[47] C. J. Speerchneider and C. H. Li, The Role of Filler Geometrical Shape in Wear and Friction of Filled PTFE, Wear 5 (1962), pp 392-399.

[48] J. Bijwe, C. M. Logani and U. S. Tewari, Influence of Fillers and Fibre Reinforcement on Abrasive Wear Resistance of Some Polymeric Composites, Wear, pp 92-102.

[49] S. V. Prasad and P. D. Calvert, Abrasive Wear of Particle-Filled Polymers, Journal of Materials Science 15 (1980), pp 1746-1754.

[50] A. C. Mcgee, C. K. H. Dharan and I. Finie, Abrasive Wear of Graphite Fibre-Reinforced Polymer Composites Materials, Wear 114 (1987), pp 97-107.

[51] W. Simm and S. Freti, Abrasive Wear of Multiphase Materials, Wear 129 (1989), pp 105-121.

[52] M. M. Khruschov, Principles of Abrasive Wear, Wear 28 (1974), pp 69-88.

[53] Stephen L. Rosen, Fundamental Principles of Polymeric Materials, A Wiley Interscience Publication, John Wiley & Sons, pp 303-311.

[54] Lawrence E. Nielsen, Mechanical Properties of Polymers and Composites, Vol. 2, Marcel Dekker, New York (1974).

[55] J. M. Thorp, Abrasive Wear of some Commercial Polymers, Tribology International, 15 (1982), pp 59-68.

[56] K. Friedrich, Wear of Reinforced Polymers by Different Abrasive Counterparts. In K. Friedrich (ed.), Friction and Wear of Polymer Composites – Composite Materials Series 1, Elsevier, Amsterdam (1986), pp 233-287.

[57] M. Cirino, R. B. Pipes and K. Friedrich, The Abrasive Wear Behaviour of Continuous Fibre Polymer Composites, Journal of Material Science, 22 (1987), pp 2481-2492.

[58] K. H. Zum Gahr, Microstructure and Wear of Material, Tribology Series 10, Elsevier, Amsterdam (1987).

[59] J. K. Lancaster, Friction and Wear, in A. D. Jenkins (ed.), Polymer Science, A, Material Science Handbook, North Holland, Amsterdam (1972).

[60] S. V. Prasad, P. D. Calvert, Abrasive Wear of Particle-filled Polymers, Journal of Materials Science, 15 (1980), pp 1746-1754.

[61] K. H. Zum Gahr, Wear by Hard Particles, New Direction in Tribology, I. M. Hutchings (ed.), published by Mechanical Engineering Publications Limited (1997), pp 483-494.

[62] L. Nicolais, E. Drioli and R. R. Landel, Mechanical Behaviour and Permeability of ABS/Glass Bead Composites, Polymer, Vol. 14 (1973), pp 21-26.

[63] R. T. Quazi, S. N. Bhattacharya and E. Kosior, The Effect of Dispersed Paint Particles on the Mechanical Properties of Rubber Toughened Polypropylene Composites, Journal of Materials Science, 34 (1999), pp 607-614.

[64] A. Meddad, B. Fisa, Filler-Matrix Debonding in Glass Bead-filled Polystyrene, Journal of Material Science, 32 (1997), pp 1177-1185.

[65] I. M. Hutchings, Tribology: Friction and Wear of Engineering Materials, Edward Arnold (1992).

[66] Lee, H. L., Orlowski, J. A., Kidd, P.D., Glace, R. W., and Enable, E.: Evaluation of wear resistance of dental restorative materials, in Advances in Polymer Friction and Wear. Lee, L.-H., ed., Plenum Press, New York (1974), pp 705-722.

[67] K. Tanaka, S. Kawakami, Effect of Various Fillers on the Friction and Wear of Polytetrafluoroethylene-Based Composites, Wear 79 (1982), pp 221-234.

[68] M. M. Krushchov and M. A. Babichev, Resistance to Abrasive Wear of Structurally Inhomogeneous Materials, D.A.N., SSSR, Vol. 107 No. 1 (1956), pp 5-23.

[69] R. T. Quazi, S. N. Bhattacharya and E. Kosior, The Effect of Dispersed Paint Particles on the Mechanical Properties of Rubber Toughened Polypropylene Composites, Journal of Materials Science 34 (1999), pp 607-614.

[70] B. M. Sole and A. Ball, On the abrasive wear behaviour of mineral filled polypropylene, Tribology International, Vol. 29 (1996), pp 457-465.

[71] C. J. Speerschneider and C. H. Li, Some Observation on the Structures of Polytetrafluoroethylene, Journal of Applied Physics, 33 (1962), pp 1871-1875.

[72] D. G. Bellow and N. S. Viswanath, An Analysis of the Wear of Polymers, Wear 162-164 (1993), pp 1048-1053.

[73] P. Godard, Y. Bomal and J. J. Biebuyck, Influence of Interactions on the Tensile Behaviour of Polystyrene Filler with Calcium Carbonate, Journal of Materials Science 28 (1993), pp 6605-6610.

[74] A. J. Kinloch, D. L. Maxwell and R. J. Young, The Fracture of Hybrid-Particulate Composites, Journal of Materials Science, 20 (1985), pp 4169-4184.

[75] F. F. Lange, The Interaction of a Crack Front with a Second-phase Dispersion, Philosophical Magazine, 22 (1970), pp 983-992.

[76] Z. Z. Zhang and Q. J. Xue, Friction and Wear Characteristics of Metal Sulphides and Graphite-Filled PTFE Composites Under Dry and Oil-Lubricated Conditions, Journal of Applied Polymer Science, Vol. 72 (1999), pp 751-761.

[77] A. Saito, H. Takahashi, The Influence of Filler Geometrical Shape on the Friction and Wear of Particle Filled Polymers, Science and Engineering of Composite Materials, Vol. 6 (1997), pp 95-109.

[78] D. Gong, Q. Xue and H. Wang, Study of the wear of filled polytetrafluoroethylene, Wear 134 (1989), pp 283-295.

[79] S. Bahadur and D. Tabor The wear of filled polytetrafluoroethylene, Wear 98 (1984), pp 1-13.

[80] Y. Uchiyama, Y. Uezi and A. Kudo, Effect of temperature on the wear of unfilled and filled liquid crystal polymers, Wear 16 (1993), pp 656-661.

[81] L. Yu, S. Bahadur and Q. Xue, An investigation of the friction and wear behaviors of ceramic particle filled polyphenylene sulfide composites, Wear 214 (1998) pp 54-63.

[82] I. C. Visconti, A. Langella and M. Durante, The Wear Behaviour of Composite Materials with Epoxy Matrix Filled with Hard Power, Applied Composite Materials, Vol. 8 (2001), pp 179-189.

[83] D. R. Morey, Impact Testing of Plastics, Industrial and Engineering Chemistry, Vol. 37 (1945), pp 255-263.

[84] H. Burns, Encyclopedia of Polymer Science and Technology, Vol. 7, Interscience, New York (1967), pp35-57.

[85] P. I. Vincent, Impact Tests and Service Performance of Thermoplastics, Plastics Institute, London (1971).

[86] Lawrence E. Nielsen, Mechanical Properties of Polymers, Reinhold Publishing Corporation (1962).

[87] C. H. Adams, G. B. Jackson, and R. A. McCarthy, The Utility of Impact Testing as a Measure of Toughness, Society of Plastics Engineering Journal, Vol. 12 (1956), pp13-16.

[88] D. Telfair, T. S. Carswell and H. K. Nason, Creep properties of molded phenolic plastics, Modern Plastics, 20 (1943), pp 137-147.

[89] D. E. Driscoll, Reproducibility of Charpy Impact Test, Symposium on Impact Testing, ASTM STP 176 (1955), pp 70-77.

[90] R. A. Horseley, Impact Testing of Plastic, Transaction of Plastics Institute, Vol. 30 (1962), pp 164-171.

[91] P. I. Vincent, Tensile Impact Tests, Materials (1962), pp 133-135.

[92] Willam G. Perkins, Polymer Toughness and Impact Resistance, Polymer Engineering and Science, Vol. 39 (1999), pp 2445-2460.

[93] W. E. Wolstenholme, Characterizing Impact Behavior of Thermoplastics, Journal of Applied Polymer Science, Vol. VI, No. 21 (1962), pp 332-337.

[94] R. D. Cadle and W. C. Thuman, Filters From Submicron-Diameter Organic Fibers, Industry and Engineering Chemistry, Vol. 52 (1960), pp 315-316.

[95] D. Telfair and H. K. Nason, Impact Testing of Plastic, Part II-Factors Which Influence the Energy Absorbed by the Specimen, Modern Plastics, 22 (1945), pp 145-149.

[96] J. A. Schmitt and H. Keskkula, Short-Time Stress Relaxation and Toughness of Rubber-Modified Polystyrene, Journal of Applied Polymer Science, Vol. III, No. 8 (1960), pp 132-142.

[97] E. G. Bobalek and R. M. Evans, An Investigation of Some Variables Affecting Impact Resistant Thermoplastics, Transaction of Society of Plastic Engineering, Vol. 1 (1961), pp 93-100.

[98] R. Bueche and L. E. Nielsen, Multiple Dispersion Regions in Rigid Polymeric Systems, Journal of Polymer Science, 15 (1955), pp 1-8.

[99] E. H. Merz, G. C. Claver and M. Baer, Studies on Heterogeneous Polymeric Systems, Journal of Polymer Science, 22 (1956), pp 325-341.

[100] N. Takeda, D. Y. Song and K. Nakata, Effects of temperature and water content on impact properties of injection-molded glass nylon-6 composites, Advanced Composite Materials, Vol. 5 (1996), pp 201-212.

[101] S. Y. Ho and C. W. Fong, Temperature dependence of high strain-rate impact fracture behavior in highly filled polymeric composite and plasticised thermoplastic propellants, Journal of Materials Science 22 (1987), pp 3023-3031.

[102] T. Huff, C. J. Bushman and J. V. Cavender, A Study of the Effect of Branching on Certain Physical and Mechanical Properties of Stereoregular Polypropylene, Journal of Applied Polymer Science, Vol. 8 (1964), pp 825-837.

[103] R. Pritchard, T. Dunn and P. Kelly, Effects of Morphology and Molecular Structure on Tensile Impact Behavior of Linear Polyethlene, Journal of Applied Polymer Science, Vol. 8 (1964), pp 1751-1762.

[104] T. S. Carswell, D. Telfair and R. U. Haslanger, Temperature vs. Strength for Phenolics, Modern Plastics, Vol. 19 (1942), pp 65-69.

[105] A. Mamat, T. Vu-Khanah, P. Cigana, B. D. Favis, Impact fracture behavior of nylon-6/ABS blends, Journal of Polymer Science, Part B: Polymer Physics, Vol. 35 (1997), pp 2583-2592.

[106] A. E. Johnson, D. R. Moore, R. S. Prediger, P. E. Reed and S. Turner, The falling weight impact test applied to some glass-fibre reinforced nylons, Journal of Materials Science 21 (1986), pp 3153-3161.

[107] C. C. Lee, W. Rovatti, S. M. Skinner and E. G. Bobalek, Effects of mixing variables and talc fillers on tensile and impact fatigue properties of some thermoplastic blends of poly(vinyl chloride) with acrylonitrile-butadiene copolymer rubber, Journal of Applied Polymer Science, Vol. 9 (1965), pp 2047-2070.

[108] T. Xu, H. Lei and C. S. Xie, Investigation of impact fracture process with particle-filled polymer materials by acoustic emission, Polymer Testing 21 (2002), pp 319-324.

[109] T. Labour, G. Vigier, R. Seguela, C. Gauthier, G. Orange and Y. Bomal, Influence of the ß-crystalline phase on the mechanical properties of unfilled and calcium carbonate-filled polypropylene: ductile cracking and impact behavior, Journal of Polymer Science, Part B: Polymer Physics, Vol. 40 (2002), pp 31-42.

[110] M. –Y. Tang, A. Letton and J. E. Mark, Impact resistance of unfilled and filled bimodal thermosets of poly(dimethylsiloxane), Colloid & Polymer Science, 262 (1984), pp 990-992.

[111] R. W. Cahill, Charpy impact fracture testing – a precise measure of ductile-brittle transition in a filled polymer system, Polymer Engineering and Science, Vol. 21 (1981), pp 1228-1233.

[112] T. J. Hutley and M. W. Darlington, Impact strength – d.s.c. correlation in mineral-filled polypropylene, Polymer Communications, Vol. 25 (1984), pp 226-228.

[113] T. J. Hutley and M. W. Darlington, Further observations on impact strength – d.s.c. correlation in mineral-filled polypropylene, Polymer Communications, Vol. 26 (1985), pp 264-267.

[114] M. Niinomi, K. Uwai, T. Kobayashi and A. Okahara, Impact fatigue properties of epoxy resin filled with SiO_2 particles, Engineering Fracture Mechanics, Vol. 38 (1991), pp 439-449.

[115] L. S. Chen, Y. W. Mai and B. Cotterell, Impact fracture energy of mineral-filled polypropylene, Polymer Engineering and Science, Vol. 29 (1989), pp 505-512.

[116] F. Sahnoune, J. M. Lopez-Cuesta and A. Crespy, Effect of elastomer interfacial agents on tensile and impact properties of CaCO3 filled HDPE, Journal of Materials Science 34 (1999), pp 535-544.

[117] T. Huff, C. J. Bushman and J. V. Cavender, A study of the effect of branching on certain physical and mechanical properties of stereoregular polypropylene, Journal of Applied Polymer Science, Vol. 8 (1964), pp 825- 837.

[118] R. Pritchard, T. Dunn and P. Kelly, Effects of morphology and molecular structure on tensile impact behavior of linear polyethylene, Journal of Applied Polymer Science, Vol. 8 (1964), pp 1751-1762.

[119] P. W. R. Beaumont, P. G. Riewalid and C Zweben, Methods for improving the impact resistance of composite materials, ASTM STP 568, American Society for Testing and Materials, Philadelphia (1975), pp 134-158.

[120] Kishore, S. M. Kulkarni, D. Sunil and S. Sharathchandra, Effect of surface treatment on the impact behavior of fly-ash filled polymer composites, Polymer International 51 (2002), pp 1378-1384.

[121] A. W. Levering and K. TE Nijenhuis, Influence of the interphase on impact properties of zirconium silicate filled high-density polyethylene, Journal of Adhesion, Vol. 45 (1994), pp 137-148.

[122] J. Z. Liang, Tensile and impact properties of hollow glass bead filled PVC composites, Macromolecular Materials Engineering, Vol. 287 (2002), pp 588-591.

[123] Y. Wang, and J. S. Huang, Single screw extrusion compounding of particulate filled thermoplastics: state of dispersion and its influence on impact properties, Journal of Applied Polymer Science, Vol. 60 (1996), pp 1779-1791.

[124] Y. Nakamura, M. Yamaguchi, M. Okubo and T. Matsumoto, Effects of particle size on mechanical and impact properties of epoxy resin filled with spherical silica, Journal of Applied Polymer Science, Vol. 45 (1992), pp 1281-1289.

[125] Y. Nakamura, M. Yamaguchi and M. Okubo, Instrumented Charpy impact test of epoxy resin filled with irregular-shaped silica particles, Polymer Engineering and Science, Vol. 33 (1993), pp 279-283.

[126] Y. Nakamura, M, Yamaguchi, M. Okubo and T. Matsumoto, Effect of particle size on impact properties of epoxy resin filled with angular shaped silica particles, Polymer Vol. 32 (1991), pp 2976-2979.

[127] J. Suwanprateeb, Instrumented impact behavior of particulate-filled composites, Polymer-Plastic Technology Engineering, Vol. 39 (1) (2000), pp 83-94.

[128] M. Arroyo-Ramos and Miguel Angel Lopez-Manchado, Impact behavior of modified talc filled PP/LDPE blends, Journal of Polymer Engineering, Vol. 14 (1995), pp 237-252.

[129] J. Z. Liang, R. K. Y. Li and S. C. Tjong, Effects of filler content and surface treatment on drop-weight dart impact fracture behavior of glass bead-filled polypropylene binary composites, Journal of Reinforced Plastics and Composites, Vol. 19 (2000), pp 680-688.

[130] J. Z. Liang, R. K. Y. Li and S. C. Tjong, Effects of filler content and surface treatment on drop-weight dart impact fracture behavior of glass bead-filled polypropylene binary composites, Journal of Thermoplastic Composite Materials, Vol. 13 (2000), pp 241-250.

[131] C. W. Fong and R. C. Warren, The effect of filler particle size and orientation on the impact fracture toughness of a highly filled plasticized polymeric material, Journal of Materials Science 20 (1985), pp 3101-3110.

[132] G. Pritchard and Q. Yang, Microscopy of impact damage in particulate-filled glass-epoxy laminates, Journal of Materials Science 29 (1994), pp 5047-5053.

[133] M. G. Hocking, Production of Corrosion and Wear Resistant Coatings, Surface Engineering Volume II: Engineering Applications, Chapter 2.1.1, pp. 5-21.

[134] S. G. Croll, Adhesion and Internal Strain in Polymeric Coatings, Adhesion Aspects of Polymeric Coatings, ed. K. L. Mittal (1983), pp. 108-129.

[135] B. D. Beake and J. F. Smith, Development of a micro-impact tester to measure toughness properties of coatings, Proceedings of the workshop on the development and standardization of test methods for engineering coatings, 7th International Conference of Plasma Surface Engineering, Garmisch-Partenkirchen, Germany (2000), pp 68-79.

[136] B. D. Beake, Maria Jesus Ibanez Garcia and J. F. Smith, Mircro-impact testing: a new technique for investigating fracture toughness, Thin Solid Films, Vol. 398-399 (2001), pp 438-443.

[137] B. D. Beake, S. R. Goodes and J. F. Smith, Micro-impact testing: a new technique for investigating thin film toughness, adhesion, erosive wear resistance, and dynamic hardness, Surface Engineering, Vol. 17 (2001), pp 187-192.

[138] E. A. Taylor, H. J. Scott, M. Abraham and A. T. Kearsley, Hypervelocity impact on silicon wafers with metallic and polymeric coatings, Proceedings of the Third

European Conference on Space Debris, Vols. 1 and 2, ESA Special Publications Vol. 473 (2001), pp 583-589.

[139] J. K. Kim and Y. W. Mai, Effects of interfacial coating and temperature on the fracture behaviours of unidirectional Kevlar and carbon fibre reinforced epoxy resin composites, Journal of Materials Science, Vol. 26 (1991), pp 4702-4720.

[140] J. M. Nelson, New advancements in the use of internal plastic coating for enhanced oil recovery, Materials Performance, Vol. 30 (1991), pp 27-30.

[141] R. E. Lewis and D. Barbin, Selecting internal coatings for sweet oil well tubing service, Materials Performance, Vol. 39 (2000), pp 54-58.

CHAPTER 3 MATERIAL CHARACTERISATION

3.1 Introduction

This investigation will examine six different types of polymeric coatings supplied by various coating manufacturing companies. These coatings have found wide application in the oil industry and can be broadly divided into thermoplastic and thermoset coatings according to the characteristics of the polymeric materials. The coatings are identified by the simplified code so as to protect product confidentiality. Usually, a layer of "primer" is directly bonded to the mild steel substrate, on top of which the coating is deposited. The "primer" serves as a link between the steel substrate and the polymeric coating and enhances adhesion improving the bond strength between the substrate and coating.

The overall composition of a polymeric coating will influence its microstructure, especially the embedded fillers of the coating as discussed in Chapter Two. This will ultimately affect the performance of the coating, consequently, a complete characterisation of the polymeric coatings is essential. In this Chapter, characterisation consists of the following stages:

(i) A review of technical data from the coating suppliers. The information from suppliers will be given in italics in this Chapter.
(ii) Metallography on surfaces both parallel and transverse to the steel substrate. Samples were then observed by optical and scanning electron microscopy (SEM).
(iii) Quantitative metallography to determine the thickness of the coating and primer if present. Image analysis was employed to determine the amount of the filler present. These techniques are described in Section 3.3.
(iv) Energy Dispersive X-ray analysis on the fillers present in some of the coatings.
(v) Micro hardness measurements on transverse section of the coatings. For the coatings which contain fillers, efforts were made to avoid indenting large filler particles in order to obtain the hardness value of the matrix. The hardness value quoted is the average value of at least five measured values. However, the hardness

values quoted for filled polymeric coatings might overestimate the hardness of the matrix due to fillers beneath the surface of the coating indented influencing the hardness value measured.

(vi) Surface roughness measurements taken on the as received samples.

3.2 Characterisation and Application of the Polymeric Coatings

3.2.1 Experimental techniques

In the process of assessment of the coatings, the following techniques were involved.

(i) Metallographic techniques were applied to the coatings following standard procedures. The samples were ground on 120 grade to 1200 grade SiC abrasive papers followed by polishing using 5 micron and 1 micron diamond abrasives.

(ii) An optical microscope (OLYMPUS BH2-UMA 076909) was used to determine the thickness of the coatings and primer if present.

(iii) A JEOL JSM T300 scanning electron microscope was utilised throughout the work to examine the microstructural characteristics of the coatings. Energy Dispersive X-ray (IMIX) equipment attached to a JEOL JSM 6400 SEM was used to determine the elemental composition of fillers present in some of the coatings.

(iv) A Microhardness Tester (Matsuzawa Seiki Co. Ltd. 8033, model MHT-1) was employed to obtain the Vickers hardness of the matrix and primer of the coatings.

(v) The surface roughness of the coatings was measured by a Taylor Hobson Form Talysurf 120L.

3.2.2 Thermoplastic polymeric coating types T-99A and T-99B

Table 3.1 gives detailed information for the T-99 series of thermoplastic nylon coatings. "*T-99x is a highly flexible, thick film coating that is designated for general corrosive service. Formulated with a thermoplastic nylon resin, this material can withstand metal deformation and reverse impact damage where normal thermoset systems cannot*" [1].

Table 3.1 Details of the Nylon coatings

Designation	T-99A	T-99B
Colour	Black	Black
Polymer base	Thermoplastic	Thermoplastic
Resin type	Nylon powder	Nylon powder
Filler type	N/A	N/A
Filler percentage	N/A	N/A
Filler size (μm)	N/A	N/A
Filler shape	N/A	N/A
Coating thickness (μm)	950 – 980	1100 – 1200
Primer type	Phenolic	Phenolic
Primer thickness (μm)	25 – 30	26 – 30
Surface roughness (Ra, μm)	10 ± 0.5	N/A
Microhardness $HV_{0.025}$	15 ± 0.4	N/A

T-99A and T-99B are unfilled thermoplastic nylon coatings with different matrix thicknesses. Figure 3.1 presents a transverse section of the coating T-99B. The coating consists of a 26 – 30 μm thick phenolic "primer" layer directly bonded to the steel substrate, on top of which the coating is deposited. Figure 3.2 is a micrograph at higher magnification, showing the structure of the coating T-99x; note the uniformity of the coating microstructure. No fillers are present in the coating.

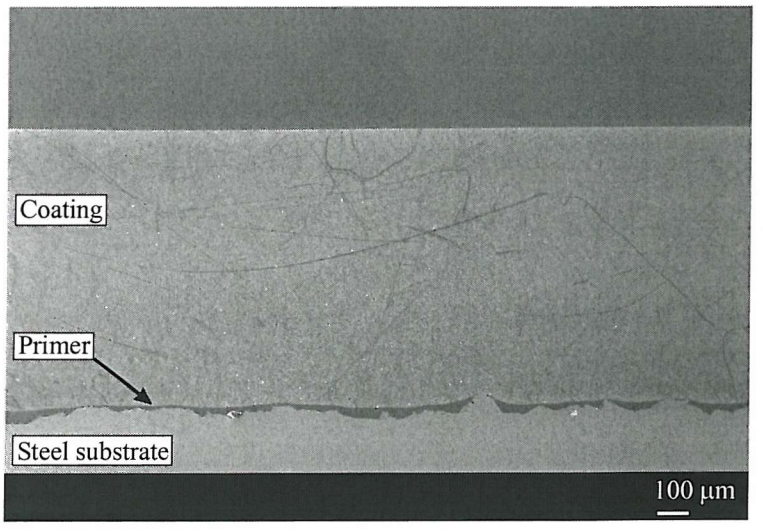

Fig.3.1 SEM image of a transverse section of the coating T-99B.

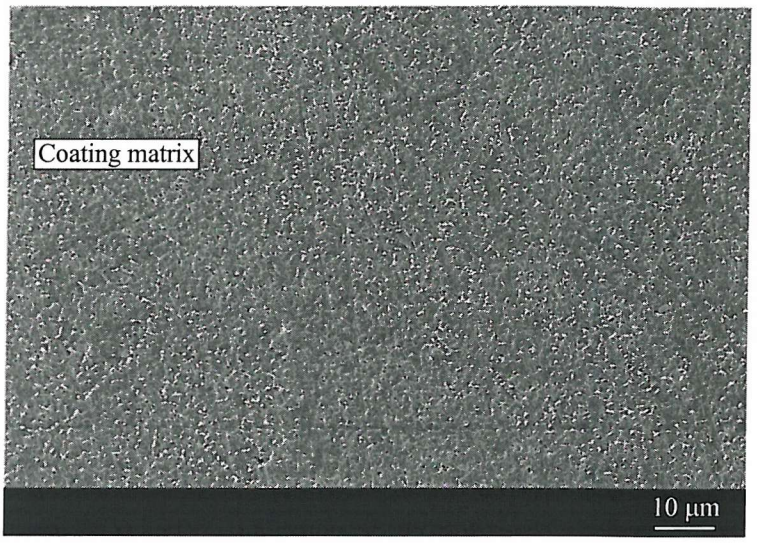

Fig.3.2 SEM image, detail of the matrix of the T-99A coating. Note the structure of this coating is uniform and no particles are in the matrix.

3.2.3 Thermoset polymeric coating types T-15A and T-15B

The information supplied by the manufacturing company, plus additional characterization results of coatings T-15A and T-15B are shown in Table 3.2. "*T-15x is a thick film, modified novolac, coating system formulated for critical environments. The modified novolac resin system utilized in T-15 produces a material with significantly improved flexibility without sacrificing chemical resistance*" [1].

Table 3.2 Details of the modified Novolac coatings

Designation	T-15A	T-15B
Colour	Dark green	Dark green
Polymer base	Thermoset	Thermoset
Resin type	Modified novolac (powder)	Modified novolac (powder)
Filler type	$CaSiO_3$	$CaSiO_3$
Filler percentage	9%	9%
Filler size (μm)	10 – 30	10 – 30
Filler shape	Angular and flake morphology	Angular and flake morphology
Matrix thickness (μm)	250 – 270	345 – 360
Primer type	Phenolic	Phenolic
Primer thickness (μm)	15 – 30	20 – 30
Surface roughness (Ra, μm)	0.20 ± 0.02	N/A
Microhardness $HV_{0.025}$	33 ± 3.5	N/A

T-15A and T-15B are modified novolac thermoset polymeric coatings supplied with a different matrix thickness. Figure 3.3 represents a transverse section of the T-15A coating, the fillers present in this coating have a large range of sizes as can be appreciated from Figure 3.3. Figure 3.4 shows the transverse section of the coating T-15A under high magnification. The fillers can be seen to be well bonded with the coating matrix. However, a number of gaps are apparent at the filler / resin interface, in addition cracks are also evident within the fillers. These are believed to be caused by metallographic polishing of the sample. The chemical composition of the filler was examined by EDS, the results of which are shown in Figure 3.5. The elements Si and Ca shown are consistent with the information obtained from the manufacturing company as listed in Table 3.2, i.e. $CaSiO_3$ present in the coating. Ti was also found in the spectrum which suggests that Titania (TiO2) was also present. Coatings T-15A and T-15B were shown to have a 9% particle content when examined by Image Analysis.

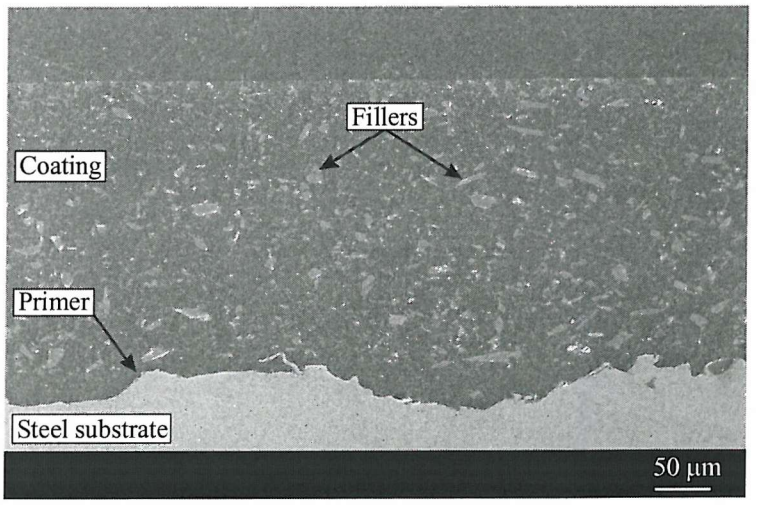

Fig. 3.3 SEM image of a transverse section of the T-15B coating. Note the two shapes (angular and flake) of particles.

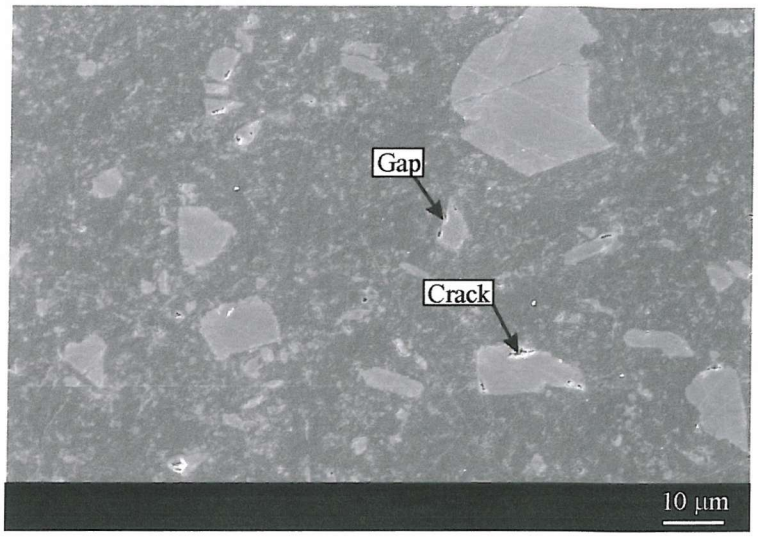

Fig. 3.4 SEM image, detail of the large fillers in the T-15B coating. Note the fillers are well bonded with the coating matrix.

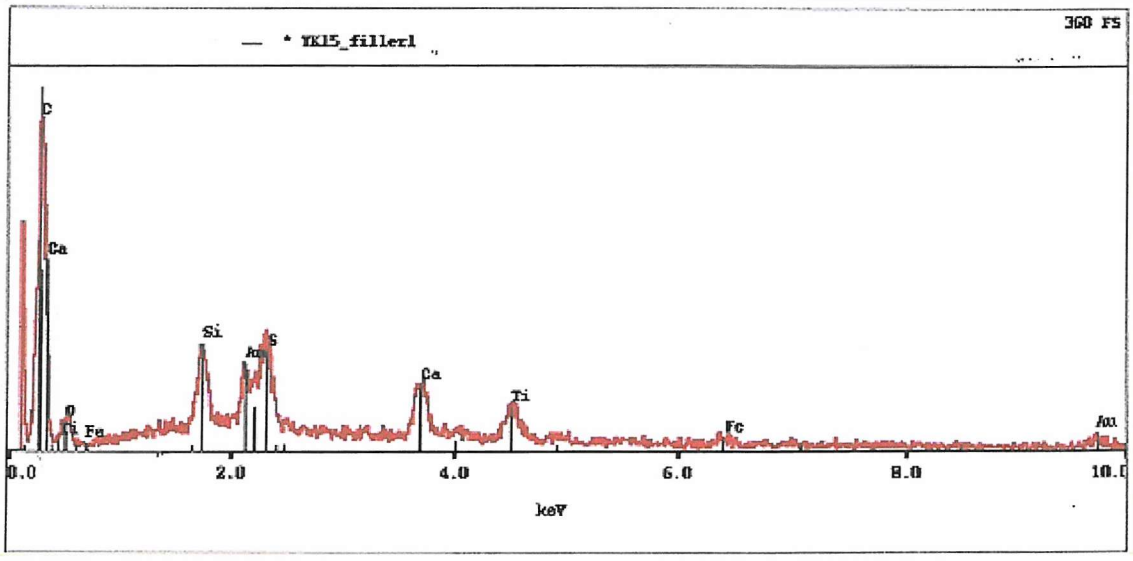

Fig. 3.5 EDS record of the chemical composition of the fillers in coating T-15x. Note, elements Si and Ca shown are consistent with the information obtained from the manufacturing company that $CaSiO_3$ is present in the coating; Ti was also found in the spectrum which suggests that Titania (TiO_2) was also present.

3.2.4 Thermoset polymeric coating types T-34A and T-34B

Table 3.3 presents the properties for coatings T-34A and T-34B from the manufacturing company and characterisation results from this study. *"T-34x coating, the first abrasion resistant drill pipe coating specifically formulated to provide for improved wear resistance in drilling environments. The liquid resin system utilized in this material renders a coating that maximizes adhesion to the steel substrate and cohesion within the cured field"* [1].

Table 3.3 Details of the modified Epoxy-phenolic coatings

Designation	T-34A	T-34B
Colour	Dark green	Dark green
Polymer base	Thermoset	Thermoset
Resin type	Modified epoxy-phenolic (liquid)	Modified epoxy-phenolic (liquid)
Filler type (in matrix)	Al_2O_3	Al_2O_3
Filler percentage (in matrix)	20%	20%
Filler size (in matrix) (μm)	10 – 30	10 – 30
Filler shape (in matrix)	Angular	Angular
Matrix thickness (μm)	135 – 145	250 – 260
Primer type	Phenolic	Phenolic
Primer thickness (μm)	50 – 100	45 – 90
Filler type (in primer)	$CaSiO_3$	$CaSiO_3$
Filler percentage (in primer)	35%	35%
Filler size (in primer) (μm)	50 – 100	50 – 100
Filler shape (in primer)	Angular and flake	Angular and flake
Microhardness $HV_{0.025}$ of coating matrix	54 ± 4	50 ± 6
Microhardness $HV_{0.025}$ of primer	113 ± 6	105 ± 8
Surface roughness (Ra, μm)	3.50 ± 0.25	N/A

T-34A and T-34B are dark green modified epoxy-phenolic coatings with two different thicknesses. The primer of this coating also includes fillers and is much thicker than other similar types of coatings. The filler in the coating matrix is alumina with a volume fraction of 20%. The filled primer contains approximately 35% of calcium silicate particles. Figure 3.6 presents a SEM image of a transverse section of the T-34A coating, a 135 – 145 μm thick layer of coating is deposited on a 50 – 100 μm layer of phenolic primer. The filler in the coating is angular in shape and comprises Al_2O_3 particles in the

matrix, see Figure 3.6; while the filler in the primer consists of $CaSiO_3$ in an angular or flake shape, see Figure 3.7. Figure 3.7 shows clearly the characteristics of the bond between the fillers and the coating matrix and primer, as well as the boundary between the matrix and primer. The composition of fillers in the matrix and primer were examined by EDS and the results are shown in Figure 3.8. The Al peak (red line) reflects the main element of the filler Al_2O_3 in the coating matrix, while the Si and Ca peaks (blue line) reflects the main elements of the filler $CaSiO_3$ in the primer. The primer for this coating has a higher micro-hardness than the coating matrix, this is probably caused by the high percentage of fillers within the primer and the characteristics of coating matrix and primer. The chemical compositions of the fillers in the matrix and the primer are shown in Figure 3.8, revealing the consistence between the measured results and the information shown in Table 3.3.

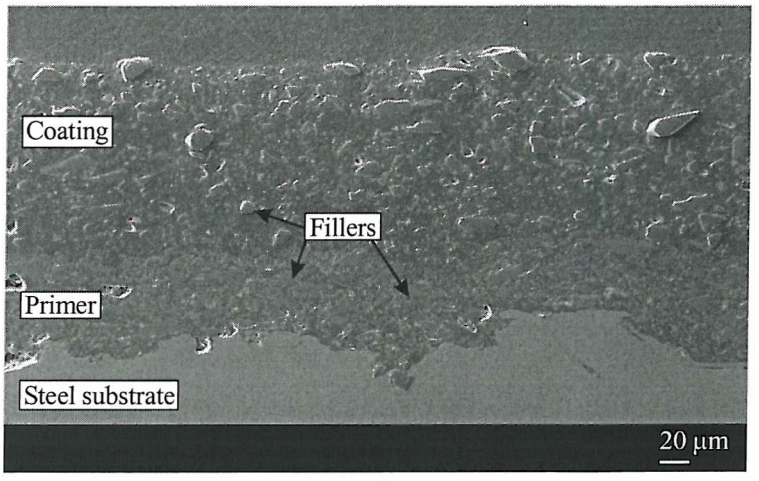

Fig. 3.6 SEM image of a transverse section of the T-34B coating. Note both the matrix and the primer have fillers in this coating, and the primer is much thicker than the usual primer used in other coatings.

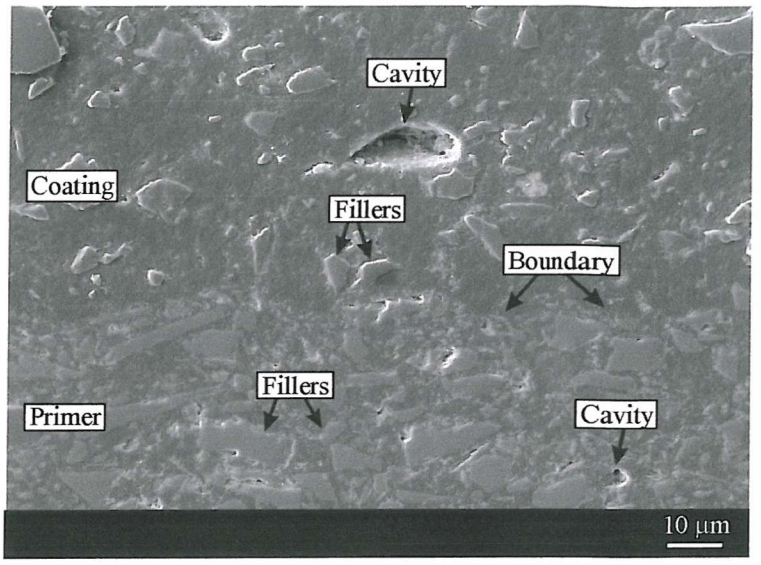

Fig. 3.7 SEM image at higher magnification showing particles in the coating matrix and primer. Note the fillers are well bonded with the matrix and the primer.

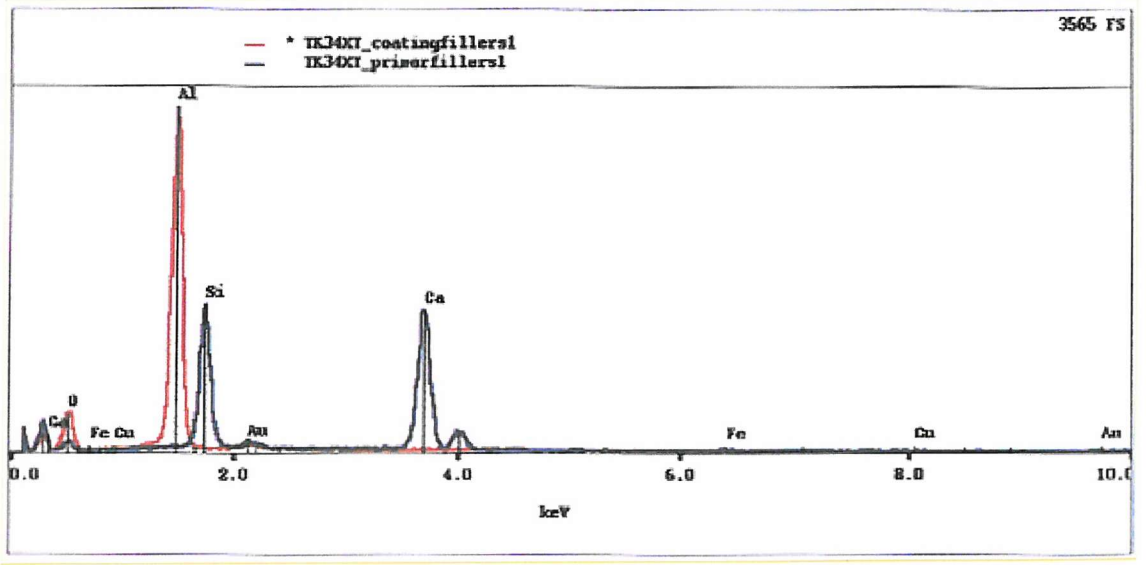

Fig. 3.8 EDS record of the chemical composition of the fillers in coating T-34x. Note the red trace represents fillers in the coating matrix (Al_2O_3) and the blue trace represents fillers in the primer ($CaSiO_3$).

3.2.5 Thermoplastic coating types F-4001A, F-4001B and F-4001C

Information relating to the F-4001A, F4001-B and F-4001C coating specifications is shown in Table 3.4. These three types of coatings are thermoplastic fluoropolymer coatings having thicknesses of 500, 1000 and 1500 μm, respectively. "*Compared to other available polymeric coating systems, F-4001x series coatings offer the widest overall compliance in terms of: chemical resistance, adhesion to steel work, toughness and abrasion resistance, and temperature tolerance (-100 to +160 °C)*" [2].

Table 3.4 Details of the Fluoropolymer coatings

Designation	F-4001A	F-4001B	F-4001C
Colour	Black	Black	Black
Polymer base	Thermoplastic	Thermoplastic	Thermoplastic
Resin type	Fluoropolymer (powder)	Fluoropolymer (powder)	Fluoropolymer (powder)
Filler type (in matrix)	CaF_2	CaF_2	CaF_2
Filler percentage (in matrix)	2%	2%	2%
Filler size (in matrix) (μm)	20 – 40	20 – 40	20 – 40
Filler shape (in matrix)	Rounded	Rounded	Rounded
Matrix thickness (μm)	500	1000	1500
Primer type	Unknown	Unknown	Unknown
Primer thickness (μm)	80 – 200	80 – 200	80 – 200
Fill type (in primer)	SiC	SiC	SiC
Fill percentage (in primer)	12%	12%	12%
Filler size (in primer) (μm)	5 – 10	5 – 10	5 – 10
Filler shape	Angular	Angular	Angular
Surface roughness (Ra, μm)	0.26 ± 0.02	0.26 ± 0.02	0.26 ± 0.02
Microhardness of coating matrix $HV_{0.025}$	7.04 ± 0.27	7.04 ± 0.27	7.04 ± 0.27
Microhardness of primer $HV_{0.025}$	9.8 ± 0.34	9.8 ± 0.34	9.8 ± 0.34

Figure 3.9 shows a SEM image of a transverse section of the coating F-4001B. Note this type of coating has a thick layer of primer (80 – 200 μm) and both the fluoropolymer matrix and the primer contains filler with a volume fraction of 2% and 12%, respectively. Figure 3.10 is a higher magnification view of the transverse section of the coating close to the boundary between the coating matrix and the primer. Two features are apparent from Figure 3.10: the boundary between the matrix and the primer cannot be easily distinguished indicating that the bond between them is good; the fillers in the primer are

not evenly distributed, which is the result of the manufacturing process. Figure 3.11 represents the EDS examination result of the chemical composition of the fillers in fluoropolymer matrix and primer. The two peaks revealing the presence of Si and Ca are consistent with the information listed in Table 3.4.

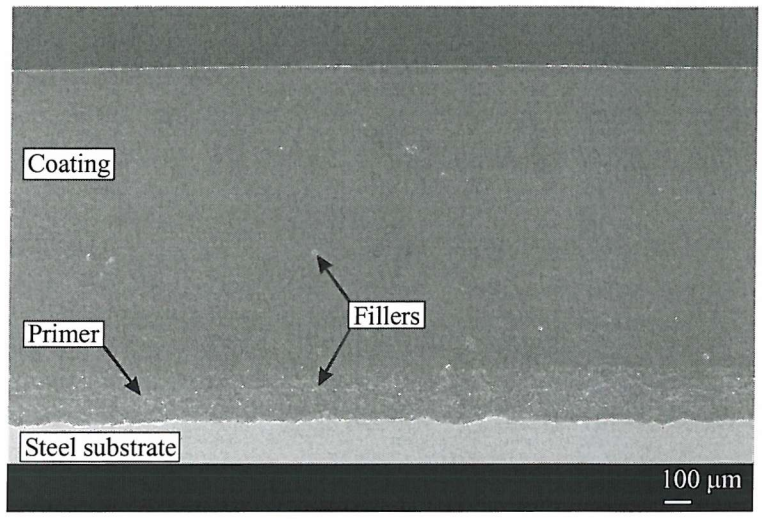

Fig. 3.9 SEM image of a transverse section of the coating F-4001B. Note both the matrix and the primer consist of fillers with a volume fraction of 2% and 12% respectively.

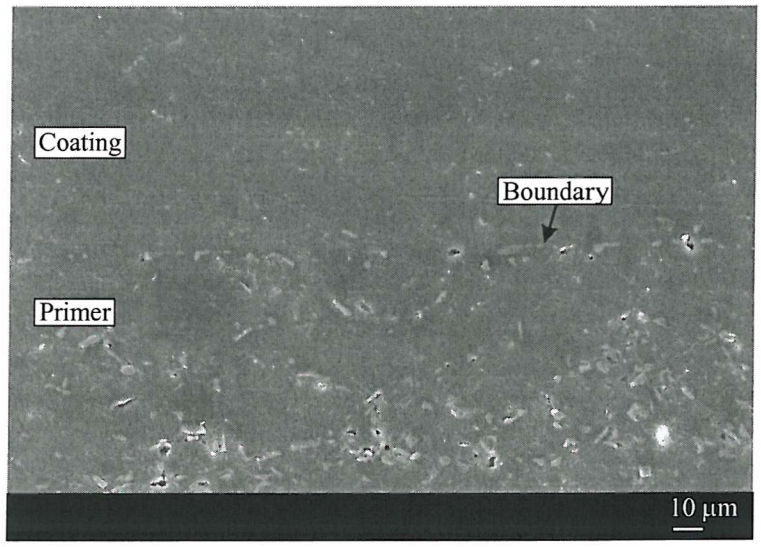

Fig. 3.10 SEM image at a higher magnification of the boundary between the coating and the primer. Note the bond between the coating and the primer is good, and the filler in the primer is not evenly distributed.

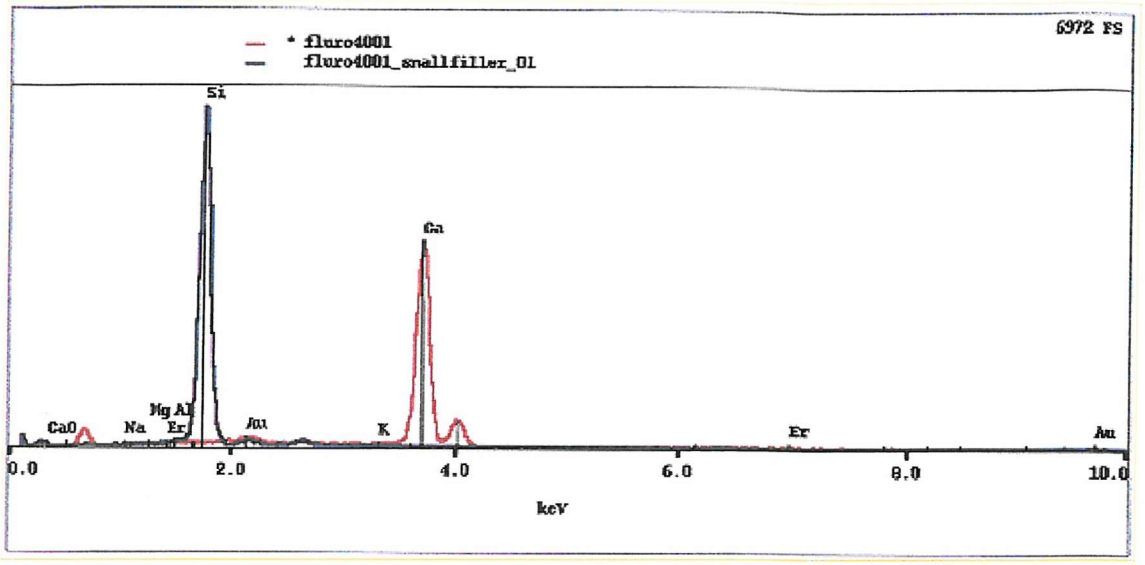

Fig. 3.11 EDS record of the chemical composition of the fillers in the matrix and primer of the F-4001x coating. The red trace represents fillers in the coating matrix and the blue trace represents the fillers in the primer.

3.2.6 Thermoplastic coating type P-A

Table 3.5 presents detailed information for the thermoplastic coating P-A. P-A is a 600 – 650 μm thick semi-crystalline thermoplastic PVDF powder coating, free from any additives. PVDF is obtained by polymerising vinylidene fluoride. "*This engineering resin has been proven as a thermal and chemical barrier in the harsh environments of downhole and subsea oil production as a replacement for metals and more widely used plastics which suffer deterioration and deformation when exposed to corrosive environments*" [3].

Table 3.5 Details of the Fluorinated coating P-A

Designation	P-A
Colour	Yellow
Polymer base	Thermoplastic
Resin type	Fluorinated semi-crystalline thermoplastic PVDF
Filler type	None
Coating thickness (μm)	600 – 650
Primer type	None
Surface roughness (Ra, μm)	1.5 ± 0.5
Microhardness $HV_{0.025}$	12 ± 0.8

The thermoplastic powder coating P-A is manufactured by electrostatic spraying on to substrate plates. Figure 3.12 shows the top surface of the P-A coating, voids are visible located at the boundaries between the unmelted powder particles, possibly as a result of the manufacturing process, which gives rise to a honeycomb structure; in addition, there were cracks linking the voids. Figure 3.13 is a SEM image of a transverse section of the P-A coating close to the surface, note the voids on the coating surface (Figure 3.12) have a depth of approximate 20 μm. Figure 3.14 shows a transverse section of the coating at the substrate boundary, note no primer has been used in this type of coating. There is thus evidence of unmelted PVDF powder particles close to the substrate, and of a poor bond between the coating and the steel substrate.

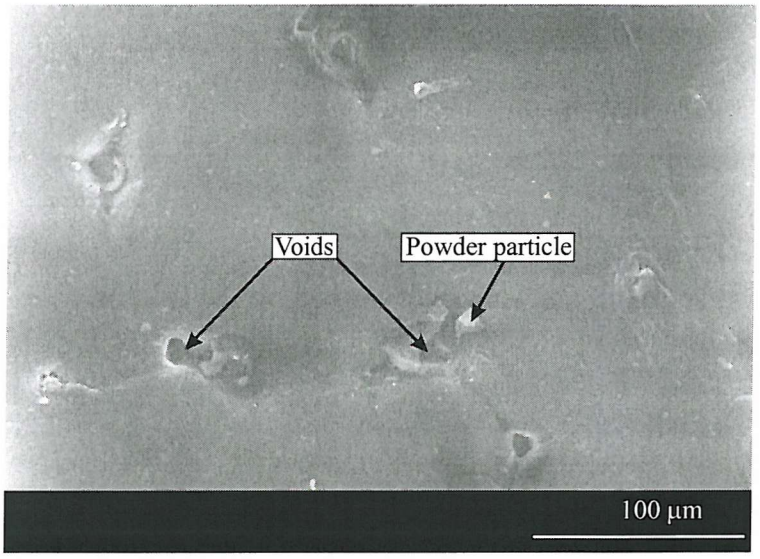

Fig. 3.12 SEM image of the surface of the PVDF coating (P-A). Note the voids located at the junctions between unmelted powder particles.

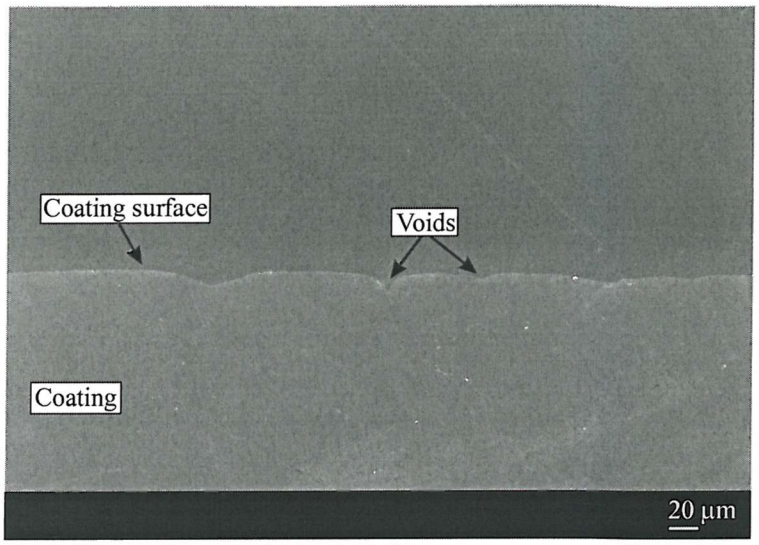

Fig. 3.13 SEM image of a transverse section of the PVDF coating. Note the voids on the coating surface penetrating into the coating.

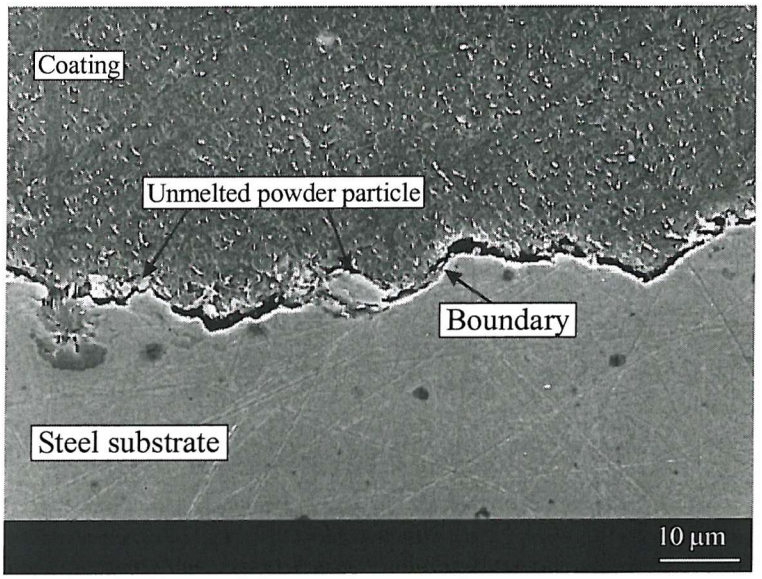

Fig. 3.14 SEM image of a transverse section of the PVDF coating. Note there is no primer linking the coating and steel substrate, and the bond between the coating and the steel substrate is poor.

3.2.7 Thermoplastic coating type I-1100A

Table 3.6 presents the specification for the thermoplastic coating I-1100A. Coating I-1100A is based on a nylon-11 resin system. "*I-1100A is a thick-film fusion bond nylon coating with high performance levels in regard to flexibility and damage resistance*" [4].

Table 3.6 Details of the Nylon-11 coating

Designation	I-1100A
Colour	Black
Polymer base	Thermoplastic
Resin type	Nylon 11 powder
Filler type	Mica/quartz/chlorite, dolomite
Filler percentage	23%
Filler size (μm)	5 – 10
Filler shape	Rounded
Coating thickness (μm)	750 – 780
Primer type	Phenolic
Primer thickness (μm)	10 – 30
Surface roughness (Ra, μm)	0.40 ± 0.05
Microhardness $HV_{0.025}$	22 ± 2

Coating I-1100A is a thermoplastic fusion bond nylon powder coating filled with 23% by volume of silica and dolomite fillers with a particle size of 5 to 10 μm, see Figure 3.15. No bonding agent is used for coating I-1100A, possibly explaining the presence of large gaps between the fillers and the polymeric matrix shown in Figure 3.16, indicating that the bond between the filler and the matrix is poor. EDS examination of the fillers in coating I-1100A is shown in Figure 3.17 revealing that elements Ca and Mg are the two main constituents of the filler.

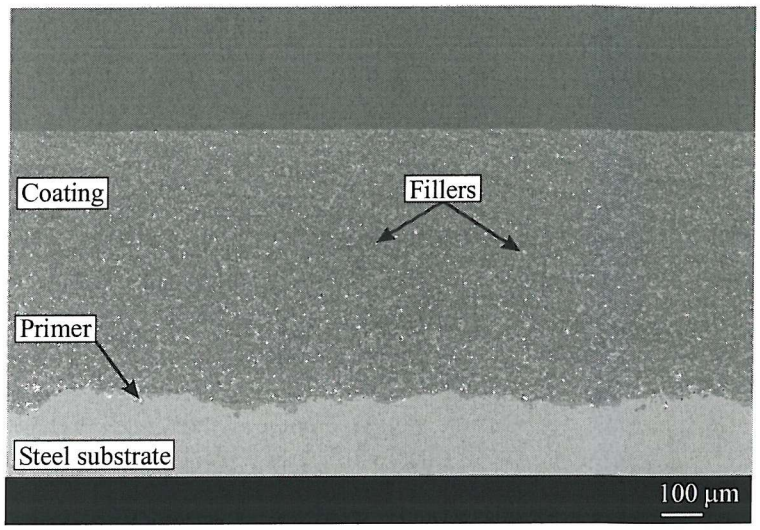

Fig. 3.15 SEM image of a transverse section of the coating I-1100.

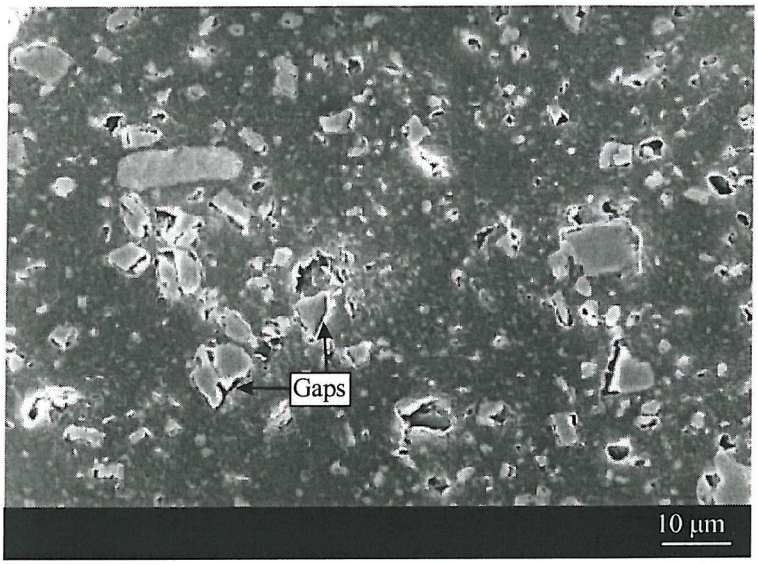

Fig. 3.16 SEM image, higher magnification view of the particles distributed in the coating matrix. Note the bond between the particles and the matrix is poor.

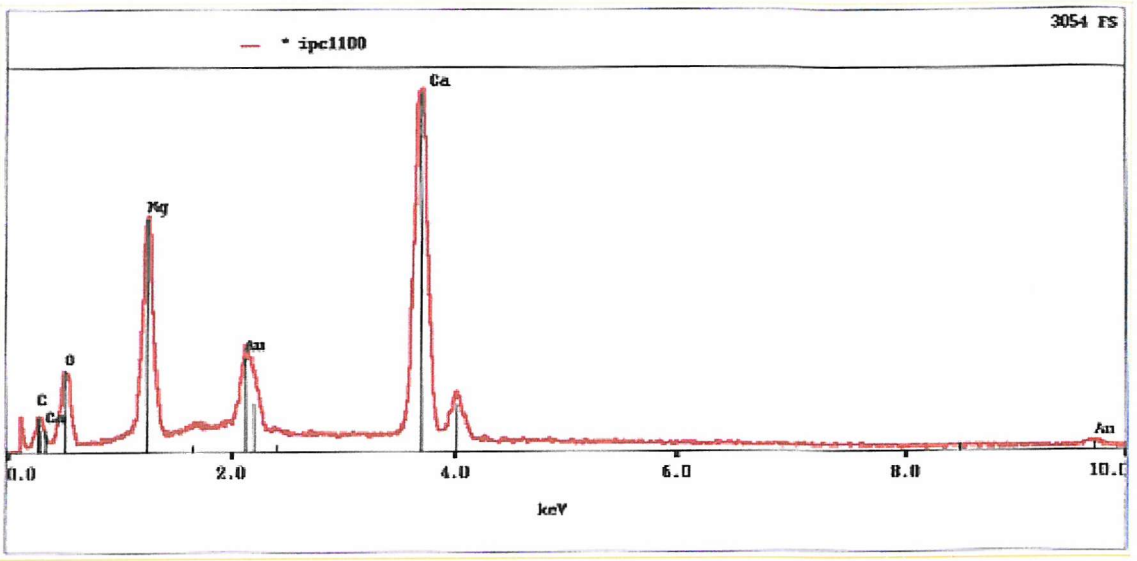

Fig. 3.17 EDS record of the chemical composition of the filler in the coating I-1100. Note the Au peak was caused by sputtering the sample with gold.

3.3 Investigation of the Volume Fraction of Fillers by Image Analysis

3.3.1 Introduction

The experimental measurement of both size and volume fraction of discrete particles (second phase particles) embedded in a matrix material from an opaque, plane section has been considered by many authors, notably by Fullman [5]. It is assumed that, when the specimen is sectioned, the particles are also sectioned, so that the diameters of the particles within the plane of the cross section are measured.

Volume fraction is the volume of particles per unit volume of material [6]. As discussed in Section 2.3.3, the volume fraction of fillers in polymeric coatings is an important factor which influences the microstructure of the coating matrix and thus its characteristic properties. The wear and impact resistant behaviour of those coatings are therefore dependent on the volume fraction of each coating. In this section, the procedure for the measurement of the volume fraction of the filler in a coating by using IA (Image Analysis) will be introduced.

3.3.2 Image analysis system

The KS 300 C Z Vision Imaging System was employed in order to measure the volume fraction. KS 300 is primarily designed as an automatic system for image processing and image analysis.

3.3.3 Sample preparation

In practice, the shape, size and distribution of dispersed particles are not uniform, and of necessity the various formulae relate to the average values of the relevant parameters [7]. However, this does not lead to serious error in the quantitative description of microstructures provided, because the particles are distributed randomly (as distinct from uniformly) and that evaluations are based on a statistically significant coverage of representative samples.

In this work, three 10 x 10 mm square samples were cut from each type of particle filled polymeric coatings in order to measure the average volume fraction of the filler in the coating. The square sample was mounted in epoxy resin with the transverse section facing up. After that, the transverse section of the mounted sample was prepared following the standard metallographic method by using SiC abrasive paper from 600 grade (20 – 30 micron) to 1 micron diamond polishing paste. In order to be measured by image analysis, each sample coating was examined in a JEOL T300 scanning electron microscope and a SEM image of the transverse section of the sample was taken. Before measuring the filler volume fraction by analysing the images with the KS 300 system the images must be digitized, therefore the SEM images were scanned and saved as TIF image files in a storage media for later analysis.

3.3.4 Binarisation

For the purpose of measuring the volume fraction of the fillers in a coating sample by the method of image analysis, the digitized images need to be binarised. Binary images are a

special kind of grey scale image. They contain only two grey values, normally 0 and 1 or 0 and 255. Binary images are a necessary step to transfer original to quantitative data, they define the areas of the regions which are to be analysed. Initial binaries of the reinforced phase were generated by thresholding the grey images over a given range of grey levels. Grey images can be enhanced with a range of image processing functions such as contrast enhancement or normalization, smoothing, edge improvement and grey morphology. A number of processing stages were subsequently required to obtain truly representative binaries. At first, holes within binary objects caused by the large difference of contrast or brightness in the same object were automatically "Filled". Then, the "Scrap" function allows user filtering of the objects that only appear like a particles by defining the size of the real particles. Finally, "Field-specific" measurements can be taken by using either the entire image or the regions of an image of interest. The main steps in binarising an image of a sample F-4001B are illustrated by a series of digitised images shown in Figure 3.18 (a) to (d).

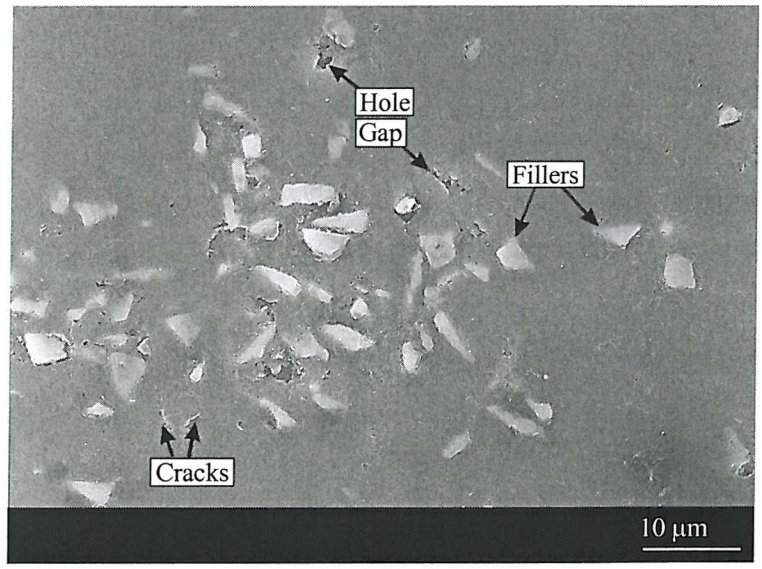

(a)

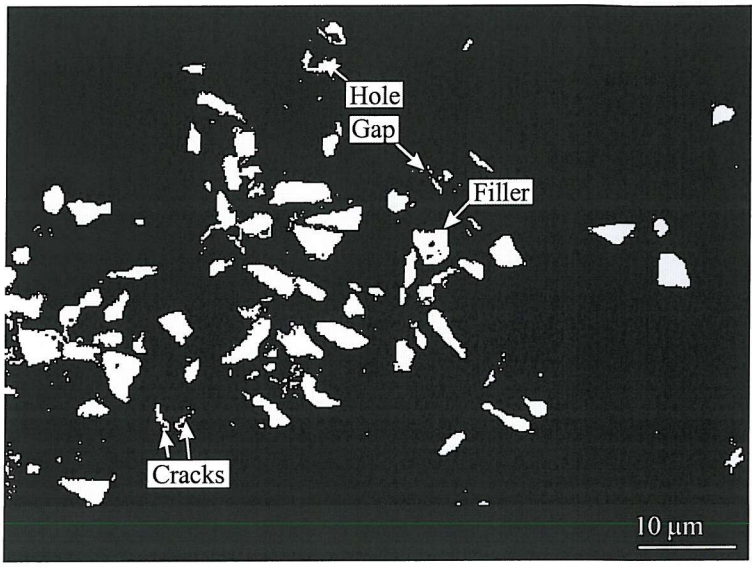

(b)

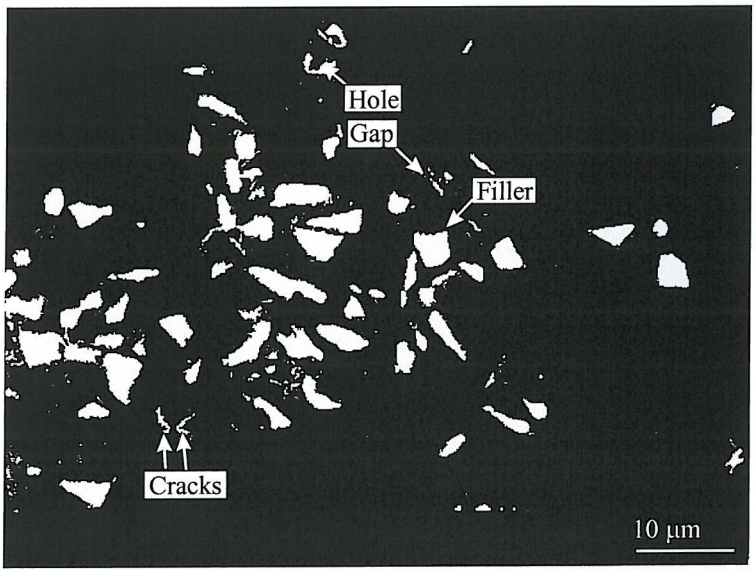

(c)

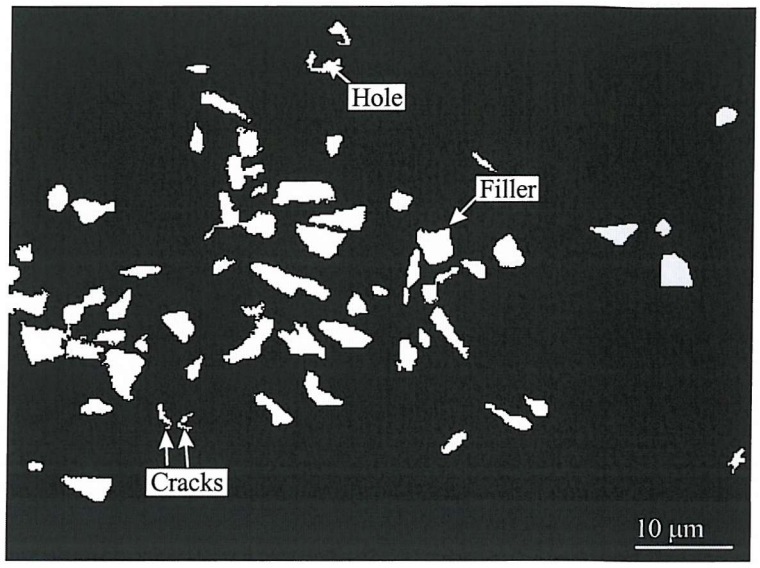

(d)

Fig. 3.18 Sequence of digitised images of a sample F4001B illustrating binarisation: (a) scanning from SEM photograph (b) grey image processing by thresholding (c) automatically filling the holes in objects and (d) filtering out the non-particle objects.

3.3.5 Limitations of Image Analysis (IA) technique

Although the method of Image Analysis is an effective method of measuring the volumetric fraction of fillers in the coating matrix or primer, there are limits to using this method in practice. Some factors will influence the result producing errors in the IA results.

(i) As described in Section 3.3.3, the distribution of dispersed particles is not ideally uniform, therefore only the average values of the volumetric fraction of the fillers can be obtained. Thus, an error will be produced between the calculated values and the real values.

(ii) The polishing process of a section of the test specimen will influence the accuracy of the final result. The quality of a SEM image will also affect the analysis result.

(iii) All the steps described in the procedure of Binarisation, which is the main procedure during the whole calculation process, are dependent on the human operator. During the steps of thresholding a grey image, automatically filling holes and filtering non-particle objects, criteria values have to be inputed to the IA system in order to distinguish the matrix and fillers. Because of the influence of brightness or contrast on an SEM image, the IA system may not be able to distinguish the matrix and fillers properly. For instance, holes, gaps or cracks shown in an image may be recognised as filler so that the calculated volume fraction will be increased, as shown in Figure 3.18 (b); or a part of filler may be taken into account as matrix so that the calculated result will be decreased. Therefore, a compromise needs to be made by the operator so that the optimised criteria values could be inputed for those steps and the best binarised image obtained which can properly reflect the real case of the sample. The limits of the binarisation procedure will ultimately induce an error to the final calculated result, though effort can be made to reduce this error by defining the regions of interest which represent well the sample microstructure or by averaging more sample images to lower the errors.

Nevertheless, the Image Analysis method has been proved to be a fast and effective way to assess the volume fraction of the fillers in coating matrix or primer and has thus been adopted by the present research work.

3.3.6 Result of Image Analysis

The volume fraction of each particle filled coating was examined by method IA illustrated previously. The measurement results are shown in Figure 3.19. Note the volume fraction of fillers in the coating matrix and coating primer was examined separately for those coatings containing fillers in both the matrix and the primer. The error bars shown in the graph for each sample are based on three test results.

As can be seen the filled coatings contain between 2 and 35 % fillers. However, most of the filled coatings have 10 – 20 % filler.

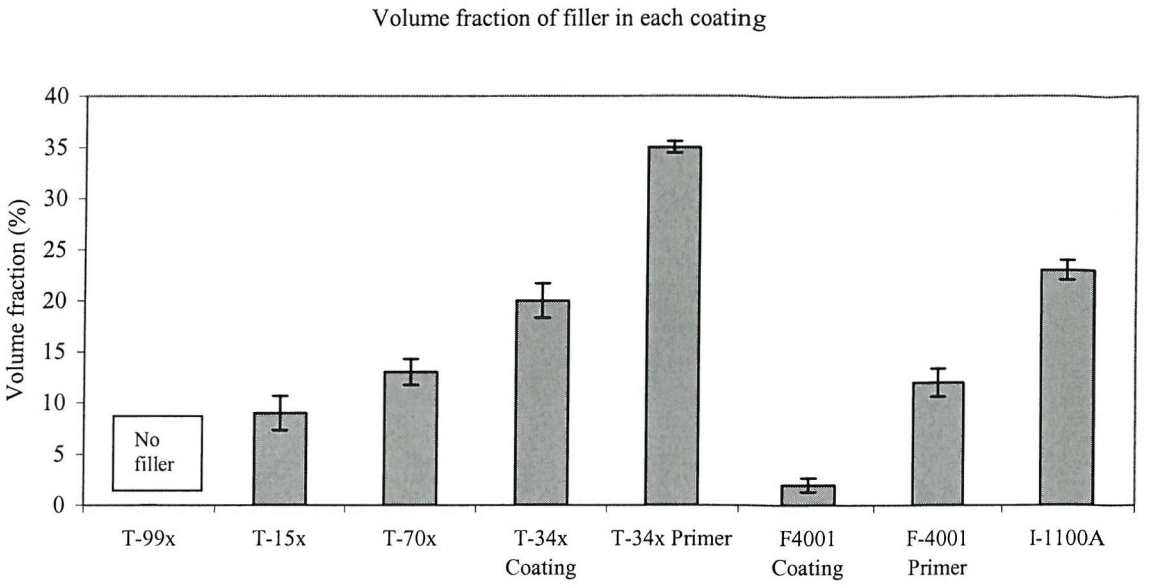

Fig. 3.19 Volume fraction of fillers for the particle filled polymeric coatings.

REFERENCES:

[1] Information Manual Brochure, Tuboscope Vetco International.

[2] Information of Fluorocarbon Coating, Fluorocarbon Company (1998).

[3] N. Maquet, Translated by E. R. Dilley, The Use of SOLEF PVDF for Anti-corrosion Coatings and Linings, Engineering Polymer SOLVAY (2000).

[4] Information Manual, ICO Corrosion Control Services (1998).

[5] R. L. Fullman, Measurement of Particle Sizes in Opaque Bodies, Trans. Met. Soc., AIME, Vol. 197 (1953), pp 447-452.

[6] M. F. Ashby and R. Ebeling, On the Determination of the Number, Size, Spacing, and Volume Fraction of Spherical Second-Phase Particles from Extraction Replicas, Transactions of the Metallurgical Society of AIME, Vol. 236 (1966), pp 1396-1405.

[7] C. W. Corti, P. Cotterill, and G. A. Fitzpatrick, The Evaluation of the Interparticle Spacing in Dispersion Alloys, International Metallurgical Reviews, Vol. 19 (1974), pp 77-88.

CHAPTER 4 WEAR OF POLYMERIC COATINGS (I) – PRELIMINARY STUDY FOR THERMOPLASTIC COATINGS

4.1 Introduction

Thermoplastic and thermoset polymer matrix composites are utilised as coating materials for the bore of downhole tubulars used as water injectors in the oil industry. These coatings are primarily employed for corrosion resistance, however the coatings must also resist mechanical damage from the inspection tools lowered at speed down the tubing. This mechanical damage is produced by the wearing action of the supporting wire against the coating (wireline wear) and by direct impact of the tool against the coating. Previous work on wireline wear has indicated that the wear mechanism is predominantly that of abrasive wear [1, 2]. In this preliminary study, three types of thermoplastic polymeric coatings (T-99A, I-1100A and P-A) were chosen from the polymeric coatings supplied and were subjected to wear tests. Both abrasive wear tests, using silicon carbide papers as the abrasive, and wireline wear tests, utilising a true tribocouple consisting of the coating and a length of "slickline" wire on a modified pin on disc apparatus, were carried out to study the wear resistance of these three coatings. The influence of the bonding between matrix and fillers on the wear mechanism has been specifically addressed. Detailed scanning electron microscopy was performed on the wear tracks produced to elucidate the wear mechanism and in particular the role of fillers.

Most of the information presented in this Chapter has been published in Wear of Materials (2001) [3].

4.2 Experimental

4.2.1 Specimen preparation

Thermoplastic coatings T-99A, I-1100A and P-A were chosen for initial investigation for the present wear tests. The properties and the microstructural characteristics of these three coatings can be found in Sections 3.2 of Chapter 3.

Square blocks (pins) of dimension 10 ± 0.5 mm were cut from each of the three polymer coated plates. These blocks were clamped in a pin holder. Before weighing by a high precision electronic balance, surface contamination was removed from the coated surface with a Compressed-Gas Duster. After weighing, the specimen pin was kept in a plastic bag to prevent contamination of the surface.

4.2.2 Abrasive wear tests

In abrasive wear tests, a pin-on-disc (POD) unit was employed. An aluminium alloy plate 205 mm in diameter and 30 mm thick was used as the disc. The disc surface roughness was Ra 0.18 μm. In order to obtain a rough counterface, waterproof silicon carbide abrasive papers were stuck on to the disc surface. Preliminary results indicated that excessive wear rates, for the thickness of coating present, were obtained with 120 and 600 grade papers (surface roughness Ra 10.6 and 5.5 μm respectively), hence 1200 grade papers (surface roughness Ra 3.9 μm) were used in subsequent tests. Figure 4.1 shows schematically the polymer coated pin sliding on the abrasive paper in the abrasive wear tests.

The rotational speed of the disc was controlled by a speed control box attached to the main motor. The load applied, P, to the pin was from an adjustable spring, which had been calibrated prior to the experiment. Tap water was supplied during the abrasive wear tests by a recirculatory lubricant system attached to the main motor to prevent the

temperature of the pin rising when it was sliding across the abrasive paper. Another objective of the water lubricant is to rinse away the wear debris produced in the tests.

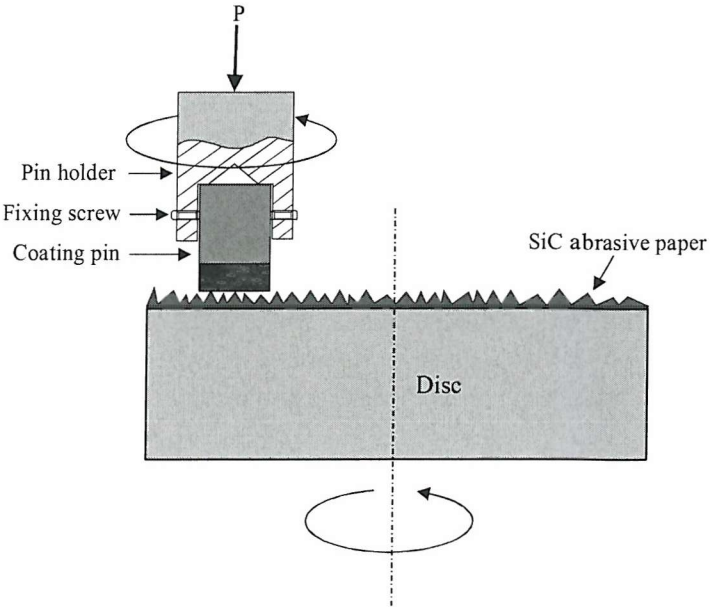

Fig. 4.1 Schematic diagram of abrasive wear test.

The pin-holder was connected to a separate motor that allowed the sample pin to be rotated while sliding on the abrasive paper. The reasons for pin rotation were:

1) In the downhole working condition when the inspection tool, attached by a wireline, is lowered into the well some twisting results, so the sliding route of the wire against the coating is complex rather than just in a straight line. Therefore, in this study, an attempt was made to simulate this complex motion.
2) Rotating the pin holder minimises the effect of edge loading on the pin surface in tests due to inclination of the pin holder caused by friction between the polymeric coating and the abrasive paper.

The abrasive wear test conditions are detailed in Table 4.1. After each test the pin was carefully dried and weighed. This was repeated until a constant weight loss was obtained. The weight loss was then converted into a volume loss using the densities given in Table 4.2.

Table 4.1 Experimental conditions for the abrasive wear tests

Load (N)	5 N
Rotational speed of disc (rpm)	100
Radius of wear track on disc (mm)	80
Rotational speed of pin holder (rpm)	0 and 33
Testing time (s)	48, 72, 96, 120, 144
Water lubricant (ml/min)	1000

Table 4.2 Densities of the coatings

Coating	T-99A	I-1100A	P-A
Density (kg/m^3)	980*	1200*	1780**

* Experimentally determined

** Data from manufacturer

4.2.3 Wireline wear tests

A true tribocouple consisting of the coating and a length of "slickline" wire on a modified pin-on-disc apparatus was utilised; slickline wire is the type of wire used in practice to suspend the inspection tools downhole. A circular loop of slickline wire was clamped on the surface of an aluminium alloy disc and the pins were slid over the wire loop. Figure 4.2 shows schematically the polymer coated pin sliding on a circular loop of slickline wire in the wireline wear tests. The wire itself was 3.2 mm in diameter and the radius of the loop was 80 mm. The surface roughness of the slickline wire was Ra 0.35 μm along the axis of the wire. The wire could be replaced if a significant change in Ra occurred during the test programme. Figures 4.3 (a) and (b) show the roughness profiles of the slickline wire before and after the tests. After a large number of tests had been carried out, the Ra had decreased to 0.23 μm. Such a decrease in Ra is believed not to affect the results significantly.

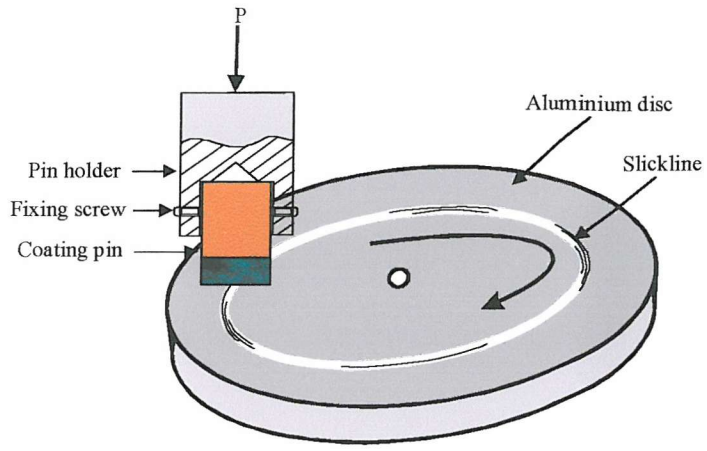

Fig. 4.2 Schematic diagram of wireline wear test.

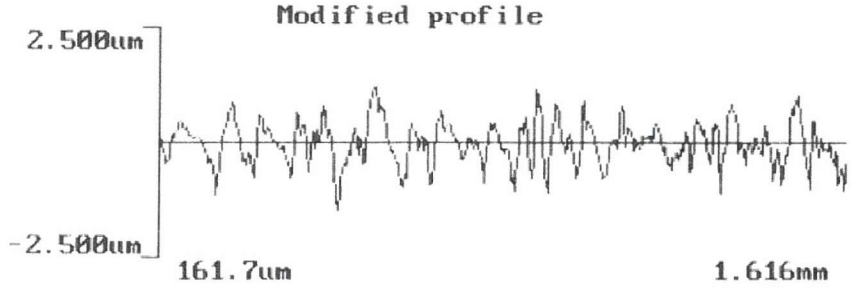

(a)

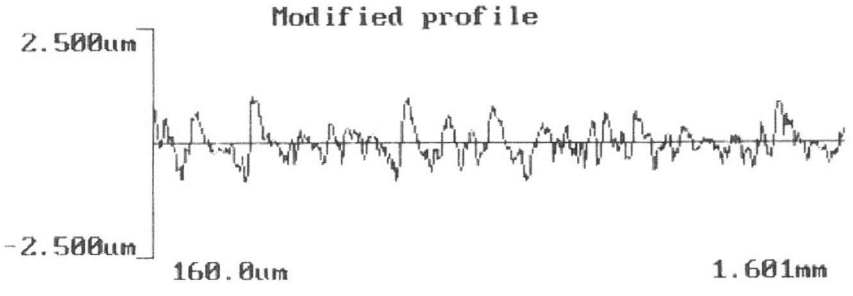

(b)

Fig. 4.3 Profiles of the slickline wire before (a) and after (b) all wear tests.

The adjustable spring used in the abrasive wear tests was not utilised to apply the load due to its maximum load limitation, and was replaced by weights clamped on the pin holder. Preliminary experiments indicated that the sliding distance was not the main factor affecting the wear rate of the polymeric coatings; the load applied to the pin affected the wear rate much more significantly. Therefore, the wear rate as a function of the applied load was determined for each type of coating. The applied load varied from 35 N to 300 N, which was equivalent to 3.5 to 30 N/mm line load. Table 4.3 shows the experimental conditions of the wireline wear tests. Generally, the running time of the wireline wear test was from 1 minute to 30 minutes. Times were selected to give appreciable wear and in addition to ensure that the coating was not worn through completely during the test. Wireline wear rates were determined in a similar manner to that used for the abrasive wear tests.

The polymer coated pins were not rotated in wireline wear tests as the primary objective of the wireline wear tests was to observe the wear scars on the coating surface caused by the slickline wire.

Table 4.3 Experimental conditions for the wireline wear tests

Load (N)	35 to 300
Rotational speed of disc (rpm)	100
Radius of slickline wire loop (mm)	80
Speed of pin holder (rpm)	0
Testing time (s)	60 to 1800
Water lubricant (ml/min)	1000

4.3 Results and Discussion

In recent years, a rapid growth in the use of thermoplastic polymers, both reinforced and non-reinforced, has been seen in the oil production industry. The semi-crystalline polymer nylon is especially popular as a matrix. For higher temperature applications a PVDF (polyvinylidene fluoride) matrix offers considerable advantages. Fillers in the form of particulates and fibres are often embedded into a polymeric matrix to improve its mechanical properties. Fillers whose hardness and modulus are greater than those of the polymer will increase the strength and initial modulus of the mixture, at least in the case of good adhesion [4, 5] and hence are effective in reducing wear in dry sliding conditions involving adhesive transfer and fatigue. However, embedded fillers can either enhance or degrade other properties because performance depends strongly on the type of test, on the type of reinforcement, and upon the nature of the interface and the strength of the adhesion between the phases. In the case of polymer composites, the effect of fillers on abrasive wear is not, by any means, predictable [6]. Friedrich [7] has reported that the wear rate of thermoplastics is not improved by adding short fibres if the wear mechanism is highly abrasive in nature. In contrast, in the case of continuous fibre reinforcement, an increased wear resistance has been reported [8,9]. Lancaster [10] has studied the effect of short carbon fibres (30%) in 13 polymers and reported that in six of them abrasive wear increased due to fibre reinforcement while in the remaining seven polymers a decrease in wear occurred. Bijwe et. al. [11] tested polyamide (nylon 6), polytetrafluoroethylene (PTFE) and their various composites in abrasive wear under dry and multipass conditions against silicon carbide (SiC) paper on a pin-on-disc device. Particulate fillers (except a bronze powder in PTFE) were observed to be detrimental to wear performance and polymers without fillers had better abrasive wear resistance than their composites. The abrasive wear rate of quartz and glass particle-reinforced PMMA polymer composites has been investigated by Prasad and Calvert [12]. Their experimental results revealed that the increased wear rate of these PMMA composites was due to enhanced chipping of the filler at the filler/matrix interface. When filled PMMA was abraded by soft abrasives, filler removal was mainly by particle pull-out which was very dependent on the filler/matrix interfacial strength. All the above indicates that the effect of fillers on the

abrasive wear of polymers and their composites is determined by the properties of the matrix materials, the nature of the fillers, the amount and distribution of the embedded particles, and the interfacial bonding between the matrix and filler particles [13-16].

4.3.1 Abrasive wear

During all abrasive wear tests, no significant edge loading on the pin samples was detected. Figures 4.4 and 4.5 show the specific wear rate ($m^3/N \cdot m$) of polymeric coatings T-99A, I-1100A and P-A as a function of the sliding distance of the pin in abrasive wear tests without and with pin rotation respectively. The volumetric loss for each data point shown in the results was calculated from the weight loss which is the difference of weight before and after the abrasive test for each coating pin. For tests carried out with pin rotation, pin rotation leads to an additional distance slid. However, the magnitude of this additional distance varies across the pin, being greatest at the perimeter of the pin. Calculations showed that the additional distance slid by the perimeter of the pin was less than 1.5% of the total distance slid. Hence, this additional distance was not taken into account in calculating the sliding distances given in Figures 4.4 and 4.5. Error bars are included for the data in Figures 4.4 and 4.5 where duplicate tests were carried out. Based on numerous experiments the error in each individual determination is estimated as less than ± 5%.

Comparing the results shown in Figures 4.4 and 4.5 of the abrasive wear tests for the three types of coatings, the ratio of the wear rate between with pin rotation and without pin rotation is calculated and shown in Table 4.4.

Table 4.4 Ratio of wear rate between with pin rotation / without pin rotation

Coating	Ratio
T-99A	2 – 3
I-1100A	1.2 – 1.5
P-A	2 – 3

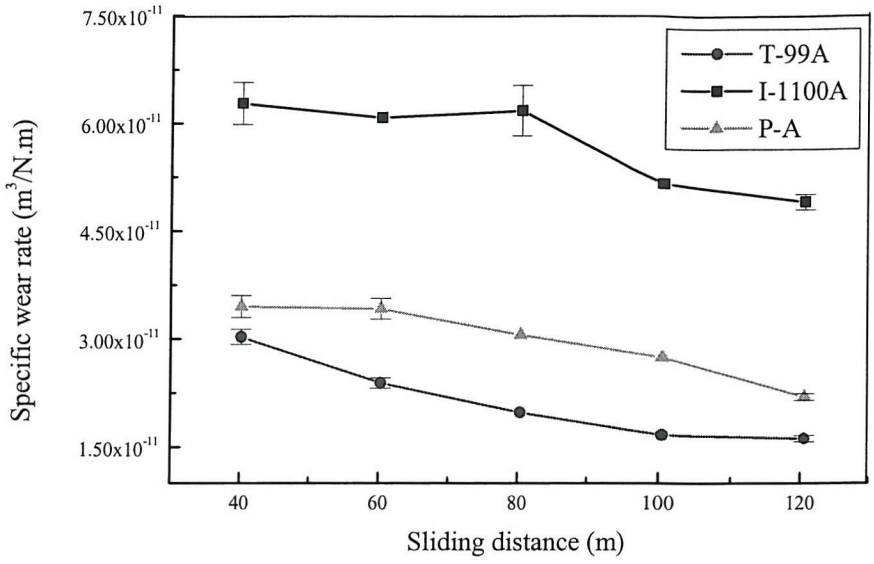

Fig. 4.4 Specific wear rate of the three polymeric coatings as a function of sliding distance in abrasive wear tests without pin rotation.

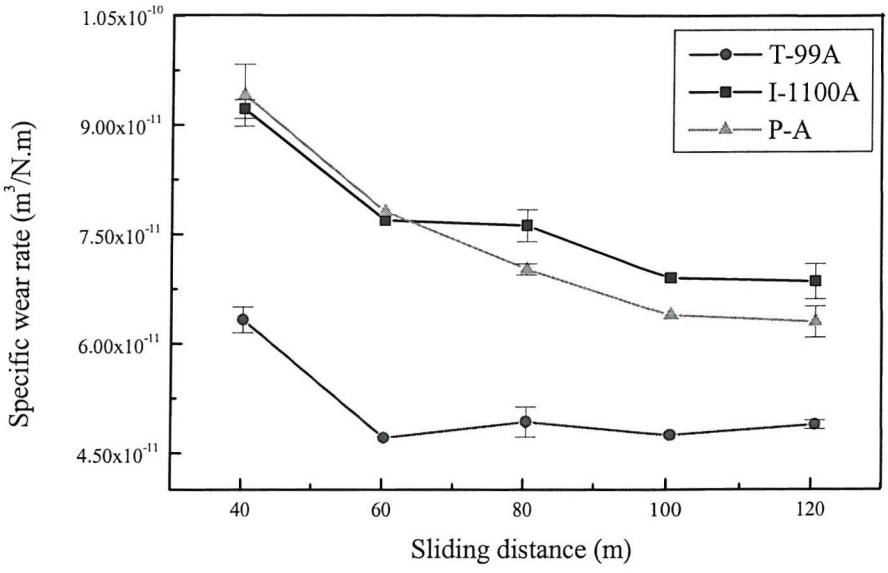

Fig. 4.5 Specific wear rate of the three polymeric coatings as a function of sliding distance in abrasive wear tests with pin rotation.

In the tests without pin rotation, the filled polymeric coating I-1100A had a much higher specific wear rate than coatings T-99A and P-A. Figures 4.6 to 4.9 detail reasons for this result. Figure 4.6 shows the wear scars on the unfilled polymeric coating T-99A. Long smooth ploughed furrows are present which indicate that the coating behaved in a predominantly ductile manner and most material was displaced with only some being cut and detached from the surface, resulting in low wear rates determined from weight loss measurements. Figure 4.7 presents the wear scars on the filled polymeric coating I-1100A. Instead of smooth and ductile furrows, short and fragile furrows and swarf-like tendrils were found on the surface of coating I-1100A. The fillers present in the coating can be seen at the position where fracture of the furrow has occurred. Thus, the filler is aiding the detachment of material. In addition as the bond between the fillers and the matrix is poor, fillers are easily detached and contribute to abrade the surface. Figure 4.8 gives a clear view of the fillers, after being detached from coating I-1100A, on the swarf-like tendrils. Furthermore, the voids left on the surface of the coating due to filler detachment act as stress raisers and produce cracks, so aiding the detachment of large sections of the coating. All the above features will exacerbate the wear rate of coating I-1100A. Figure 4.9 shows the wear scars present on the polymeric coating P-A. Its surface exhibits features seen in both coatings T-99A and I-1100A. The ploughed furrows were smooth, however, their fracture can be clearly seen. This was caused by the voids and the unmelted powders in the coating disrupting the furrows and causing their detachment. This effect was more severe in coating I-1100A due to the greater volume fraction of filler and to the abrasive nature of the fillers themselves. Hence coating P-A has a wear rate intermediate between that of coatings T-99A and I-1100A.

In the abrasive wear tests with pin rotation, the wear mechanism of these three coatings changed considerably, although the ranking of the specific wear rate of these three coatings was almost the same as in the tests without pin rotation. Comparing the results in Figures 4.4 and 4.5, it can be seen that the specific wear rate of filled coating I-1100A with pin rotation was only 1.2 to 1.5 times greater than that without pin rotation while coatings T-99A and P-A showed a 2 to 3 times increase. Figure 4.10 to 4.12 present the wear scars on the three coatings abraded with the pin rotating at 33 rpm. Very deep

intersecting ploughed furrows can be seen on coatings T-99A and P-A which were produced by an abrading action caused by the sliding and rotating action of the pin. The long ploughed furrows along the sliding direction were cut into shorter ones when the pin rotated. The short ploughed furrows on coatings T-99A and P-A were then easily detached from the matrix material and the specific wear rates, derived from weight loss measurements, were 2 to 3 times greater than without pin rotation. In the case of filled coating I-1100A, although the specific wear rate with pin rotation was higher than that without pin rotation, the difference between the two values was not as much as that for coatings T-99A or I-1100A. Figures 4.7 and 4.11 show the surface of coating I-1100A worn by the non-rotating and rotating pin. No deep furrows were found for the case of the non-rotating pin. The ploughed furrows caused by the pin rotating were shallower than the main ploughed furrows along the sliding direction of the pin. Thus, rotating the pin would be expected to have comparatively less effect on the wear rate of filled coating I-1100A than on coatings T-99A and P-A.

It is noticeable that for both tests without and with pin rotation on each type of coating, the specific wear rate reduced with increasing sliding distance. This is because during each of the abrasive wear tests, the coated pins slid on the same track on the SiC abrasive paper. After several traversals the abrasive grits on the abrasive paper tended to become somewhat clogged by the tendrils of polymers thus reducing their ability to abrade. Figure 4.13 shows the SiC abrasive paper after wear testing coating T-99A. The transferred polymer tendrils are clearly visible. Figure 4.14 shows the wear debris transferred to the SiC paper for coating I-1100A. However, the SiC grit particle is still proud and thus still capable of causing abrasive wear of the polymeric coating.

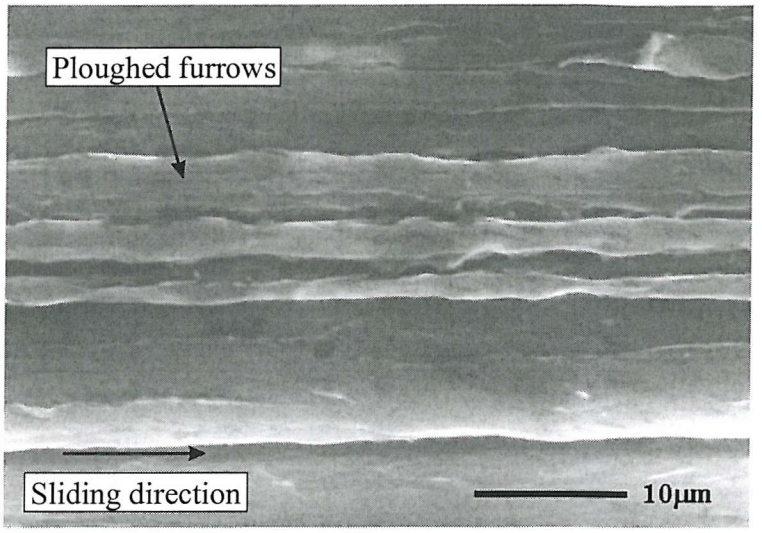

Fig. 4.6 Surface of coating T-99A after sliding 120 seconds without pin rotation in an abrasive wear test. Note the long ploughed furrows.

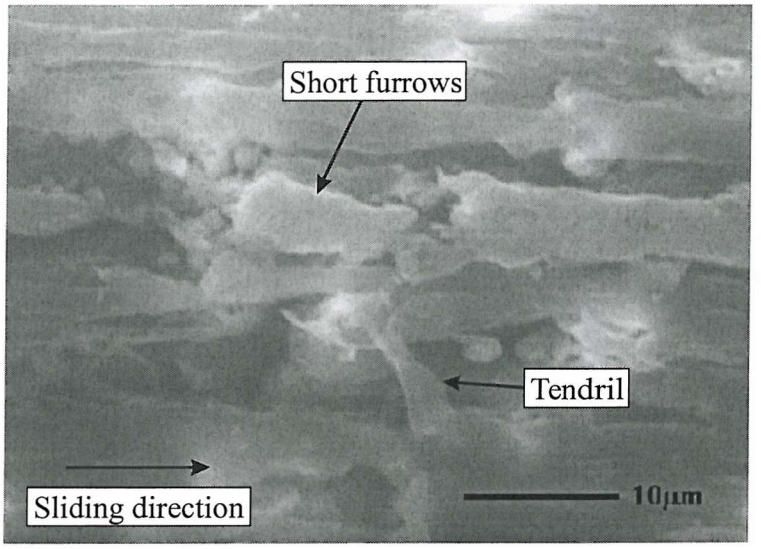

Fig. 4.7 Surface of coating I-1100A after sliding 120 seconds without pin rotation in an abrasive wear test. Note the short furrows and tendril production.

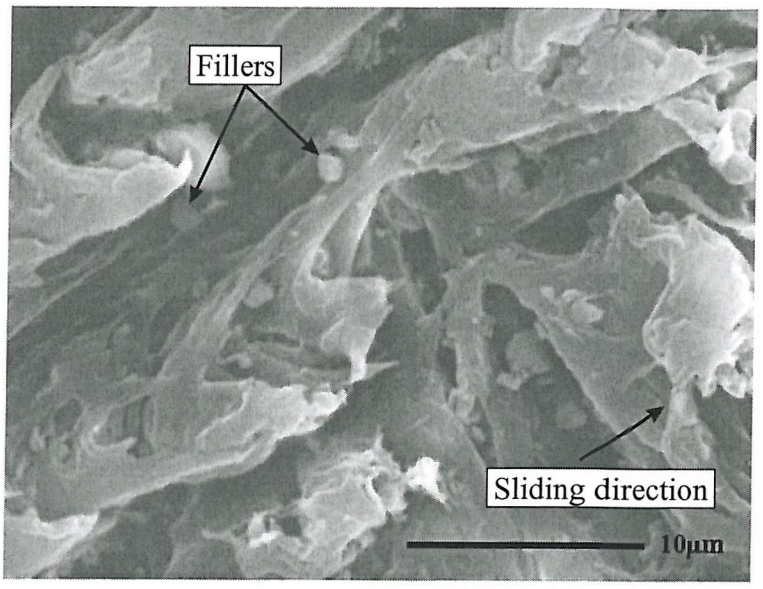

Fig. 4.8 Surface of coating I-1100A after sliding 90 seconds without pin rotation in an abrasive wear test. Note the fillers present on the swarf-like tendrils.

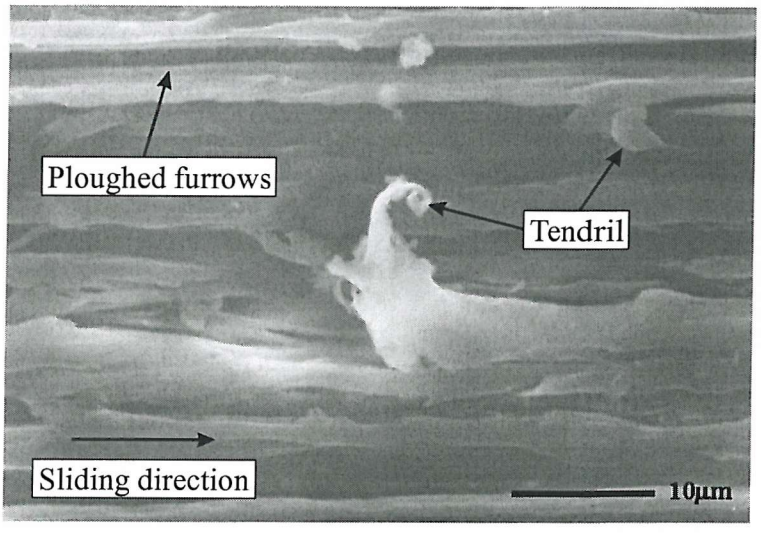

Fig. 4.9 Surface of coating P-A after sliding 150 seconds without pin rotation in an abrasive wear test. Note the ploughed furrows and tendril production.

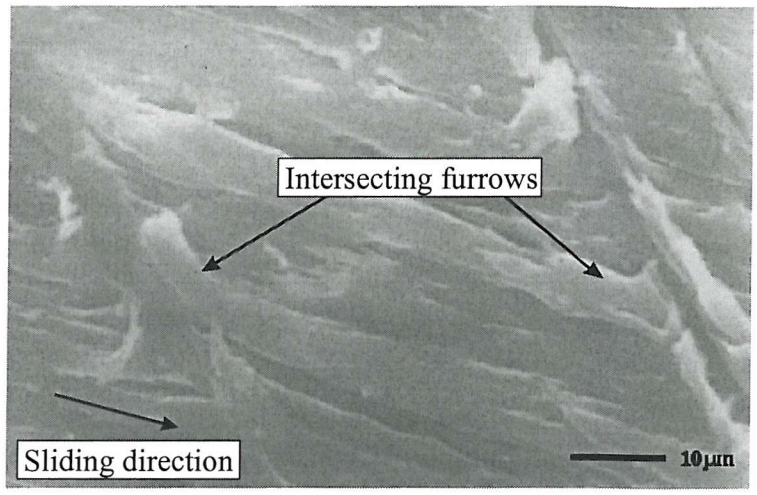

Fig. 4.10 Surface of coating T-99A after sliding 144 seconds with pin rotation in an abrasive wear test. Note the intersecting furrows.

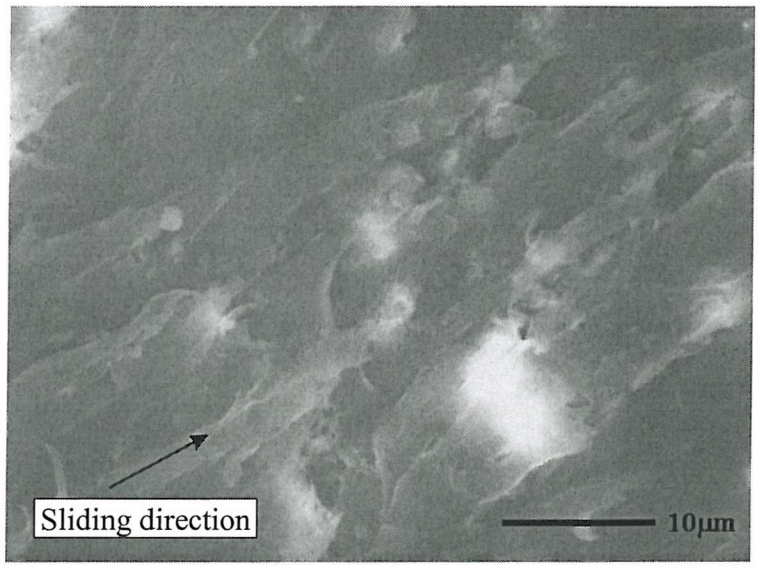

Fig. 4.11 Surface of coating I-1100A after sliding 120 seconds with pin rotation in an abrasive wear test. Note the furrows caused by the pin rotating were shallower than those along the main sliding direction of the pin.

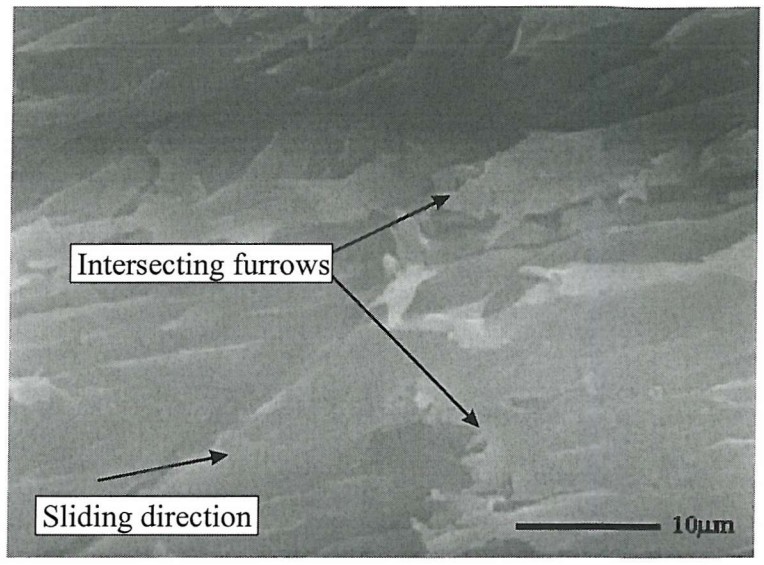

Fig. 4.12 Surface of coating P-A after sliding 120 seconds with pin rotation in an abrasive wear test. Note the intersecting furrows.

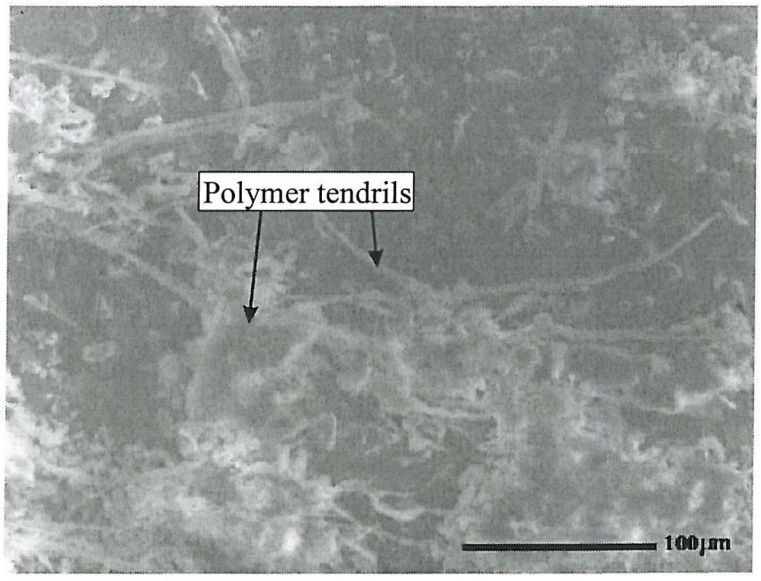

Fig. 4.13 Abrasive paper after 150 seconds in an abrasive wear test on coating T-99A with no pin rotation. Note the transferred polymer tendrils.

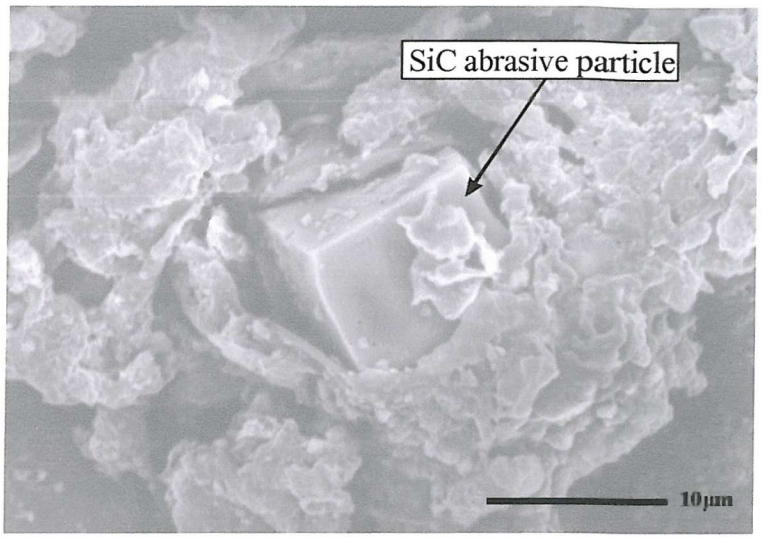

Fig. 4.14 SiC abrasive paper after 120 seconds of an abrasive wear test on coating I-1100A with no pin rotation. Note the transferred polymer and the SiC particle is still proud.

4.3.2 Wireline wear

Figures 4.15 (a), (b) and (c) show the slickline traces on the surface of tested samples T-99A, I-1100A and P-A, separately, after wireline wear tests. No significant edge loading on the pin samples was detected.

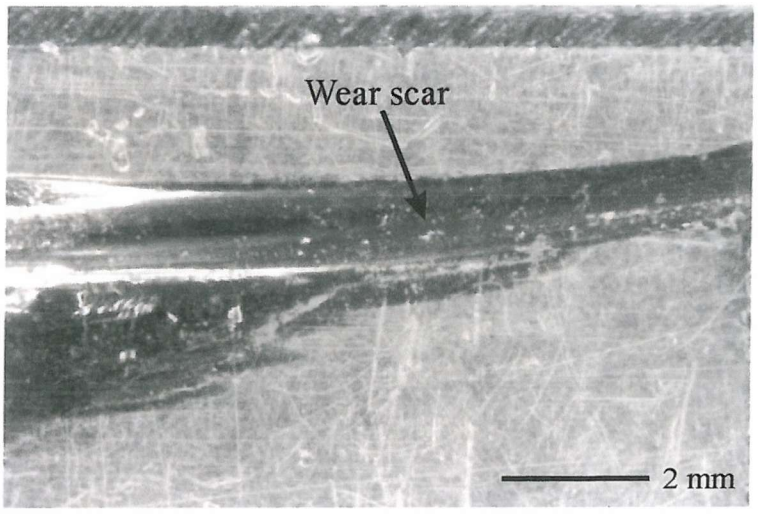

(a) T-99A

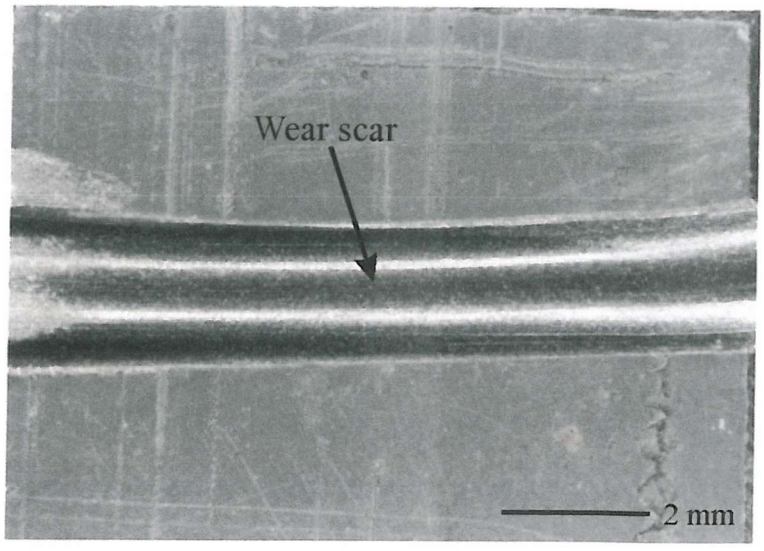

(b) I-1100A

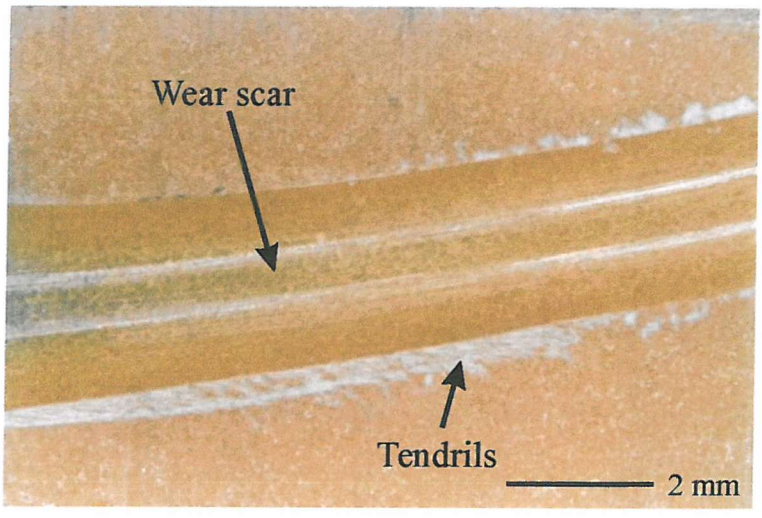

(c) P-A

Fig. 4.15 Slickline traces on the surface of the tested samples of T-99A, I-1100A and P-A.

Figure 4.16 shows the results of the volumetric wear rate (m^3/h) as a function of line load (N/mm) in the wireline wear tests. Coating T-99A had a very good wear resistant performance. Very shallow furrows were found at the bottom of the wear scar on coating T-99A, Figure 4.17. These were much smoother and shallower than those found in the abrasive wear tests. Below a line load of 12 N/mm, no wear was apparent on the surface of coating T-99A.

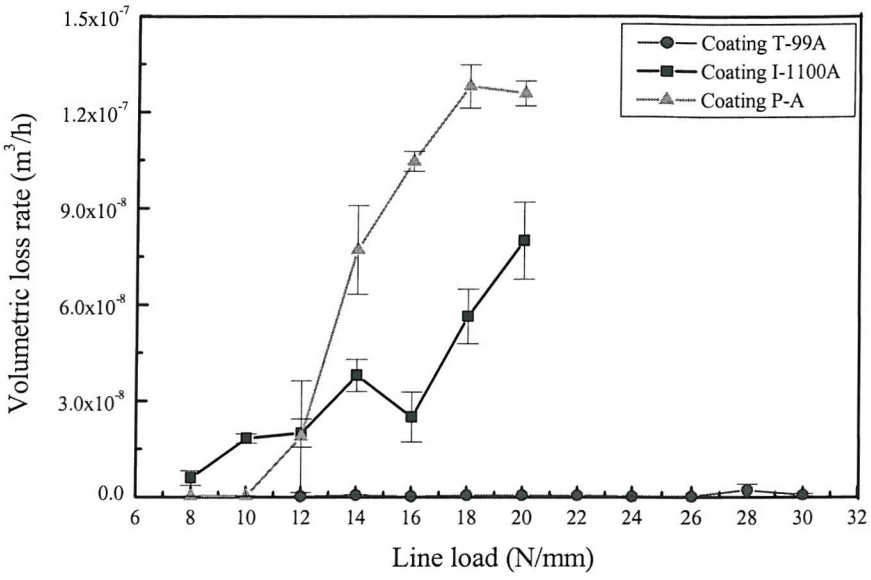

Fig. 4.16 Volumetric wear rate of coatings T-99A, I-1100A and P-A as a function of line load in wireline wear tests.

Coating P-A exhibited good wireline wear resistance when the line load was less than 10 N/mm. This was because the roughness of the slickline wire was less than that of the SiC paper. However, once the applied line load was greater than 12 N/mm, the wear rate increased dramatically. At the bottom of the scar, rod shaped fragile debris cut off from the coating could be seen together with many voids and cracks linking voids, Figure 4.18. Swarf-like tendrils starting at the perimeter of the voids were noted, Figure 4.19. It was thus easier for the asperities of the wire to cut and detach material from the edge of a void rather than from the bulk material. Hence, the voids in coating P-A impair its wireline wear resistance.

Coating I-1100A started to wear at a low line load of 8 N/mm; this was similar to its behaviour in the abrasive wear tests. Because of the weak bond between the fillers and the polymer matrix, the fillers were detached under load, and cut off the ploughed furrows. Figure 4.20 shows the swarf-like tendrils which were very similar to those found in abrasive wear tests. However, the fillers in the side wall of the scar could support part of the load and impede the wire from cutting deeper into the coating. Therefore, the presence of fillers might account for the wear resistance of coating I-1100A being somewhat better than that of coating P-A at line loads of above 12 N/mm.

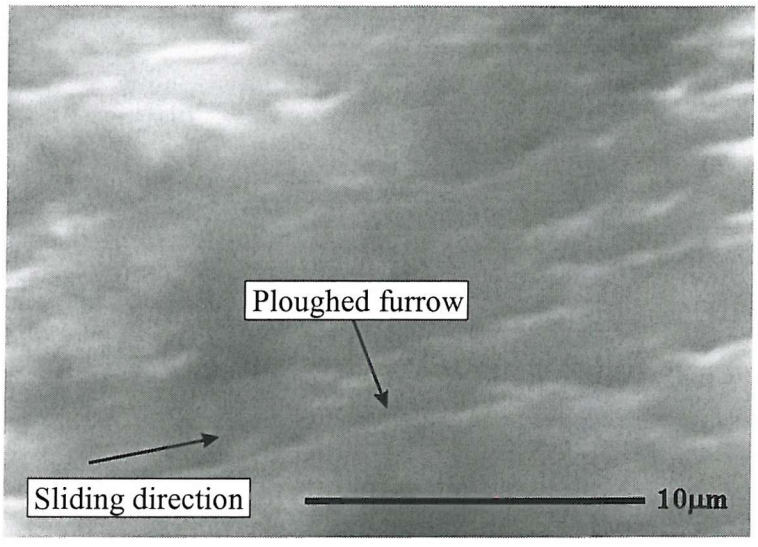

Fig. 4.17 Surface of coating T-99A after a wireline wear test under a line load of 26 N/mm. Note the very shallow furrows in the wear scar.

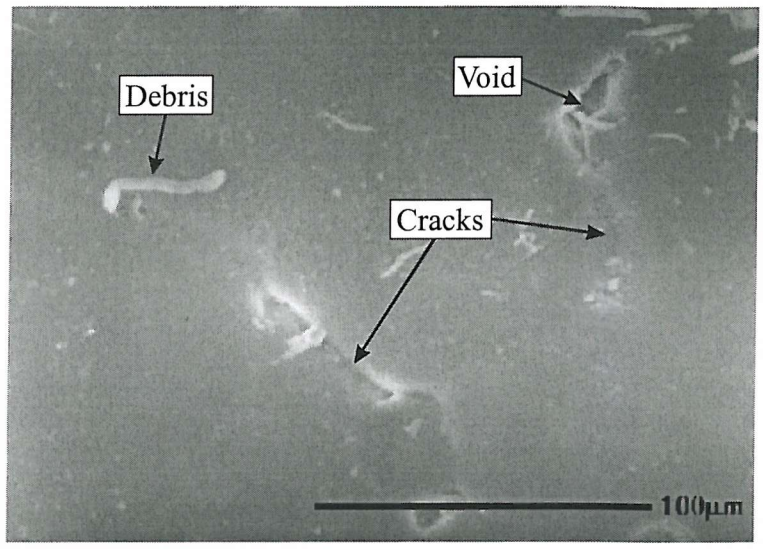

Fig. 4.18 Surface of coating P-A after a wireline wear test under a line load of 18 N/mm. Note the swarf-like tendrils starting at the perimeter of the voids in the wear scar.

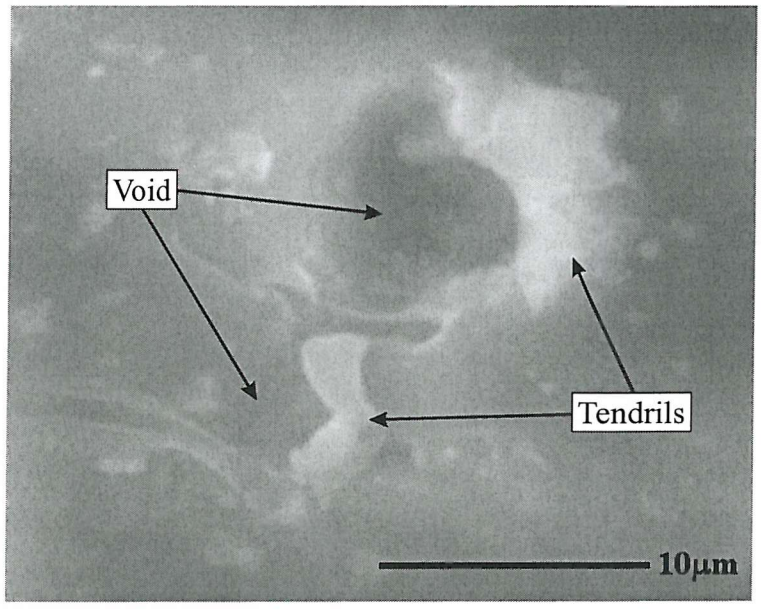

Fig. 4.19 Surface of coating P-A after a wireline wear test under a line load of 16 N/mm. Note the swarf-like tendrils in the wear scar.

UNIVERSITY OF SOUTHAMPTON LIBRARY

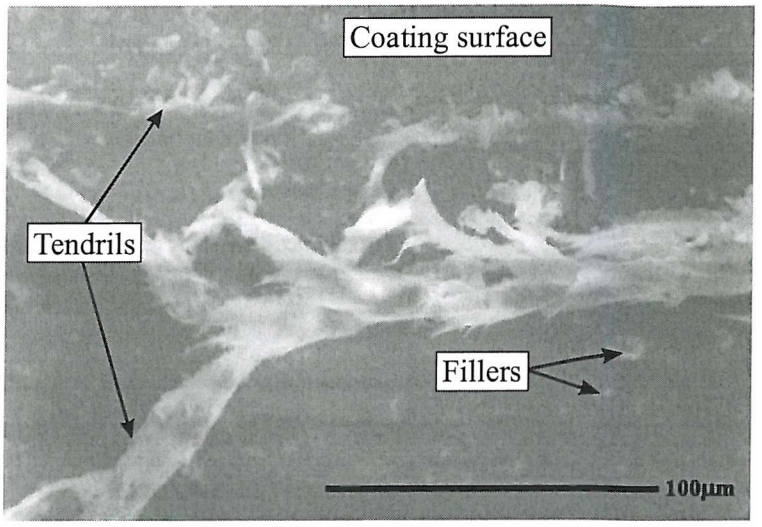

Fig. 4.20 Surface of coating I-1100A after a wireline wear test under a line load of 16 N/mm. Note the swarf-like tendrils at the edge of the wear scar.

4.4 Conclusions

In abrasive wear a polymer with a brittle filler has a higher wear rate than an unfilled polymer due to the fact that the brittle fillers can be easily fractured and detached from the polymer matrix. In general, the weak bond between the filler and a thermoplastic polymer matrix leads to the filler particles detaching from the matrix causing enhanced wear. In wireline wear the presence of voids and unmelted particles is particularly deleterious.

In this study, the unfilled nylon coating T-99A had the best wear resistance. The silica and dolomite filled polymeric coating I-1100A was found to have the worst abrasive wear resistance. This was because when the coated pin was slid on the abrasive paper, the fillers, rather than supporting the load, were pulled out due to the poor bond between the fillers and the matrix material. The poor bond also caused cracks associated with the fillers. The cracks reduced the wear resistance of the coating. The unfilled PVDF coating P-A had a worse abrasive wear resistance than coating T-99A because the presence of many voids and unmelted powder particles reduced the cohesive strength and aided fracture of the ploughed furrows.

It was found that unfilled coatings T-99A and P-A had worse wear resistance when the pin was rotated rather than not rotated because the deep ploughed furrows were cut into short intersecting ones which were easily detached from the coating. Rotating the pin produced a less significant increase in the wear rate of coating I-1100A than for coatings T-99A and P-A.

The presence of voids and unmelted powder particles in coating P-A were the main reasons for its poor wireline wear resistance.

4.5 New Pin-on-Disc Rig

The pin-on-disc rig described in the preliminary study on the thermoplastic coatings was prone to edge loading unless extreme care was taken during positioning the sample in the holder. Edge loading is an unwanted phenomenon for the wear test because the contact area of the specimen with the counterface will become uncontrolled. This can be solved by using a testing system with high rigidity. Therefore, after the preliminary study, a more robust pin-on-disc rig has been designed for future study of wear. The main frame used for new POD rig was an aluminium extrusion modular frame bolted on the concrete floor. Apart from the rigidity of the frame, another advantage of the new rig is its good design flexibility compared to the one described in Section 4.2 and this can be appreciated from the following aspects:

(i) The load applied in an experiment can be adjusted simply and accurately by placing the required weights on a plate on the top of the pin holder connected to the pin by a steel bar;
(ii) The alignment of a sample relative to the counterface can be adjusted easily;
(iii) The sliding radius of the pin can be simply changed according to the size of the available abrasive disc / radius of the slickline;
(iv) The pin holder can be fixed at different vertical heights in order to compensate for different thicknesses of the disc underneath the sample pin, etc.

It should be noticed that these flexibilities do not influence the rigidity of the main frame. The profile of the newly designed POD rig is shown in Figure 4.21.

The maximum speed which the new POD rig can approach is quite close to the theoretical maximum speed suggested by the oil industry. Thus, it is apparent that the newly designed wear rig can achieve the objectives of the present research work, utilising a true tribocouple to simulate better the working conditions in downhole tubulars.

The engineering drawing of the new pin-on-disc (POD) rig is given in Appendix A.

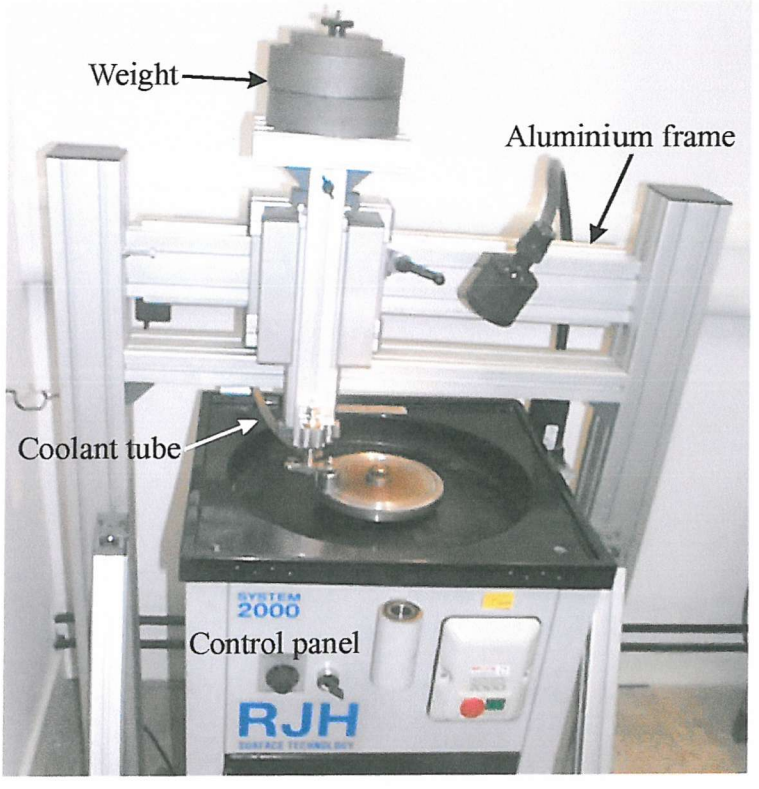

Fig. 4.21 Newly designed POD rig.

REFERENCES:

[1] N. Symonds, B. G. Mellor, Polymeric Coatings for Impact and Wear Resistance I: Wear, Wear 225-229 (1999), pp 111-118.

[2] N. Symonds, B. G. Mellor, R. J. K. Wood and S. Grooves, Wireline Wear Resistance of Polymeric Corrosion Barrier Coatings for Downhole Applications, Corrosion 2000, NACE International, Orlando, Florida, USA, paper 00170/1-12.

[3] Y.M. Xu and B.G. Mellor, The Effect of Fillers on the Wear Resistance of Thermoplastic Polymeric Coatings, Wear 251 (2001), pp 1522-1531.

[4] Stephen L. Rosen, Fundamental Principles of Polymeric Materials, A Wiley-Interscience Publication, John Wiley & Sons (1982), pp 303-311.

[5] Lawrence E. Nielsen, Mechanical Properties of Polymers and Composites, Volume 2, Marcel Dekker, New York (1974).

[6] J. M. Thorp, Abrasive Wear of some Commercial Polymers, Tribol. Int., 15 (1982), pp 59-68.

[7] K. Friedrich, Wear of Reinforced Polymers by Different Abrasive Counterparts. In K. Friedrich (ed.), Friction and Wear of Polymer Composites – Composite Materials Series 1, Elsevier, Amsterdam (1986), pp 233-287.

[8] M. Cirino, R. B. Pipes and K. Friedrich, The Abrasive Wear Behaviour of Continuous Fibre Polymer Composites, Journal of Material Science, 22 (1987), pp 2481-2492.

[9] K. H. Zum Gahr, Microstructure and Wear of Material, Tribology Series 10, Elsevier, Amsterdam (1987).

[10] J. K. Lancaster, Friction and Wear, in A. D. Jenkins (ed.), Polymer Science, A, Material Science Handbook, North Holland, Amsterdam (1972).

[11] J. Bijwe, C. M. Logani and U. S. Tewari, Influence of Fillers and Fibre Reinforcement on Abrasive Wear Resistance of some Polymeric Composites, International Conference on Wear of Materials, Denver, CO, U.S.A., April 8-14 (1989), pp 75-92.

[12] S. V. Prasad, P. D. Calvert, Abrasive Wear of Particle-filled Polymers, Journal of Materials Science, 15 (1980), pp 1746-1754.

[13] K. H. Z. Gahr, Wear by Hard Particles, New Direction in Tribology, I. M. Hutchings (ed.), published by Mechanical Engineering Publications Limited (1997), pp 483-494.

[14] L. Nicolais, E. Drioli and R. R. Landel, Mechanical Behaviour and Permeability of ABS/Glass Bead Composites, Polymer, Vol. 14 (1973), pp 21-26.

[15] R. T. Quazi, S. N. Bhattacharya and E. Kosior, The Effect of Dispersed Paint Particles on the Mechanical Properties of Rubber Toughened Polypropylene Composites, Journal of Materials Science, 34 (1999), pp 607-614.

[16] A. Meddad , B. Fisa, Filler-Matrix Debonding in Glass Bead-filled Polystyrene, Journal of Material Science, 32 (1997), pp 1177-1185.

CHAPTER 5 WEAR OF POLYMERIC COATINGS (II) – COMPARATIVE STUDY BETWEEN THERMOPLASTIC & THERMOSET COATINGS

5.1 Introduction

In the preliminary study (Chapter 4), three types of thermoplastic polymeric coatings (T-99A, I-1100A and P-A) have been chosen and subjected to abrasive and wireline wear tests. The influence of the coating structure and the bonding between matrix and fillers on the wear mechanism has been specifically addressed. However, the different wear mechanisms of thermoset and thermoplastic polymeric coatings under wear conditions have not been clarified. In this comparative study, two types of thermoset polymeric coatings, a modified novolac containing calcium silicate fillers and a modified epoxy containing alumina as the filler, and one type of thermoplastic coating, a fluoropolymer with 2% calcium fluoride filler, were selected for wireline wear tests. A true tribocouple consisting of the coating and a length of slickline wire on the newly designed pin-on-disc (POD) apparatus was used to study the wireline wear resistance of these three coatings as a function of applied load and sliding distance. The different wear mechanisms between thermoplastic and thermoset polymeric coatings have been investigated. The influence of fillers on wear mechanisms has been further studied. Detailed scanning electron microscopy (SEM) was carried out on the wear tracks produced to investigate the wear mechanisms. Energy Dispersive X-ray (EDX) spectroscopy was used to X-ray map the wear scars so as to quantify the amount and size distribution of filler present in the wear scar compared to that in the bulk material and thus elucidate the role of fillers in the wear mechanism.

In the present study, wireline wear tests have been carried out on three types of polymeric coatings (one thermoplastic and two thermoset) to determine wear rates, wear mechanisms and the effect of fillers.

5.2 Wireline Wear Tests

5.2.1 Coating characterisation

Two thermoset coatings T-15, T-34 and one thermoplastic coating F-4001 were chosen for the present wireline wear tests. The properties and the microstructural characteristics of these three coatings can be found in Section 3.2 of Chapter 3. For ease of comparison of the three coatings, the basic microstructural characteristics of the coatings are listed in Table 5.1. Details of the primer layer present on these coatings are not given, as the primer plays no role in determining the wear resistance.

Table 5.1 Details of the three types of polymeric coatings tested

Coating	Generic name	Resin type	Filler type	Filler size (μm)	Filler percentage	Coating density (kg/m^3)	Coating thickness (μm)
T-15	Thermoset	Modified novolac powder	$CaSiO_3$	10~30	~9 %	690	345 ~ 360
T-34	Thermoset	Modified epoxy-phenolic	Al_2O_3	10~30	~20 %	740	250 ~ 260
F-4001	Thermoplastic	Fluoropolymer powder	CaF_2	20~40	~2 %	1380	1500

5.2.2 Experimental apparatus

The newly designed pin-on-disc (POD) rig was utilised to simulate wear of a polymeric coating in a water injector undergoing inspection [1]. The replicated event was that of linear wear of a suspension wire against a section of internally polymeric coated tube. In the laboratory a 'true tribocouple' test condition was achieved. In the present study, a length of commercially available suspension wire marketed as "slickline" was embedded on a stainless steel disc for use with a POD apparatus. The slickline wire itself was 3.2 mm in diameter and was formed into a circular loop of 80 mm radius. The surface roughness of the slickline wire was Ra 0.35 μm along the axis of the wire. Its Vickers

hardness, 30 kg load, was 435. Coating samples were cut from the polymeric coated plates to form square pins with dimension of 10 ± 0.5 mm, which were then loaded against the revolving circular loop of wire. Figure 5.1 shows a photograph of the POD experimental apparatus, presenting the polymeric coating pin clamped in a pin holder with the slickline wire sliding beneath it.

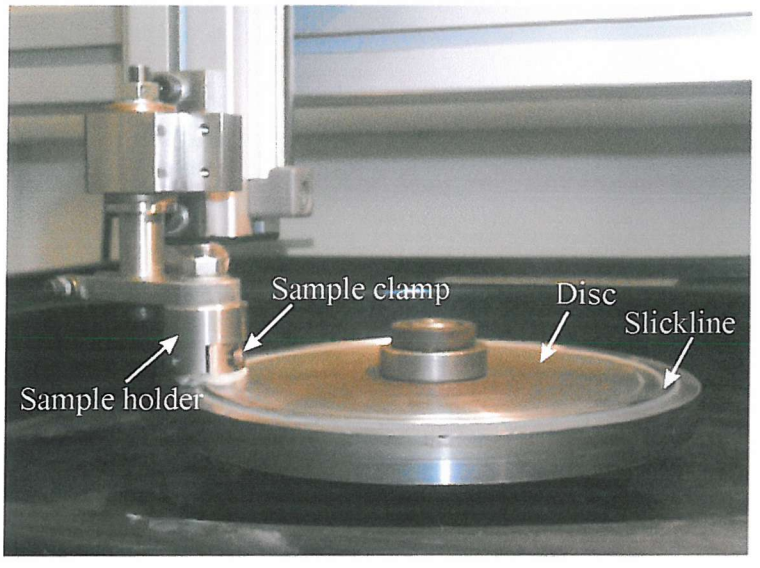

Fig. 5.1 The newly designed POD apparatus for wireline wear tests.

5.2.3 Experimental procedure and conditions

Two types of comparative experiments have been carried out on the polymeric coatings in this study – firstly an investigation of the influence of applied load on wear rate and secondly an investigation of the influence of sliding distance on volumetric loss. In the real offshore service, the inspection tools used are from 40 to 200 kg and the contact length between the slickline which the tool is attached and the tubulars is around 50 to 100 mm. For the study on the influence of load, the load applied to the sample pins was varied from 80 N to 220 N while the sliding distance was maintained constant at 500 m. Thus, these line loads were selected as they are approximately equal to the line loads seen in service. To study the influence of sliding distance, the load applied to the coatings was fixed at 150 N and the sliding distance was varied from 250 m to 1250 m. For both types

of experiments the rotational speed of the disc was 100 rpm and tap water coolant was supplied during the experiment to prevent the temperature rising from the sliding action of the coating pin against the slickline wire. The experimental conditions are detailed in Table 5.2.

During the wear test the coating and the wire will wear. Wear of the asperities on the wire might result in a lower wear rate of a coating subsequently tested against this "worn" wire. In order to eliminate the influence of wear of the wire in the two types of comparative study carried out on the three different polymeric coatings, a new slickline wire loop was used for each polymeric coating for both types of experiment. Additionally, in order to study quantitatively the influence of the "worn" wire on the wear rate of the polymeric coatings, the "worn" wire was used to repeat the wear test carried out with the lowest applied load.

Table 5.2 Experimental conditions for the wireline wear tests

	Tests at various loads	Tests at various sliding distances
Load (N)	80, 115, 150, 185, 220	150
Sliding distance (m)	500	250, 750, 1250
Rotational speed of disc (rpm)	100	100
Testing time (min)	10	5, 15, 25
Volume of coolant water (l/min)	1	1

5.3 Experimental Results and Discussion

5.3.1 Wear rates of polymeric coatings from wireline wear tests

The mass loss of each specimen after wear testing was determined and converted into volume loss in order to calculate volumetric wear rate (m^3/h) of the polymeric coating.

Figure 5.2 shows the volumetric wear rate of the three polymeric coatings T-15, T-34 and F-4001 as a function of the load applied. Error bars are included for the data where duplicate tests were carried out. The thermoplastic polymeric coating F-4001 showed, in general, the highest wear rates of the three polymeric coatings tested. Figure 5.2 shows an increase in wear rate for all three polymeric coatings with increasing applied load. However, the wear rate of the thermoplastic coating F-4001 showed little increase in wear rate with loads above 150 N. The thermoset coating with the highest percentage of filler particles, T-34, exhibited a linear increase in wear rate with load while the wear rate of the thermoset coating T-15 with fewer filler particles showed a sudden increase in wear rate between loads of 150 N and 185 N. Figure 5.3 indicates that volumetric loss increases with sliding distance. Note only the data from coating T-15 would seem to extrapolate in a linear manner through the origin of the plot.

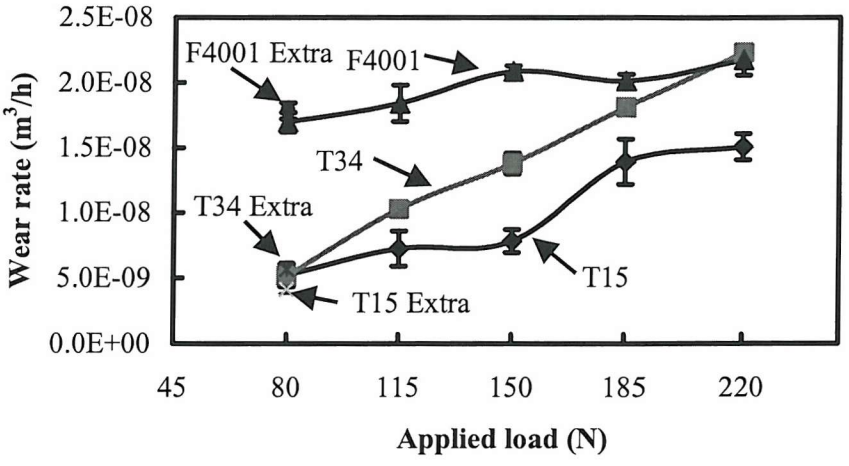

Fig. 5.2 Wireline wear rates of the three polymeric coatings tested as a function of applied load.

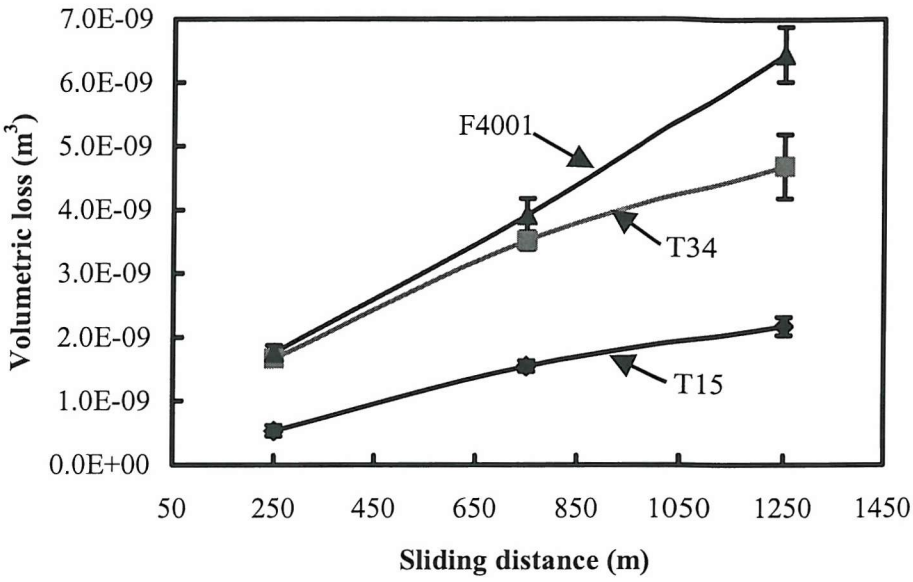

Fig.5.3 Volumetric loss of the three polymeric coatings tested as a function of sliding distance.

5.3.2 Wear mechanisms

Several mechanisms have been proposed by Zum Gahr [2] to explain the processes of two-body abrasive wear that are possible when a single abrasive tip traverses a surface of a polymeric material. These mechanisms were defined as microploughing, microcutting, microfatigue and microcracking. Because of the complexity of abrasion, no one mechanism completely accounts for the loss of material under any given condition. Generally, microploughing and microcutting are the dominant processes on ductile materials while microcracking becomes important on brittle materials.

Fillers, in the form of particulates and fibres, are often added to polymeric materials to improve their stiffness and strength [3]. This second phase filler material will influence the wear resistance of the composite material. There are many references that illustrate the influence of fillers and fibre reinforcement on the abrasive wear resistance of polymeric composites [4, 5, 6]. Under controlled testing a given phase shows a specific wear mode and wear rate, which is determined by its individual properties. Consequently,

when various phases are combined to form a multiphase material, it is expected that the overall performance will be a function of the respective contribution of each phase [7]. Nevertheless, the influence of the structure of composites on abrasive wear is a complex function of the properties and interactions of the matrix, the reinforcing constituent, and the interface between them [8] and experimentally it is found that fillers can either enhance or degrade the wear resistance of polymeric composites [9]. Tanaka and Kawakami [10] studied the effect of different fillers on PTFE based composites. They recommended a filler size ranging from several micrometres to about 30 μm as the most suitable for PTFE (Polytetrafluorethylene) based composites. Small fillers within PTFE result in poor wear resistance of the PTFE. This is due to the fact that small fillers on the frictional surfaces cannot prevent large scale destruction of the banded structure of the PTFE matrix and thus very small fillers are easily removed from the wearing surface together with the PTFE film and transferred onto the counterface. PTFE and PEI (Polyetherimide) proved to be good wear-resistant materials in a study by Bijwe et al. [4]. However, adding fillers resulted in an inferior wear performance for both materials. SEM analysis of the pin surface revealed that a number of deep cracks were present which propagated in a direction normal to the abrasion furrows. Poor adhesion of the filler to the matrix gave rise to the initiation of these cracks and hence increased the wear rate. In conclusion, wear of polymeric composites is influenced by the properties of the filler, of the matrix and of the interface, by the relative hardness of the filler to that of the abrasive grit or counterface, by the content, shape, size, distribution and orientation of filler, by the abrasiveness of filler against the matrix and last but not least by the loading conditions during abrasive wear.

In present study, wearing the slickline wire against the surface of a specimen of polymeric coating produced a scar that contained features of the wear mechanisms for each coating. When studying the wear scar using scanning electron microscopy, it was noted that the key evidence on the wear mechanism operative was not only to be found at the bottom of the wear tracks themselves, but also at the areas close to the edges of the scars. The slickline wire had a curved surface, so the coating was worn in an ever

widening and deepening track until the diameter of the wire was reached or the test finished. Therefore, the edge of the track was the last area of virgin surface to be worn.

Figure 5.4, a SEM micrograph of the wear scar of coating F-4001 tested at a load of 80 N, shows both microploughing and microcutting wear mechanism are operative at this low load. These features were found on all specimens of the thermoplastic coating F-4001 tested. Figure 5.5 shows the debris left at the edge of the wear scar on the thermoplastic coating F-4001 tested under a higher load of 185 N. This debris is produced by an extrusion mechanism. This was also found at lower loads but to a more limited extent. Microploughing furrows were also present on this wear scar. These mechanisms of material loss are responsible for the high wear rate exhibited in Figure 5.2. Figure 5.6 shows the bottom of the wear scar of coating F-4001 tested under the highest applied load, 220 N. Microcracking can be seen in the direction normal to the microploughing furrows. High friction force between the slickline wire and the coating surface under this high applied load was the main reason for microcracking. Additionally, higher loads forced the water coolant out from the contact area increasing the friction force dramatically. This might induce thermal cracking. However, as can be appreciated from Figure 5.2 microcracking at loads above 150 N did not produce an increase in wear rate because the F-4001 coating was not removed by this mechanism due to the tough, ductile nature of the thermoplastic matrix.

Figure 5.7 shows a wear scar on the thermoplastic coating T-15 tested under an applied load of 80 N, microcracking and microploughing can be seen as the main wear mechanisms at the bottom of the wear scar. Microcracking initiated from the filler particles and the cracks propagated into the matrix; the microploughing furrows were shallower than the furrows found in the wear scar of the thermoplastic coating F-4001. Under the applied load, stress was concentrated around the filler particles causing cracks between the fillers and matrix. However, the filler particles were not detached from the matrix material under this low load due to the good bonding between the fillers and matrix. Figure 5.8, a SEM micrograph close to the edge of the wear scar on T-15 under a 80 N load, shows microcracks around the fillers and large fillers which have been

fractured and fragmented but which are still held in the matrix material. This indicates that the filler particles have good bonding with the matrix and that they can support part of the load in the wireline wear tests. Figure 5.9 shows that under a higher load of 150 N large filler particles were fractured into fragments and many small filler particles were detached from the matrix material leaving cavities in the matrix. These cavities were themselves stress concentrations and resulted in more cracks in the matrix and a higher wear rate as was seen in Figure 5.2. At an even higher load (185 N), Figures 5.10 and 5.11 show that severe microcracking took place around the edge of the wear scar and at its bottom. Large sections of matrix were removed causing even larger filler particles to be detached from the matrix. Thus the fillers do not now support the load resulting in a sudden increase in the wear rate as shown in Figure 5.2. It was noted as for F-4001 that at large loads water was forced out from under the contact for T-15. Thus it is possible that some of the cracks seen in Figures 5.10 and 5.11 may have a thermal origin.

Figures 5.12 and 5.13 show wear scars on the thermoset coating T-34 after testing under a low load of 80 N and a high load of 220 N. Very similar wear features were found for all the loads applied to this coating. Microcracking of the matrix material was the main wear mechanism operative. The matrix material exhibited very poor wear resistance in wireline wear tests as it was fractured and removed even before the filler particles were detached from the matrix. This is in agreement with that shown in the SEM micrograph of the metallographically prepared cross section of coating T-34 shown in Figure 3.7 where many fillers are observed to be proud of the coating matrix after the metallographic polishing process. Figure 5.14 shows poor bonding between the filler and the matrix; the fillers were easily detached from the matrix under a low load of 80 N leaving cavities whose boundaries were the same shape as the filler particles removed. Many cavities within the matrix material structure lead to many stress concentrations in the matrix resulting in higher local stresses, microcracking and in consequence a high wear rate. Additionally, the high percentage (20%) of fillers in coating T-34 degraded the wear resistance of the coating because the fillers themselves caused stress concentrations in the matrix. Furthermore, the detachment of fillers causes the adjacent matrix to be poorly supported and hence is subjected to greater stress and thus more susceptible to fracture.

Figure 5.15 shows a large crack in the matrix, normal to the sliding direction, which formed after neighbouring fillers had been detached. This would give rise to a high volume loss of matrix.

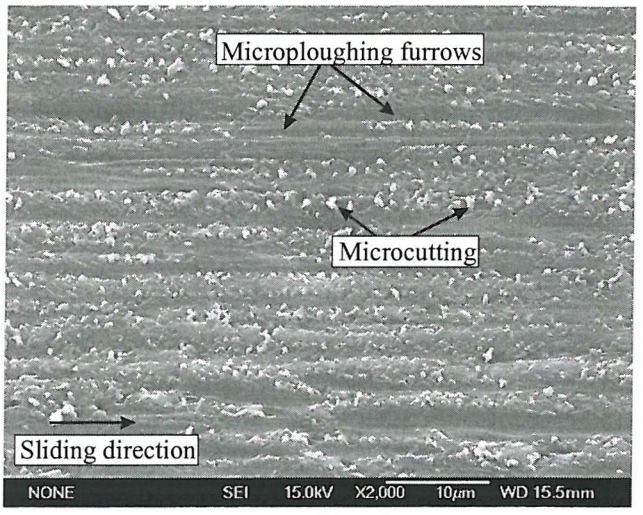

Fig.5.4 Wear scar on the thermoplastic coating F-4001 under a load of 80 N, showing microploughing and microcutting to be the dominant wear mechanisms causing loss of material.

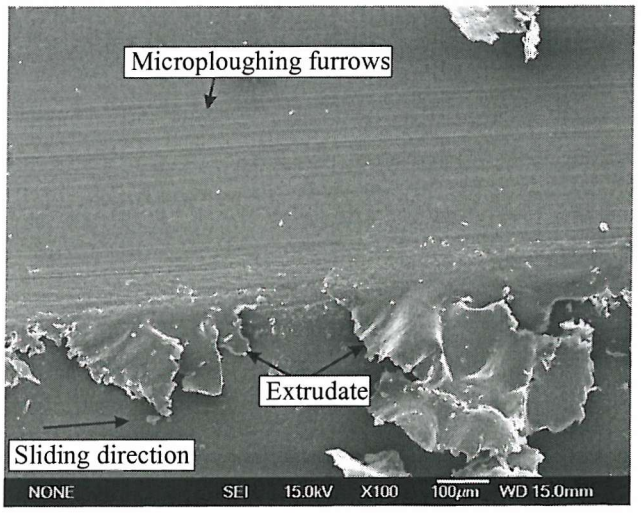

Fig. 5.5 Wear scar on the thermoplastic coating F-4001 under a load of 185 N. Note the extrudate left on the edge of the wear scar and the microploughing furrows.

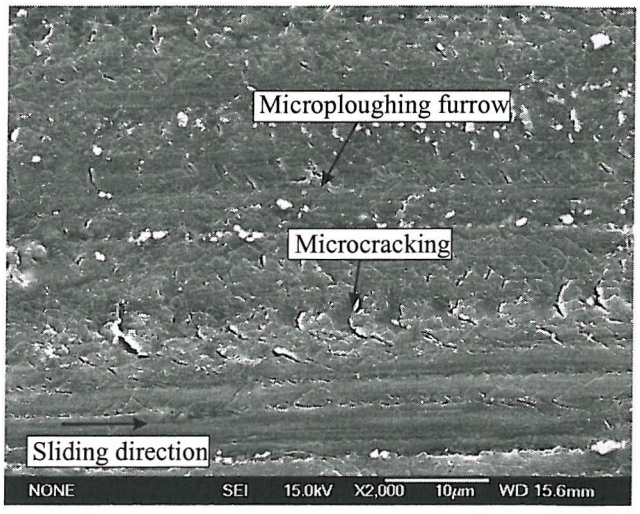

Fig. 5.6 Bottom of the wear scar on thermoplastic coating F-4001. Note the microcracking occurring under a load of 220 N. However, the microcracks did not propagate leading to material removal.

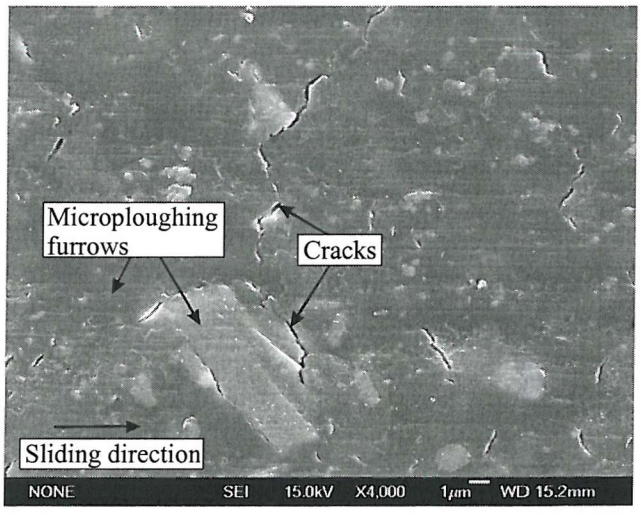

Fig. 5.7 Wear scar on the thermoset coating T-15 under a load of 80 N. Note the cracks initiating from the fillers and propagating into the matrix. Microploughing furrows were also found on the surfaces of both fillers and matrix indicating that the fillers supported the load applied from the slickline wire.

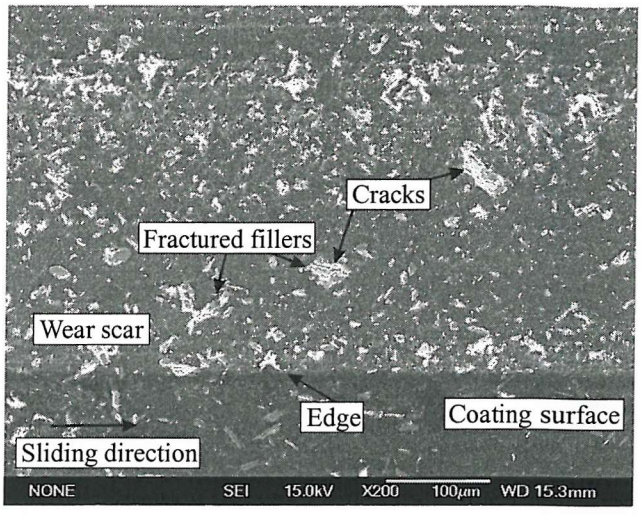

Fig. 5.8 Wear scar on coating T-15 under a load of 80 N. Note the fillers fragmented but the fragments were retained in the matrix to support part of the load applied from the slickline wire.

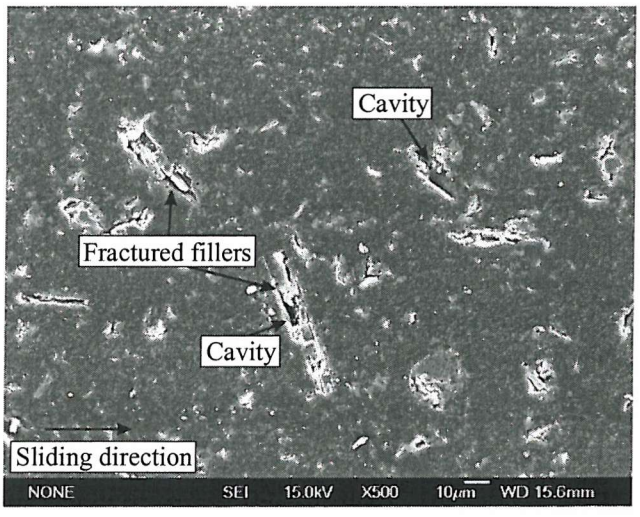

Fig. 5.9 Wear scar on coating T-15 under a load of 150 N. Note the fillers were fragmented and detached from the matrix with this higher load.

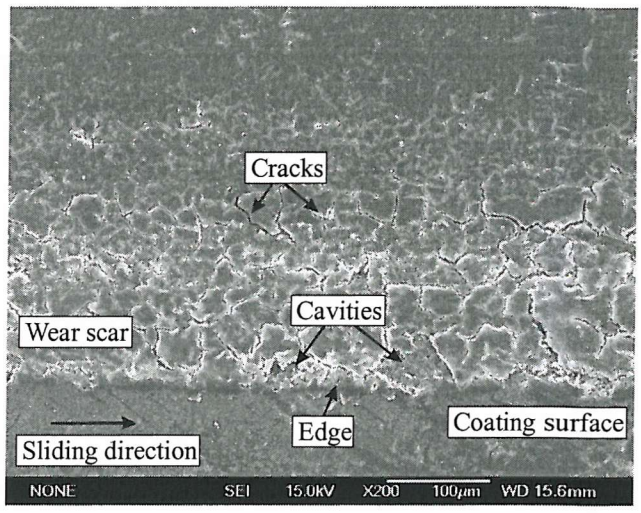

Fig. 5.10 Wear scar on coating T-15 under a load of 185 N. Note severe microcracking of the coating matrix along the edge of the wear scar.

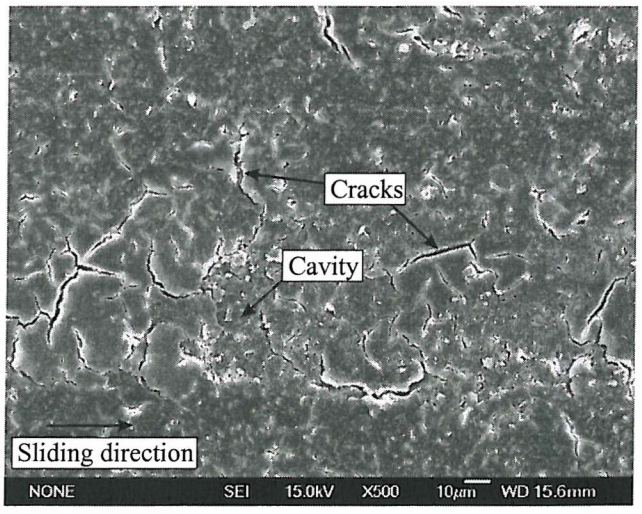

Fig. 5.11 Wear scar on coating T-15 under a load of 185 N. Note large cracks were found at the bottom of the wear scar and contributed to matrix removal.

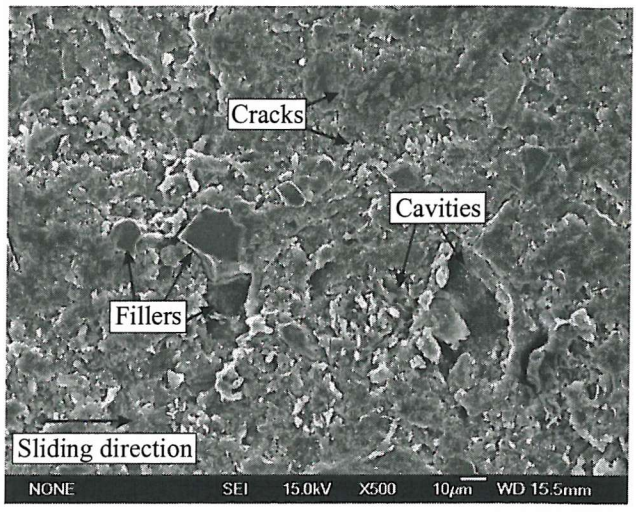

Fig. 5.12 Wear scar on coating T-34 under a load of 80 N. Note the poor wear resistance of the matrix material. The matrix material was fractured and removed from the coating surface leaving the fillers proud of the matrix; the fillers then detached leaving the cavities in the matrix.

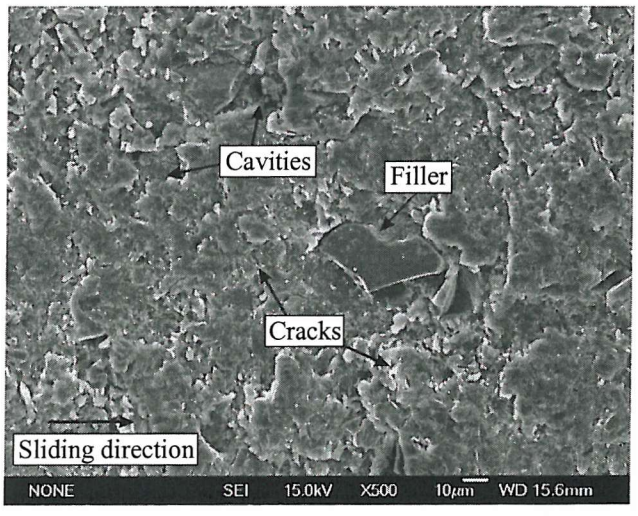

Fig. 5.13 Wear scar on coating T-34 under a load of 220 N. Note the similarity of features found on samples tested at both 80 and 220 N.

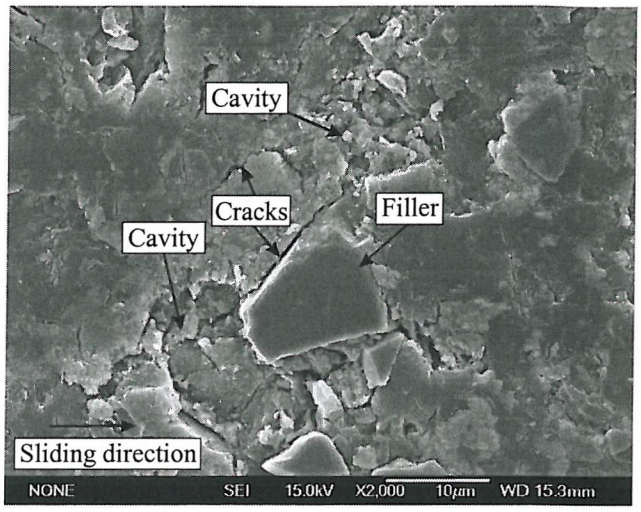

Fig. 5.14 Wear scar on coating T-34 under a load of 80 N. Note the poor bonding between the fillers and matrix causing the fillers to detach easily.

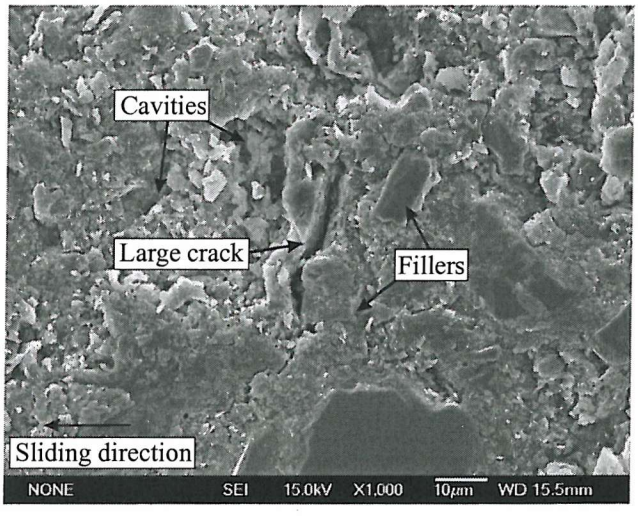

Fig. 5.15 Wear scar on coating T-34 under a load of 80 N. Note the large crack in the matrix normal to the sliding direction formed after neighbouring filler particles had detached.

5.3.3 Influence of the topography of the slickline wire on the wear of polymeric coatings

During the wear test the slickline wire itself will wear somewhat especially when the polymeric coating contains abrasive filler particles. Figure 5.16 shows part of the slickline wire loop after concluding wear testing at various loads for coating T-15 and clearly reveals the difference between the "worn" wire and the wire which has not been in contact with the filled polymeric coating. The asperities on the surface of the slickline wire in contact with the coating have polished somewhat (Ra = 0.21 μm as compared to the original value of Ra 0.35 μm), however longitudinal ridges and grooves are still present on the "worn" wire.

The wear rates of the three polymeric coatings using the "worn" slickline wire and conditions of 80 N load and 500 m sliding distance are also shown in Figure 5.2 (identified as "extra"). The wear rate of T-15 by the "worn" slickline wire was approximately 21% less than that by the "new" slickline wire. Thus, although some asperities are removed from the slickline wire during this wear test its microploughing ability is maintained by the longitudinal ridges still present on the "worn" wire. It should be noted that the "worn" wire used for the repeat experiments and that shown in Figure 5.16 was that corresponding to after all the experiments with varying load had been concluded on that coating type. Therefore, the difference in wear rates between any two adjacent tests carried out on the T-15 coating attributable to the different condition of the slickline wire should be much less than 21%.

The wear rates of T-34 and F-4001 by the "worn" slickline wire were 11% and 5% higher than that by the "new" wires, however, these values are within the experimental error range which suggests for these coatings less polishing of the asperities on the slickline wire is taking place. In the case of the filled polymeric coating T-34 it was noted that the filler particles were readily removed from the matrix and thus did not support the applied load appreciably. Hence they would be expected to abrade the slickline wire less.

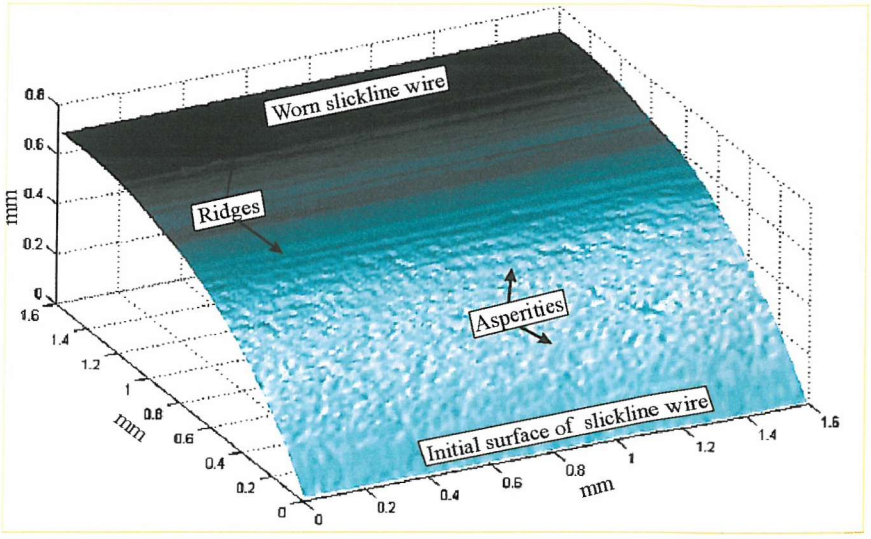

Fig. 5.16 A section of the slickline wire loop after concluding the wireline wear tests under various loads for coating T-15. Note the difference between the surface of the "new" slickline wire and the "worn" slickline wire; asperities on the wire surface have been polished, however ridges can still be seen running along the longitudinal sliding direction.

5.3.4 The influence of load and sliding distance on wear rate

A simple model of abrasive wear, based on the Archard equation, predicts that the volume of material removed by two-body abrasion should be directly proportional to the normal load and also directly proportional to the sliding distance [2]. Figure 5.2 shows that, in general, the wireline wear rate of the three polymeric coatings increases as the load increases but the three coatings exhibit different relationships between wear rate and load. Little increase in wear rate with load was observed for the thermoplastic coating F-4001 above a load of 150 N. Microcracking was found at loads above 185 N in this material. As these microcracks did not propagate, this wear mechanism did not lead to additional material removal and an increase in wear rate with load. A large amount of microcracking was found on the thermoset coating T-15 at loads of 185 N and above. These microcracks propagated resulting in a sudden increase in wear rate as large filler particles were removed from the matrix material. No change in wear mechanism with load was detected for the thermoset coating T-34, therefore the wear rate of this coating

increased in a constant manner with load as shown. As noted above wear rate should be directly proportional to load. Fitting a power law relationship to the data in Figure 5.2 for coating T-34 and to the data for loads less than or equal to 150 N for coatings T-15 and F-4001 gives power law exponents equal to 1.4, 0.89 and 0.27 respectively. Only the data for coating T-15 give an exponent close to 1 suggesting that the simple wear model does not hold for coatings T-34 and F-4001.

As noted above the simple abrasive wear model would predict that the volume of material removed should be directly proportional to the sliding distance, i.e. the volumetric loss per unit sliding distance should be a constant. Figure 5.17 presents the volumetric loss per unit sliding distance as a function of sliding distance. This figure indicates that the volumetric loss per unit sliding distance of the thermoplastic coating F-4001 and particle filled thermoset coating T-34 decreased by approximately 25% as the sliding increased from 250 to 750 m, while for sliding distances between 750 and 1250 m the volumetric loss per unit sliding distance did not changed significantly. The volumetric loss per unit sliding distance of the thermoset coating T-15 did not change appreciably for all the three sliding distances tested. In the case of a wear test in which the nominal size of the wear contact increases with sliding distance, it is not at all obvious that the wear volume per unit sliding distance should necessarily remain constant [12]. During the wireline wear tests the nominal area of the wear contact is continually increasing and consequently the nominal contact pressure is continually decreasing. For a constant asperity density on the wireline surface this would imply that the load on the individual asperity decreases as the nominal contact pressure decreases [12]. In order for the volumetric loss per unit sliding distance to be independent of the sliding distance, it must also be independent of the load per asperity. This is predicted by some wear models [13], which implies that the total wear given by the sum of the wear caused by each individual asperity is constant for a given load. However, the changing geometry of the wear track with sliding distance might mean that the above equality does not always hold. Indeed, Figure 5.18 shows the volumetric loss per unit sliding distance as a function of the nominal contact pressure based on the projected area of the wear scar. This figure would seem to suggest that above a certain nominal contact pressure, or load per asperity, the volumetric loss per unit

sliding distance is independent of nominal pressure but below a certain value the volumetric loss per unit sliding distance decreases as the nominal contact pressure decreases.

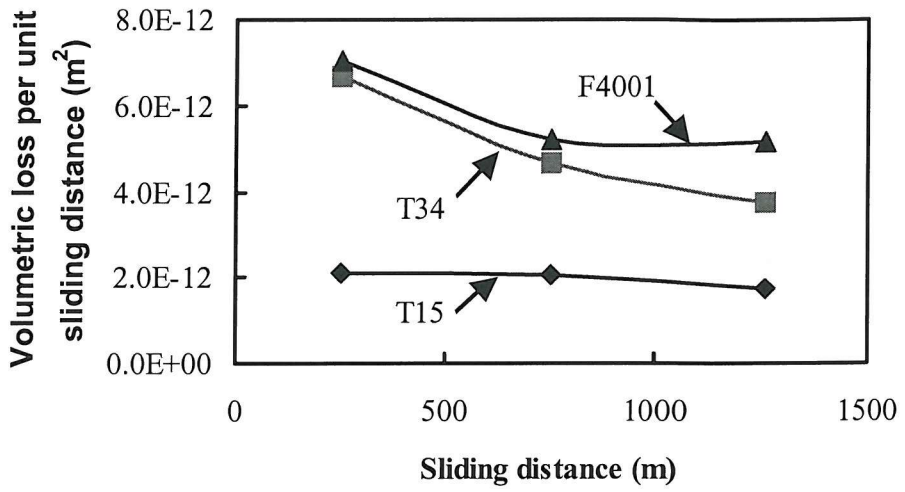

Fig. 5.17 Volumetric loss per unit sliding distance as a function of sliding distance for the three polymeric coatings tested.

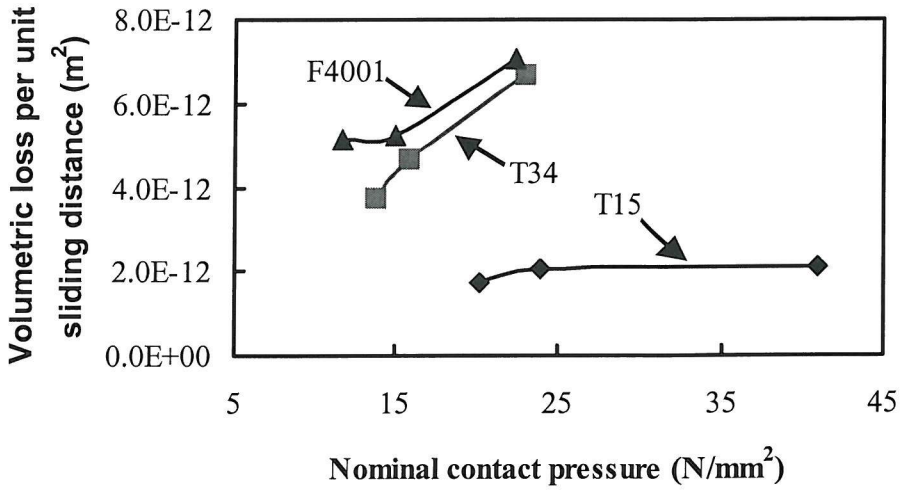

Fig. 5.18 Volumetric loss per unit sliding distance as a function of nominal contact pressure for the three coatings tested.

5.3.5 Role of the filler in wireline wear of polymeric coatings

Filler particles play an important role in determining the wear rates of the filled polymeric coatings, therefore it is important to study how the number and size of these filler particles evolve during wireline wear. Figures 5.19 (a), (b) and (c) show the SiKα X-ray maps of the surface of the coating T-15 before the wireline wear tests and of the wear track after tests at 150 N and 185 N. A suitable magnification was chosen so that the whole width of the wear scar was included in the map. The same magnification was used for all X-ray maps. Similarly, Figures 5.20 (a) and (b) and (c) show the AlKα X-ray maps of the surface of the coating T-34 before the wireline wear tests and of the wear track after tests at 150 N and 185 N. These X-ray maps were subject to standard image analysis techniques to determine the number of filler particles present in a given area and their size distribution. Figure 5.21 presents the area percentage of fillers present initially and in the wear track after tests at loads of 150 and 185 N. This confirms that fillers are more easily lost for the coating T-34 than for coating T-15. After testing at 150 N load coating T-15 had only lost 18 % of the fillers originally present while coating T-34 had lost 58 %. After testing at 185 N the corresponding values are 37% and 61%. Figures 5.22 and 5.23 show the number of filler particles in various size ranges present in coatings T-15 and T-34 initially and after wireline wear testing at loads of 150 and 185 N. Wireline wear of coating T-15 produces a large number of smaller particles by fragmentation of larger particles. At a load of 150 N these smaller filler particles are retained while at 185 N these particles have detached and are no longer present to help support the load. The drop of filler content from 7.8 % after testing at 150 N to 6.0 % after testing at 185 N (a 23 % change) combined with the detachment of the smaller filler particles would appear to be responsible for the sharp increase in wear rate of this coating noted in Figure 5.2.

On the other hand Figure 5.23 indicates that for T-34 small filler particles of area centred on 30 μm^2 are readily detached even at a load of 150 N, due to their poor bonding to the matrix, and thus cannot contribute to support the load. The drop of filler content from 18.5 % initially to 7.8 % (58 % decrease) after testing at 150 N together with the

detachment of a large number of small filler particles after testing at 150 N would appear to be responsible for the higher wear rate of this coating at this load compared to T-15.

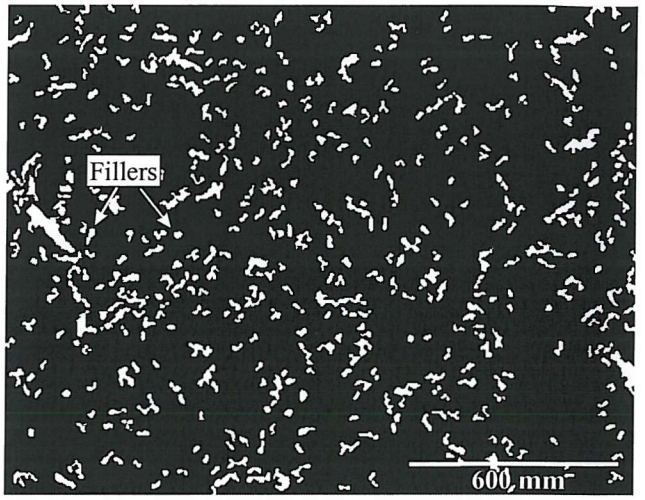

(a) Initial surface of coating T-15 containing 9.5% $CaSiO_3$ fillers.

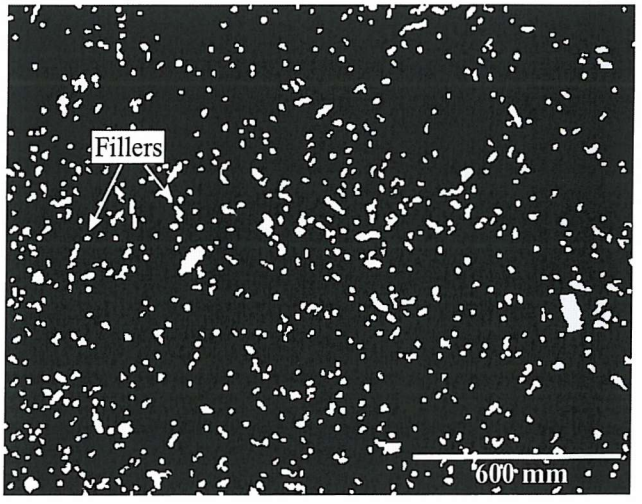

(b) Wear track produced by a load of 150 N, note the large fillers in the initial surface have fragmented into smaller ones and some of these have been removed. Area of filler equals 7.8%.

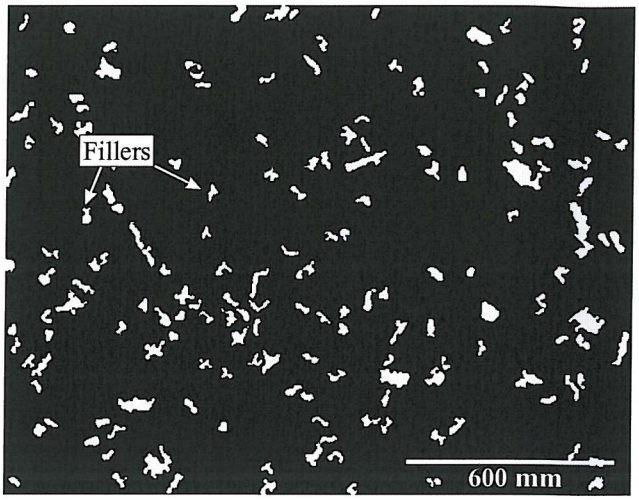

(c) Wear track produced by a load of 185 N, note many fillers particles have been removed. Area of filler equals 6.0%.

Fig. 5.19 SiKα X-ray map from coating T-15.

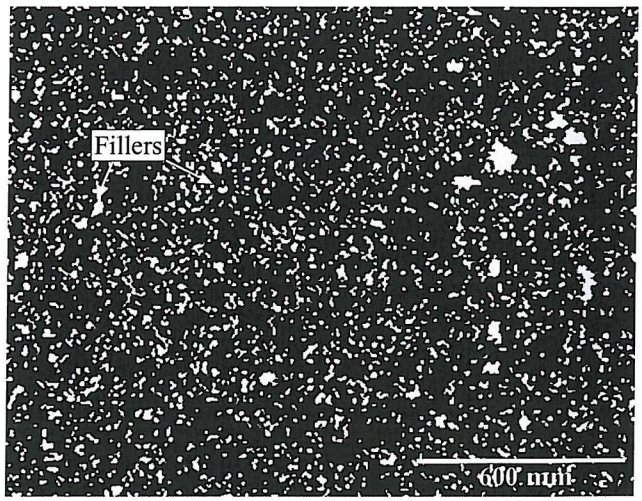

(a) Initial surface of coating T-34 containing 18.5% Al_2O_3 fillers.

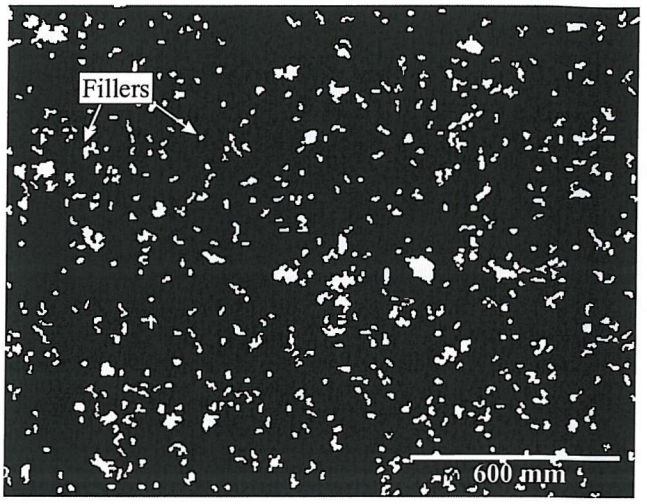

(b) Wear track produced by a load of 150 N, note both small and large fillers have been detached. Area of filler equals 7.8%.

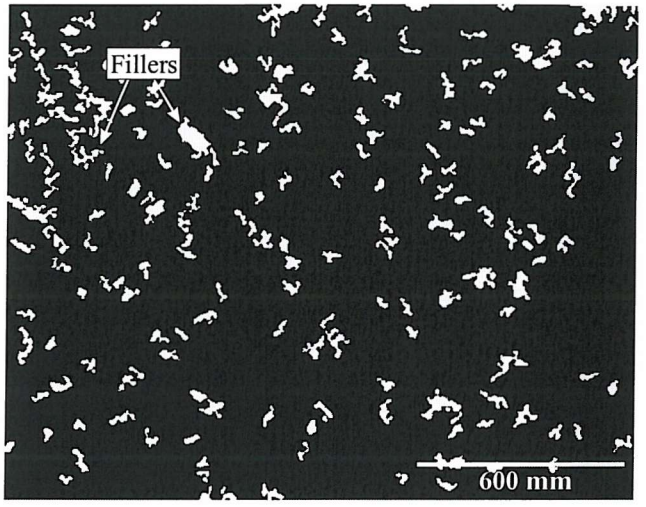

(c) Wear track produced by a load of 185 N, note the number of filler particles of 30 μm^2 is considerably less than that seen in (b). Area of filler equals 7.1%.

Fig. 5.20 AlKα X-ray map from coating T-34.

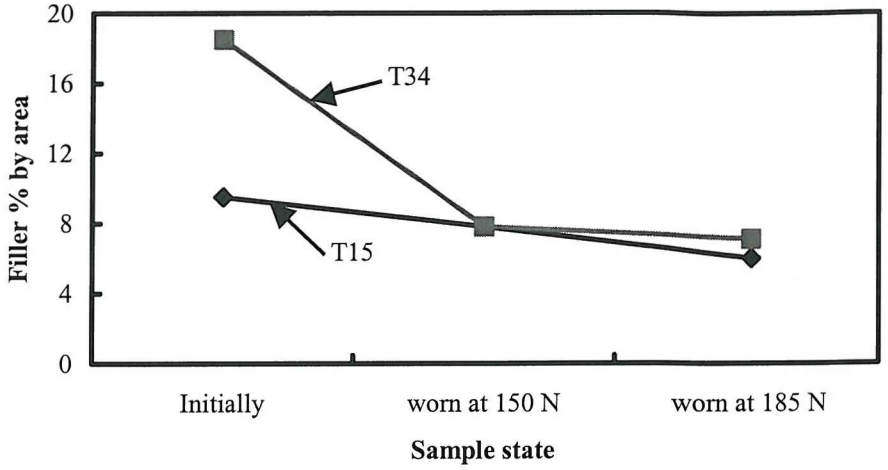

Fig. 5.21 Area percentage of fillers present initially and after wireline wear testing under applied loads of 150 and 185 N for coatings T-15 and T-34.

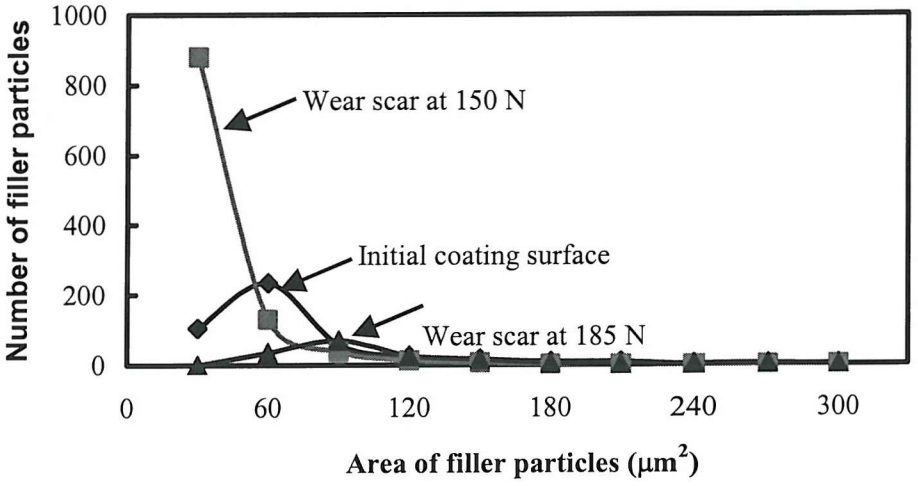

Fig. 5.22 Number of filler particles in various particle size ranges present in coating T-15 initially and after wireline wear testing at loads of 150 and 185 N.

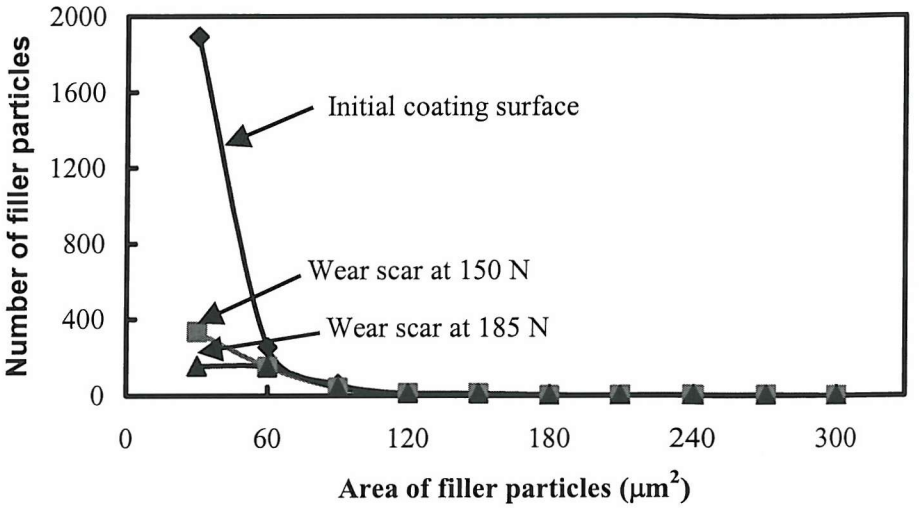

Fig. 5.23 Number of filler particles in various particle size ranges present in coating T34 initially and after wireline wear testing at loads of 150 and 185 N.

5.4 Conclusions

Wireline wear tests have been carried out on three polymeric coatings under different applied loads and for different sliding distances. The wear rates of the specimens tested have been calculated and the wear mechanisms of wireline wear analysed. The load applied during the tests influenced the wear mechanisms and wear rates of these polymeric coatings significantly while sliding distance influenced the wear rates only at relatively short sliding distances. Microcutting and microploughing were the main mechanisms causing wear of the thermoplastic coatings, microcracking was found at higher applied loads. However, this did not change the wear rate significantly because the microcracks did not propagate and thus did not lead to material removal. Microcracking was the dominant wear mechanism for the thermoset coatings because the cracks on the wear scar propagated detaching segments of the matrix resulting in material loss. The fillers in the thermoset coating T-15 had good bonding to the matrix and supported the load from the slickline wire under moderate applied loads although the larger filler particles fragmented but these fragments were retained. However, they were detached

from the matrix under higher applied loads resulting in a sudden increase of wear rate. The fillers in the coating T-34 detached very easily due to their poor bonding with the matrix. The cavities produced by filler detachment acted as a stress concentrations causing more cracking and material removal. The slight wear of the slickline wire during the wireline wear test did not affect the wear mechanisms operative nor did it have a significant effect on the wear rates, especially for coatings T-34 and F-4001. Image analysis on X-ray maps of the wear tracks was found to be a useful tool in analysing the break up and detachment of fillers in wireline wear.

REFERENCES:

[1] Y. M. Xu and B. G. Mellor, The Effect of Fillers on the Wear Resistance of Thermoplastic Polymeric Coatings, Wear 251 (2001), pp 1522-1531.

[2] K. H. Zum Gahr, Formation of Wear Debris by the Abrasion of Ductile Metals, Wear 74 (1981), pp 353-373.

[3] S. L. Rosen, Fundamental Principles of Polymeric Materials, A Wiley-Interscience Publication, John Wiley & Sons (1982), pp 303-311.

[4] J. Bijwe, C. M. Logani and U. S. Tewari, Influence of Fillers and Fibre Reinforcement on Abrasive Wear Resistance of Some Polymeric Composites, Wear 138 (1990), pp 70-92.

[5] S. V. Prasad and P. D. Calvert, Abrasive Wear of Particle-Filled Polymers, Journal of Materials Science 15 (1980), pp 1746-1754.

[6] A. C. Mcgee, C. K. H. Dharan and I. Finie, Abrasive Wear of Graphite Fibre-Reinforced Polymer Composites Materials, Wear 114 (1987), pp 97-107.

[7] W. Simm and S. Freti, Abrasive Wear of Multiphase Materials, Wear 129 (1989), pp 105-121.

[8] K.H. Zum Gahr, Microstructure and Wear of Materials, Elsevier (1987), pp 513-524.

[9] J. M. Thorp, Abrasive Wear of some Commercial Polymers, Tribology International, 15 (1982), pp 59-68.

[10] K. Tanaka, S. Kawakami, Effect of Various Fillers on the Friction and Wear of Polytetrafluoroethylene-Based Composites, Wear 79 (1982), pp 221-234.

[11] Tribology, Friction and Wear of Engineering Materials, I. M. Hutchings, Edward Arnold (1992), pp 143.

[12] R. I. Trezona, D. N. Allsopp and I. M. Hutchings, Transitions between Two-body and Three-body Abrasive Wear: Influence of Test Conditions in the Microscale Abrasive Wear Test, Wear 225-229 (1999), pp 205-214.

[13] E. Rabinowicz, L. A. Dunn and P. G. Russell, A Study of Abrasive Wear under Three-body Conditions, Wear 4 (1961), pp 345–355.

CHAPTER 6 IMPACT PROPERTIES OF POLYMERIC COATINGS

6.1 Introduction

Within this chapter, the topic of impact resistance of downhole polymeric coatings will be studied. Both Fourier Fast Transform (FFT) and Wavelet transform methods will be utilised to analyse the impact response. The impact processes of the polymeric coatings will be considered from the static and dynamic point of view, and the impact results will be discussed and correlated with material properties.

6.2 Instrumentation of Impact Experiments

6.2.1 Rig structure

The impact rig was designed by Symonds [1] and built at Southampton University as part of a previous investigation in this area. The rig can be classed as a 'falling-weight' type of impact rig, as opposed to other standard impact rigs such as Izod or Charpy introduced in Section 2.4.2.

Figure 6.1 schematically shows the structure of the impact rig. The rig was constructed from angle-iron lengths bolted together into two 'A' frames 3 metres high on a square base. A guide tube in which the tup falls was fixed to one of the 'A' frames. The tup is connected to a counter balance with 5 mm diameter yachting rope via three ball bearing pulleys for minimum resistance. Because the tup is tethered, it falls straight and is prevented from bouncing away during angled impact tests. Using a counterbalance, low impact speeds can be achieved even though the tup is dropped from relatively high drop levels, in addition the counter balance allows different impact energies to be obtained from a constant height (up to 2.75 m). Beneath the guide tube is the sample holder into which the 38 x 38 mm samples are fixed. The sample holder also contains a 'rebound catcher' used to prevent double impacts on the sample from the rebounding tup during

ninety degree (relative to the tup) impact tests. The rebound catcher consists of a plate that is driven out to protect the sample by a pneumatic piston activated by a foot pedal.

Although the objective of this research project is for downhole tubulars under impact, flat samples have been used for their ease of operation in laboratory testing. An attempt was made to simulate a large mass of steel coated in polymeric material, and this was achieved by clamping a flat section sample (polymeric coating on a steel substrate provided by the manufacturer) onto a large block of stainless steel resting on the concrete floor. Clamps were put along three edges of the sample with the fourth one being free. The free side allowed angled impacts to be performed without the tup striking the clamp.

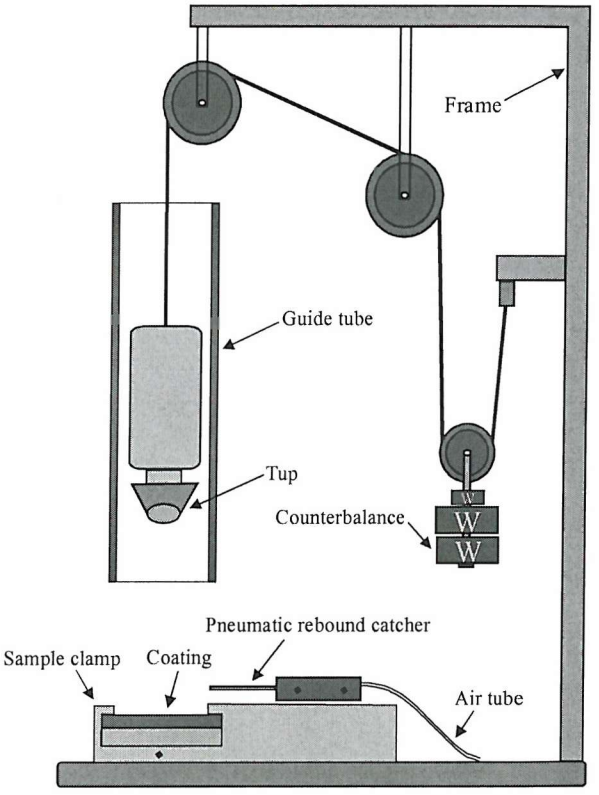

Fig. 6.1 Schematic diagram of the impact rig (side view).

6.2.2 Modification of the tup

The assembly of the tup consists of two parts: (1) the nose, the profile of which affects the impact damage and (2) the main body, the mass of which also affects the impact damage. The tup nose was made of a 22.2 mm diameter ball bearing. The mass of the tup used was 1.9 kg. In previous work, the accelerometer (which was used to obtain the impact response and will be introduced in Section 6.2.3) was mounted on the top of the tup. This position was considered not the most ideal position to collect the signal from the impact response because it was too far away from the tup nose which is the contacting point during the impact. The distance between the accelerometer and impacting point could cause serious attenuation during signal transmission and also the collected signals might be distorted after the signal has been reflected many times inside the long tup body. These limitations will affect the overall quality of the measured data.

In the present investigation, an additional section, the housing body which contained the accelerometer was connected between the tup body and the tup nose. With this arrangement the accelerometer is located as near as practically possible to the tup nose. The structure of the tup is shown schematically in Figure 6.2. As a third housing part was added to the tup, some grooves have been machined on the original tup body to keep its weight as 1.9 kg, which is important in order to maintain the comparability of this research work with previous investigations [1].

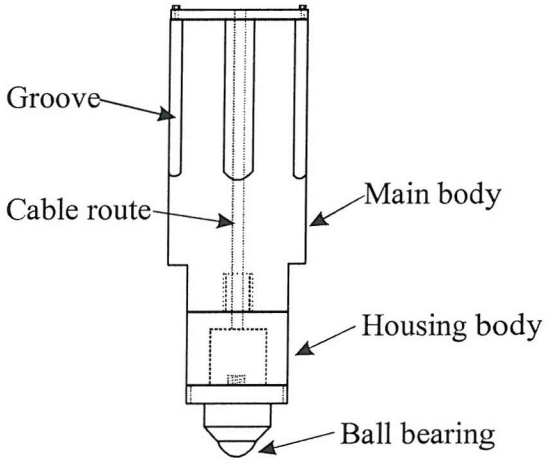

Fig. 6.2 Detailed structure of the impact tup.

6.2.3 Force-time data acquisition

Instrumented impact testing has become an increasingly acceptable technique in order to obtain complete impact information and to understand fully the impact mechanisms involved with various materials [2, 3]. The results obtained from standard impact tests (see Section 2.4.2) are usually a single value such as the energy spent on a particular sample in an impact test. This is of limited value in describing the impact performance of a material. Instrumenting impact rigs to yield information on forces, velocities, displacement and energies of the impactor at any time during the impact can give additional information. In this section, the instrumentation process of the existing falling-weight impact rig and the measurement of force and velocity, displacement and energy will be discussed.

There are many types of instruments available for recording the force of impact on the specimen. Through a review of suitable apparatus, an appropriate method for this investigation will be established.

(a) Strain gauges

Strain gauges work on the principle that all materials resist deformation to a certain degree, so for deformation to take place a force must be applied. As this force can be related to the resistance (piezoelectric effect) of a strain gauge, if it is located at the point the force is being applied, any deformation or strain felt by the object is registered by the gauge, producing an electrical output which is proportional to the force being applied [4].

However, certain problems are apparent with this method. Strain gauges only measure along one axis, thus more than one gauge may be required to record impact signals. With the specimens only 38 x 38 mm in size, space is limited making this impractical. In addition, although a strain gauge is basically only a resistor bound onto an elastic backing which is fixed to the point of interest [5], attaching it for every test would be time consuming, and more importantly the positioning of the strain gauge will be inconsistent

with the point of impact, as the exact impacting point cannot be predetermined with the present rig.

(b) Load cells

Load cells eliminate the problem of mounting the strain gauges on the specimen for each individual test. The cell is an easily movable component with bound-foil strain gauges within its protective casing. However, its suitability for the proposed application is questionable, as load cells are known to have little resistance to side loads [6]. Load cells are somewhat of an unknown quantity, as recording impact force is not one of their recognised applications. As the results obtained from a load cell may not be reliable for impact tests, the load cell does not have sufficient advantages to warrant the risk involved in its selection.

(c) Force transducers

A force transducer is used in fixed locations and works by being placed at the point of interest with the impact creating a charge across the piezoelectric element, which is proportional to the force [5]. Force transducers are frequently used in the instrumentation of impact tests. However, they are extremely hard to calibrate and great care is needed when mounting the transducer to prevent any change to their characteristics, or increased errors will be created due to their high sensitivity [7, 8].

(d) Accelerometers

The use of an accelerometer to instrument an impact rig is based on Newton's Second Law ($F = ma$). Knowing the acceleration of the mass in the impact direction yields the total force on the impactor in the impact direction. The accelerometer produces a voltage signal proportional to the acceleration. As with force transducers a charge is produced from the piezoelectric element when it is excited. As can be seen in Figure 6.3, the piezoelectric element has a seismic mass attached to it, and any vibration produced on the

accelerometer results in a force equal to the mass of the accelerometer and the acceleration of the seismic mass acting on the piezoelectric element. As the seismic mass and the accelerometer base vibrate at the same magnitude and phase, the output charge of the accelerometer is thus proportional to the surface on which the base is mounted [8, 9].

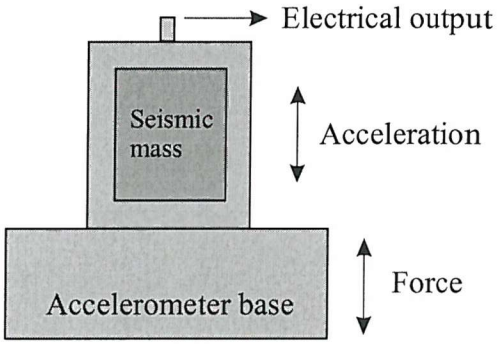

Fig. 6.3 Principle of the accelerometer.

(e) Conclusion

All four methods investigated have the capability of recording the force on impact. However, the force transducer and the accelerometer are clearly the most suited transducers, with the recording of impacts being a typical application of both. The accelerometer possesses some clear advantages, in particular its ease of mounting without any induced error, which is difficult to achieve with a force transducer.

A Bruel & Kjaer accelerometer type 4369 was used in the current impact tests. The principle advantage of this type is its ability to experience high shock acceleration loads (up to 10,000g) compared to that of other accelerometers. Values greater than this were considered impossible to be reached on this rig, so the tup could be released from any height under free fall conditions without ever going over the maximum shock acceleration of the transducer.

6.2.4 Velocity measurements

During a falling-weight impact using the present impact rig, the impact velocity can be determined through the common method of balancing the energy relationship in a system:

Total energy gain = Total energy lost from the system

Several cases have been considered previously [1] to calculate the impact velocities.

(a) In the free fall case:

$$\frac{1}{2}m_t v_t^2 = m_t gh \qquad \Rightarrow \qquad v_t = \sqrt{2gh} \qquad (6.1)$$

where m_t = mass of the tup

v_t = velocity of the tup

h = drop height

g = 9.8 ms^{-2}

(b) If the counterbalance is used in the test, assuming a frictionless system:

$$\frac{1}{2}m_t v_t^2 + \frac{1}{2}m_c gh + \frac{1}{2}m_c(\frac{1}{2}v_t)^2 = m_t gh$$

$$\Rightarrow \qquad v_t = \sqrt{\left\{\left[(m_t - \frac{1}{2}m_c)/(\frac{1}{2}m_t + \frac{1}{8}m_c)\right]gh\right\}} \qquad (6.2)$$

where m_c = mass of the counterbalance

v_c = velocity of counterbalance

(c) If the counterbalance is used in the test, assuming friction in the pulleys:

$$v_t = \sqrt{gh\left(\frac{m_t - \frac{1}{2}m_c - m_t(1-Q)\left[1-\frac{2Km_t - m_c}{m_c + 2Km_t}\right]}{\frac{1}{2}m_t + \frac{1}{8}m_c}\right)} \qquad (6.3)$$

where μ = the coefficient of friction between the yachting rope and pulleys

$$Q = -\mu^3 + 3\mu^2 - 3\mu + 1$$

$$K = -\mu^3 + 4\mu^2 - 5\mu + 2$$

Free falling impact without using a counterbalance as in case (a) was very rarely done in the present impact rig. In order to obtain a low impact energy with a high drop height a counterbalance is always used. The frictionless system assumed in case (b) is an ideal situation which would never occur in reality. The only possible application of case (b) is when the coefficient of friction μ between the yachting rope and the pulleys is small enough to be ignored. In case (c), the coefficient of friction μ depends on the weight of the counterbalance and the velocity of the rope moving through the pulleys, and thus on the height from which the tup falls. The coefficient of friction was thus considered to vary during the descent of the tup since the relative velocity between the rope and the pulleys changes [1].

A high-speed video camera had been used in the present impact rig and the real impact speed obtained from the high-speed video camera compared with the predicted one calculated from the Eqns (6.2) and (6.3). The real velocity was less than the velocity predicted by Eqn (6.2). This indicated that there were losses due to friction in the rope and the pulleys. By substituting a value of $\mu = 0.2$ into Eqn (6.3) the predicted and measured velocities were found to agree approximately. However, the actual velocity

measured had a spread and was probably caused by inaccuracies in the velocity measurements as recorded by the video camera, as a result of limitation of frame speed.

Although the high-speed video camera could be used to calculate the impact velocity, using it for each impact would be very time consuming. The main objective of using the high-speed video camera was to reveal the impact process itself. Therefore, Symonds [1] used theoretically predicted impact velocities in the analysis of her work. This has the disadvantages discussed above.

The most common method of measuring the velocity is to measure the elapsed time between the signals produced by two detectors [10, 11]. As long as the distance between the two detectors is small, the velocities can be assumed to be constant [10]. Lee and Zahuta [12], requiring an accurate velocity measurement with time, used a Linear Velocity Transducer (LVT), although this only works when the tup is guided by two rails, a method commonly used with high mass falling weights [13, 14]. Hodgkinson and Williams [15] used a laser-doppler velocimeter that allows the changing velocity of a falling projectile to be monitored extremely accurately.

In this research, inductive proximity transducers were adopted to measure elapsed time. Two sensors in an M30 fixing thread were fixed on the impact rig 65 mm apart and at a sensing distance of 10 mm based on the centre of the guide tube. A 10V power supply is required with the transducer's triggering a Racal 9905 universal counter timer. Figure 6.4 schematically shows the two Carlo Gavazzi inductive proximity switches positioned just 30 mm above the sample holder. The maximum error of impact velocity caused by this positioning method was calculated to be less than 5 percent.

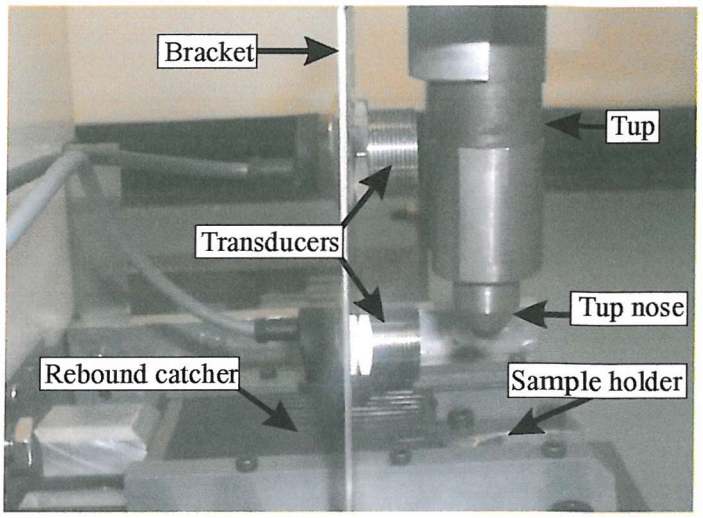

Fig. 6.4 Positioning of the inductive proximity transducers.

6.2.5 Impact signal recording

Figure 6.5 shows in schematic form the signal processing (recording and analysing) system connected to the present impact rig.

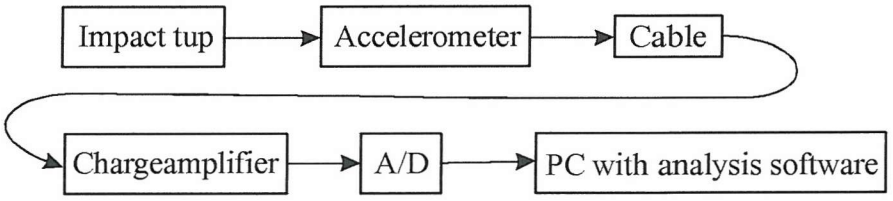

Fig. 6.5 Flow chart of impact signal processing system.

A Kistler 5001 charge amplifier was used to integrate the charge developed from the piezoelectric elements in the accelerometer. An output voltage is produced by the charge amplifier which is proportional to the charge received at the input [4, 9, 15], and therefore also to the acceleration of the accelerometer. The accelerometer will require some means of connection to the charge amplifier. This is best done through cables [5], although their use can cause certain problems such as a decrease in accelerometer sensitivity and its

high frequency response. An increase in electrical noise level as well as in the low-frequency response of the accelerometer is possible. Most of these problems are proportional to the cable capacitance, as the accelerometer is a piezoelectric transducer, which acts like a capacitive source [5]. However, if the accelerometer cables are used in conjunction with a charge amplifier, many of the problems associated with the cables can be eliminated. Very short or long cables can be used without changing the overall sensitivity if a charge amplifier is utilised [9].

An A/D converter installed in a Personal Computer (PC) was connected to the output of the Kistler 5001 charge amplifier and used to convert the analogue signals collected from the accelerometer and the charge amplifier to digital codes. In order to ensure the trace being recorded by the A/D converter on the PC was representative of the analogue signal, a Gould Classic digital storage oscilloscope was connected in series with the computer so the same impact was recorded by both. Comparison between the analogue signal recorded by the oscilloscope and the digital signal recorded by the A/D converter is shown in Figure 6.6 (a) and (b).

The traces can be seen to be almost identical in their shape although the oscilloscope trace possesses more detail. This is simply because the oscilloscope was recording at a higher frequency than the 20 kHz of the A/D converter. Despite the trace from A/D converter possessing less detail, no significant peaks/points have been eliminated. The advantage of using the PC with the A/D converter is that the digital signal is easy to transfer and analyse. However, missing information is undesirable. Increasing the sampling rate (recording frequency) can solve the problem effectively. Thus, the maximum permissible sampling rate, 250 kHz, of the current recording system was determined to be used in all the impact tests; this frequency was thought to be high enough to obtain detailed information from the test.

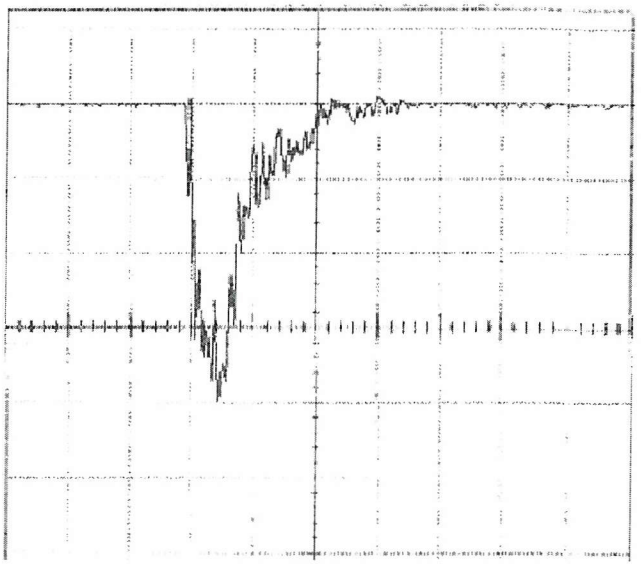

(a) Signal recorded by the oscilloscope.

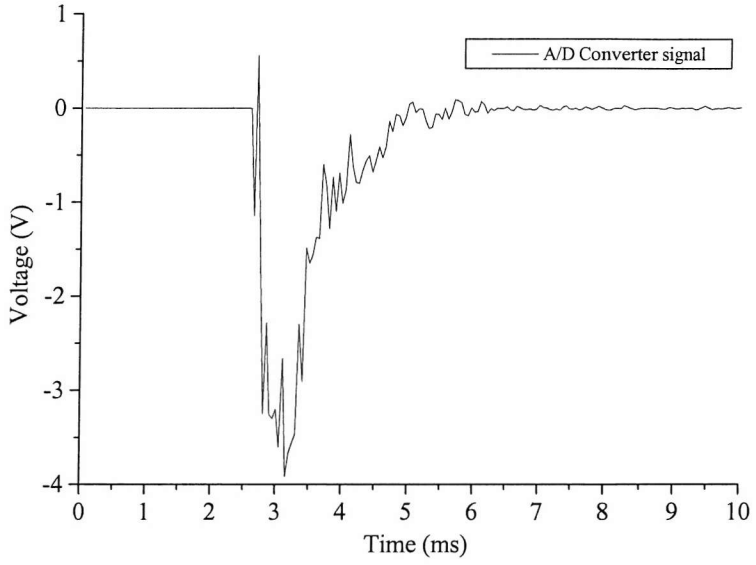

(b) Signal recorded by the A/D converter, sampling frequency – 20 kHz.

Figure 6.6 Comparison between the signals obtained from the oscilloscope and the A/D converter in an impact test. Note the two responses are almost identical.

6.2.6 Optimum position for the accelerometer

As discussed in Section 6.2.2, the position for mounting the accelerometer is an important factor that will influence the signals recorded. In this section, the optimum position for the accelerometer in the present rig was determined through impact tests on UPVC (Unplasticised-Polyvinyl Chloride).

Figure 6.7 shows three possible fixing positions for the accelerometer in the impact rig. Each position has been subjected to ten impacts on the UPVC samples with the same procedure being followed for each one. Each test was carried out with the tup falling from a height of 300 mm with a 1 kg counterbalance weight, resulting in an impact energy of 2.8 J. The sample rebound catcher was not used in these tests as the use of the rebound catcher would result in damage occurring to the accelerometer in position three (on the top of the tup) and might induce some unnecessary noise for each position. The consistency, quality and accuracy of the traces resulting from the impact tests were assessed for each of the sensor locations.

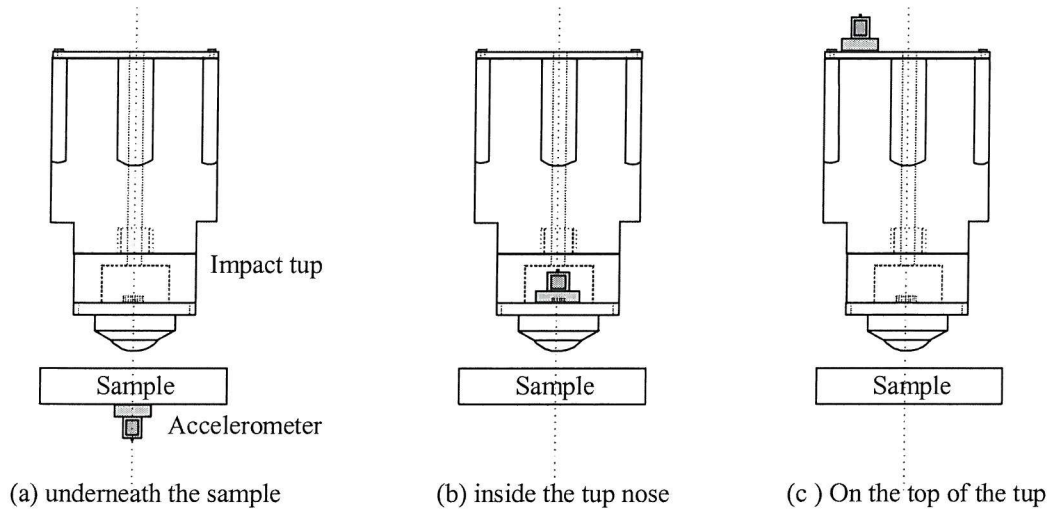

Fig. 6.7 Three possible positions of the accelerometer.

(a) Position one — underneath the specimen

A hole was drilled in the sample holder in order to accommodate the accelerometer underneath the test sample, as described in Figure 6.7 (a). Although the proposed method of mounting in this position for coated samples was to use a magnetic stud, clearly this is not applicable for bulk UPVC. In this position, an adhesive was used to connect the accelerometer to the bottom of the samples. Figure 6.8 shows two of the ten responses obtained from the accelerometer over the whole impact time. The graph displays a good level of consistency between the two traces and the two plots shared the same characteristic of an initial downward peak followed by a positive peak before levelling off after approximately 3 ms. Although the two responses were similar to each other, detailed inspection showed some variance. This was thought to be caused by the inconsistency of the impact point on the sample in relation to the accelerometer in different tests.

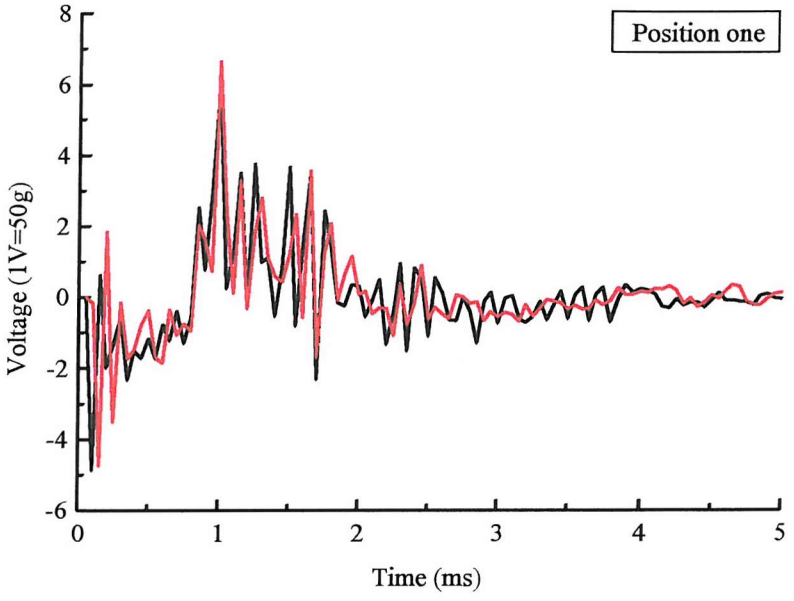

Fig. 6.8 Accelerometer responses in position one for impact energy of 2.8 J. Note the variance between the two traces.

(b) Position two — inside the tup nose

As discussed in Section 6.2.2, in order to mount the accelerometer as close to the impacting ball bearing as possible the tup has been modified accordingly. The transducer cable travelled up through the hole drilled in the tup body, passed through the tup guide, and was fed back to the charge amplifier.

Two representative responses of the ten impacts in position two for the accelerometer are revealed in Figure 6.9. They are self-evidently different from those obtained in position one and consistent with each other. There would appear to be negligible interference from the experimental set up, especially with regard to the transducer cable.

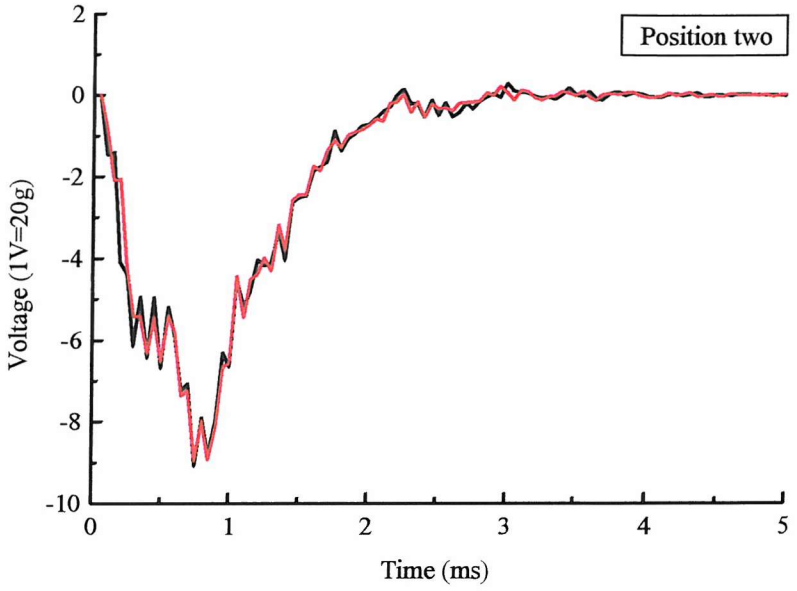

Fig. 6.9 Accelerometer responses in position two for impact energy of 2.8 J. Note the good consistency between the traces.

(c) Position three — on the top of the tup

The cable was subjected to similar conditions to those experienced in position two. From the traces shown in Figure 6.10, it can be seen that the two representative responses are nearly identical. This position also offered a high level of consistency and appeared similar to the responses obtained from position two, both of which seem more consistent than those obtained from position one. However, small differences can be seen around the peaks of the two traces indicating an inferior repeatability of position three than position two.

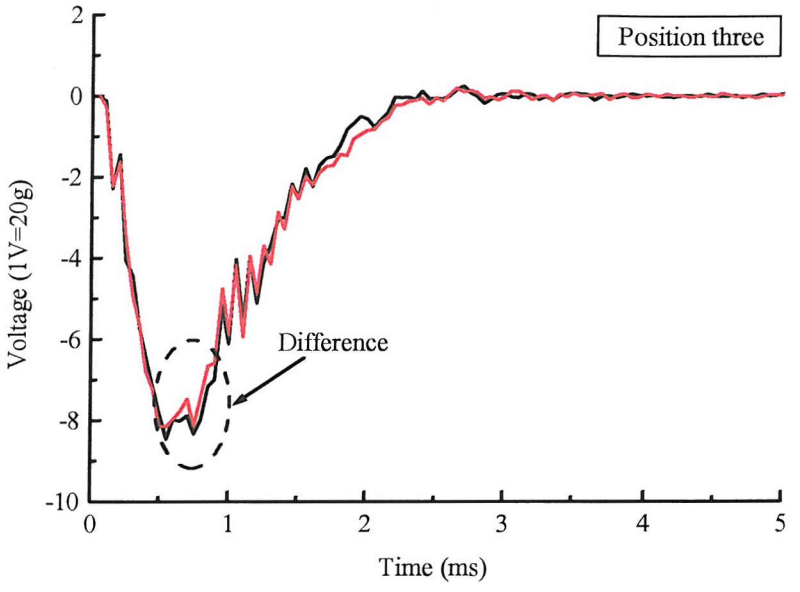

Fig. 6.10 Accelerometer responses in position three for impact energy of 2.8 J. Note the differences between the two traces around the peaks of the two traces.

(d) Meaning of the impact responses

The responses revealed in Figures 6.8 to 6.10, consisting of both positive and negative peaks, depend on the location of the accelerometer. In fact, the overall form / shape of the peaks in the response depended on how the accelerometer was accelerated / decelerated in relation to its orientation. A positive peak is produced if the accelerometer is accelerated in the direction it is facing or decelerated in the direction it is not facing; and a negative peak is produced if the accelerometer is decelerated in the direction it is facing or accelerated in the direction it is not facing.

From position one, the accelerometer was initially accelerated backwards on impact, hence the negative peak. Figure 6.8 shows this negative peak becoming a positive peak after approximately 1 ms. This phenomenon indicated that the accelerometer was accelerating up in the direction it was facing when the sample was returning back to its original position.

Positions two and three consisted of just one negative peak having the same time period (about 2.5 ms) as the two peaks (negative and positive) experienced in position one. This negative peak represented the deceleration experienced by the accelerometer on impact followed by the acceleration when the sample reacted. Although when the accelerometer was falling with the tup it was experiencing an acceleration in the direction it was facing (positive value), it was only to the magnitude of one g, which was not visible on the graphs compared to the hundreds of g experienced with deceleration on impact.

(e) Propagation of waves

When the tup impacts the specimen a sudden stress is applied to both tup and specimen, resulting in the disturbance propagating through the medium in the form of a stress wave. Stress waves propagate from an impact in three forms: compressive wave (P); shear wave (S); and Rayleigh wave (R) [16]. The speed at which these waves travel can be evaluated with the following formulae [16]:

$$C_P = \sqrt{\frac{E}{\eta} \times \frac{(1-\upsilon)}{(1+\upsilon)(1-2\upsilon)}}$$

$$C_S = \sqrt{\frac{E}{\eta} \times \frac{1}{2(1+\upsilon)}} \qquad (6.4)$$

$$C_R = \frac{0.87+1.12\upsilon}{1+\upsilon} \times C_S$$

Where E = Young's Modulus of Elasticity (N/m^2)

η = The mass density (kg/m^3)

υ = Poisson's ratio

A point of interest in examining the position of the accelerometer, particularly on or in the tup, is that a stress wave decreases in energy density with path length as a result of divergence and attenuation [16].

Divergence describes the spreading of the wave form as it travels along the medium. For a point impact such as that being developed in these experiments, the amplitude of the stress wave decreases inversely with the square of the distance from the source [16]. Attenuation is a result of energy losses experienced as the wave propagates. This is caused by scattering and absorption of the wave due to discontinuities and interfaces in the path of travel. As there were a number of interfaces present in the modified structure of the tup, it is clear that to have the accelerometer positioned as close to the impact point as possible was desirable.

(f) Comparison between different positions

Positions two and three offered very similar traces with both possessing high levels of consistency – which is an essential factor for the trace to be of any use in analysing impacts. However, the theory behind the generation of the response due to excitation of the accelerometer suggests that the two responses should have a difference. A slight decrease in output voltage with increased distance from the impact point can be seen

through a closer examination of the peaks of position two and position three. This would be consistent with the prediction of the response expressed above. Furthermore, an inferior repeatability can be found in position three than that in position two. The variation in signals shown in position three could be caused by the refraction of the waves while they were travelling the greater distance. Although the differences between the two positions are small, position two is a more desirable location with the accelerometer being exposed to a "cleaner" excitation, and therefore producing a more accurate response to the impact.

The same argument would suggest that position one would produce the "cleanest" response, with both divergence and attenuation being less than that experienced in position two due to the proximity of the accelerometer to the impact. However, a quick inspection of Figure 6.8 makes it immediately apparent that the response lacks the consistency experienced from the other two positions. This was thought to be due to the variation of the impact point in relation to the accelerometer. The rig does not allow the point of impact on the sample to be controlled to the accuracy required to eliminate this variable.

(g) Conclusion

From the above investigations position two, i.e. the accelerometer mounted as close to the impacting tup nose as possible, can be regarded as the best mounting point for the accelerometer. This was used in all subsequent experiments.

6.3 Impact Tests on Polymeric Coatings

In this section, impact test results on thermoset and thermoplastic polymeric coatings will be presented and discussed. Before the experiments were carried out, the present researcher discussed the impact problem with experts in vibration analysis in order to design proper experimental conditions for the present tests. The thickness of the coating and its substrate could influence impact performance as different thicknesses of sample would cause different resonant frequencies and these frequencies may affect the damage on the sample tested [17, 18]. Therefore, samples with various coating and steel substrate thicknesses have been used in order to assess the main factors influencing the impact resistance of the coatings. Static and dynamic components will be extracted from the raw impact response and related to the impact results of the polymeric coatings.

6.3.1 Test samples and experimental conditions

Two types of thermoset polymeric coatings T-15 and T-34, and a thermoplastic coating F-4001 have been investigated. The dimension of each coating sample was 38 mm x 38 mm, and the thickness of each sample varied. In order to investigate the influence of the substrate on the impact test on the coating, the steel substrate of each coating type was machined to two thicknesses namely 2 and 4.5 mm.

T-15 is a thermoset coating with 9% $CaSiO_3$ fillers present in the coating matrix. No fillers were embedded in the primer layer. Two thicknesses of coating were tested. The thinner coating layer with a 4.5 mm thick steel substrate was designated as T-15A. The steel substrate of the thicker coating, T-15B, had two thicknesses, 2 mm and 4.5 mm, designated as T-15B1 and T-15B2 respectively.

T-34 is a thermoset coating with 20% Al_2O_3 fillers present in the coating matrix. The coating has a thick layer of primer (0.05 ~ 0.1 mm) between the coating and the steel substrate containing a high percentage (35%) of $CaSiO_3$ fillers. The samples: T-34A had a coating thickness of 0.14 ~ 0.15 mm and a steel substrate 4.5 mm thick; T-34B1 had a

thickness of 0.25 ~ 0.26 mm and a steel substrate 2 mm thick; T-34B2 had a same coating thickness as T-34B1 but a steel substrate 4.5 mm thick.

F-4001 is a thermoplastic coating with a very low percentage (2%) of CaF_2 fillers embedded in the coating matrix. F-4001 has a relatively thick primer layer (0.08 ~ 0.2 mm) containing 12% SiC fillers. Two types of coating thickness were available, 0.5 and 1.5 mm. These were designated F-4001A and F-4001C respectively. Samples F-4001A had the steel substrate 4.5 mm thick. Samples F-4001C1 and C2 had the steel substrate 2 and 4.5 mm thick respectively.

The samples were clamped into the sample holder as shown in Figure 6.4. Various impact energies were applied to the polymeric coatings in order to produce different failure patterns which ranged from a small plastic indent to large fractures. The designated sample code and generic experimental conditions for each coating sample are listed in Table 6.1.

Table 6.1 Experimental conditions of impact tests on polymeric coatings

Coating sample code	Thickness of the coating (mm)	Thickness of the substrate steel (mm)	Impact energies tested (J)
T-15A	0.25 ~ 0.27	4.5	4, 7, 10, 14
T-15B1	0.35 ~ 0.36	2	4, 7, 10, 14
T-15B2	0.35 ~ 0.36	4.5	4, 7, 10, 14
T-34A	0.14 ~ 0.15	4.5	7, 10, 14, 18, 22
T-34B1	0.25 ~ 0.26	2	4, 7, 10, 14, 18, 22
T-34B2	0.25 ~ 0.26	4.5	7, 10, 14, 18, 22
F-4001A	0.5	4.5	7, 10
F-4001C1	1.5	2	10, 14, 18, 22
F-4001C2	1.5	4.5	14, 22

6.3.2 Impact test performed and damage assessment

(a) T-15A, T-15B1 and T-15B2

Plastic indents, radial and circumferential/ring cracks, delamination between coating, primer and steel substrate layers were observed on the coating surface and the cross section of the coating specimen for the different coatings under various impact energies. Generally, the impact indents on the coating surface became deeper and larger as the impact energy increased; radial and circumferential cracks, delamination between different layers and facture were observed after the plastic indent as the impact energy increased. Typical impact damage morphology of coating T-15 is given below.

Figures 6.11 (a) to (c) show the surface of the coating T-15B1 and a transverse section through the centre of the impact indent after testing with an impact energy of 14 J. Radial cracks were apparent on the coating surface initiating from the periphery of the impact indent and propagating into the coating surface. Figure 6.11 (c) shows at higher magnification region A presented in (b), delaminations were evident at the interfaces between the coating, primer and steel substrate layers.

On each coating surface, the impact test induced plastic deformation in the form of a crater. The radius and the depth of the crater on each coating surface were measured by using a Talysurf traversing the middle of the crater. Table 6.2 presents measurements of the radius and the depth of the crater on each coating of T-15 tested.

Table 6.2 Radius and depth of the crater on thermoset coating T-15 for various impact energies

Impact energy, J	T-15A		T-15B1		T-15B2	
	Radius, mm	Depth, mm	Radius, mm	Depth, mm	Radius, mm	Depth, mm
4	1.88	0.13	2.0	0.09	1.83	0.09
7	2.25	0.18	2.30	0.15	2.0	0.11
10	2.30	0.21	2.50	0.19	2.45	0.20
14	2.30	0.27	2.88	0.27	—	—

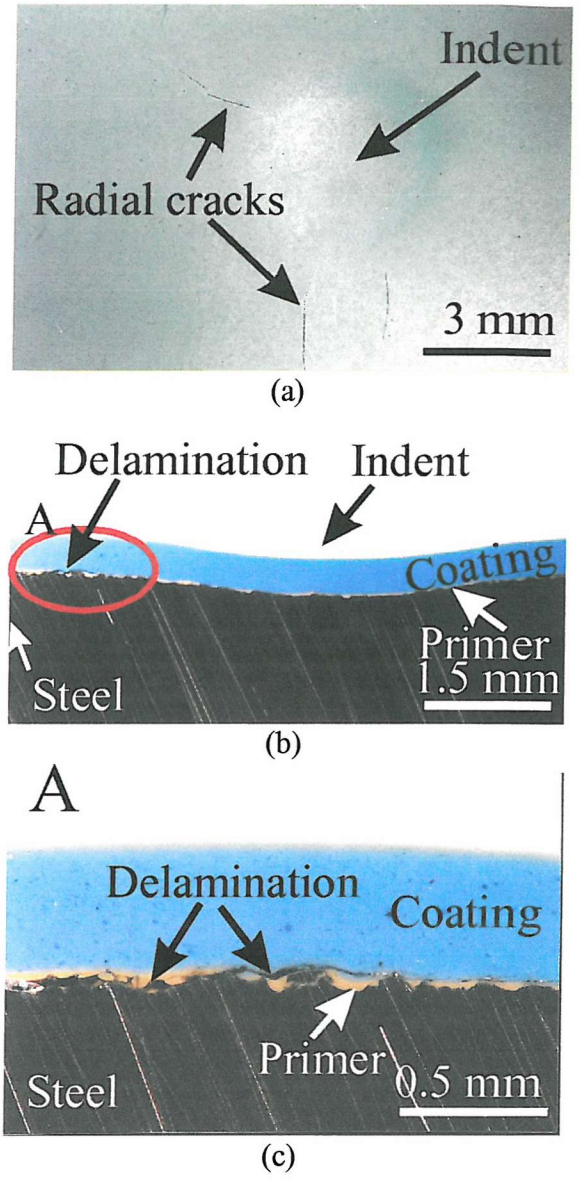

Fig. 6.11 Surface and a transverse section of the coating T-15B1 after testing with an impact energy of 14 J. Note radial cracks were apparent on the coating surface initiating from the periphery of the impact indent and propagating into the coating surface.

(b) T-34A, T-34B1 and T-34B2

Similar to coating T-15, plastic indents, radial and circumferential cracks, delamination between coating, primer and steel substrate layers are the typical damage observed on the coating surface and the cross section for the different T-34 coatings under various impact energies. The circumferential cracks within the coating layer became wider and extended closer to the primer layer as the impact energy increased.

Figures 6.12 (a) to (c) show the result of a 22 J impact test on the coating T-34A. Delamination of the primer layer was observed, which was associated with the extension of the circumferential crack.

Table 6.3 summarises the dimensions of the radius and the depth of the crater on each coating of T-34 tested.

Table 6.3 Radius and depth of the crater on thermoset coating T-34 for various impact energies

Impact energy, J	T-34A		T-34B1		T-34B2	
	Radius, mm	Depth, mm	Radius, mm	Depth, mm	Radius, mm	Depth, mm
4	—	—	1.88	0.13	—	—
7	2.20	0.20	2.83	0.25	2.20	0.17
10	2.38	0.23	2.40	0.21	2.30	0.20
14	2.53	0.27	2.68	0.25	2.58	0.26
18	2.70	0.33	2.68	0.28	2.63	0.27
22	2.80	0.34	2.95	0.34	2.75	0.31

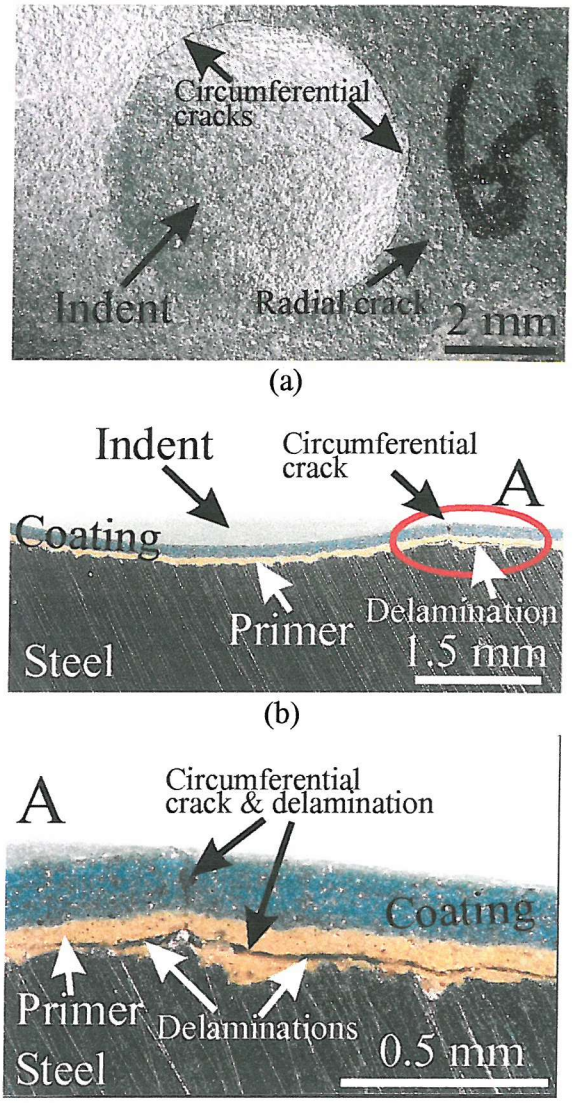

Fig. 6.12 Impact test results on coating T-34A with an impact energy of 22 J. Note delamination of the primer layer associated with the circumferential crack.

(c) F-4001A, F-4001C1 and F-4001C2

Substantial plastic deformation of the coating surface was observed for the thicker thermoplastic coatings. There was no circumferential crack observed on thermoplastic coatings F-4001. The periphery of the impact indent was piled up during the impact process. The primer layer was not deformed during the impact on F-4001. Figures 6.13 (a) and (b) show the typical damage of an impact test on coating F-4001C2 with an impact energy of 14 J.

Table 6.4 gives the radius and the depth of the crater on each coating of F-4001 tested.

Table 6.4 Radius and depth of the crater on coating F-4001 for various impact energies

Impact energy, J	F-4001A		F-4001C1		F-4001C2	
	Radius, mm	Depth, mm	Radius, mm	Depth, mm	Radius, mm	Depth, mm
7	3.35	0.55	—	—	—	—
10	3.50	0.62	3.30	0.44	—	—
14	—	—	3.90	0.60	3.65	0.54
18	—	—	4.15	0.64	—	—
22	—	—	4.25	0.80	4.1	0.74

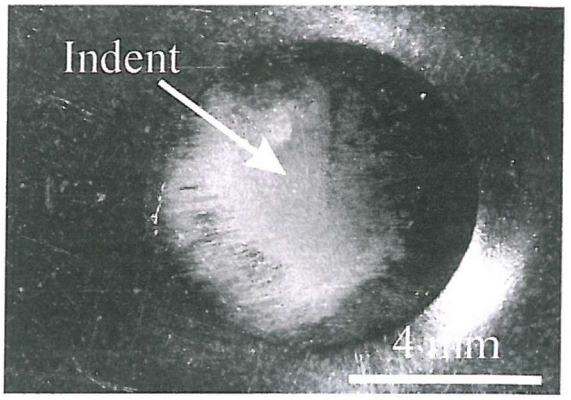

(a)

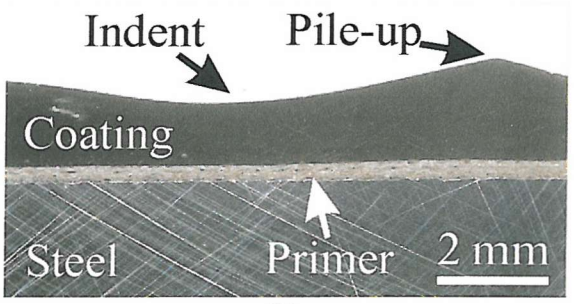

(b)

Fig. 6.13 Typical damage from an impact test on coating F-4001C2 with an impact energy of 14 J. Note the plastic deformation of the coating surface and the pile-up around the indent.

6.3.3 Evaluation of maximum mean force by impact response analysis

The maximum loading force during an impact test is always associated with the damage or fracture of the material during an impact test [19]. Oscillations in the force-time signals have been found in most of the impact tests [20] and sometimes these high frequencies can show up in the measured impact signal [19]. These high frequency signals in the force-time trace make it difficult to read the maximum loading force from the force-time trace. Therefore, in order to obtain the maximum mean force during an impact test the high frequency signals have to be removed from the original force-time trace.

(a) Frequency analysis by using Fast Fourier Transform (FFT)

Figure 6.14 shows a typical force-time trace of an impact response collected from the impact test on the polymeric coating T-15B1 under an impact energy of 7 J, where only a plastic indent was produced on the tested sample. From the original impact response it can be clearly seen that the impact process happened approximately within 2 milliseconds. The initial contact point and the point at which contact is lost between the tup and the sample can be recognised from the force-time impact response. However, the "noise" on the signal makes further analysis very difficult. A previous study [1], using a similar experimental set-up, had also reported that high frequency signals were observed in the impact response of polymeric coatings. It was suggested that this high frequency response originated from a steel block support situated underneath the sample. The present researcher suggests that these high frequency signals are not only from the steel block underneath the sample but also from the other parts of the impact system, i.e. the natural frequency of the impactor or the test sample can be picked up by the transducer.

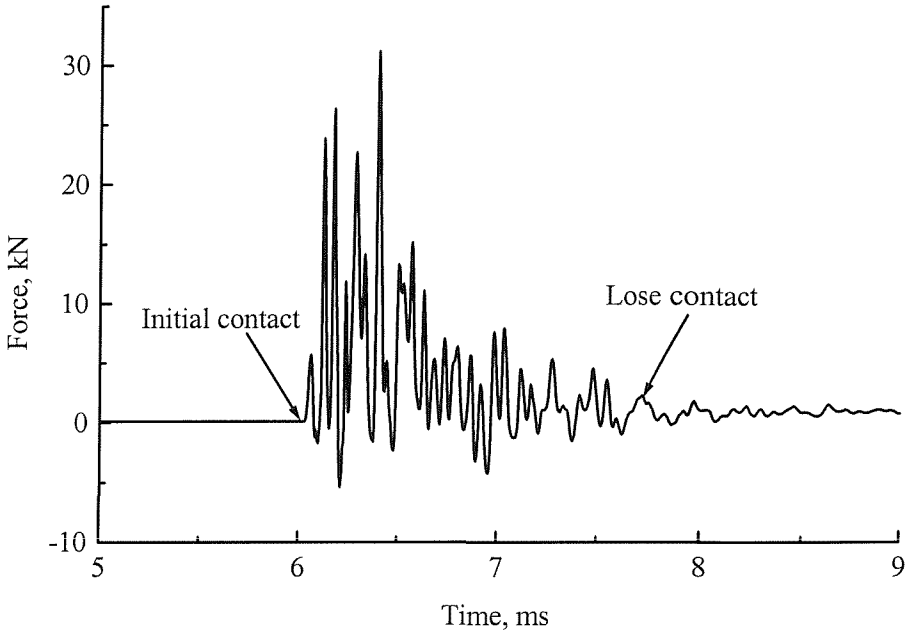

Fig. 6.14 Impact response collected from an impact test on polymeric coating T-15B1 under an impact energy of 7 J. Note the origin on the time axis is arbitrary.

In order to investigate the frequencies present in the impact signal, the FFT method was used to analyse the impact response. Figure 6.15 shows the FFT analysis of the impact response shown in Figure 6.14. From the magnitude of the frequency signal it can be recognised that several dominant frequencies are registered during the impact test. They were at approximately 3~5 kHz, 6~9 kHz, 13~15 kHz and 17~22 kHz. It is apparent that these high frequency signals were the main components shown in the force-time trace which make it difficult to interpret. However, it is not known clearly that these high frequency signals are mainly associated with the individual impact test process or the impact system. A comparison test on bulk polymeric material PMMA was carried out to make further investigation on these high frequency signals.

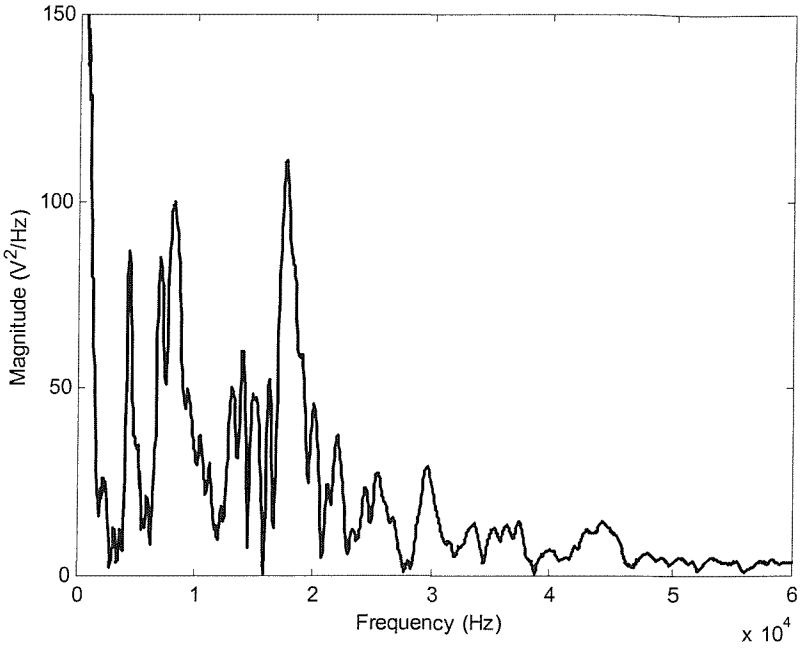

Fig. 6.15 The corresponding frequency analysis result of the impact response of the impact test on the coating T-15B1 under an impact energy of 7 J.

(b) Impact test on bulk polymeric material PMMA

An impact test on bulk polymeric material PMMA under an impact energy of 3 J was carried out to distinguish the frequencies arising from the impact rig. The test sample has the same surface dimension as the polymeric coatings (38 x 38 mm) with a thickness of 5 mm; a 4.5 mm thick steel pad was placed underneath the sample in order to simulate the test on the coating sample. Figure 6.16 schematically shows the clamping conditions and the relative positions of different parts of the rig involved in the impact test. The generic experimental conditions are shown in Table 6.5. The impact result is shown in Figure 6.17. Complete circumferential cracks are apparent on the surface of the sample.

Table 6.5 Experimental conditions on bulk polymeric material PMMA

Sample	Size (length x width x thickness, mm)	Impact energy, J	Clamping conditions
PMMA	38 x 38 x 5	3	3 edge fixed

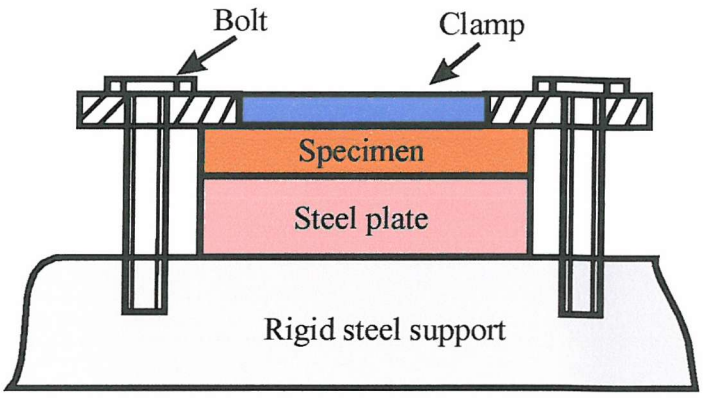

(a) Side view of the sample holder

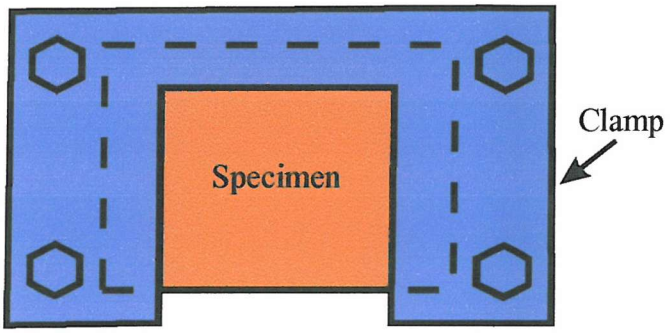

(b) Top view of the sample holder

Fig. 6.16 Schematic diagram of the sample clamped in the testing rig and the relative positions of the steel plate underneath the test piece and the clamping arrangement.

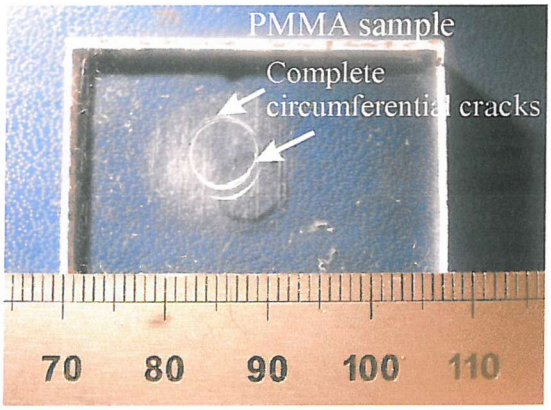

Fig. 6.17 PMMA sample after a 3 J impact test with a 4.5 mm thick steel plate underneath. Note the complete circumferential cracks on the surface of the sample.

The impact response and the corresponding FFT analysis are shown in Figure 6.18 (a) and (b). From the original force-time response, Figure 6.18 (a), the initial contact and the point at which contact between the impactor and the test sample is lost can be easily recognised; high frequency signals were picked up and are shown in the trace. By using the FFT method, several dominant frequencies are identified in Figure 6.18 (b). They were approximately at 3~5 kHz, 6~10 kHz, 13~19 kHz and 19~25 kHz. In addition, the comparison of the FFT analysis results between the impact tests on the coating T-15B1 and the bulk polymer material PMMA is shown in Figure 6.18 (c).

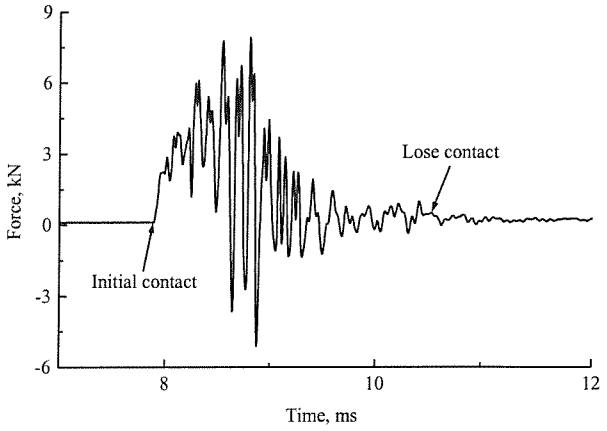

(a) Original force-time response from the impact test on PMMA under an impact energy of 3 J.

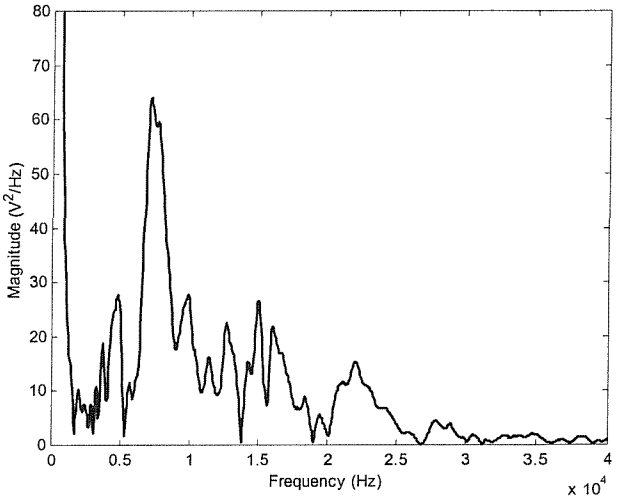

(b) FFT analysis of the original impact response from the impact test on PMMA.

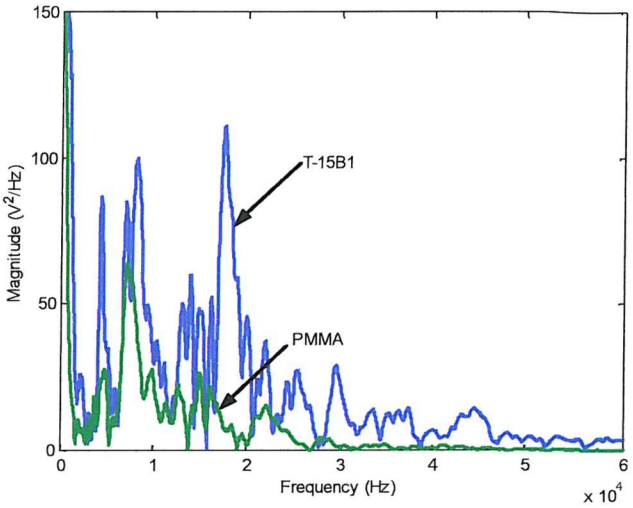

(c) Comparison of FFT analysis between the impact tests on the coating T-15B1 and the bulk polymer material PMMA.

Fig. 6.18 Original impact response and the corresponding FFT analysis result from the impact test on the bulk polymeric sample PMMA under an impact energy of 3 J; and comparison of the FFT analysis results between the impact tests on the coating T-15B1 and the bulk polymer material PMMA.

(c) Comparison of the results of FFT analysis on polymeric coating T-15B1 and on bulk PMMA

Two impact tests on different materials under different impact energies with the same test rig produced different results on the sample surface: a plastic indent was produced on the surface of the coating sample T-15B1 and complete circumferential cracks were produced on the surface of the bulk PMMA. Nevertheless, the FFT analysis shows that the two experiments had quite similar dominant frequency bands below 25 kHz, see Figure 6.18 (c). The FFT analysis of the impact test on the coating sample shows some higher frequencies above 25 kHz, which is believed to be caused by the higher impact energy applied during this test because the higher natural frequencies of the parts being involved in test could be aroused under the higher impact energy. Through these comparative results, it can be concluded that the high frequency components in the impact signal are mainly associated with the present impact system rather than the individual impact processes themselves.

(d) Maximum mean force during each impact test

Through the above discussion, it can be concluded that the maximum mean force can be obtained from the force-time trace after the high frequency signals which are associated with the impact system have been removed from the impact response.

Figure 6.19 shows the original impact response from the impact test on the polymeric coating T-15B1 under an impact energy of 7 J together with the signals filtered above 15 kHz, 6 kHz, 4 kHz and 2 kHz respectively. Table 6.6 shows the maximum impact force obtained from the filtered force-time trace shown in Figure 6.19. It can be seen that when the original signal is filtered above 15 kHz and 6 kHz the filtered signals have a similar shape to the original signal though the peak value has been obviously reduced, indicating that high frequency signals still remain in the filtered signals. When the original signal is filtered above 4 kHz and 2 kHz, the filtered signals are very smooth. However, the signal filtered above 2 kHz shows a lower peak value of the maximum impact force than the signal filtered above 4 kHz, indicating that the original signal has been over filtered and the real maximum mean force cannot be read from it. Therefore, in order to get the correct maximum mean force, it was decided to remove frequencies above 4 kHz from the original impact response. This conclusion is consistent with the findings of the comparative experiments on the polymeric coatings T-15B1 and on the bulk PMMA which indicated that the high frequency signals above 4 kHz were related to the impact system.

Thus, all the impact tests on the polymeric coatings carried out with the present impact system have been evaluated by the FFT filtering method, and the high frequency signals above 4 kHz have been removed from the original impact response in order to obtain the maximum mean force during an impact test. Table 6.7 summarises the maximum mean force in each impact test on the polymeric coating samples obtained by the FFT filtering method. The maximum mean force will be used to discuss the impact damage on the coating sample in Section 6.5.

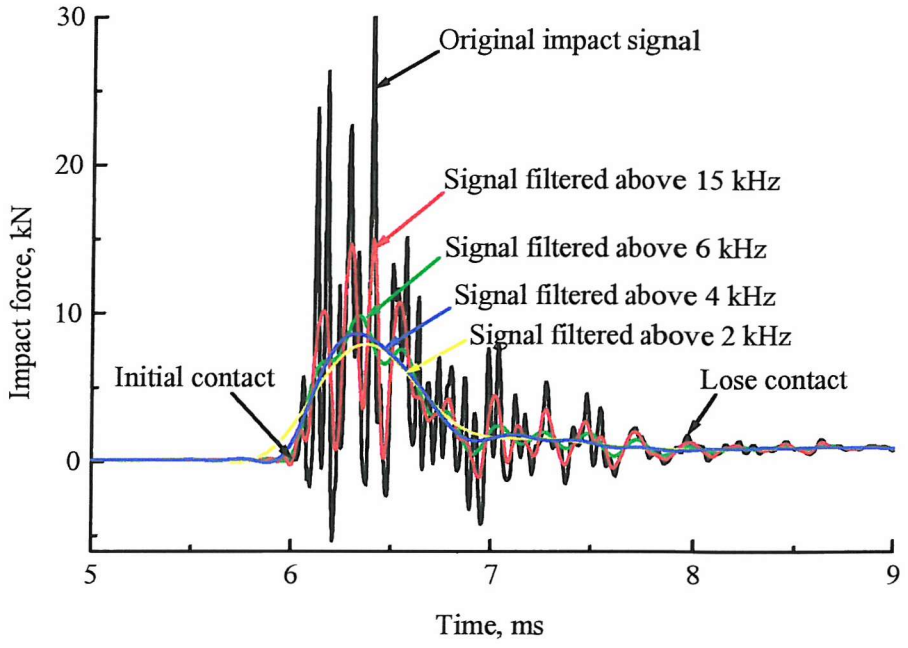

Fig. 6.19 Original impact response from the impact test on polymeric coating T-15B1 under an impact energy of 7 J together with the signals filtered above 15 kHz, 6 kHz, 4 kHz and 2 kHz respectively.

Table 6.6 Maximum impact force obtained from the filtered force-time traces shown in Figure 6.19

	Maximum force, kN
Original impact signal	30
Signal filtered above 15 kHz	15
Signal filtered above 6 kHz	9.8
Signal filtered above 4 kHz	8.6
Signal filtered above 2 kHz	7.9

Table 6.7 Maximum mean force during each impact test as obtained by the FFT filtering method

Impact energy, J	Maximum impact force in each test (kN)								
	T-15A	T-15B1	T-15B2	T-34A	T-34B1	T-34B2	F-4001A	F-4001C1	F-4001C2
4	6	5.8	6	—	6	—	—	—	—
7	8.5	8.6	9.6	10.2	9.2	8.9	7.5	—	—
10	9.4	9.6	9.8	11.9	10.8	10.9	9.5	8.1	—
14	13.9	13.5	14.8	15	13.8	13.8	—	11.5	10.5
18	—	—	—	15.2	15.5	15.9	—	—	—
22	—	—	—	18.2	—	18.5	—	13.6	13.4

6.4 Theoretical Considerations

6.4.1 Indentation behaviour of polymer coatings

Polymer coatings are widely used as protective coatings on relatively rigid substrate such as ceramics or metals. The protection given by these coatings depends on their adhesion to the substrate and their resistance to penetration as a result of impact. Although there have been numerous studies on the indentation resistance of thin metal and ceramic coatings [21 - 23], there has been relatively little research on the indentation resistance of polymer coatings [24]. That research has largely employed indentation testing using instrumented hardness testers as the means of studying the penetration resistance of polymer coatings. Various geometries of indenter have been used ranging from Vickers indenter [24], spherical indenter [25] and flat punch [26].

As the indenter penetrates the coating the material of the coating is displaced radially outwards. When the indenter penetrates through the polymer coating and into the substrate the coating material displaced by the indenter is squeezed upwards to the surface due to the constraint imposed by the substrate and surrounding coating material. This creates a pile up of the coating material underneath the face of the indenter which affects the load-depth behaviour. The load-depth behaviour and the extent of the pile-up was reported [24] to be independent of whether or not localised debonding at the substrate coating occurred and on the time for indentation. Ritter [24] also reported that prior to the indenter penetrating the substrate the volume of the pile-up of the coating

material is at least an order of magnitude less than the volume displaced by the Vickers indenter.

6.4.2 Plastic deformation due to indentation

If the elastic deformation under indentation is much less than the plastic deformation, then the average indentation pressure (applied load divided by the projected area of contact between the indenter and sample) is equivalent to the conventional hardness when the area of contact is measured after unloading. This is the case for glass, but polymers can exhibit viscoelastic recovering after unloading, causing conventional hardness values to increase with time. For example, Ritter [24] quotes that for epoxy and epoxy acrylate coatings conventional hardness increased by up to about 10% in 30 minutes after unloading, while with a urethane acrylate coating the indent disappeared completely after 30 minutes from unloading. To avoid this problem Ritter [24] uses the hardness under load and plots the indentation pressure values measured for the coating as a function of depth of penetration normalised to the thickness of coating, i.e. d/h, where d is the total depth of indentation and h is the coating thickness. His results suggest that for these relatively soft polymers the average indentation pressure is not influenced by the substrate for d/h values less than 1.0. This appears true for epoxy and epoxy acrylate coating but for the softer urethane acrylate the indentation pressure increased with penetration depth ($d/h < 1$). For $d/h > 1$, Ritter determined the overall average indentation pressure, H_0, of the polymer/glass system he was studying (H_0 defined as load/projected area of the indent at the coating surface measured to top of piled up ridge) and found that the ratio of H_0/Hc (Hc=coating hardness) increased rapidly with depth of penetration d/h >1. The fact that H_0 did not approach Hs (substrate hardness) for large d/h values was a reflection of the fact that the pile-up of coating material will always support a significant proportion of the load.

6.4.3 Cracking in coatings

When a spherical indentor is pressed onto the surface of a material, a complex stress field is set up in the sample and around the indentor. The geometry of the contact region for a plane sample surface and purely elastic deformation has been predicted by Hertz (1881). A complete solution for the stress field was subsequently provided by Huber [27]. The subject of Hertzian indentation and its implications has been reviewed by Lawn and Wilshaw [28].

Under a normal load, w, contact will occur between the indentor and the plane surface over a circular area of radius a, given by the following equation due to Hertz:

$$a = (\frac{3wr}{4E})^{1/3} \qquad (6.5)$$

Here r is the radius of the spherical indentor and E is an elastic modulus which depends on Young's moduli, E_1 and E_2, and on the Poisson's ratios, ν_1 and ν_2, for the material of the indentor and the plane in the following way:

$$\frac{1}{E} = \frac{(1-\nu_1^2)}{E_1} + \frac{(1-\nu_2^2)}{E_2} \qquad (6.6)$$

The area of contact between the spherical indentor and the plane, πa^2, is then given by:

$$\pi a^2 \approx 0.83\pi(\frac{wr}{E})^{2/3} \qquad (6.7)$$

For this case, in which the deformation is purely elastic, the area of contact is therefore proportional to $w^{2/3}$. The mean pressure (normal stress), p_{mean}, over the contact area is $w/\pi a^2$, and thus varies as $w^{1/3}$. This stress is not uniform over the circular area of contact, but has a maximum at the centre and fall to zero at the edge. Below the indentor the stresses within the plane sample are compressive while outside the contact circle in

the sample surface there is a radially directed tensile stress, σ_r . The tensile stress, σ_r , in the plane surface reaches a maximum value $\sigma_{r\max}$ just at the edge of the circle of contact, given by

$$\sigma_{r\max} = (1-2\nu)p_{mean} \qquad (6.8)$$

It is this tensile stress component $\sigma_{r\max}$ which gives rise to fracture. When the normal load on the indented material is sufficiently high, the tensile stresses will create a ring crack around the contact zone. According to the Hertz theory, these ring cracks should be formed at the edge of the contact zone, where the tensile stress has its maximum. Later work [29, 30] has shown that this is not always the case. Often the ring crack is formed outside the contact zone.

Many analyses have taken place on the cracking of hard coatings. Abdul-Baqi and Van der Giessen [31] have considered the case of indentation induced cracking of thin brittle coatings on a ductile substrate. The model, however, is for the case of a hard coating, and the coating is assumed to be linear elastic, while the substrate is perfectly plastic. In the present research, the filled thermoset coatings (T15 and T34) can be considered as linear elastic, the fillers promoting brittle fracture and decreasing the amount of plasticity possible. Note the two thermoset coatings used in the present study have much lower Young's modulus than the substrate, which is not the normal case. Coating cracking is one of the common events associated with indentation experiments on brittle coatings. Radial or circumferential cracks might initiate from the coating surface or from the coating side of the interface and may grow into a through thickness crack. Based on FE, Abdul-Baqi and Van der Giessen [31] show that a tensile radial stress is found outside the contact area with a maximum at $r \approx 1.25a$, where a is the indentation contact radius. The location of this maximum is said to be strongly dependent on the ratio t/R, where t = thickness of coating and R = indentation depth, the smaller the ratio t/R, the closer the location of the maximum tensile stress to the contact edge. A radial tensile stress is also seen along the coating site of the interface. It is located in the contact region, $r < a$, with

a maximum at the symmetry axis. This suggests that a circumferential crack is likely to initiate from the interface at $r < a$ or at the coating surface at $r \approx 1.25a$ due to the maximum tensile radial stresses at those regions.

Persson, Breder and Rowcliffe [32] studied the loading rate effect during indentation and impact on glass with small spheres. They found that at higher velocity impacts the damage began to change from that encountered in quasi-static indentations. The differences are that the impacted glass processes show radial cracks in almost all cases above a certain impact energy ($v \geq 35$ ms^{-1}) and at higher impact energies ($v \geq 45$ ms^{-1}) the central area below the impacting sphere is crushed. The size of the ring crack (the largest one in cases where more than one was present) was compared to the theoretical contact zone. The ratio between measured ring crack and theoretical contact zone was 1.285. This is in good agreement with Chaudri and Yoffe [33] and Johnson et al [34].

Figures 6.20 (a) and (b) schematically show the damage changing from plastic deformation to ring crack and radial crack during an impact test under different levels of impact energies. Figure 6.20 (a) shows the circumferential crack produced by tensile stress on the sample surface. Low energy impact of a polymeric material produces a permanent (plastic) indent straining the surface of the sample tested, producing a tensile stress in the radial direction. A stress raiser or other weak point initiates a ring crack that grows either into a partial or complete circumferential crack. Figure 6.20 (b) shows a schematic diagram for the production of radial cracks on the surface of the sample tested under higher impact energy. A higher impact energy will result in large-scale plastic deformation and the redistribution of material, creating a raised lip that surrounds the impact indent. A hoop stress is created in the surface layer; at the weakest point on the surface, radial cracks are initiated and grow.

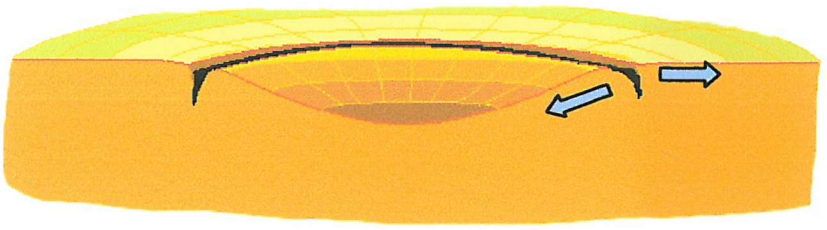

Fig. 6.20 (a) Schematic displaying circumferential cracking as a result of low energy impact. Note the radial surface tension introduces a circumferential crack.

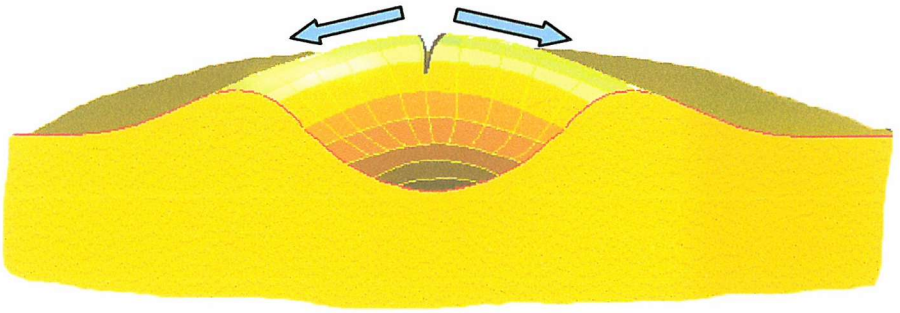

Fig. 6.20 (b) Schematic displaying radial cracking, a result of medium energy impact. Note the circumferential hoop stress produces a surface tension, which results in the initiation of radial cracks.

6.4.4 Relationship between maximum impact force and velocity

Equations for the maximum dynamic load delivered to a target have been derived, assuming that all the kinetic energy of the impacting sphere is transformed into strain energy in the target [28, 35]. The analysis is based on Hertz, i.e. $a^3 = \frac{3}{4E} wr$, and distance of mutual approach, $z = \frac{a^2}{r}$.

Rearranging so as to have w as a function of z,

$$w = \frac{4}{3} E r^{1/2} z^{3/2} \qquad (6.9)$$

Equating kinetic energy and strain energy,

$$\frac{1}{2}mv^2 = \int_0^{z_{max}} w(z)dz$$

$$= \int \frac{4}{3}Er^{1/2}z^{3/2}dz$$

$$= \left[\frac{4}{3}Er^{1/2}\frac{2}{5}z^{5/2}\right]_0^{z_{max}}$$

$$= \frac{8}{15}Er^{1/2}z_{max}^{5/2} \qquad (6.10)$$

Expressing z_{max} in terms of w_{max} (i.e. load at z_{max})

$$w_{max} = \frac{4}{3}Er^{1/2}z_{max}^{3/2} \qquad (6.11)$$

so

$$z_{max} = \left(\frac{3w_{max}}{4Er^{1/2}}\right)^{2/3} \qquad (6.12)$$

Substituting (6.12) in (6.10)

$$w_{max} = 1.944\left(\frac{1}{2}mv^2\right)^{3/5}(E^2r)^{1/5} \qquad (6.13)$$

Note this equation is derived from static and fully elastic conditions and may not be fully accurate when cracking occurs in the material.

In order to utilise Eqn (6.13), the material properties of the two parts involved in the test were necessary, i.e. ball bearing of the impactor and the polymeric coating. The Young's modulus and Poisson's ratio of steel were adopted as the material properties of the impactor. However, the material properties of the polymeric coatings were not given by the manufacturer. Several methods were utilised by the present author to measure the

Young's modulii of the coating materials, they are introduced in Appendix B. However, due to the difficulty of separating the coating from the substrate material it was not able to obtain reliable values of Young's modulii. Therefore, the present author referenced the Materials Property Database [36] and adopted the values of the Young's modulus and Poisson's ratio for the polymeric coatings T-15 and T-34 from the commercial products which have the same polymeric material and similar microstructure as these two coatings. The material properties of the impactor and the polymeric coatings are given in Table 6.8.

Table 6.8 Mechanical properties of the materials involved in the impact test

Material properties	Impactor	F4001	T-15	T-34
Young's modulus, GPa	207	2.5	6	7
Poisson's ratio	0.31	0.35	0.35	0.35

* Data obtained from the MatWeb Materials Property Database

6.5 Discussion of Impact Results

Based on Eqn (6.13), theoretically predicted maximum impact force in the present impact test can be obtained. The predicted maximum force based on Eqn. (6.13) during each impact test were calculated and given in Table 6.9.

Table 6.9 Predicted maximum force in each impact test as obtained by Eqn (6.13)

Impact energy, J	Maximum impact force in each test (kN)								
	F-4001A	F-4001C1	F-4001C2	T-15A	T-15B1	T-15B2	T-34A	T-34B1	T-34B2
4	—	—	—	13.5	13.5	13.5	—	14.3	—
7	7.1	—	—	18.9	18.9	18.9	20.1	20.1	20.1
10	8.8	8.8	—	23.4	23.4	23.4	24.9	24.9	24.9
14	—	10.7	10.7	28.7	28.7	28.7	30.4	30.4	30.4
18	—	—	—	—	—	—	35.4	35.4	35.4
22	—	14.1	14.1	—	—	—	39.9	—	39.9

6.5.1 Thermoplastic coating F-4001

During the impact test on the thermoplastic coating F-4001, impact produced a plastic indentation, i.e. the test is really a form of dynamic hardness testing with a spherical indenter. If the test were conducted statically it is simply a Brinell hardness test. Note the Brinell hardness is load divided by curved surface of the indentation and is not a pressure. The Meyer hardness is load divided by cross section area of indent, i.e. $w/\pi a^2$, where 2a is the diameter of the indent.

In the present tests, the impactor is indenting a coating. In this context it is interesting to note that Brinell Hardness Test Method [37] states that the test piece for a Brinell hardness test should be not less than 8 times the depth of the indent, i.e. for the hardness indent to be independent of the depth of sample, the ratio of the depth of indent to thickness of sample must be less than 0.125. However, it can be seen from Table 6.10 that the values of ratio of the depth of the indent to the coating thickness for the coating F-4001 are greater than 0.125.

Table 6.10 Ratio of the depth of the indent to the thickness of the coating in samples of F-4001 tested

Impact energy, J	Depth of indent / Coating thickness		
	F-4001A	F-4001C1	F-4001C2
7	1.10	—	—
10	1.24	0.30	—
14	—	0.40	0.36
18	—	0.43	—
22	—	0.53	0.49

Figure 6.21 shows the radius of the indent as a function of maximum mean force measured for all the thermoplastic coatings F-4001. The plot of radius of indent as a function of maximum mean force seems to show little effect of coating thickness nor substrate thickness. Figure 6.22 shows the depth of indentation as a function of maximum

mean force for all the thermoplastic coatings F-4001. The data apparently show no effect of substrate thickness, but the thinner coating seems to give a deeper indent for a given maximum force than the thicker coating. It can be concluded from this result that the thinner coating has less resistance to the impact than the thicker coating under the same impact force. Figure 6.23 shows the average indentation pressure (i.e. Meyer hardness) calculated from the maximum mean force and the residual indent size as a function of the depth/thickness of coating ratio. All of the values of the depth/thickness ratio are greater than 0.125. However, the average indentation pressure does not change markedly as the depth/thickness ratio increases. This is in agreement with the result of Ritter discussed in Section 6.4.2.

Standard Brinell hardness tests were carried out on the thermoplastic coatings F-4001 with 0.5 mm and 1.5 mm thicknesses under different load in order to complement the results of impact test. A 2 mm diameter ball was used for the Brinell tests. The radius of indents made on the coating surface were measured immediately after the indentation and 68 hours later, respectively. Figure 6.24 shows the Meyer hardness values of coating F-4001 as a function of depth of indent/thickness of coating ratio. It can be seen that the measurements immediately and 68 hours later are similar. However the Meyer hardness values increased gradually as depth/thickness increases.

Comparing the Meyer hardness values between the impact test and the Brinell test, it can be seen that for a given value of depth/thickness the indentation pressure from the Brinell test is lower than that from the impact test. Different test conditions could be the reason for the above results. Figures 6.25 and 6.26 show the Meyer hardness as a function of radius (a)/thickness of coating ratio for the impact test and Brinell hardness test, respectively. It can be seen that the impact data have very different values of a/thickness than the Brinell test. This indicates that there was a greater pile up effect for the Brinell hardness test. With a bigger diameter of ball (11.2 mm) as in the impact test, the stress field from the ball extended to a greater distance than from the small ball (2 mm) used in the Brinell hardness test. Hence at a given depth/thickness of coating ratio the stress field from the bigger ball extended to a greater depth and so took into account more the

substrate. For the small 2 mm diameter ball for low loads in the Brinell hardness test, the stress field of the ball is largely confined to the coating and hence a smaller value of Meyer hardness was obtained. As the load is increased and the depth of the indent increased, the stress field from the ball extends into the substrate and the hardness increased. Additionally, the difference between the impact and Brinell test is the strain rate. The strain rate was higher in the impact and that would tend to give rise to a higher hardness value because the dynamic effect increases the pressure during the initial stage of impact [38].

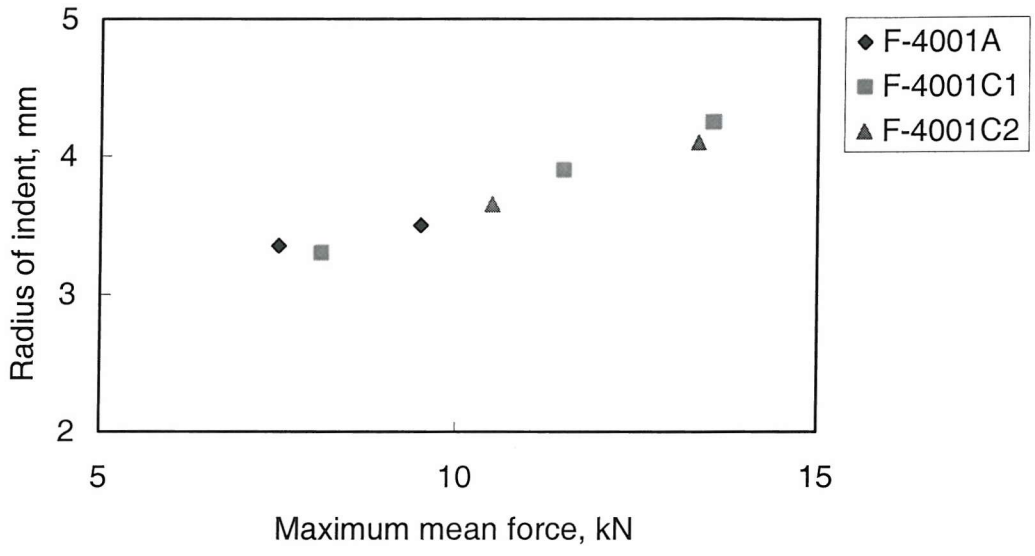

Fig. 6.21 Radius of indents as a function of maximum mean force for the thermoplastic coating F-4001. Note little effect of coating thickness, nor substrate thickness on maximum mean force.

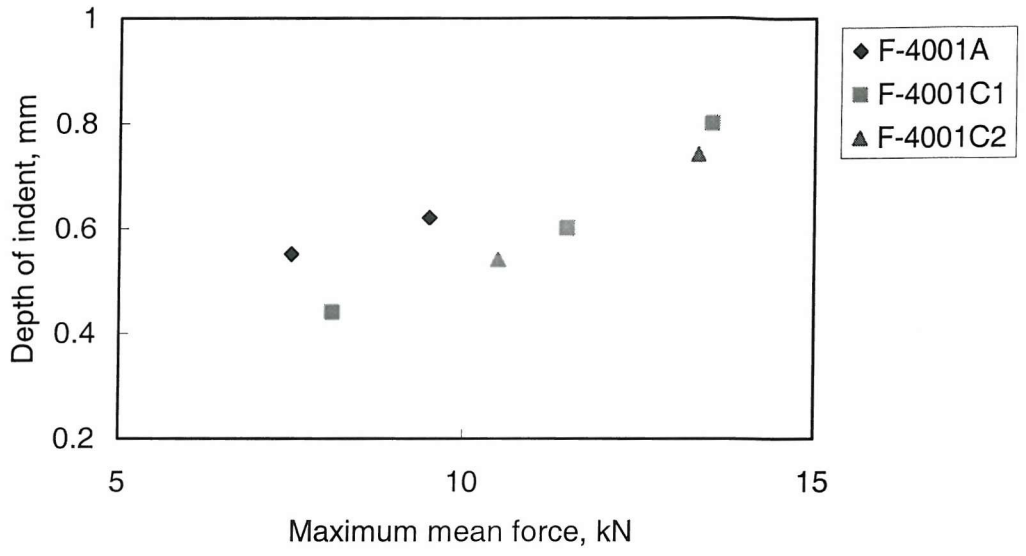

Fig. 6.22 Depth of indents as a function of maximum mean force for the thermoplastic coating F-4001. Note the thinner coatings show deeper indent on the thermoplastic coatings.

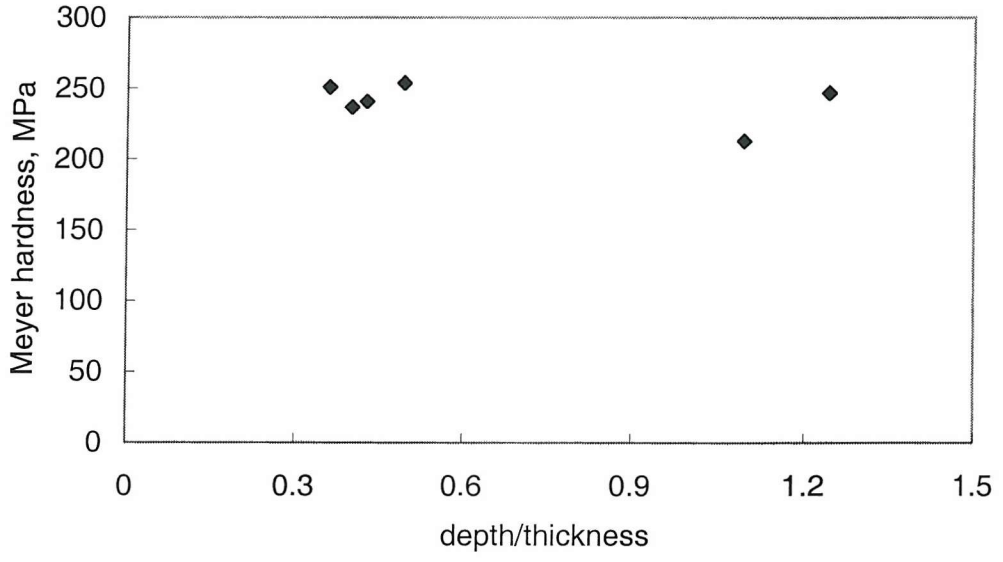

Fig. 6.23 Average indentation pressure (Meyer hardness) calculated from the maximum mean force and the residual indent size from the impact tests as a function of depth of indent/thickness of coating ratio. Note the average indentation pressure does not change markedly as the depth/thickness ratio increases.

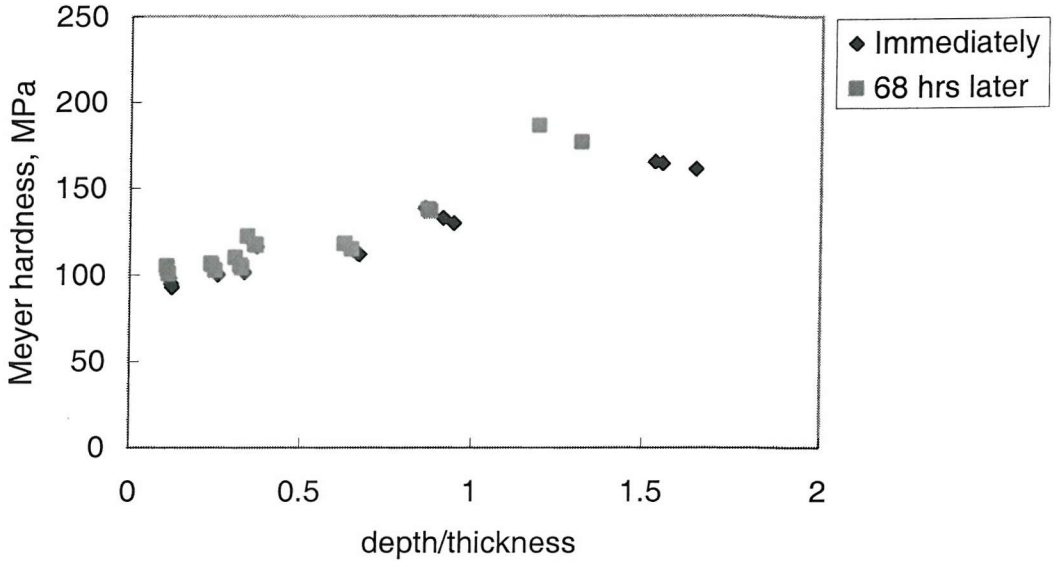

Fig. 6.24 Meyer hardness of coating F-4001 as a function of depth of indent/thickness of coating ratio obtained from the Brinell hardness test. Note the similarity of measurements between immediately after the indentation and 68 hours later.

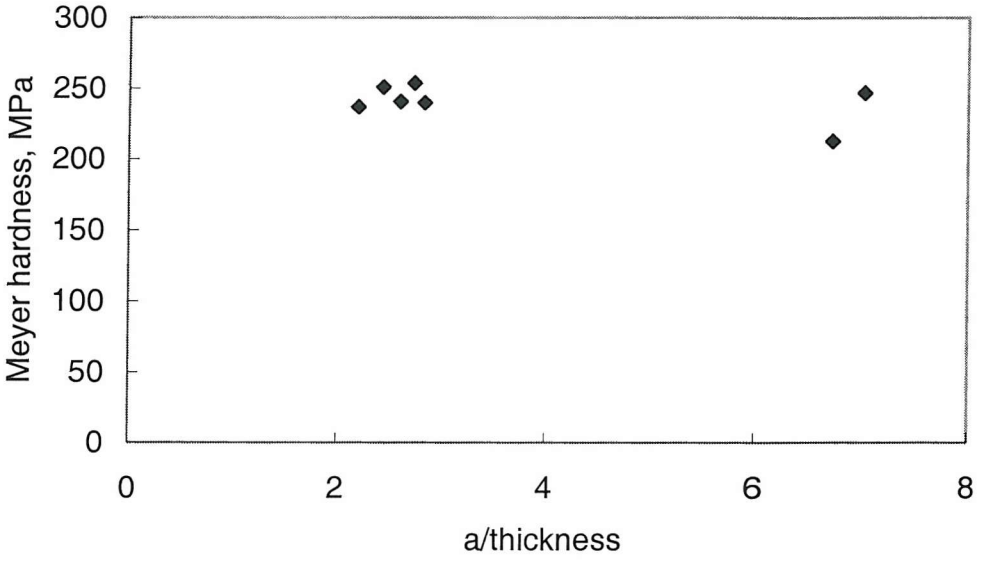

Fig. 6.25 Meyer hardness of coating F-4001 as a function of radius of indent a/thickness of coating ratio during the impact test. Note the large range of the values of a/thickness.

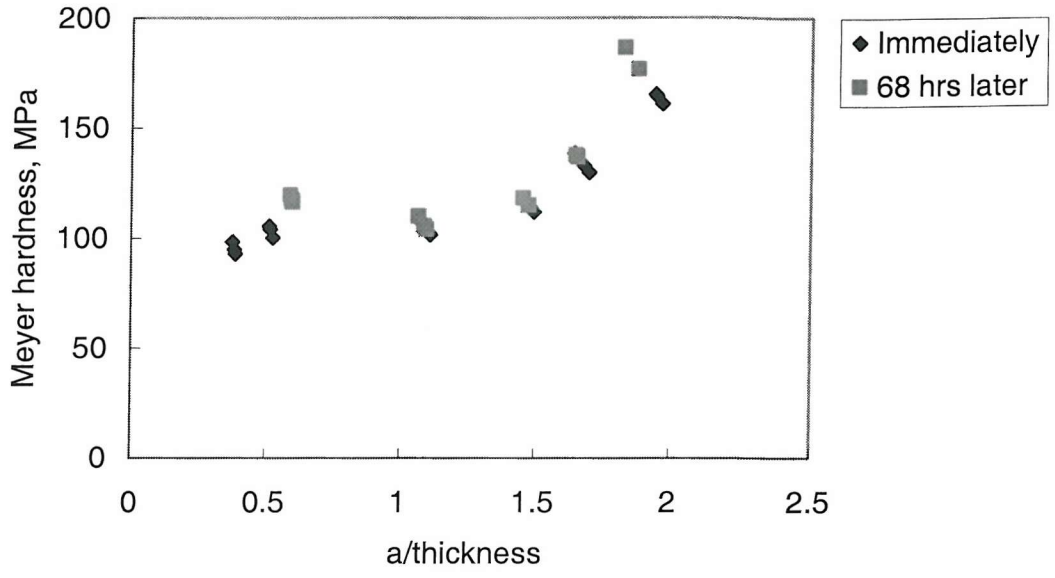

Fig. 6.26 Meyer hardness of coating F-4001 as a function of radius of indent a/thickness of coating ratio during the Brinell hardness test. Note the a/thickness ratios are smaller than in the impact test data.

Figure 6.27 shows the maximum force as a function of impact energy used in the impact test. A power trend line can be fitted through all the data points, an exponent of 0.53 given by the trend line is not far different from the exponent of 0.6 we expect theoretically, shown in Eqn (6.13). Figure 6.28 presents the maximum force measured and predicted from Eqn (6.13) during the impact tests for F-4001 coatings. However, Eqn (6.13) is based on an elastic analysis which is obviously not valid for the present case when a plastic indent is produced. In the present case the kinetic energy of impact is absorbed by both elastic and plastic deformation. It is interesting to note that the experimental and theoretical elastic predictions can be brought into agreement if a value of Young's modulus E of 0.5 GPa (rather than 2.5 GPa) is assumed, as an "Effective elastic" modulus to describe this process. This can be understood by considering the energy absorbed as being effectively represented by the area under the stress strain curve of the material, Figure 6.29. For a given maximum force, a smaller value of E would give the same energy absorbed (i.e. area under the stress-strain curve) as that from elastic-plastic behaviour.

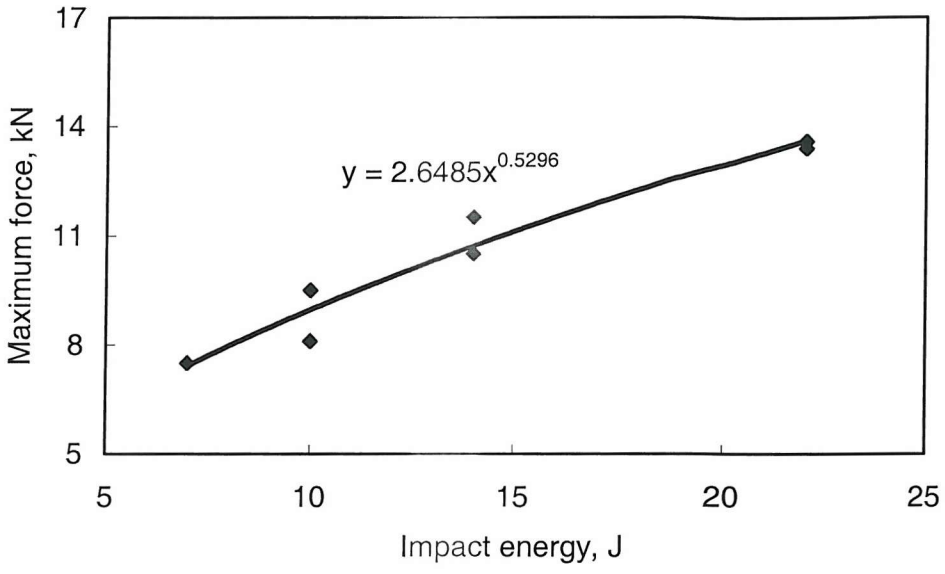

Fig. 6.27 Maximum force as a function of impact energy for the thermoplastic coating F-4001. Note the exponent of the power trend line 0.53 is not far from the theoretical value 0.6.

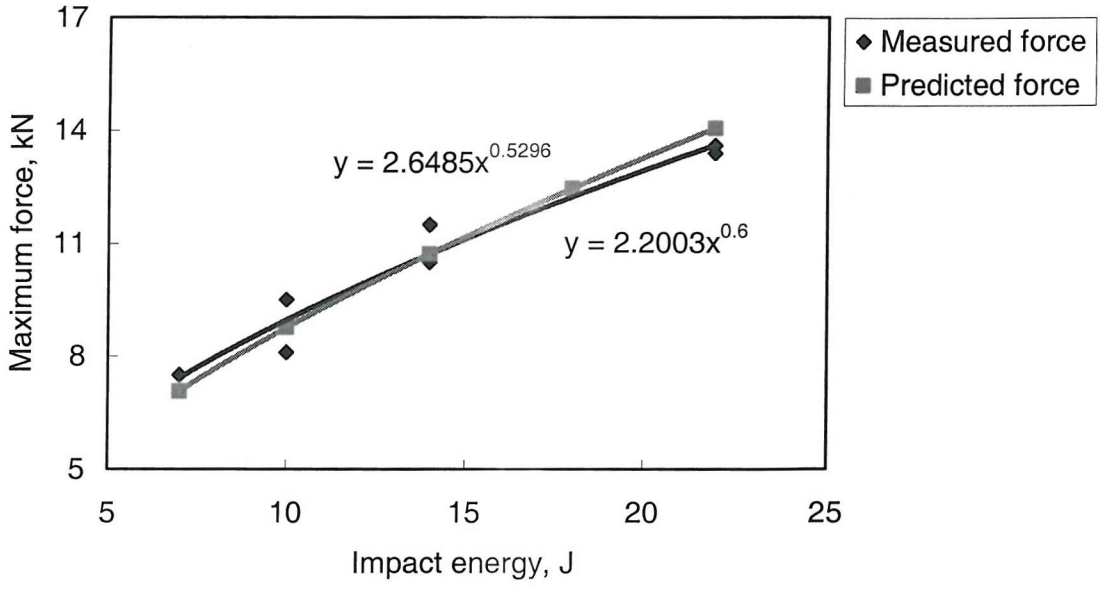

Fig. 6.28 Maximum force as a function of impact energy. Note measured force and predicted force are similar if the effective E is taken as 0.5 GPa.

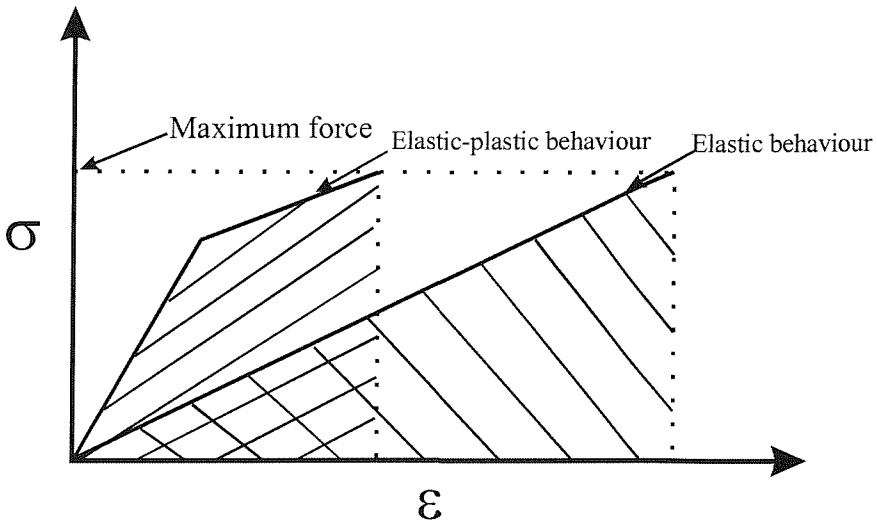

Fig. 6.29 Schematic diagram showing the same energy absorbed and same maximum force as elastic-plastic behaviour, but with an effective E smaller than the true E for the assumed elastic behaviour.

6.5.2 Thermoset coatings T-15 and T-34

The two types of thermoset coating T-15 and T-34 have 9% calcium silicate ($CaSiO_3$) and 20% alumina (Al_2O_3) fillers respectively. As fillers are added, among other things, to increase the stiffness, i.e. Young's modulus, the E is expected to be higher with greater fillers volume fractions. For a discontinuous and randomly oriented composite, this expectation is based on a Rule of Mixtures, that is

$$Ec = KE_fV_f + E_mV_m \qquad (6.14)$$

Where Ec is the Young's modulus of the composite, E_f and E_m are the Young's moduli of the particles and matrix; V_f and V_m are the volume factor of the particles and matrix; K is a fibre efficiency parameter which depends on V_f and the E_f/E_m ratio. K is usually between 0.1 to 0.6. Table 6.11 shows the properties of the filler particles used in the two types of thermoset coatings T-15 and T-34. For a given K, the Ec of T-34 could be expected to be higher than that of T-15 as the V_f of T-34 is 2.2 times greater than T-15,

and based on the hardness of Al_2O_3 in T-34 being greater than that of the $CaSiO_3$ in T-15, E_f of Al_2O_3 could be higher than that of $CaSiO_3$.

Table 6.11 Properties of particles in the two types of thermoset coatings T-15 and T-34 *

	% Fillers	E, GPa	Mohs hardness
$CaSiO_3$	9	?	4.5-5
Al_2O_3	20	370	9

*Data from Dictionary of Ceramic Science and Engineering, 2nd Edition, Ian J. McColm, Plenum Press, 1994 [39].

(a) T-15

Figure 6.30 gives the radius of the circumferential cracks as a function of the maximum force measured for all the impact tests on the T-15 thermoset coatings. There does not appear to be a very marked influence of coating thickness. Only the point at 13.9 kN for the thin coating T-15A shows a smaller radius than the thicker coating. This point seems to lie off the trend line of all other experimental data. This could be caused by experimental error or reading error during the measurement of the indent.

The radius of circumferential cracks for the thermoset coating T-15 can be predicted from the Hertzian Eqn (6.5), and the predicted values of contact radius are given in Table 6.12. Note the important parameters Young's modulus, E, and Poisson's ratio for the coating were adopted by the present author, and different E values can cause different predicted contact radius.

Figure 6.31 gives the experiment results for all the impact tests on T-15, including the predicted Hertz contact radius, measured contact radius, and 1.285 times the Hertz predicted contact radius [40]. The measured data give an exponent of 0.36 which is not far from the theoretical 0.33. It also can be seen that the values of 1.285 times Hertz radius are closer to the measured indent radius, implying a good agreement to the other

researchers [34, 35] who have reported that the circumferential cracks appear outside the diameter predicted by Hertz [40].

Figure 6.32 shows the maximum mean force as a function of impact energy. Data for the measured force and predicted force are given. Obviously the predicted value depends on the value of Young's modulus taken for the coating. The exponent of the power fit for the measured data is similar to that for the predicted data, as 0.64 against 0.6. The predicted and measured data can be made to agree if the effective Young's modulus chosen for the coating is approximately 0.8 GPa, see Figure 6.33. This approach was discussed in Section 6.5.1.

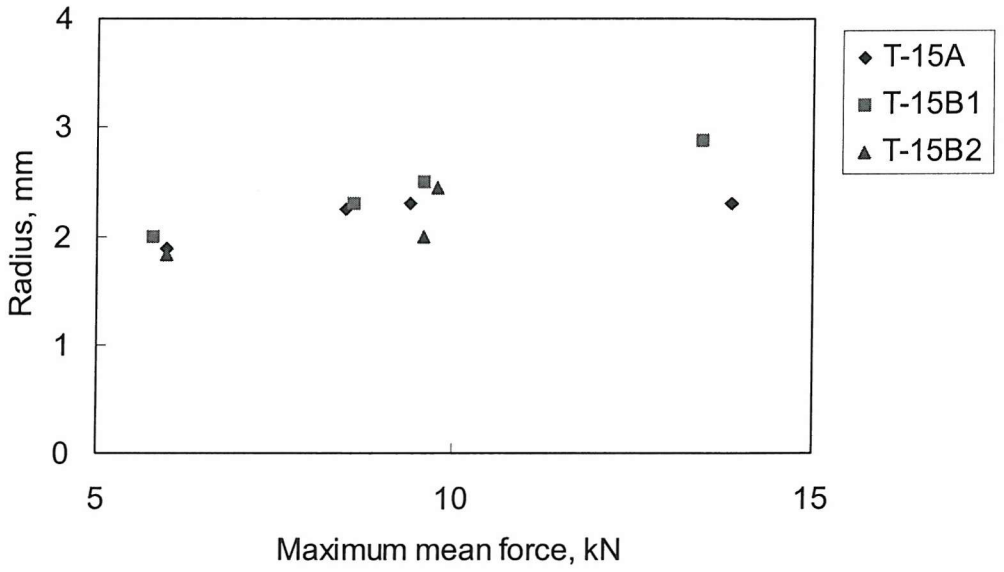

Fig. 6.30 Radius of indents as a function of maximum mean force for the thermoset coating T-15. Note there was little effect of coating thickness nor substrate thickness on maximum mean force.

Table 6.12 Radius of theoretically predicted contact zone on the T-15 coatings (E=6 GPa)

Impact energy, J	Radius of contact zone by Hertzian theory, mm		
	T-15A	T-15B1	T-15B2
4	1.57	1.56	1.57
7	1.77	1.77	1.84
10	1.83	1.84	1.85
14	2.08	2.06	2.13

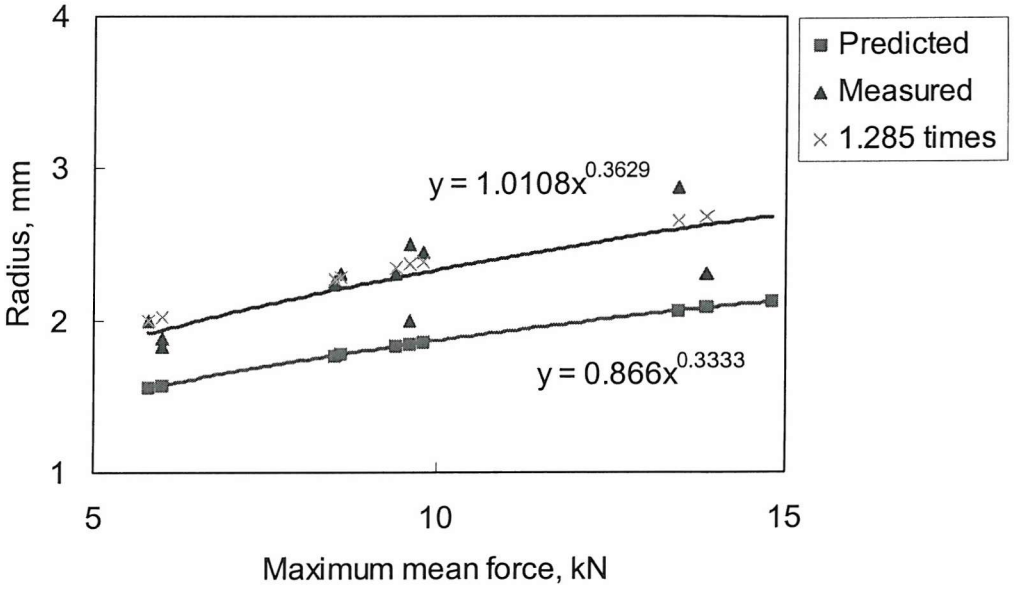

Fig. 6.31 Radius of indent as a function of maximum mean force for the thermoset coating T-15. Note the measured data has a similar exponent to the predicted data and the value of 1.285 times Hertz radius is very close to the measured radius.

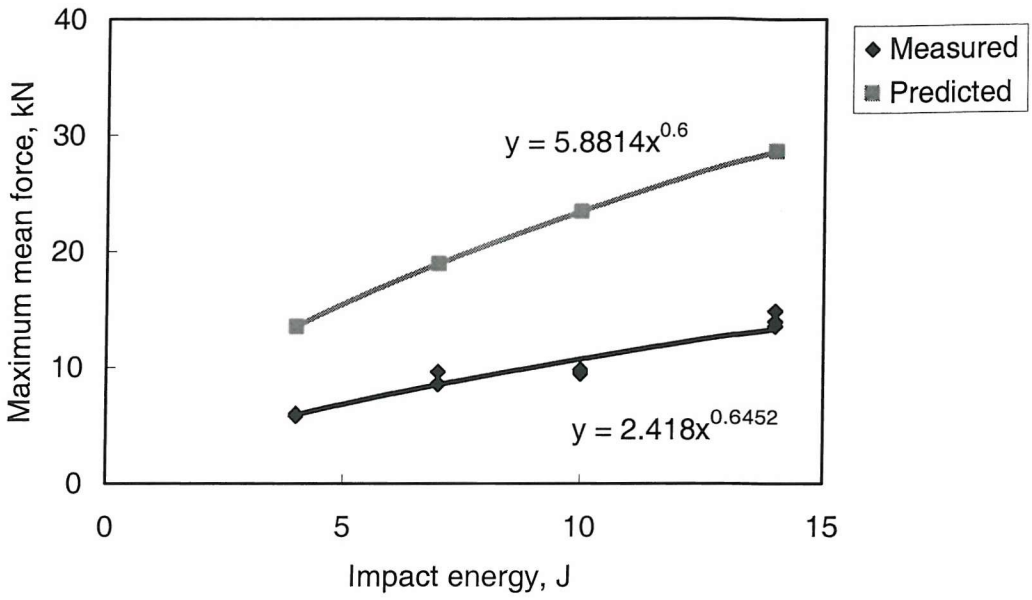

Fig. 6.32 Maximum force as a function of impact energy for the thermoset coating T-15. Note the measured data has a similar exponent to the predicted data, however the predicted value is greater than the measured value (E = 6 GPa).

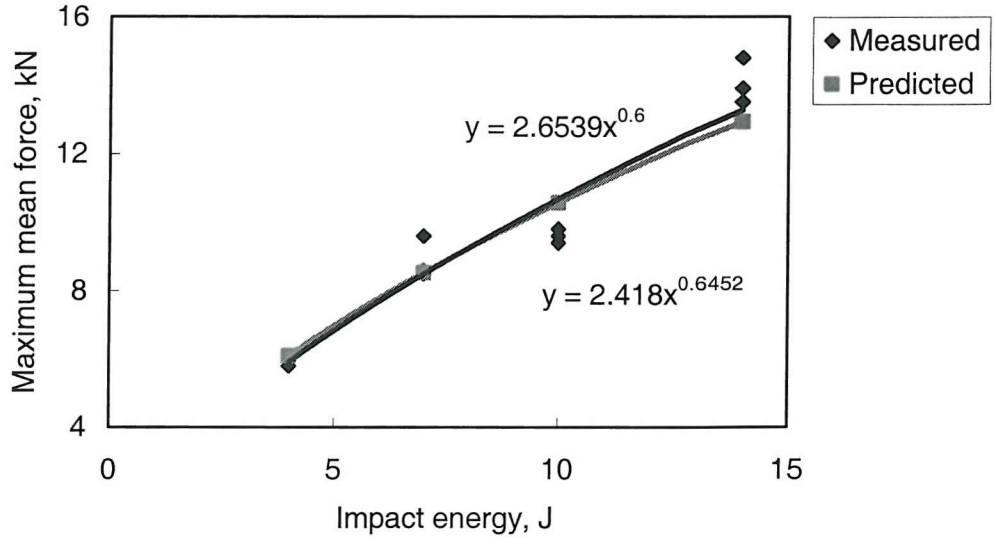

Fig. 6.33 Maximum force as a function of impact energy for the thermoset coating T-15. Note the predicted and measured data can be made to agree if the effective Young's modulus chosen for the coating is approximately 0.8 GPa.

(b) T-34

Figure 6.34 shows the radius of the circumferential cracks as a function of maximum force for the thermoset coating T-34. Little difference in radius is noted between the thin and thick coatings nor for different substrate thickness.

Table 6.13 gives the theoretically predicted contact radius for the thermoset coatings T-34 based on the Hertzian Eqn (6.5).

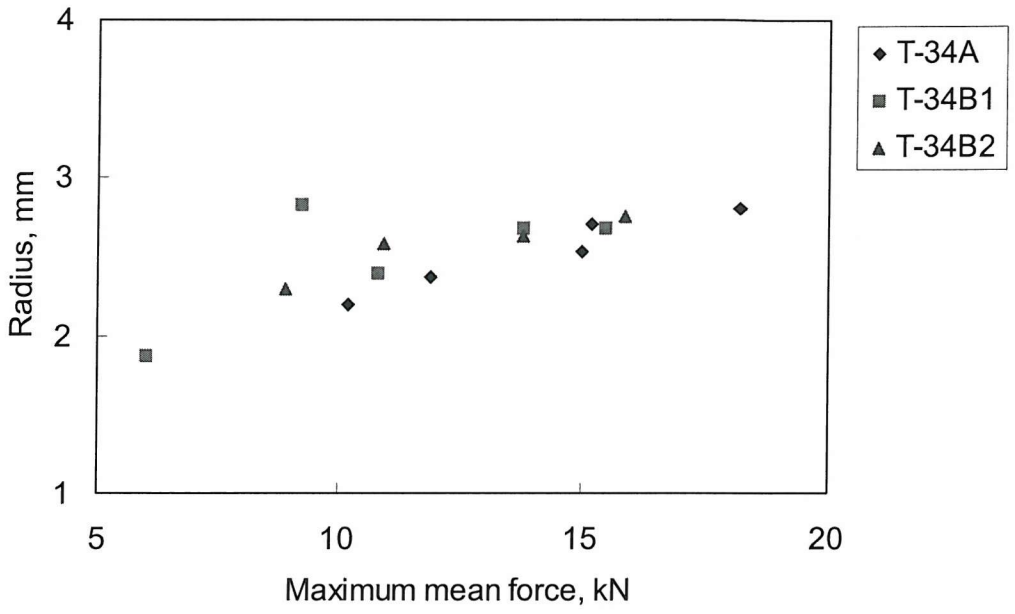

Fig.6.34 Radius of circumferential cracks as a function of maximum mean force for the thermoset coating T-34. Note the little difference in radius between the different coating and substrate thickness.

Table 6.13 Radius of theoretically predicted contact zone on the T-34 coatings (E=7 GPa)

Impact energy, J	Radius of contact zone by Hertzian theory, mm		
	TK35A	T-34B1	T-34B2
4	—	1.57	—
7	1.88	1.81	1.79
10	1.98	1.91	1.92
14	2.14	2.08	2.08
18	2.15	2.16	2.18
22	2.28	—	2.29

Figure 6.35 presents the radius as a function of maximum force for all the data from coating T-34. By choosing a value of 7 GPa for Young's modulus E for the coating, the data can be made to agree with the prediction at the 1.285 times Hertzian's radius. The exponent for the measured data is 0.3 which is similar to the predicted value of 0.33.

Figure 6.36 presents the maximum mean force as a function of impact energy for both measured and predicted force values. The power exponent for the measured data is 0.61 which is very close to the predicted value of 0.6. However, the measured values are approximately 2.2 times smaller than the predicted values. The predicted maximum mean force can be brought into agreement if Young's modulus E is chosen as 0.95 GPa, see Figure 6.37.

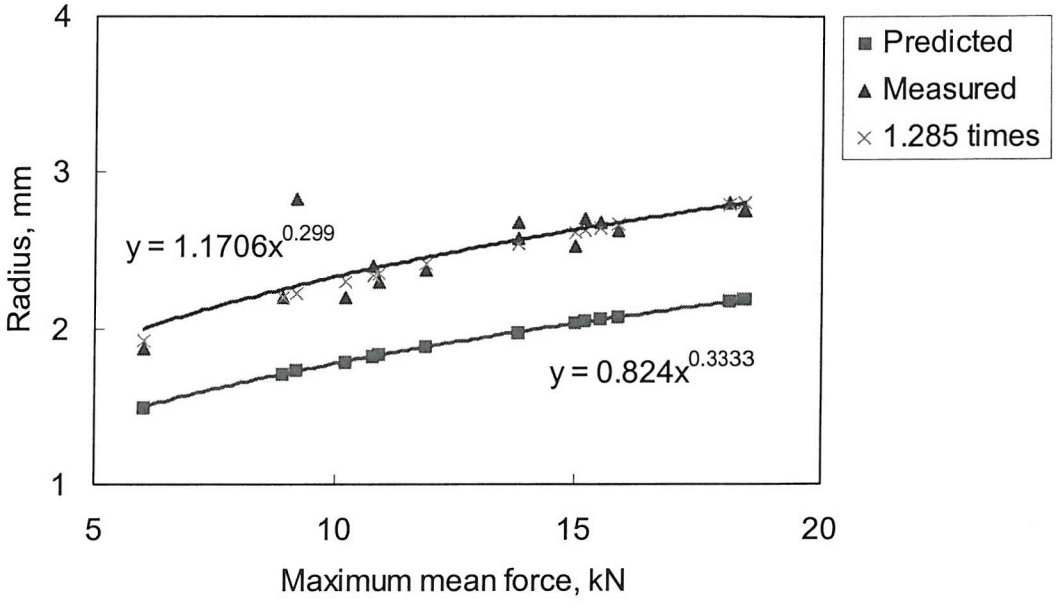

Fig. 6.35 Radius of circumferential cracks as a function of maximum mean force for the thermoset coating T-34. Note the measured data has a similar exponent to the predicted data and the value of 1.285 times Hertz radius is very close to the measured radius (E = 7 GPa).

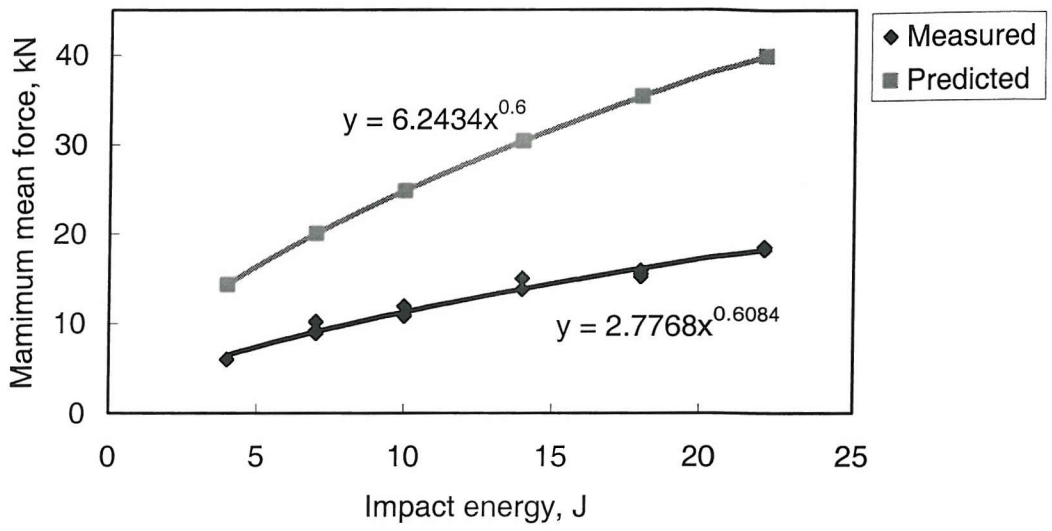

Fig. 6.36 Maximum force as a function of impact energy for the thermoset coating T-34. Note the measured data has a similar exponent to the predicted data, however the predicted value is greater than the measured value (E = 7 GPa).

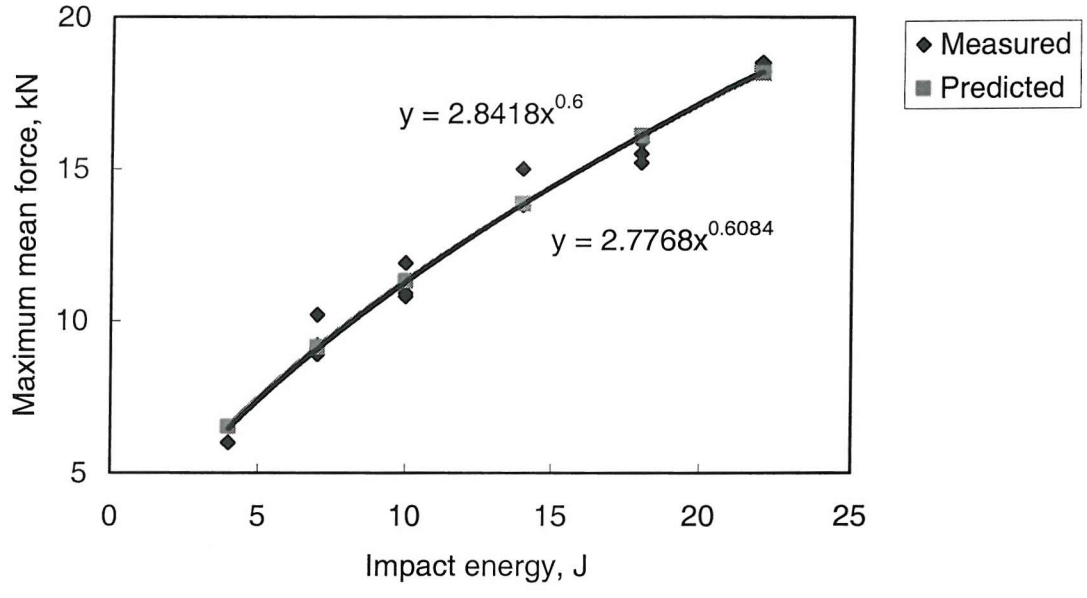

Fig. 6.37 Maximum force as a function of impact energy for the thermoset coating T-34. Note the predicted and measured data can be made to agree if the Young's modulus chosen for the coating is approximately 0.95 GPa.

6.5.3 Comparison between T-15, T-34 and F-4001

Figure 6.38 gives all the data for the thermoset coatings T-15 and T-34 without distinguishing the thickness of coating and substrate. Note that the power line fit for both sets of data is very similar, i.e. exponents for T-15 and T-34 are 0.36 and 0.30 respectively. It is also interesting to note that the values of the radius for a given maximum force are very similar for all the impact tests. This would imply that the "coatings" (or system measured) have a similar value of Young's modulus E. However, as noted in Section 6.5.2 as coating T-34 is filled with approximately twice the filler content as T-15, the two coatings would be expected to have different values of E, with T-34 being higher. This suggests that the fibre efficiency parameter (K in Eqn. (14)) for T-34 is less than that for T-15. This indicates that the alumina particles in T-34 are poorly bonded to the matrix whereas the calcium silicate particles are better bonded to the matrix in T-15. Thus the impact results agree with the wear studies on these two filled polymeric materials (see wear discussion in Section 5.3.2).

Figure 6.39 shows the maximum mean force as a function of impact energy for both coatings T-15 and T-34. Note that the T-34 trend line is only slightly higher than the T-15 trend line. This might imply that T-34 has a slightly higher effective E.

Figure 6.40 shows the maximum mean force as a function of impact energy for all the coatings tested, i.e. T-15, T-34 and F-4001. It is of interest to note that this figure indicates that the maximum mean force for all samples are broadly similar for a given impact energy, being in the ascending order F-4001, T-15 and T-34.

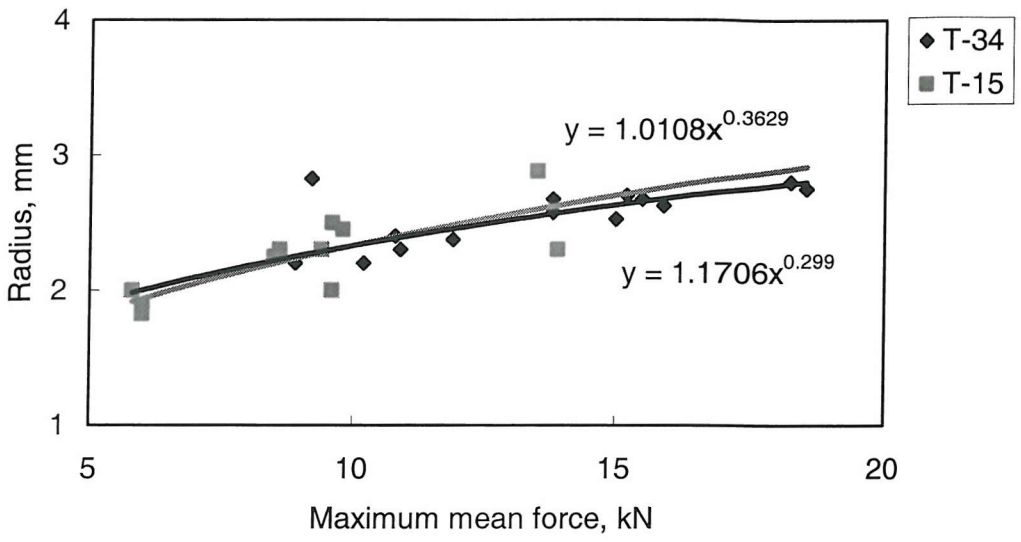

Fig. 6.38 Radius of circumferential cracks as a function of maximum force for the thermoset coatings T-15 and T-34. Note the power line fit for both sets of data are similar and the radius value is similar for the two coatings under a given maximum force.

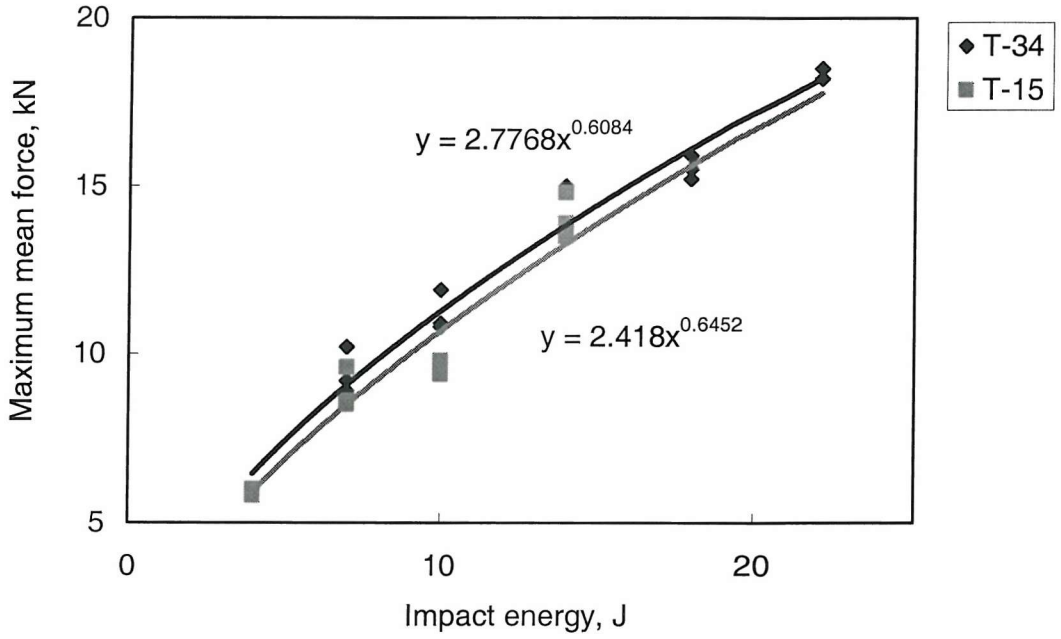

Fig. 6.39 Maximum mean force as a function of impact energy for thermoset coatings T-15 and T-34. Note the values for T-35 are slightly higher than T-15, implying that T-34 has a slightly higher effective E.

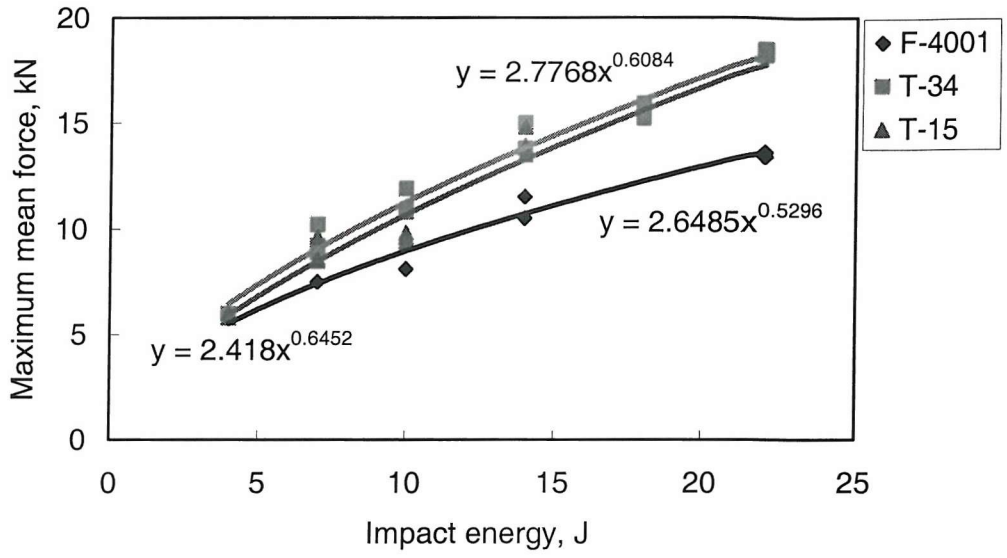

Fig. 6.40 Maximum mean force as a function of impact energy for all the polymeric coating tested. Note that the maximum mean force for all samples are broadly similar for a given impact energy.

6.6 Discussion of Impact Results by Using Wavelet Analysis

As discussed in section 6.4, the high frequency signals present in the impact response were caused by the impact system, i.e. the natural frequency of the sample, impactor or other parts of the impact rig were picked up by the transducer during the impact. Therefore, it is important to investigate further these high frequency signals in the impact test as in the dynamic case, evaluation of the frequency of vibration makes it possible to identify the onset of damage as the sudden change in load gives rise to vibrations in both the sample and the impactor [41, 42]. Thus it seems likely that the major part of the superimposed vibration originates from the signal from damage travelling back and forth in the impactor which can be picked up by the transducer positioned in it. Typically, the classical Fast Fourier Transform (FFT) is utilised to analyse the impact response recorded from an impact event [43]. However, because of the transient, non stationary, nature of the signal, standard frequency (spectral) methods of analysis, such as Fourier, have

inherent problems, because they are unable to provide a view of what happens both in the frequency domain and in the time domain, so that the frequencies obtained by FFT cannot be analysed clearly [44]. The wavelet transform was introduced in order to remedy this [45-47].

Recently, wavelet analysis has been recognised as an effective method for interpreting the raw force signal obtained during instrumented falling weight impact testing [48]. The advantage of using wavelets to analyse the impact response is that information on frequency and time can be obtained simultaneously so that the frequencies due to the equipment, materials and the damage to the materials can be distinguished effectively. Vandergheynst et al. [48] have shown that the time-frequency method allows precise detection of discontinuities in the signal, the moment of rupture, if any, and the frequencies that are excited at impact. It has been suggested that an advantage of the wavelet transform is that it can be used to discriminate between the true impact signal and the signal resulting from equipment vibration since it is reasonable to expect that the frequencies caused by equipment vibration will be present throughout the signal, including parts which are not involved in the impact itself; furthermore, those frequencies will be approximately the same whatever test is performed.

6.6.1 Introduction to the method of wavelet analysis

A wavelet, as its name implies, is a small wave that grows and decays essentially in a limited time period. A wavelet function, $\psi(t)$, has to satisfy two basic properties: (1) the time integral must be zero, i.e.,

$$\int_{-\infty}^{+\infty} \psi(t)dt = 0 \qquad (6.15)$$

and (2) the square of $\psi(t)$ integrated over time is unity:

$$\int_{-\infty}^{+\infty} \psi^2(t)dt = 1 \qquad (6.16)$$

While Eqn. (6.16) implies that $\psi(t)$ has to make excursions away from zero, Eqn. (6.15) indicates that any excursions $\psi(t)$ made above zero must be cancelled out by excursions below zero, so $\psi(t)$ must resemble a wave. Hence, Eqns. (6.15) and (6.16) are conditions that lead to the definition of a 'small wave' or wavelet. The most common of such wavelets result from successive derivatives of a Gaussian function:

$$\psi_{(n)}(t) = \frac{d^n}{dt^n}\exp(\frac{-t^2}{2\sigma^2}) \qquad (6.17)$$

where the width σ can be adjusted in order to get the best resolution. Figure 6.41 shows examples of three common wavelets, the first Gaussian derivative, the second Gaussian derivative ('Mexican hat' wavelet) and the third Gaussian derivative ('Morlet' wavelet).

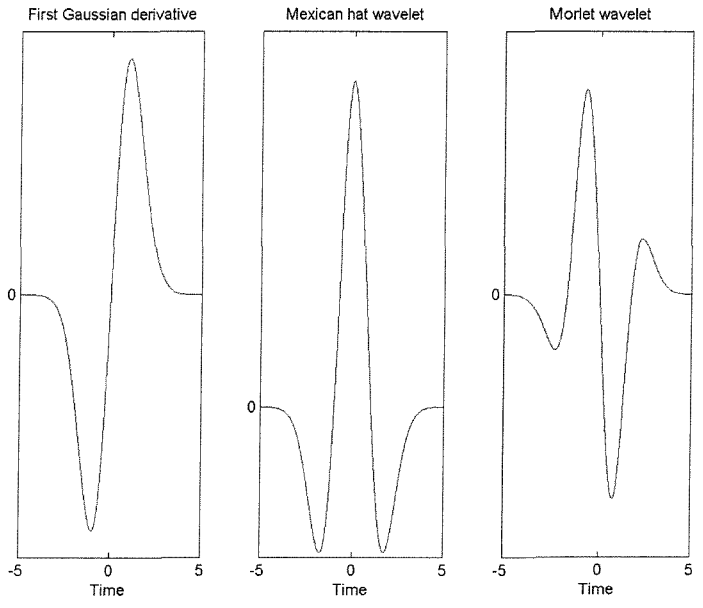

Fig. 6.41 Examples of wavelet derived from the Gaussian function.

The wavelet transform (W_f) of a time series, $f(t)$, can be defined as the convolution of the time series with a scaled and translated version of $\psi(t)$. The generalised form of the wavelet transform is defined by:

$$Wf(u,s) = \int_{-\infty}^{+\infty} f(t) \frac{1}{\sqrt{s}} \psi\left(\frac{t-u}{s}\right) dt \qquad (6.18)$$

The wavelet is centred at u (where $u \in R$), the position parameter, with a scale parameter s ($s > 0$). The scaling parameter compresses or expands the wavelet without changing the number of oscillations (the time span of $\psi(t)$ is different at each scale), while u, shifts the wavelet to a different local region for analysis. When s is increased a set of wavelets is generated that can accommodate a wide range of scales in the signal. By varying the scale and translating along the localised time index, the wavelet transform amplitude reveals any features in $f(t)$ at that scale, s. Small values of the scale parameter provide information on the high-frequency contributions to a time series. Large values of scale provide information on the low-frequency contributions. Wavelet analysis is a time-scale analysis where the scale parameter, s, behaves as the inverse of frequency ($\sim 1/s$).

In the present study, the time series function $f(t)$ is the signal from the impact event. The Morlet wavelet (the third Gaussian derivative) will be used to compute the wavelet transform through the convolution with $f(t)$. It has been demonstrated that Morlet wavelets are well localised in the frequency space and are often used to detect sharp signal transitions [48]. Suppose that ψ is a real wavelet. Since it has a zero average, the wavelet integral of Eqn. (6.18) measures the variation of f in a neighbourhood of u, whose size is proportional to s. When the scale s goes to zero, the decay of the wavelet coefficients characterises the regularity of the impact signal (f) in the neighbourhood of u. This has important applications for detecting transients and analysing fractals [49].

6.6.2 Impact test results analysed by wavelet transform

In this section, the analysis of impact tests on polymeric coating samples by using the wavelet method is reported. Using wavelet analysis, the dominant frequencies during the impact can be discriminated [48] because the wavelet transform provides information on the frequency composition power occurring within a signal, which cannot be achieved by conventional methods such as FFT analysis. Therefore, using wavelet analysis the sources of the dominant frequencies can be evaluated, and ultimately the impact processes and damage mechanisms correlated with the dominant frequencies.

During the impact experiment, raw data were collected by the accelerometer transducer attached to the falling tup. In order to perform the Morlet wavelet, a data length of 4096 ($= 2^{12}$) centred on the original impact event has been extracted from the data recorded for subsequent analysis. The wavelet transform is presented in the form of a contour map where the change of the amplitude of the frequency components is plotted as a function of time; the value of the amplitude (power) is reflected by the different colours within the contour map. An advantage of wavelet analysis is that by decomposing a signal into a frequency-time representation, it allows the determination of the dominant frequencies and how these frequencies vary in time. Dominant frequencies can be distinguished from the highest positions (peaks) of the contour map. In this section, the representative wavelet transforms for each type of the polymeric coating are shown and discussed.

Figures 6.42, 6.43 and 6.44 show the original impact responses and their corresponding wavelet transforms of the impact tests on the polymeric coating samples T-15B1, T-34B1 and F-4001C1 under an impact energy of 7 J, 7 J and 14 J respectively, i.e. for impact tests which did not produce cracks but only plastic indent in the surface.

For each impact test, several dominant frequencies have been found from the wavelet analysis: 3~5 kHz, 6~9 kHz, 13~15 kHz and 17~22 kHz. These dominant frequencies were consistent with the FFT analysis result for the impact test on T-15B1 under an impact energy of 7 J, see Figure 6.15. These dominant frequencies were from the

vibration frequencies (natural frequencies) of the parts of the impact system involved in the impact, which have been excited during the impact. All structures will vibrate/oscillate at their own natural frequencies when sufficient impact energy is applied. The natural frequencies will depend on the geometry of the structure and the material properties, which include density, Young's modulus and Poisson's ratio. For this investigation, how each sample was held within the clamping assembly (boundary condition) also had an influence on the natural frequencies.

From the wavelet transforms of the impact responses, it can be seen that the low frequency component, centred approximately at 7.5 kHz, did not change significantly during impact, suggesting that the part of the impact system causing this frequency remained relatively constant. However, the high frequency component shifted significantly during the impact, indicating that the part of the impact system associated with this has a dynamic influence. The high frequency components increased at the initial contact stage between the impactor and the sample and after reaching the peak value of power decreased as the impact process proceeded. Assuming that all the plastic deformation occurred within the sample for the present tests, it can be concluded that the low frequency components were associated with the natural frequency of the impact tup, and the high frequency components between 13 to 22 kHz were from the test sample. The shift of the high frequencies could be caused by the stress state of the sample. When the impactor hits the sample, the sample will be firstly deformed elastically. This deformation will generate stresses in the sample, and this stress will increase the stiffness of the sample. Therefore, the natural frequency of the sample will increase. Additionally, impact on the sample will induce more constraints to the test system than the relatively loose initial status, increasing the stiffness of the system and the natural frequencies. On the other hand, the contact status between the impactor and the sample and any plastic deformation to the sample could possibly affect the boundary conditions, i.e. the degree of constraint of the sample. The stiffness of the deformed/damaged sample will be less than the original sample, therefore, the natural frequency of the sample will decrease after the sample has been damaged throughout. Consequently, the vibration frequency may

change during the impact period. The shift of the higher frequencies was caused by the deformation or damage of the sample during the impact test.

It was noticed that two distinct parts can be seen in the wavelet transform for the thermoplastic coating F-4001A; there is a gap between the two parts occurring approximately between 7 and 7.3 ms. This was because the power of the frequencies was too small to be measured, indicating the stages of contact loss and re-contact between the impactor and the sample. Because there was a larger plastic deformation for coating F-4001C1, i.e. pile up was produced during the impact, under an impact energy of 14 J, this could cause a temporary loss of contact between the impactor and the sample due to the sudden change of the sample surface, thus producing two separate parts in the wavelet transform.

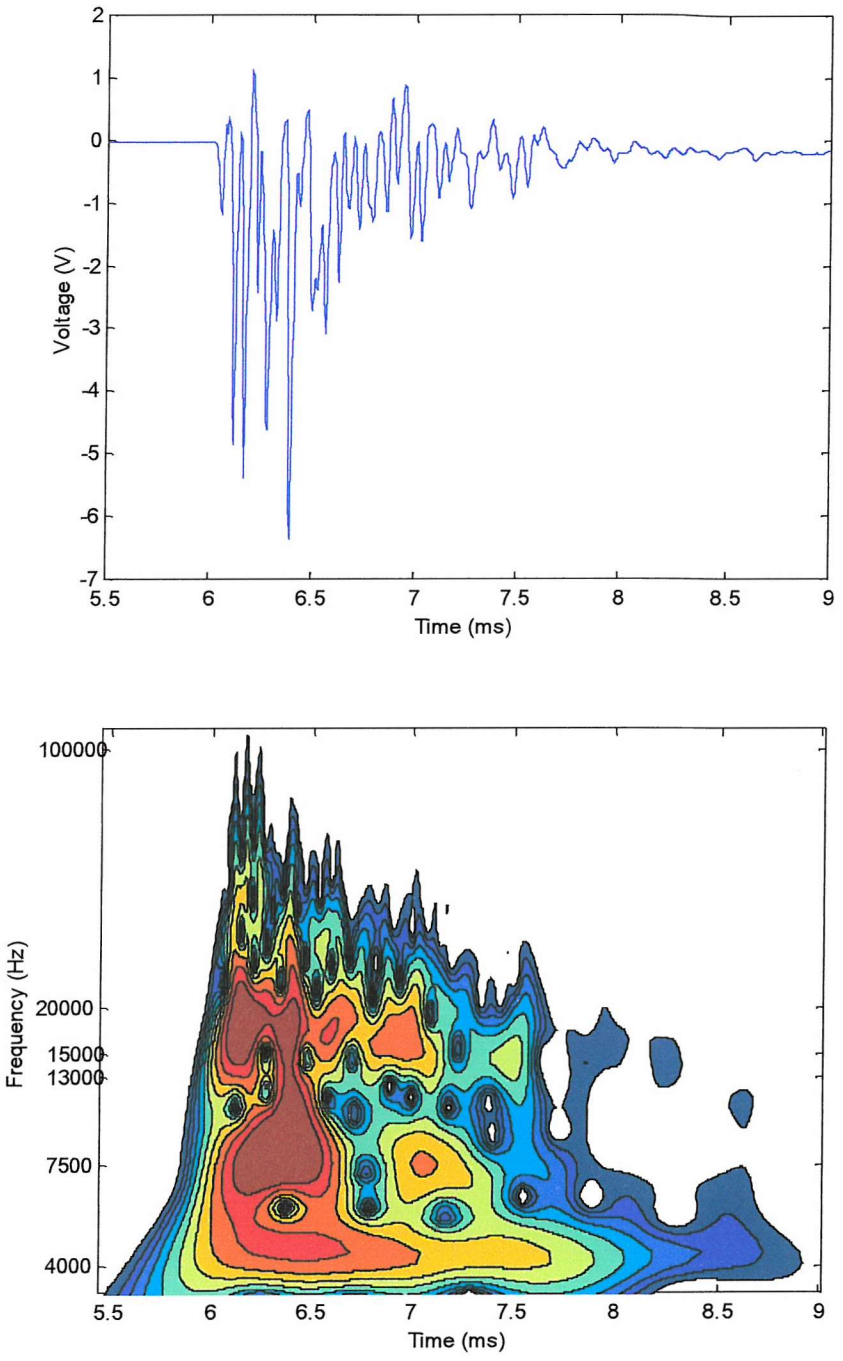

Fig. 6.42 Original impact response and its wavelet analysis result of the impact test carried out on the coating sample T-15B1 under an impact energy of 7 J.

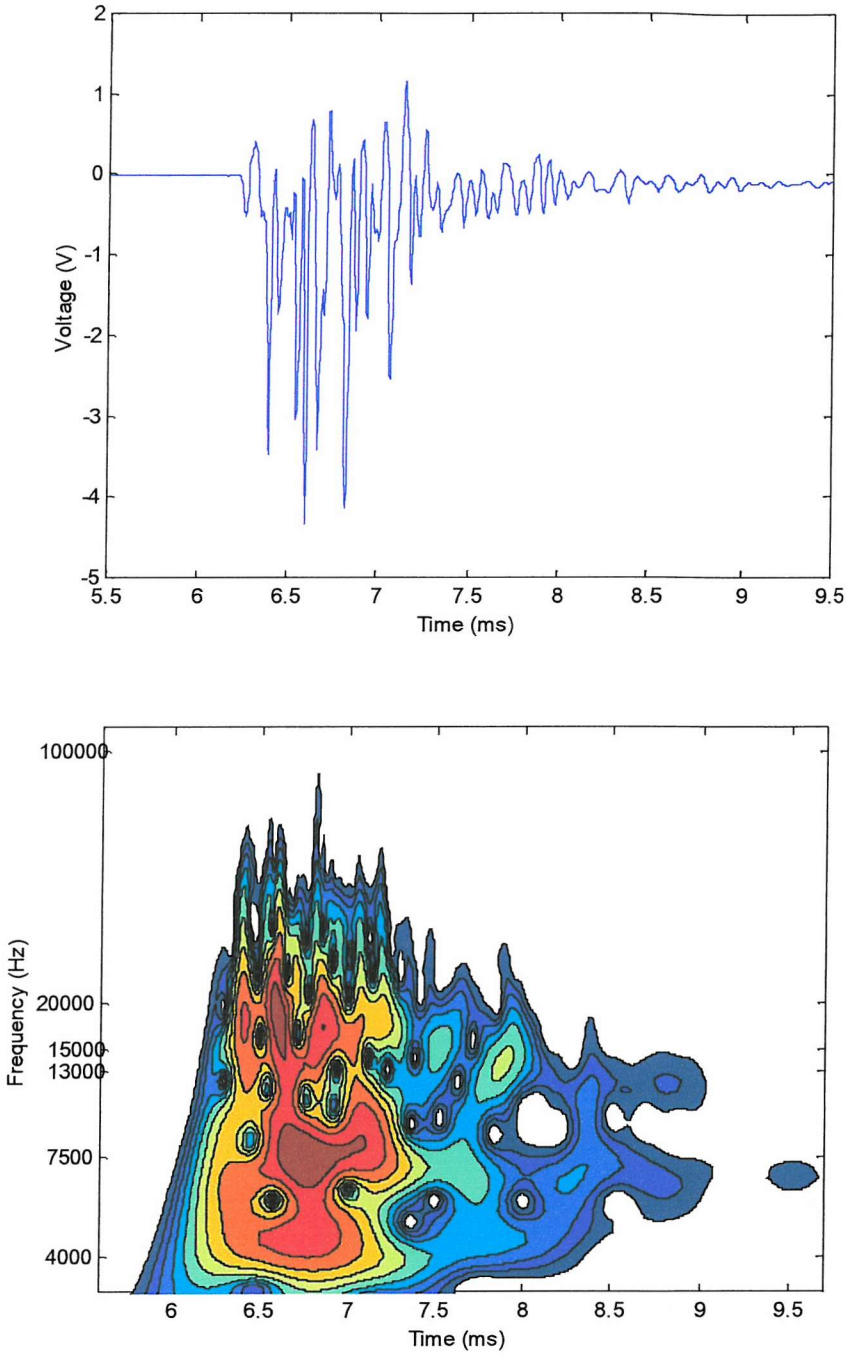

Fig. 6.43 Original impact response and its wavelet analysis result of the impact test carried out on the coating sample T-34B1 under an impact energy of 7 J.

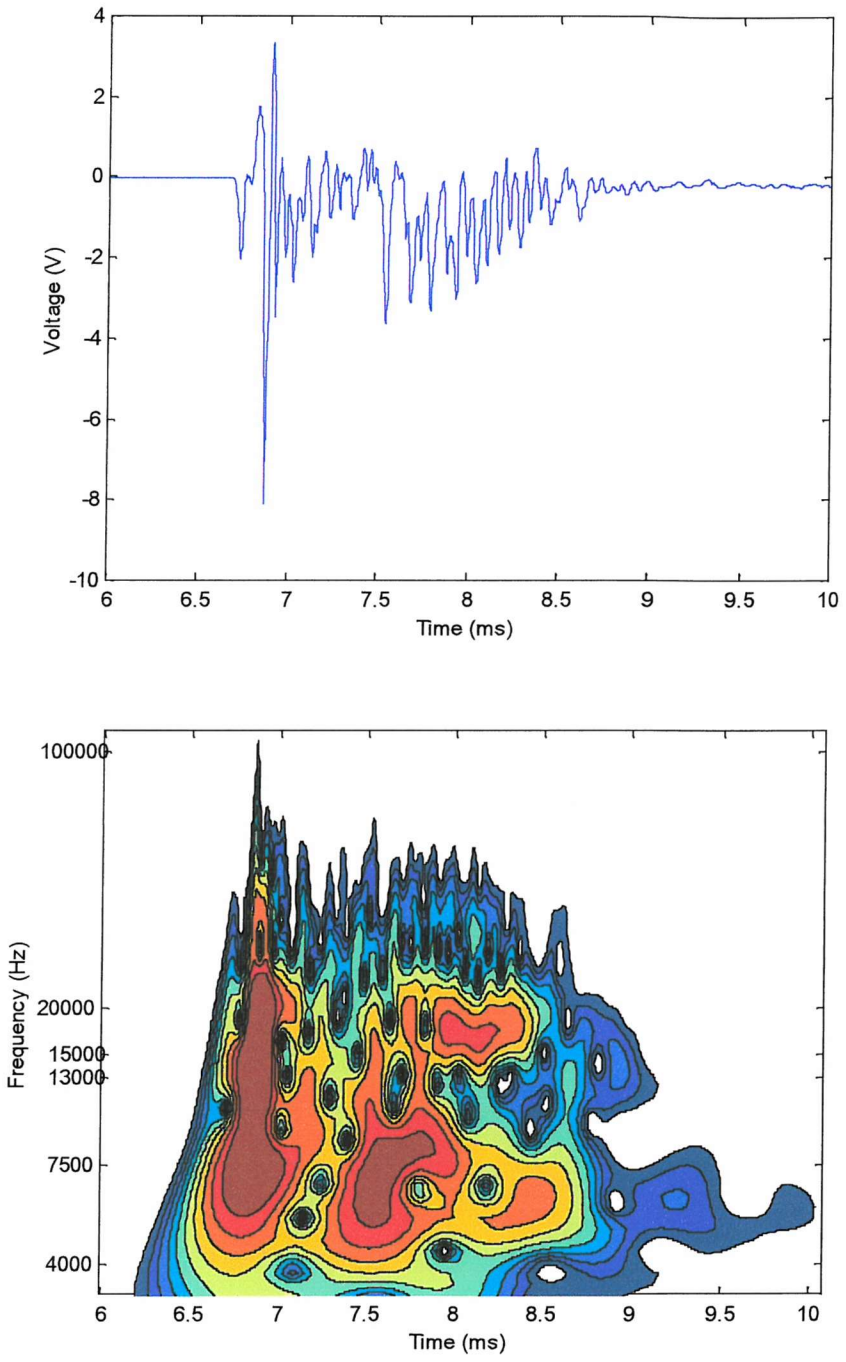

Fig. 6.44 Original impact response and its wavelet analysis result of the impact test carried out on the coating sample F-4001C1 under an impact energy of 14 J.

6.7 Conclusions

Through the above discussion, the following conclusions can be obtained for the present impact tests on the polymeric coatings:

1. Through FFT analysis, dominant frequencies can be distinguished from the original impact response. High frequency signals approximately at 3~5 kHz, 6~10 kHz, 13~19 kHz and 19~25 kHz have been recognised to be associated with the impact system used in the present study. Therefore, during the analysis of the impact results these high frequencies can be removed for ease of analysis.
2. The size of the plastic indent for F-4001 and the radius of the circumferential cracks formed on T-15 and T-34 showed no marked influence of coating thickness nor substrate thickness.
3. The radius of the circumferential cracks formed was considered to be in good agreement with that predicted by the Hertzian approach.
4. The fact that Young's modulii of T-15 and T-34 appear to be similar from Hertzian analysis of impact suggests that the fibre efficiency parameter K for T-34 is less than that for T-15 as T-34 has 2.2 times the filler volume fraction than T-15. This implies that fillers in T-34 are worse bonded to the matrix than the fillers in T-15, which is in a good agreement with the wear studies for the two coatings.
5. Wavelet analysis is an efficient method of decomposing a signal into a frequency-time representation. It allows the dominant frequencies and how these frequencies vary with time to be determined. Through wavelet analysis, the impact processes and the contact status between the impactor and the sample can be distinguished.
6. The variation of dominant frequencies may reflect the contact status between the impactor and any plastic deformation occurring on the sample tested, and thus produce useful information about the impact processes and the damage mechanisms taking place within the sample.

REFERENCES:

[1] N. Symonds, Polymer Coatings for Wireline Wear and Impact Resistance, PhD Thesis, University of Southampton (2001).

[2] A. Bezeredi., G. Voros, and B. Pukanszky, Mechanical Damping in Instrumented Impact Testing, Journal of Materials Science 32 (1997), pp 6601-6608.

[3] P. Zoller, Instrumentation for Impact Testing of Plastics, Polymer Testing 3 (1983), pp 197-208.

[4] J. Fraden, Handbook of Modern Sensors Physics – Design and Applications, American Institute of Physics (1993).

[5] D. N. Keast, Measurement in Mechanical Dynamics, McGraw – Hill (1967).

[6] B. E. Noltingk, Instrumentation Reference Book, Butterworth and Co Ltd (1988).

[7] W. Gopel, J. Hesse and J. N. Zemel, Sensors – A Comprehensive Survey, D-69451, Weinheim (Federal Republic of Germany) (1994).

[8] D. C. Ramsey, Engineering Instrumentation and Control (2^{nd} Edition), Thornes (1984).

[9] Bruel and Kjaer, Piezoelectric Accelerometers and Vibration Preamplifiers – Theory and Application Handbook, K.Larson and Son A/S (1986).

[10] F. Aymerich, P. Marcialis, S. Meili, and P. Priolo, in "Structures Under Shock and Impact IV", eds. N. Jones, C. A. Brebbia and A. J. Watson, An Instrumented Drop Weight Machine for Low Velocity Impact Testing.

[11] G. Zhou, Prediction of Impact Damage Thresholds of Glass Fibre Reinforced Laminates, Composite Structures 31 (1995), pp185-195.

[12] S. M. Lee, and P. Zahuta, Instrumented Impact and Static Indentation of Composites, Journal of Composite Materials 25 (1991), pp 204-211.

[13] N. Banthia, S. Mindess, A. Bentur and M. Pigeon, Impact Testing of Concrete Using a Drop-Weight Impact Machine, Experimental Mechanics 29 (1988), pp 63-74.

[14] J. D. Winkel, and D. F. Adams, Instrumented Drop Weight Impact Testing of Cross-Ply and Fabric Composites, Composites 16, No. 4 (1985), pp 268-280.

[15] "Operating Instructions – Charge Amplifier 5001", Kistler.

[16] V. M. Malhotra, and N. J. Carino, CRC Handbook on Non-Destructive Testing of Concrete, CRC Press (1991), pp 275-304.

[17] Moon-Saeng Kim, Hyung-Seop Shin, Hyeon-Chul Lee, The effect of back plate materials on perfect cone formation in impact-loaded soda-lime glass, International Journal of Impact Engineering 28 (2003), pp 281-290.

[18] Y.B. Zhao, G.W.Wei, Y. Xiang, Discrete singular convolution for the prediction of high frequency vibration of plates, International Journal of Solids and Structures 39 (2002), pp 65-88.

[19] J. F. Kalthoff, On the Validity of Impact Energies Measured With Polymeric Specimens in Instrumented Impact Tests, Impact and Dynamic Fracture of Polymers and Composites, ESIS 19 (1995), pp 21-31.

[20] P. Vandergheynst, J.-P. Antonine, E.Van Vyve, A. Goldberg, I. Doghri, Modeling and Simulation of an Impact Test Using Wavelets, Analytical Solutions and Finite Elements, International Journal of Solids and Structures, Vol. 38 (2001), pp 5481-5508.

[21] B. Jonsson and S. Hogmark, Hardness measurements of thin films, Thin Solid Film, 114, 257 (1984), pp 257-269.

[22] P. J. Burnett and D. S. Rickerby, The mechanical properties of wear-resistant coatings : I: Modelling of hardness behaviour, Thin Solid Film, 148, 41 (1987), pp 41-50.

[23] A. K. Bhattacharya and W. D. Nix, J., Analysis of elastic and plastic deformation associated with indentation testing of thin films on substrates, International Journal of Solids and Structures, 24, 1287 (1988), pp 1287-1298.

[24] J. E. Ritter, D. R. Siou and T. J. Lardner, Indentation Behavior of Polymer Coatings on Glass, Polymer Engineering and Science, Vo. 32 No. 18 (1992), 1366-1371.

[25] R. Warren, Measurement of the Fracture Properties of Brittle Solids by Hertizan Indentation, Acta Metallurgica, Vol. 26 (1978), 1759-1769.

[26] Y. Lu and D. M. Shinozaki, Microindentation Induced Debonding of Polymer Thin Films From Rigid Substrates, Journal of Materials Science 37 (2002), pp 1283-1293.

[27] M.T. Huber, The theory of rigid contact between elastic bodies, Am. Physik 14, Vol. 153 (1904).

[28] B. Lawn and R. Wilshaw, Microfracture beneath point indentations in brittle solids, Journal of Material Science, Vol. 10 (1975), pp 113-122.

[29] K. L. Johnson, J. J. O'Connor and A. C. Woodward, The effect of the indenter elasticity on the Hertzian fracture of brittle material, Proc. R. Soc. Lond. A 334 (1973), 95.

[30] A. G. Evans and T. R. Wilshaw, Quasi-static solid particle damage in brittle solids– –I. Observations analysis and implications, Acta Metallurgica, 24 (1976), pp 939-956.

[31] A. Abdul-Baqi and E. Van der Giessen, Numerical Analysis of Indentation-induced Cracking of Brittle Coatings on Ductile Substrates, International Journal of Solids & Structures, 39 (2002), pp 1427-1442.

[32] J. Persson, K. Breder, D. J. Rowcliffe, Loading Rate Effects During Indentation and Impact on Glass with Small Spheres, Journal of Materials Science 28 (1993), pp 6484-6489

[33] M. M. Chaudhri and E. H. Yoffe. The Area of Contact Between a Small Sphere and a Flat Surface, Philosophical Magazine A-Physics of Condensed Matter Structure Defects and Mechanical Properties, 44 (3) (1981), pp 667-675.

[34] K. L. Johnson, 100 Years of Hertz Contact, Proceedings of the Institution of Mechanical Engineers, 196 Dec (1982), pp 363-378.

[35] C. G. Knight, M. V. Swain & and M. M. Chaudhri, Impact of Small Steel Spheres on Glass Surface, Journal of Materials Science 12 (1977), pp 1573-1586.

[36] MatWeb Materials Property Database, The Online Materials Information Resource.

[37] BS EN ISO 6506-1:1999 Metallic Materials Brinell hardness test method.

[38] D. Tabor, The Hardness of Metals, Clarendon Press, Oxford (1951), pp 178

[39] Dictionary of Ceramic Science and Engineering, 2nd Edition, Ian J. McColm, Plenum Press (1994).

[40] I. M. Hutchings, Tribology – Friction and Wear of Engineering Materials, Edward Arnold (1992).

[41] O. Peter Sjoblom and J. Timothy Hartness, On Low-Velocity Impact Testing of Composite Materials, Journal of Composite Materials, Vol. 22 (1988), pp 30-52.

[42] S.M. Lee and P. Zahuta, Instrumented Impact and Static Indentation of Composites, Journal of Composite Materials, Vol. 25 (1991), pp 204-222.

[43] P. J. Cain, Digital Filtering of Impact Data, Instrumented Impact Testing of Plastics and Composites, ASTM STP 936 (1987), pp 81-102.

[44] P. Abry, P. Goncalves, P. Flandrin, in: Wavelets and Statistics, Springer Lecture Notes in Statistics, Vol. 103 (1995), pp 15.

[45] P. Goupillaud, A. Grossman, J. Morlet, Cycle-Octave and Related Transforms in Seismic Signal Analysis, Geoexploration, 23 (1) (1984), pp 85-102.

[46] A. Grossman, J. Morlet, SIAM (Soc. Ind. Appl. Math.) Journal of Mathematical Analysis and Applications, 15 (1984), pp 723-732.

[47] L. Streit (Ed.), Mathematics and Physics, Lectures on Recent Results, World Scientific, Singapore (1985).

[48] P. Vandergheynst, J. P. Antoine, E. Van Vyve, A. Goldberg and I. Doghri, Modeling and Simulation of an Impact Test Using Wavelets Analytical Solutions and Finite Elements, International Journal of Solids and Structures, 38 (2001), pp 5481-5508.

[49] S. Mallat, A Wavelet Tour of Signal Processing, Academic Press (1999), pp 79-80.

CHAPTER 7 APPLICATION OF ACOUSTIC EMISSION TO DETECT DAMAGE MECHANISMS IN POLYMERIC COATINGS

Microstructural information on the polymeric coatings used in this research work has been investigated through the use of SEM images and introduced in Chapter 3. Likewise, it is important to understand the mechanical characteristics of these coatings. It is known that the mechanical properties of a particulate filled polymeric coating are dependent on not only the material characteristics of the constituents of the coating but also on its microstructural characteristics, such as the bond strength between the different phases present. To understand the performance of the polymeric coatings in wear or impact tests it is important that the influence of microstructural characteristics on mechanical properties is fully understood. In this chapter the mechanical properties of the polymeric coatings will be studied using the experimental technique of Acoustic Emission (AE) applied to Four Point Bend tests.

7.1 Principles of Acoustic Emission

Recently, the field of acoustic emission has grown rapidly. Evidence for this can be found in the rapid growth of references relating to AE and the number of companies that are selling commercial AE equipment [1].

Acoustic emission can be defined as transient elastic stress waves, generated at a source by the rapid release of strain energy within a material [2]. The terms "acoustic emission" and "acoustic emission signal" are often used interchangeably. Strictly speaking, an acoustic emission is an acoustic wave generated by a material and an acoustic emission signal is the electrical signal produced by a sensor in response to this wave. Acoustic emission instrumentation analyses the signal, and from this attempts are made to deduce what microscopic events generated the acoustic signal. The characteristics of the signal are determined by the mechanism which generates the emission, the means by which it travels through the material and the sensor which transforms the emission into the signal.

Acoustic emission can be generated by a large number of mechanisms. Some of these are: fracture of crystallites; micro-crack initiation and growth; several mechanisms involving dislocations; fracture of inclusions in a material; phase transformations in solids; plastic deformation; and electrical discharge [3]. Unfortunately, as any combination of these source mechanisms may be active at any time, the interpretation of AE signals can be difficult [2].

7.2 Reasons for Using AE for Composite Materials

Composite materials generally exhibit a variety of failure modes including matrix cracking, debonding, fibre breakage resulting from the statistical distribution of fibre strength, delamination, and void growth [4]. The technique of acoustic emission is ideally suited to study variables with time control and stress dependent damage processes in fibre composites [5]. The reasons that lead to the usefulness of AE data are:

(i) Real-time monitoring of damage processes as a function of changes in other variables (e.g. time and load level);
(ii) High sensitivity (e.g. individual filament fractures, individual filament debonding, as well as matrix cracking and delamination can all be monitored);
(iii) Total volume sensitivity to the regions of the test sample which are stressed; and
(iv) Location of regions in the sample in which damage is accumulating.

7.3 AE Instrumentation

An AE system always consists of a sensor, a preamplifier, postamplifier and signal processors of various kinds. Recently, microprocessor-based systems have become commercially available. These are capable of performing all the standard methods of single channel analysis as well as performing source location for two to eight AE channels. A basic acoustic emission detection system is schematically shown in Figure 7.1.

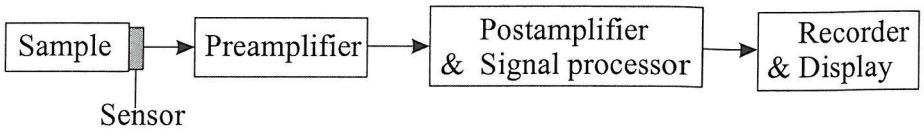

Fig. 7.1 Schematic representation of a basic AE detection system.

A sensor is a device, which generates an electrical signal when it is stimulated by an acoustic wave. An ideal sensor would produce a voltage-time curve identical to the amplitude-time curve of the wave at the point where the sensor is located. The large majority of acoustic emission sensors are piezoelectric transducers.

A preamplifier consists of a low noise input stage, bandpass filters and a low impedance output stage. Acoustic emission preamplifiers are designed to have a relatively flat frequency response between about 20 kHz and 2 MHz, they almost always have a fixed gain of either 40 or 60 dB.

Many systems have variable gain post-amplifiers. This allows the use of signal processors with fixed input ranges or thresholds in conjunction with fixed gain preamplifiers. The total gain of the system is, of course, the sum of the preamplifier and postamplifier gains. Many postamplifiers also have bandpass filters which give an additional noise rejection capability to the system.

Most AE signal processing methods measure the characteristic of the individual burst emission signals. An analogue system will usually present these characteristics either as a running sum or as a sum per unit time. A microprocessor based system can store the measurements in memory for future analysis as well as presenting these same sums in real time.

7.4 Characterisation of AE Signal

When deformation processes occur in a material strain energy is released in the form of vibrations or stress waves; if enough energy is released, audible sounds are produced [1]. In general, an AE event is detected by a piezoelectric transducer when energy is released from localized sources within a material. The output is amplified, and then a threshold voltage is set to screen out the background noise. The separation of AE into continuous and burst emission is a natural result of the appearance of the signals on an oscilloscope [3]. AE burst signals are distinct signals where the beginning and end can be recognised. Common examples include crack growth, particle impact, partial discharge, or other source mechanisms of short duration. Continuous AE are endless with the amplitude and frequency content continuously changing, i.e. flow noise from leaks and rubbing noise. A rapid sequence of overlapping burst signals can also appear as a continuous signal, when the individual signals can no longer be separated.

A continuous emission exists when the signal amplitude is slightly higher than the background noise; therefore, the AE events are closely spaced in time and form a single waveform. A burst emission occurs when the signal amplitudes are appreciably larger than the background: the AE events are of short duration and are well separated in time. For continuous signals, one measures usually the averaged amplitude. A signal conditioner amplifies, rectifies, and averages the high frequency AE-signal over an integration time and by a specific method. The root mean square value (RMS – value) is often used which is the square root of the averaged signal squared. From burst signals one usually extracts a variety of features. These features include arrival time, peak amplitude, rise time, signal duration, counts and energy. Burst emission signals, appearing as individual events, offer more parameters to analyse. The acquisition threshold is the most important criterion for discriminating AE burst signals.

The acoustic emission parameters obtained after analysis of the signal are presented below (Figure 7.2).

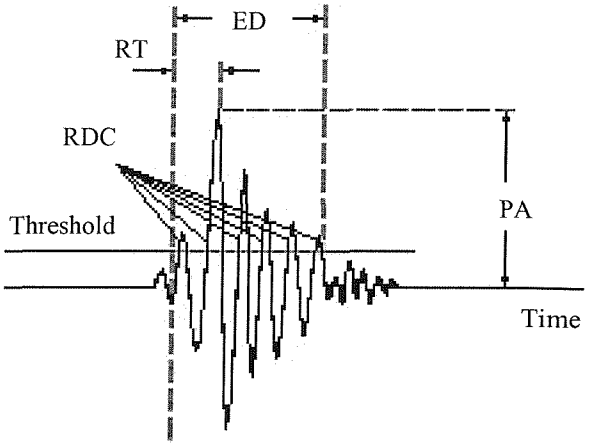

Fig. 7.2 Typical acoustic emissions parameters in an acoustic waveform.

1) TIME – The time that the event occurs, measured to the nearest 100^{th} of a second.
2) RDC – The number of ring down counts of the waveform which crosses the threshold.
3) ED – Event duration, the length of time that the burst emission signal is detectable.
4) PA – Peak signal amplitude, the maximum absolute amplitude of an AE burst.
5) RT – Signal rise time, the time period between the AE signal is first detectable above the noise level and the time when the peak amplitude occurs.

For an AE event, signal amplitude and signal energy are the most useful methods of analysing AE. An AE event is defined as a detected AE burst. The peak signal amplitude is the maximum absolute amplitude of an AE burst. Recently, the analysis of the energy of the system tends to prevail. The energy is the one characteristic of an AE signal that can be unambiguously defined. The definition is given by

$$E = \frac{1}{R}\int_0^T V(t)^2 dt \qquad (7.1)$$

where R is the resistive load for the sensor, $V(t)$ is the time dependent voltage output of the sensor, and T is the integration time. In this definition, it is assumed that there is no noise voltage.

7.5 Model of AE Signals

"In acquiring an understanding of the performance of composite structures, it is essential to accurately describe the processes leading up to crack formation in model composites under stress. To gain this understanding, a number of techniques have been developed for sensing damage to these materials prior to failure. Acoustic emission (AE) is an example of such a technique; it has been used successfully to detect areas of weakness in composite specimens prior to failure." - Dickinson et al.[12]

A model of the AE signal received by a sensor was represented by Buckly et al. [9] as follows:

$$s(t) = e^{-(t-T)/\tau}\left\{\sum_{m=1}^{Q} b_m \cos[\omega_m t + \theta_m]\right\} u(t-T) \qquad (7.2)$$

where $u(t)$ is the step function, b_m, ω_m and θ_m are the amplitude, frequency and phase of the m^{th} received AE signal component, T is the crack-to-receiver wave propagation time, and τ is the characteristic decay time of the material. An important observation for detection purposes is that although b_m and ω_m may be unknown complicated functions of the material geometry, the sensor position and response, crack position, and orientation, the decay factor τ may be simply dictated by the material type [6, 11], and thus may be available as prior information.

The formation of a microcrack in a material specimen is illustrated in Figure 7.3 [9]. The crack generates AE that propagate through the material can be sensed with AE sensors mounted on the specimen surface. AE propagation is generally complex, but direct path propagation to an AE sensor is via bulk waves with characteristic $\frac{1}{r^2}$ propagation loss (where r is distance), and surface Rayleigh waves with $\frac{1}{r}$ propagation loss. An AE sensor may receive bulk and/or Rayleigh waves, depending on its position relative to the

microcrack, and on the material geometry. To receive both wave types, AE sensors should be sensitive to pressure (vertical) and shear (horizontal) displacement. The AE sensors may also receive AE signal energy reflected at boundaries.

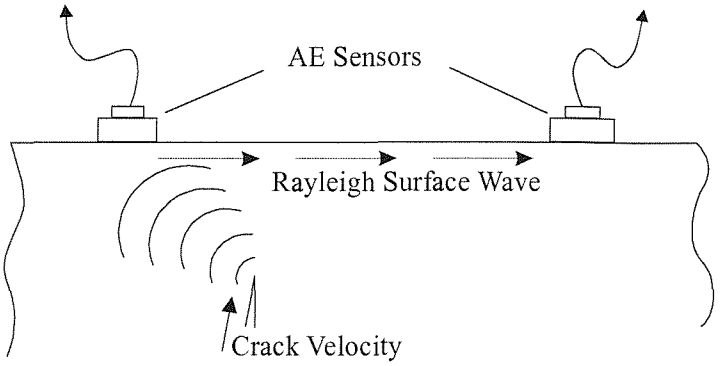

Fig. 7.3 Illustration of microcrack formation, and AE signal propagation and acquisition.

7.6 Correlation of AE Signals and Failure Mechanisms for Composite Materials and Thermal Sprayed Coatings

AE signals have been studied extensively for the characterisation of crack initiation and propagation [6-8]. The technique of acoustic emission is ideally suited to study variables, which control time and stress dependent damage in composites [5]. An early indicator of the onset of material failure due to fatigue and / or stress is the appearance of microcracks. Generation of these cracks creates propagating acoustic signals in the material [9]. There are many investigations studying the correlation of in-situ observation of AE signals with the failure mechanisms of composite materials [10, 12, 13] or thermal spray coatings [15-18].

Hamstad discussed the relation of damage processes to the acoustic emission signal for fibre composites under cyclic load and time under load [5]. Hamstad divided mechanisms in fibre composites, which could generate the acoustic emission, into two broad categories and illustrated that AE may be an important indicator of the presence of a

damage zone in a composite. These two categories are: (a) frictional mechanisms and (b) new damage mechanisms. First, a list of possible frictional mechanisms:

(i) Relative sliding (or pullout) between debonded fibres and surrounding matrix material;
(ii) Friction between matrix crack surface, or between split fibre surfaces;
(iii) Rubbing between delamination surfaces; and
(iv) Other frictional processes between damaged parts of composites that no longer fit together due to damage or permanent deformation.

Second, a list of possible new damage mechanisms:

(i) Fibre fracture and/or splitting;
(ii) Matrix cracking;
(iii) Fibre to matrix debonding;
(iv) Delamination process; and
(v) Fibre and / or matrix plastic deformation.

Dickinson et al. [12] combined measurements of electron emission (EE) with the detection of acoustic emission (AE) during the testing of single graphite fibres, pure epoxy resin and graphite-epoxy composite specimens with various fibre orientations. The AE data obtained for the flexural testing of graphite-epoxy composites was characterised as follows: first, an initial rapid rise from zero due to the initial load applied to the specimen; second, the steady build up of the AE count rate prior to failure; finally, a large burst followed by a drop in AE count rate at catastrophic failure. Further, in the study a variety of failure modes generally emitted by composite materials were distinguished including matrix cracking, debonding, fibre breakage resulting from statistical distribution of fibre strength, delamination, and void growth.

A study carried out by Fang et al. [13] focused on the utilisation of acoustic emission for the identification and characterisation of stresses released and failure modes of

continuous SiC-fibre reinforced titanium matrix composites (TMCs). It was found that AE amplitudes in the matrix are relatively low because of the ductile property of matrix sources and acoustic emission originates primarily from the fibres and their interfaces with the matrix. In addition, AE history records and amplitude distributions, coupled with the stress-strain curves and SEM observations indicate that the fracture mechanisms of SiC-TMC materials consist of debonding, fibre pull out, fibre breakage and matrix cracking.

Acoustic emission was also used by Evans et al. [14] to study the crack mechanism in a particle-associated brittle ceramic (porcelain). In this study, two types of emission have been distinguished. The first type is derived from the slow propagation of the fracture-initiating flaw before catastrophic growth. The emission measured during this process depends on the dimensions of the crack surface generated, so that the emission rate is related primarily to the crack velocity. Another source of emission in composite ceramics such as porcelain is cracking around second-phase particles (quartz particles in porcelain) resulting from the combined action of the applied stress and localised thermal and mechanical stresses. An analysis for predicting emission rates was developed in this study and formed the basis for using acoustic emission in failure prediction.

Mayuram et al. [15] presented a paper concerning the application of AE techniques in assessing the tribological characteristics of sprayed coatings. Effects of operating parameters, identification and interpretation of the AE signals associated with deformation, plastic yielding and cracking / crushing of particle were attempted in this study. Observation of AE from tests conducted on plasma sprayed surfaces subjected to dry adhesion and ploughing indicated a rapid increase in the number of events during the start; afterwards it was steady. The continuous signal without any bursts in the steady stage indicated that the coated surface has undergone steady adhesive wear without any cracking or spalling of the coating. In this study, the stressing of coating material and consequent cracking and spalling have also been identified by a steep increase in events versus time as well an increase in ring down counts.

Bordeaux et al. [18] reported the study of the failure mechanisms of thick plasma-sprayed TiC coatings subjected to severe thermal shocks using AE non-destructive evaluation during and after the thermal shocks. The experimental conditions led to the complete pick-up of the AE signals for acquisition times long enough (up to 3 seconds) for monitoring most of the AE during and after the thermal shocks. In this study, the authors used physical event description in terms of calculating the electrical energy of the AE signal instead of the more classical ring down counting method or maximum-amplitude measurements. AE and microscopic observations showed three main modes of cracking based on two mechanisms: (1) during heating, the temperature gradient induced in the coating by high heating rates led to the bending of the coating and to its delamination unless thermal stresses were released by plastic deformation at high temperatures; (2) during cooling, the remaining plastic deformation on cooling led to biaxial stresses in the coating. Being in competition, segmentation and edge delamination may appear under these conditions to release the stresses.

Arora et al. have investigated characterisation of polymer coatings by Acoustic Emission [21]. In this study, thin polymer coatings of polybutadiene (ductile) and epoxy (brittle) were applied to AISI 1010 steel plates and deformed in tension. During the tests, the specimens with or without the coating were pulled to tension at a rate of 2.8×10^{-3} mm in an Instron machine. The AE was continuously monitored as the specimens were pulled to failure. In the case of steel blanks, very few events were observed during plastic deformation. Polybutadiene coatings showed some activity during plastic deformation as compared to the epoxy coating, which shows a large number of events during plastic yielding. In the case of the polybutadiene coating, the specimen was not taken to fracture, whereas an increase in the event rate for the epoxy coating showed the fracture behaviour to be extremely "noisy" as regards to the AE which was distinguished by an obvious change in the amplitude distribution. In the case of steel blanks, the distribution was unimodal but the AE, due to the failure of coating, involved higher amplitude events, bringing about a bimodal change in the amplitude distribution from unimodal to bimodal. The epoxy coating involved a large number of high amplitude events (up to 80 db), suggesting a more brittle type of failure. Frequency spectral data was also examined for

the above three cases. The results showed the lack of any high frequency data for steel blanks and polybutadiene cases, whereas significant increase of high frequency events has been found for epoxy coating during plastic deformation. Examination of frequency results established the brittle nature of epoxy coating and the signatures of AE obtained from polybutadiene coatings representing ductile failure. Results presented in this study suggested that the AE signatures could be used to characterise polymer coatings; the technique is capable of distinguishing between the deformation behaviour of various coatings; the amplitude distribution plots can provide information on the failure mechanisms involved; the frequency spectral ratio data further assisted in understanding the deformation behaviours of a coating.

7.7 Application of Acoustic Emission to Four Point Bend Test

The technique of acoustic emission has been widely applied to four point bend tests in evaluating the properties of sprayed coatings. Coating strength, adhesion of various interfaces, and fracture mechanisms of coatings have been investigated through analysis of the AE signals. For a thermal spray coating, during service, a crack can release energy and be emitted as acoustic emission events, and these events are detected by a transducer, amplified and exploited in terms of absolute energy, amplitude, hits, etc. [23]. The utilisation of AE has been widely used to improve the understanding of failure mechanisms of the coatings during thermal cycling, and applications have been done to monitor the cracking of specimen in-situ during four point bend tests [24, 25].

Akita et al. investigated microscopic fracture mechanisms of thermal spray coatings under bending stress [26]. In this investigation, bending stress was applied to the samples and the AE properties were measured, and the microscopic fracture process of the coating was analysed by waveform analysis and in-situ crack observation during loading. It was found that cracks were generated from a very low level of applied strain, below 0.1%, in any coating. The strain at which an AE event occurs just corresponds to the start of crack initiation. It has been clarified, through comparison of the crack propagation behaviour and AE properties, that low-amplitude AE events are generated during microcrack

initiation, and high-amplitude AE events are generated during the joining of cracks. Furthermore, it has been found that the coating has high resistance against macrocrack formation if the stress concentration is dispersed by microcrack initiation throughout the entire coating. This high resistance also corresponds to the lowest rate of increase of AE events. It was concluded that it is impossible to completely remove structural defects, such as pores and cracks from coatings, so the formation of microcracks is unavoidable. Therefore, it is important to prevent the generation of macrocracks. Consequently, widely dispersed microcrack formation in the coating is ideal.

Lin et al. [27] studied free-standing alumina-13% titania specimens and AE technology was successfully able to monitor the cracking of samples in-situ during four point bend tests. The characteristics of AE such as peak amplitude and energy were analysed to discriminate between microcracking and macrocracking. The energy and amplitude distributions of AE responses for tests that were performed in either cross-section or in-plane directions did not change significantly. The AE events with high amplitude (>60 dB) and energy (>100 J) could be characterised as macrocracks. The events with lower energy (i.e., energy of <100 J) could be separated into microcracks and transitional cracks, according to the energy distribution. However, the events with lower amplitudes (<60 dB) were difficult to separate into two distinct parts, because these two distributions overlapped. Macrocracking had a tendency to occur with low event activities; i.e., when the total number of events was small, macrocracking usually dominated the cracking mechanism and catastrophic failure occurred. When the total number of events was large, microcracking before failure was commonly observed.

Characterisation of cracking within WC-Co coated materials by an AE method during four point bend tests were investigated by Dalmas et al. [23]. In this study, the failure mechanism of WC-Co coated specimens obtained by the HVOF process (High Velocity Oxy Fuel) was investigated. Two types of cracks were found in the tests: transverse cracks which were regularly spaced on the surface of the coating and interfacial cracks (delamination). Detailed information of these tests was revealed in term of amplitude, hits, absolute energy and position of the event. Load displacement curves were split into

three different zones for all the specimens tested: i) In zone one the behaviour of the composite specimen is elastic and there is no damage and no acoustic emission; ii) In zone two the behaviour of the coating specimen is still elastic, but transverse macrocracks initiate and grow in the coating; iii) In zone three, the specimens behave plastically and delamination starts.

7.8 Four Point Bend Tests with Acoustic Emission Monitoring

In the present study, four point bend tests were carried out on both uncoated mild steel specimens and polymeric coating samples, employing the acoustic emission technique to examine in-situ cracking during the four point bend tests. The test on the uncoated steel specimen was undertaken in order to understand the influence of the steel substrate on the AE measurements. Through the analysis of AE signals, the cracking behaviour of various polymeric coatings will be characterised. The correlation between the different cracking mechanisms of various polymeric coatings and their physical properties and microstructural characteristics will be studied. Finally, the cracking resistance of the polymeric coating will be evaluated.

7.8.1 Specimen preparation

The polymeric coating samples were cut into test pieces 90 mm in length and 18 mm in width in order to be of a suitable size for the four point bend test rig and the AE sensors used. Each of the as-received coating samples had a different steel substrate thickness, thus, in order to make direct comparison between the individual coatings, the steel substrates of all the test coatings were machined to 1.5 mm thick. Therefore, the influence of the steel substrate thickness on the plastic strength of different polymeric coatings is negligible. Subsequently, the size of the blank steel specimen for testing was cut into 90 mm x 18 mm x 1.5 mm.

7.8.2 Experimental rig

A schematic diagram illustrating the four point bend test set-up with the AE sensors is shown in Figure 7.4.

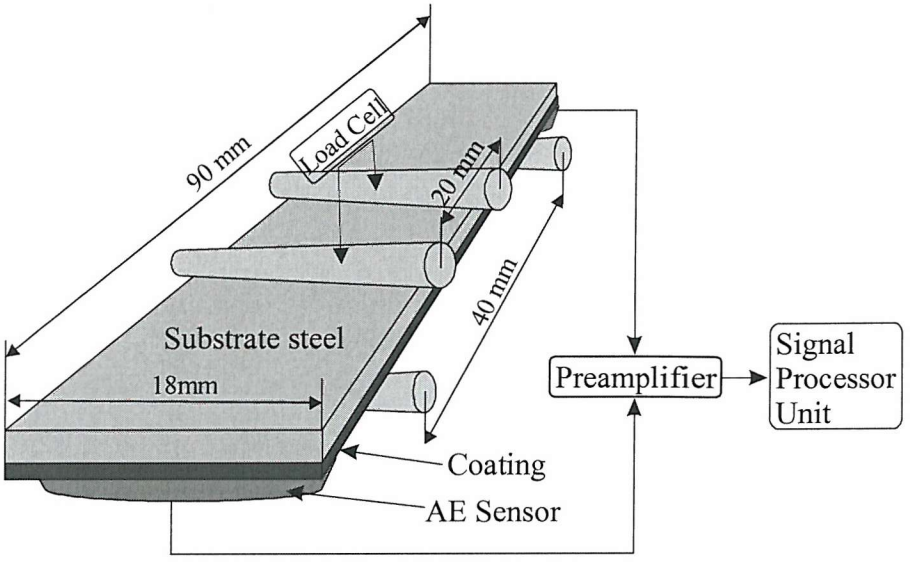

Fig. 7.4 Schematic diagram illustrating the four point bend test and AE.

Four point bend tests were carried out on an Instron 8874 Servohydraulic testing machine. A four point bend test attachment including an aluminum block with two grooves and four ceramic rollers was used to support the specimen and the load cell. The coating was loaded so that it was subjected to tensile stresses. Two ceramic rollers were fitted in the grooves on the aluminum block to support the test specimen and the other two rollers were put on the surface of the steel substrate of the sample to support the load applied from the Instron machine. The inner span length (distance between centres of the two rollers on the steel substrate) was 20 mm and the outer span length (distance between centres of the two rollers supporting the specimen) was 40 mm. The load was applied at a constant crosshead speed of 0.3 mm/min, the distance that the crosshead (load cell of the Instron machine) moved was fixed at 4 mm for all the specimens tested. Vallen AE-Suite equipment with a preamplification of 34 dB was used to monitor the in-situ cracking of the specimen during the four point bend tests.

7.8.3 AE signals recording

Two PZT transducers were mounted on the ends of samples to detect the presence of AE signals generated, see Figure 7.4. As both transducers detect signals originating from the same source, a time lag exists between the detection of the event by each of the two transducers depending on the location of the signal source. The difference between the times of first count over the predefined threshold is used to calculate the location of the signal source. The AE system also consists of a signal processor unit (SPU). Different thresholds were set in the SPU for different specimens in order to obtain the correct AE signals. While the test was being carried out, the signals obtained could be displayed on a monitor. Using the Vallen AE system various presentations of the AE response, such as peak amplitude, event, ringdown counts, and energy, can be illustrated with respect to time, in discrete (i.e. counts per a set time interval) and cumulative forms.

When a four point bend test is in progress, any AE waves generated excite the transducers and are preamplified. The resulting signals are further amplified in the SPU and compared to the threshold value. Therefore, an AE event that is characterised by a rapid rise time, high amplitude, and exponential decay may be defined as any amplified AE signal that crosses the threshold voltage. When a signal crosses the threshold, the event detector is activated; if there is no ringdown counting for a specific time (which is dependent on the system clock parameter setting), the detector deactivates. The event recording will depend on the size of AE events. In summary, the "raw-event" data that is recorded by the AE system includes the time of the event, the ringdown counts, the event duration, the peak amplitude (in decibels), the rise time, and the energy, etc.

7.8.4 Problems from the influence of threshold on measurements

Signals whose peak amplitude is not large enough to cross the threshold are not detected. Setting the threshold too high will prevent potentially important signals from being recorded. Setting the threshold too low will cause the background noise to cross the threshold and will result in a great deal of unwanted data being recorded. If the

background level rises during the test, the signals may remain above the threshold for long times, so that the AE system "sees" only a few especially long hits. In this case, despite a large number of burst signals occurring, only a small amount of data will be produced. Possibly a lot of important information is lost [28].

The optimum threshold setting depends specifically on the amplitude of the AE signals of interest and on the actual noise signals. Further, the signal amplitude depends on many factors, such as sensor sensitivity, the sensor coupling quality, the source energy, the signal attenuation related to distance between source and sensor, changes in wave propagation conditions, and so forth. With the presently available AE systems, the optimum threshold setting is of primary importance and fundamental for the success of every application that makes use of burst emission analysis. Experience is needed to recognise if acquired data is plausible and then conclude a correct threshold setting [28].

7.8.5 Experimental conditions

The specimens tested and the corresponding experimental parameters are listed in Table 7.1.

Table 7.1 The samples tested and main experimental parameters

Sample	Material Generic Information	Coating Thickness (μm)	Crosshead Speed (mm/min)	Threshold Value in SPU (dB)
Blank	Mild Steel	0	0.3	40
T-15A	Thermoset	250 – 270	0.3	52
T-15B	Thermoset	345 – 360	0.3	52
T-34A	Thermoset	135 – 145	0.3	52
T-34B	Thermoset	250 – 260	0.3	52
F-4001A	Thermoplastic	500	0.3	52
F-4001B	Thermoplastic	1000	0.3	45
F-4001C	Thermoplastic	1500	0.3	40

7.9 Experimental Results and Discussion

With the current AE system, the locations of the AE events in the test sample are calculated corresponding to the positions (Channel Positions) of the two PZT transducers which have been entered into the SPU before starting each experiment. The "Channel Positions" were determined by the following procedure: the centre of the first transducer (channel) is set as the zero point and the distance between the centres of the two transducers is set as the position of the second channel. This principle is employed based on the assumption that the AE signals are collected at the centres of the transducers. The value of "Channel Positions" is important, so that the location of the events can be determined by the AE system as described in Section 7.8.3. The relative positions of the PZT transducers and supporting rollers are schematically described in Figure 7.5 based on the size of test specimens and test rig introduced in Sections 7.8.1 and 7.8.2 .

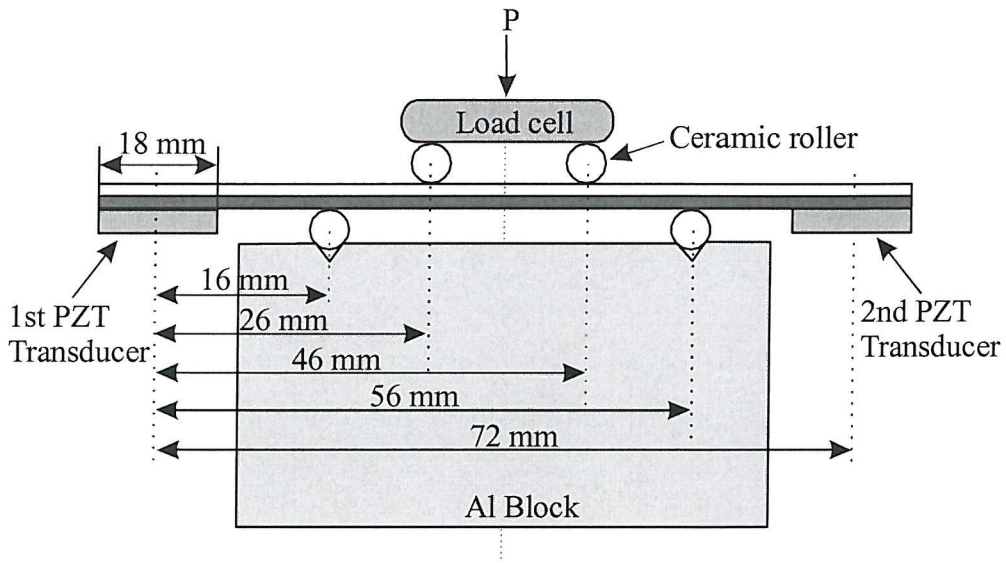

Fig. 7.5 Schematic diagram representing the detailed relative positions of the parts of the test system.

7.9.1 Results for the uncoated mild steel specimen

Initially, an uncoated mild steel specimen was tested under the conditions stated in Section 7.8.5 in order to evaluate the AE signals generated by the substrate material and any background noise processes.

Figure 7.6 shows the results obtained from the four point bend test on the uncoated steel. Figure 7.6 (a), shows the load and total number of AE events versus displacement. Note the minus values of load and displacement recorded by the system representing the compressive load applied on the specimen and the direction of the deformation of the specimen. From the load-displacement curve shown in Figure 7.6 (a), it can be seen that the steel specimen behaved elastically in the initial test period and the load-displacement curve was linear. The yield load of the blank steel specimen can be determined from the upper limit of this linear curve; the yield load for the 1.5 mm blank steel specimen was about 0.43 kN. The first AE event was observed when the specimen deformed plastically, at a load of 0.46 kN. As there is no source for the AE signal to be generated from the solid steel sample, therefore, it can be assumed that all the AE signals collected during the test were caused by the background noise including the friction between different parts of the test rig such as the friction between the ceramic rollers and the specimen or the grooves in the aluminium block. During the elastic behaviour, the applied load on the specimen was low and the deformation of the specimen was small, thus there should be no relative movement between the ceramic rollers and the steel specimen; however, during plastic deformation of the specimen, it is believed that relative movement between the ceramic rollers and the specimen occurs, thus the friction between them may cause noise generating the AE signals.

Figure 7.6 (b) shows the amplitude of AE signals detected in the test and their cumulative energy. All the AE signals were below 52 dB indicating that the level of background noise or the signals generated by friction are below 52 dB. The total cumulative energy measured by the two sensors during the test was approximately 200 eu and 280 eu. It is clear that the cumulative energies were low due to the small number and low amplitude

of the AE signals detected. The different value of cumulative energy measured by the two sensors was caused by attenuation of energy. This difference might arise if the two sensors are located at different distances from the event causing acoustic emission. In addition, minor difference in the manner of attachment of the sensors to the specimen may also cause different attenuation of AE energy. Nevertheless, the cumulative energies detected by both sensors are of the same order.

Figure 7.6 (c) shows the positions of the AE signals located in the test. Comparing this with the schematic diagram of the relative positions of parts shown in Figure 7.5 it can be seen that most of the AE events occurred around the two PZT transducers and a ceramic roller. However, rather than at the exact position of the rollers and the transducers shown in Figure 7.5, only their regions along the specimen can be distinguished. The main reasons for the difference between the theoretical positions and the positions determined shown in Figure 7.5 are:

(i) The initialised input positions of the centres of two PZT transducers measured by the operator might cause a 1 – 2 mm error;
(ii) Theoretically, all the AE signals are collected by the centres of two transducers; however, it is believed that the whole body of the transducer has the ability to pick up the signals. Therefore, the existence of the difference between the real position where the AE event happens and the position located by the system is reasonable;
(iii) The specimen tested in the four point bend test deformed plastically in the experimental procedure. The relative position of the transducers and the rollers shown in Figure 7.5 will alter which can cause an additional difference from the original positions, especially, the rolling movement of the rollers might change its relative position to the surface of the steel specimen;

The above reasons help to explain the existence of a difference between the theoretical positions where the AE signals are actually emitted and the positions given by the AE system. Thus, it is believed that the system can only locate the regions in which the AE event occurs in the test. Based on this conclusion, Figure 7.6 (c) gives effective support

for the previous assumption that the AE signals located during the four point bend test for the uncoated steel specimen were caused by: the background noise picked up by the two transducers directly, and the friction between the ceramic roller and the surface of the steel specimen. The relative amplitude of the AE signals resulting from the background noise or friction has thus been obtained, consequently, the threshold settings for the remaining experiments can be set to avoid unwanted AE events.

Figure 7.6 (b) and (c) effectively provide means of evaluating the AE events caused by background noise or friction in future tests by means of the amplitude or cumulative energies of the AE signals and their positions.

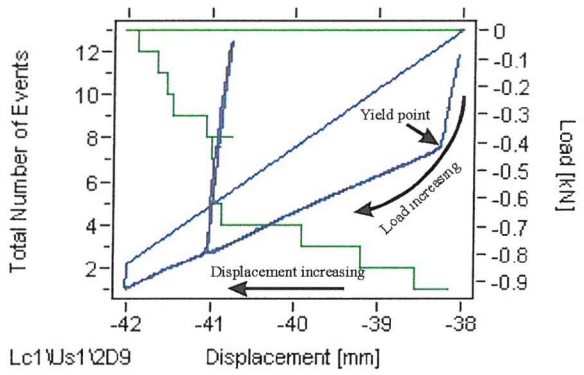

(a) Load and total number of events vs. displacement.

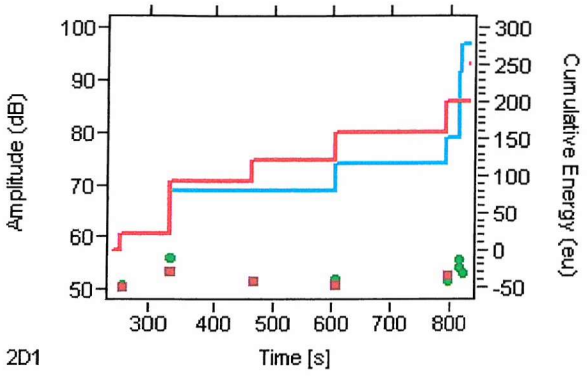

(b) Amplitude and cumulative energy of the AE signals obtained from the steel blank in the test.

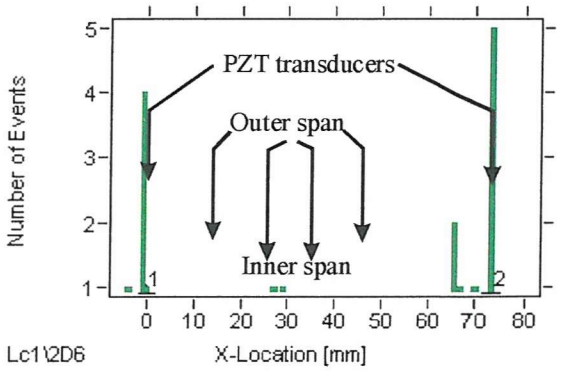

(c) Position distribution of AE signals emitted during the test for the steel blank specimen.

Fig. 7.6 Experimental results obtained from the four point bend test with AE monitoring for the steel blank showing the yield load of the specimen and the amplitude and the positions of the AE signals located.

7.9.2 Results for the thermoset polymeric coatings T-15A and T-15B

Four point bend tests for the thermoset polymeric coatings T15-A and T15-B were carried out using the threshold condition fixed at 52 dB. Figure 7.7 shows the results relating to the AE signals obtained from the tests.

Figures 7.7 (a) and (b) are the traces revealing the relationship between the number of AE events, load and the deformation of the coating samples T15-A and T15-B. From the upper limit of the linear slope of the load-displacement curves in (a) and (b), the yield load of the two coating specimens were determined to be similar at 0.65 kN. Note the yield load of the two samples are almost the same, although the two coatings have different thicknesses of 250-270 μm and 345-360 μm. This suggests that significant differences in thickness of the polymeric coating will not affect the yield load of the coated sample. This will be analysed in more detail later.

Similar to the uncoated steel specimen, no AE events were found before the specimens began to deform plastically. No AE events were observed until a compressive load of 0.93 kN was reached; after this, the number of AE events began to increase, simultaneously there was an apparent relaxation in the applied load (see Figures 7.8 (a) and (b)), which could possibly be associated with the cracking of the coating. Cracking on the surface of the coating releases the strain energy of the coating leading to a redistribution of stress to the steel substrate. In addition, cracking of the coating leads to an effective reduction in I (second moment of area) and for a given displacement this results in a lower load. Visual examinations of both test specimens are helpful to substantiate this conclusion. Figure 7.7 (i) shows the plane surfaces of the polymeric coating samples T15-A and T15-B tested. Two macrocracks are visible on the surface of the coating T15-B, while two macrocracks with three microcracks are evident on the surface of the coating T15-A. The number of cracks on the two specimens, especially the macrocracks, were coincident with the number of the relaxations of load on the load-displacement curves found in Figures 7.7 (a) and (b). This illustrates that the cracking of the coating surface produced the AE signals.

Two differences are evident between coating specimens T-15A and T-15B with respect to their relaxations in load on the load-displacement curves during their plastic deformation. First, the amplitudes of the relaxations between the two types of coated specimens are obviously different. The amplitude of the first relaxation of the coating T15-B was approximately about 0.09 kN (from 0.97 to 0.88 kN), and the second one is about 0.08 kN; whereas, the amplitudes of the first and second relaxations of the coating T15-A were only about 0.015 and 0.022 kN (from 0.92 to 0.9 kN). This was because the thinner coating released less strain energy than the thicker one during cracking, thus the load changed only slightly as there was only a slight change in the overall second moment of area. Second, the intervals between the first two relaxations of the load for the two coatings are different representing different times between the first two cracks. The interval for the T-15A was much shorter than that for the T-15B, this indicates that it took a longer time to produce another crack for the T-15B after the first one because the applied load decreased significantly so that a longer time was required for the load to reach the level which was high enough to produce the next crack.

Figures 7.7 (c) and (d) show the AE amplitudes for the coating samples T15-A and T15-B. The AE signals can be divided into three domains: few signals are found between 85 dB and 95 dB; a number of events occurred from 70 dB to 85 dB; the majority of events occurred between 52 dB and 70 dB. The amplitudes of all the AE events were beyond 52 dB, since the threshold in the AE system has been set to this level in order to filter out the AE signals resulting from the noise or friction. Note that for coating T15-A signals of amplitude 95 dB were measured throughout the test but for coating T15-B signals of this amplitude were only found in the first 1500 s of the test. The cumulative energies of the AE signals detected during the tests are also shown in the figures: at the end of the test these values are approximately 18E4 eu and 21E4 eu for the two sensors in the test for T15-A, and 35E4 eu for the two sensors in the test for T15-B. However, this increase in cumulative energy as the test progresses is not constant, bursts being observed especially for T15-A. The cumulative energies detected in these tests were much larger than those detected for the steel blanks as a much greater number of events with higher amplitude were present. The AE signals can be associated with three possible mechanisms:

initiation of cracks; propagation of cracks; delaminations of the coating from the steel substrate. However, further work is required to distinguish which level of the AE signals corresponds to which mechanism.

Figure 7.7 (e) is the graph of the number of events with respect to their locations for coating sample T-15A; Figure 7.7 (f) is the filtered data from Figure 7.7 (e) (filter condition: 70 dB ≤ Amplitude ≤ 95 dB). It is apparent from Figure 7.7 (f) that most of the high amplitude events were located at positions where the two macrocracks and three microcracks occurred. This indicates that the amplitudes for the initiation of the crack and its propagation fall into the 70 dB and 95 dB region. It is known that the number of the events caused by initiation of the crack should be less than that of propagation of the crack. Therefore, it can be concluded that the amplitude at the initiation of the crack is the highest which is between 85 dB to 95 dB; and the amplitude for the propagation of crack is less than that of the initiation which falls between 70 dB to 85 dB. Furthermore, many signals with lower amplitude distributed close to the positions of the cracks are shown in (e), which may be due to delamination of the coating from the steel substrate. This is in agreement with other authors [15-21]. Nevertheless, there appears to be a number of different mechanisms than those described previously which could result in AE signals. AE signals along the entire body of the specimen could be an evidence of that, see Figure 7.7 (e). This indicates that there must be a number of other sources which emit AE signals during the test as well. Possible sources could be: reflection of the longitudinal waves from the crack sidewall, propagation or delamination mechanisms; the cracking or debonding of the fillers in the coating matrix could also be a source of generating AE signals, this possibility will be investigated in future work; deformation of the coating surface resulting from the two outer ceramic rollers under high load; friction between the roller and the specimen because the applied load was higher than that for the uncoated steel, so the amplitudes of the AE signals caused by the friction could be high enough to cross the threshold.

Similar results for the thick coating sample T-15B were obtained and are shown in Figures 7.7 (g) and (h). Since the only difference between the two specimens was their

different coating thickness the mechanisms causing the AE signals for the two specimens are believed to be the same, thus the same explanation about the mechanisms generating the AE signals on T-15A can be applied to T-15B. High amplitude events, indicating crack initiation, occurred only during the first 1500 s of the test. However, a greater number of AE signals with lower amplitudes close to the macrocracks of the thick coating T-15B were observed and the cumulative energy measured was higher at the end of the test for T15-B than for T15-A. This indicates that the delaminations occurring in the thick coating T-15B were larger than that of the thin coating T-15A. This conclusion can be corroborated from the appearance of the specimens tested shown in Figure 7.7 (j), larger delaminations of the coating can be seen on the surface of T-15B than T-15A. The different size of delamination between thick and thin coating samples was caused by the different shear stress along the boundary between coating and steel substrate. Since the closer to the neutral axis of the sample the higher is the shear stress, for the present test sample structure the boundary line of the thick coating is closer to the neutral axis of the sample than that of the thin coating, therefore a higher shear stress was applied to the boundary between the thicker coating and its steel substrate. Hence, under the same conditions of coating the sample with the thicker coating is more likely to suffer delamination.

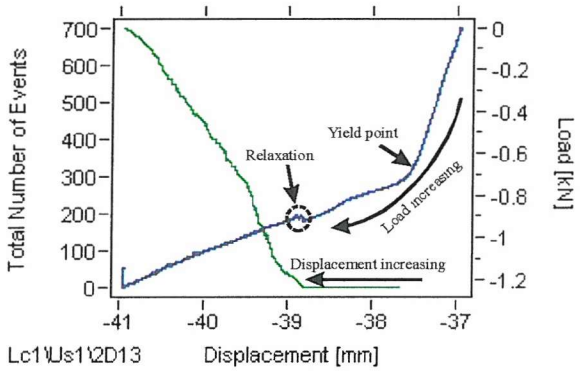

(a) Load and total number of AE events as a function of displacement for sample T-15A.

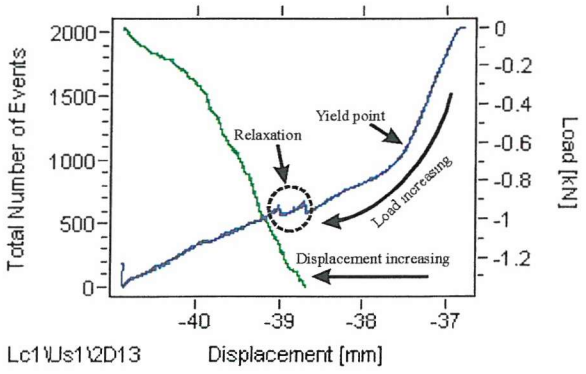

(b) Load and total number of AE events as a function of displacement for sample T-15B.

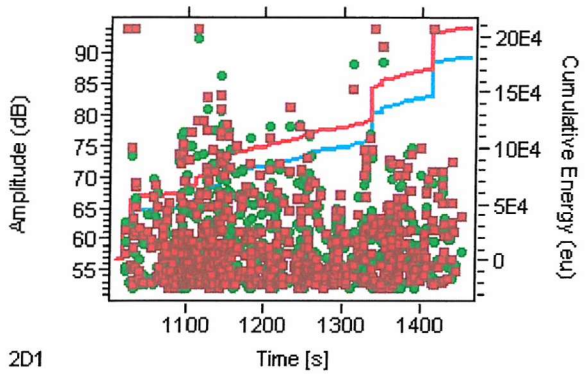

(c) Amplitude distribution and cumulative energy of AE signals for sample T-15A in a four point bend test.

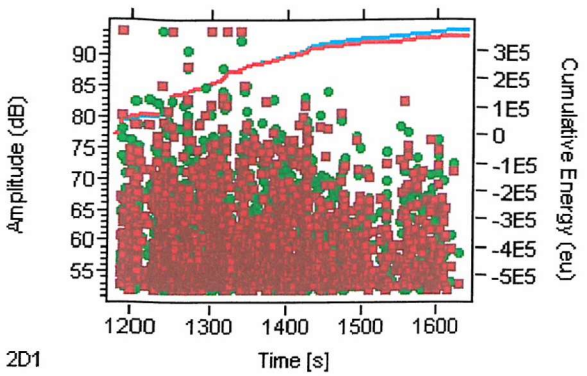

(d) Amplitude distribution and cumulative energy of AE signals for sample T-15B in a four point bend test.

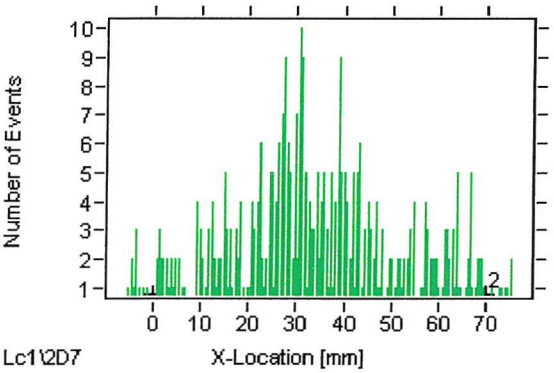

(e) Position distribution of AE signals in a four point bend test for T-15A.

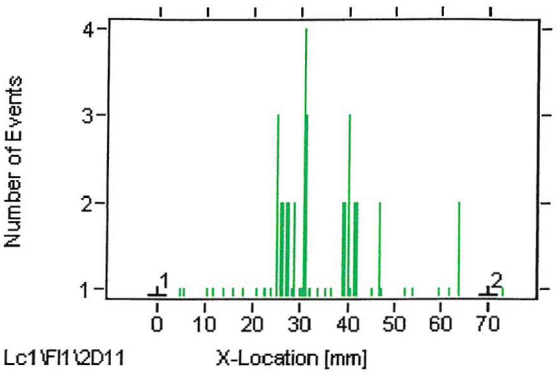

(f) Position distribution of AE signals in a four point bend test for T-15A, with filtering condition 70 dB ≤ Amplitude ≤ 95 dB.

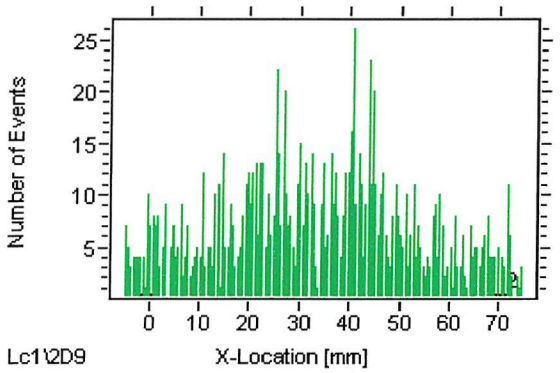

(g) Position distribution of AE signals in a four point bend test for T-15B.

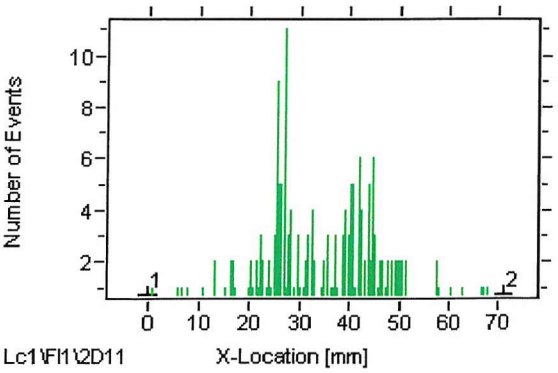

(h) Position distribution of AE signals in a four point bend test for T-15B, with filtering condition 70 dB ≤ Amplitude ≤ 95 dB.

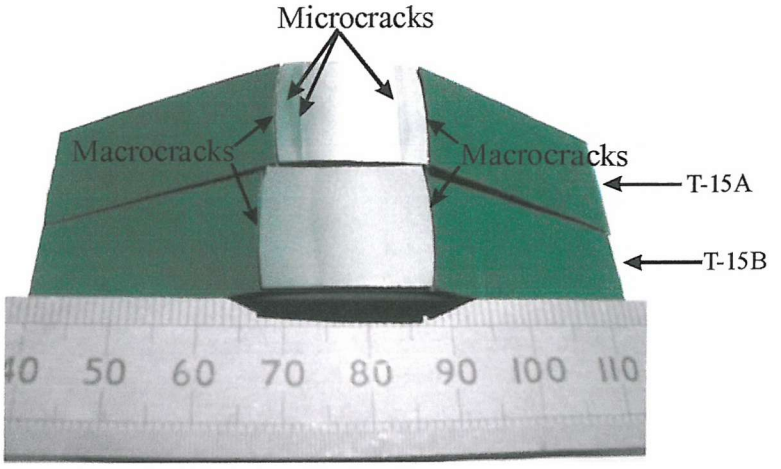

(i) Surface of coating specimens T-15A and T-15B showing two macrocracks on the surface of T-15B and two macrocracks with three microcracks on the surface of T-15A.

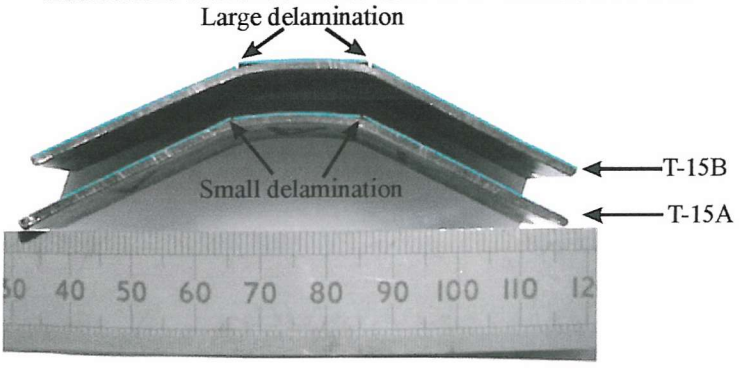

(j) Side view of coating T-15A and T-15B showing the large differences of the size of the delamination between the two coatings.

Fig. 7.7 Experimental results of four point bend tests with AE monitoring for the thermoset coatings T-15A and T-15B.

7.9.3 Results for the thermoset polymeric coatings T-34A and T-34B

Thermoset polymeric coatings T-34A and T-34B with different coating thicknesses of 135-145 μm and 250-260 μm were subjected to the four point bend tests under the same conditions as those for T-15A and T-15B, and the experimental results relating to the AE signals were analysed using the same method and are shown in Figure 7.8. Figures 7.8 (a) to (h) show the results relating to the AE signals for coating samples T-34A and T-34B, while Figures 7.8 (i) and (j) are photographs showing the specimens tested. It can be seen from Figures 7.8 (i) and (j) that there are three macrocracks on the surface of coating T-

34A with many microcracks evenly distributed; while three macrocracks with one microcrack can be found on the surface of coating T-34B. Large delaminations can be seen on the thick coating sample T-34B shown in Figure 7.8 (i), whereas small delaminations can be found close to the macrocracks on the surface of T-34A and no delaminations were evident due to those microcracks.

The yield load of the two coating samples were determined from Figures 7.8 (a) and (b), as 0.65 kN and 0.85 kN for the T-34A and the T-34B, respectively. The thick coating sample T-34B has a higher yield load than the thin coating sample T-34A, this is believed to be partially caused by a factor of two difference in coating thickness. It is also apparent from Figures 7.8 (a) and (b) that AE events began to occur during the elastic deformation process. Since the possibility of AE signals being produced by friction can be excluded because the applied loads were very low during the elastic deformation of the specimen, and no relaxation of the load was observed during the elastic deformation, it can be concluded that the AE signals collected were not from the initiation or propagation of cracks, but most probably were caused by debonding or cracking of the fillers in the coating matrix or primer of the coating T-34x. As Figure 3.10 shows, the bond between the fillers and the coating matrix or primer in the coating T-34x is bad, it can be concluded that debonding between the fillers and matrix or primer must have occurred before the coating T-34x was deformed causing AE signals.

In Figure 7.8 (c), before 2400 seconds the amplitudes of the AE signals emitted from debonding or cracking of the fillers are between 52 dB and 60 dB. This supports the previous explanation in Section 7.9.2 regarding the analysis of the domain of AE signal between 52 dB and 70 dB. Thus, it can be concluded that the amplitude of the AE signals from delamination of the coating from the steel substrate should be around 60 dB to 70 dB.

Comparing Figures 7.8 (c) and (d), more events can be observed between 70 dB and 95 dB for T-34A than for T-34B, which is consistent with the result that there were many microcracks on the surface of T-34A, thus more AE signals were produced by the

initiation and propagation of the cracks. The cumulative energies of the AE signals detected during the tests are also shown in the figures: at the end of the test these values are approximately 28E4 eu and 41E4 eu for the two sensors in the test for T34-A, and 12E4 eu and 13E4 eu for the two sensors in the test for T34-B. Note the higher values of cumulative energy for T34-A, this correlates with the greater number of microcracks seen in this sample.

Figures 7.8 (e) to (h) show the AE signals located vs. their positions for the thermoset coating samples T-34A and T-34B. The same explanations stated previously in Section 7.9.2 for the thermoset coating samples T-15A and T-15B are applicable to T-34A and T-34B. Notably, the signals located for the coating specimen T-34A shown in (f) are regularly distributed; this result is consistent with the phenomenon that the microcracks on surface of the coating T-34A are evenly distributed between the inner span of the supporting rollers, see Figure 7.8 (i).

It is apparent that both macrocracks and microcracks were evident on the surfaces of the thin and thick coatings T-34x, see Figure 7.8 (i) and (j). Notably, large delaminations were found on the thick coating T-34B close to the macrocracks which was similar to that observed for T-15B, whereas tiny delaminations were found on the thin coating T-34A. This phenomenon was consistent with the coating T-15x and the explanation of shear stress distribution between thick and thin samples is applicable to the coatings T-34x as well.

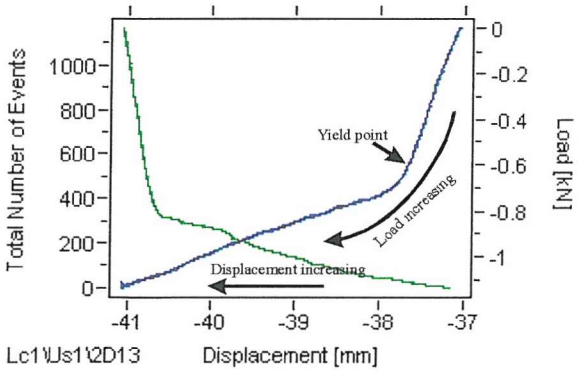

(a) Load and total number of AE events as a function of displacement for sample T-34A.

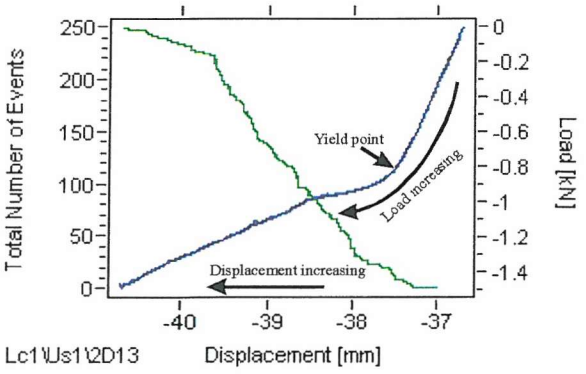

(b) Load and total number of AE events as a function of displacement for sample T-34B.

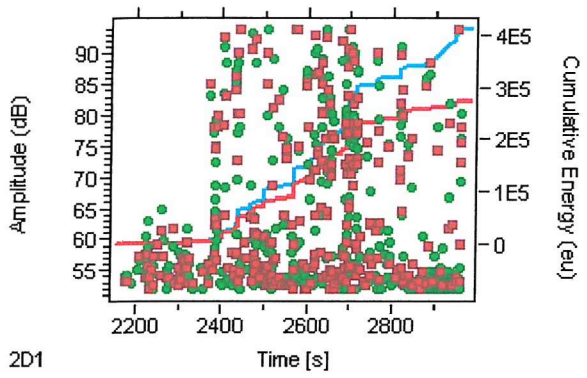

(c) Amplitude distribution and cumulative energy of AE signals for sample T-34A in a four point bend test.

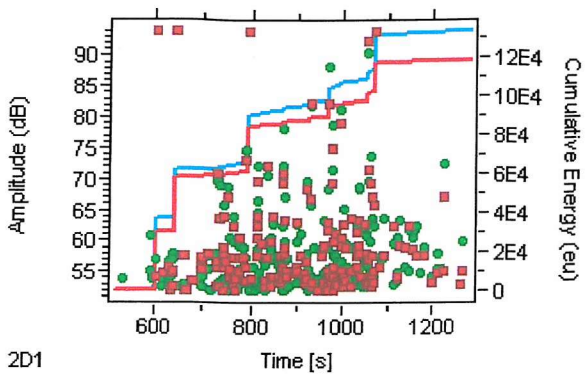

(d) Amplitude distribution and cumulative energy of AE signals for sample T-34B in a four point bend test.

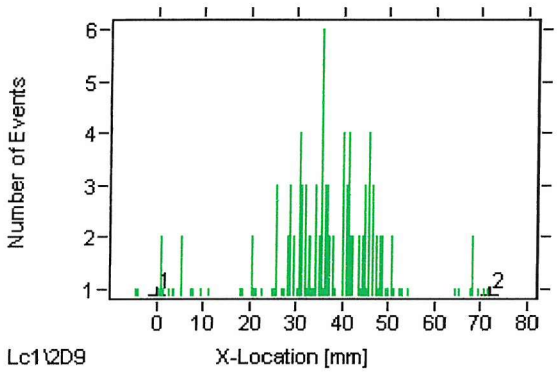

(e) Position distribution of AE signals in a four point bend test for T-34A.

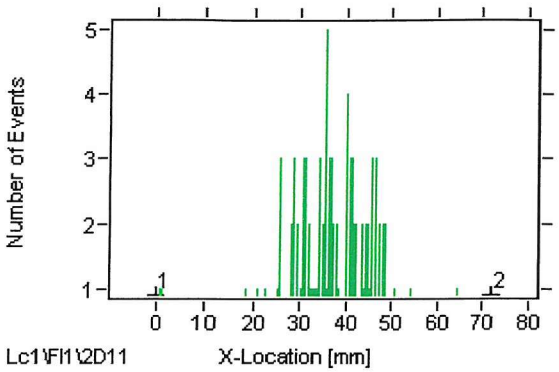

(f) Position distribution of AE signals in a four point bend test for T-34A, with filtering condition 70 dB ≤ Amplitude ≤ 95 dB.

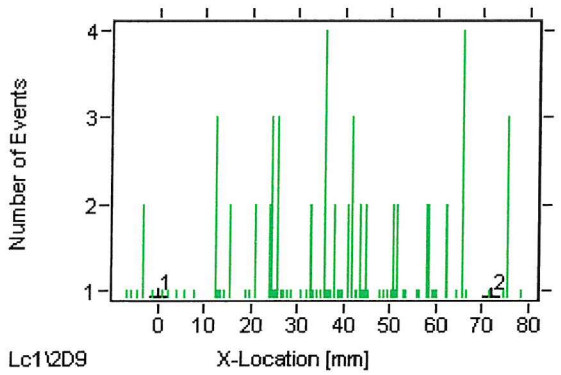

(g) Position distribution of AE signals in a four point bend test for T-34B.

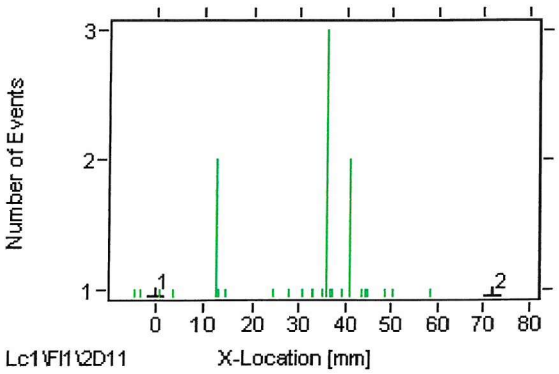

(h) Position distribution of AE signals in a four point bend test for T-34B, with filtering condition 70 dB ≤ Amplitude ≤ 95 dB.

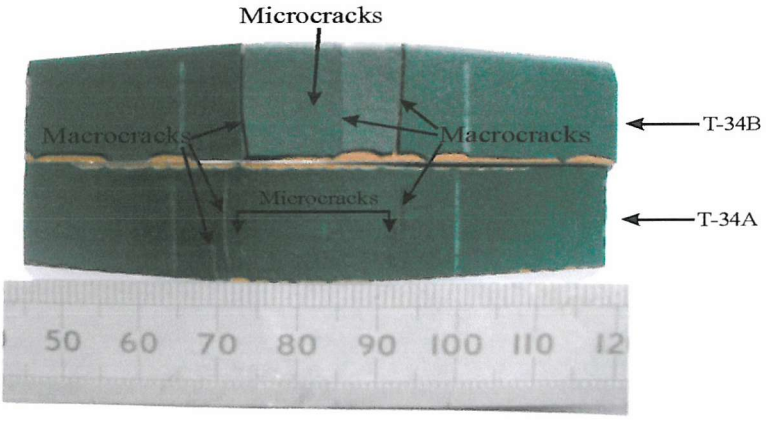

(i) Surface of coating specimens T-34A and T-34B showing three macrocracks and evenly distributed microcracks on the surface of T-34A and three macrocracks with one microcrack on the surface of T-34B.

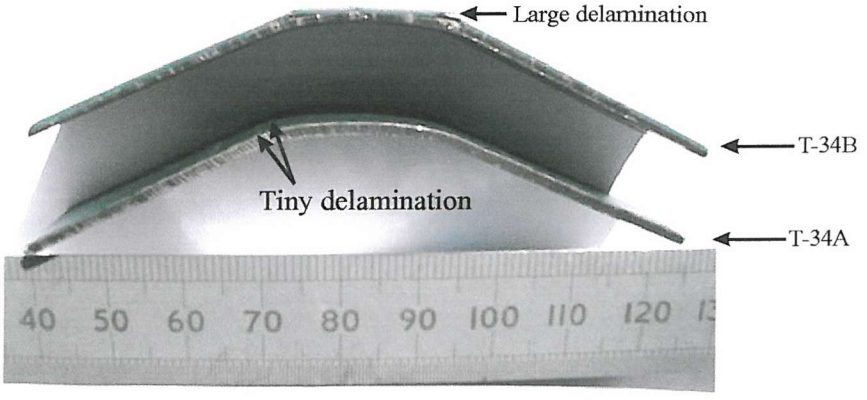

(j) Side view of coating T-34A and T-34B showing the large delaminations of coating T-34B and very tiny delamination on coating T-34A.

Fig. 7.8 Experimental results of four point bend tests with AE monitoring for the thermoset coatings T-34A and T-34B.

7.9.4 Results for the thermoplastic polymeric coatings F-4001A, F-4001B and F-4001C

Samples F-4001x are thermoplastic fluropolymer coatings of various thicknesses (0.5, 1 and 1.5 mm) having fillers embedded in both the coating matrix and primer. The four point bend test for the coating specimen F-4001A was carried out using a threshold of 52 dB which had been used for the thermoset coatings, and the relevant AE signals are shown in Figures 7.9 (a), (d) and (g). Only one located AE signal can be found from the results and this was below 60 dB. Furthermore, the sample tested F-4001A appeared to have no cracks or delaminations on the coating surface, see Figure 7.9 (j) and (k). Thus, it

can be concluded that the only AE signal was from debonding or cracking of filler in the coating, or might be noise. In addition, it was considered that the threshold of 52 dB might be too high for this type of polymeric coating specimens. Therefore, in order to get more AE information, the thresholds of the AE recording system were set at 45 dB and 40 dB for coatings F-4001B and F-4001C, respectively. All the AE signals relating to the thermoplastic coatings of F-4001x were shown in the Figures 7.9 (a) to (k).

Figures 7.9 (a) to (c) show the traces revealing the relationship between the total number of AE events, load and the deformation of the coating samples F-4001A, F-4001B and F-4001C. It is apparent from the figures that the thicker the coating the higher yield load of the specimen; 0.55 kN, 0.75 kN and 0.95 kN for F-4001A, F-4001B, and F-4001C respectively. This again is thought to be partially caused by the greater thicknesses of the coatings. This will be studied in more detail in future work.

Figures 7.9 (d), (e) and (f) show the amplitudes of the AE signals obtained during the testing process for the coatings F-4001x. It can be seen that the amplitudes of all the AE signals obtained were below 60 dB. Based on the experience obtained from analysis of thermoset coatings T-15x and T-34x, this suggests that there should be no initiation or propagation of cracks on the coatings for F-4001x. This was consistent with visual examination of the sample surfaces, see Figure 7.9 (j) and (k). However, SEM examination is necessary to confirm this result as the amplitude of the cracking or propagation of the crack of the thermoplastic coatings might be different to the thermoset coatings because of the different coating matrix. The cumulative energies obtained during the tests are also included in the figures. The cumulative energies detected by the sensors in the tests for the specimens F4001-A and F4001-B are very similar to the cumulative energy shown for the steel blank, indicating there were no cracks in the coating. However, F4001-C where the threshold was set at a low value of 40 dB, showed a considerably higher cumulative energy value, this could be caused by the large number of the AE events detected in this test though the amplitude of these AE signals was low.

Since no macrocracks and microcracks were apparent on the surfaces of the coated specimens, it is less important to investigate the information shown in Figures 7.9 (g) to (i) which relate to the positions of the located signals. However, this information could be helpful in the investigation of the SEM images of the cross sections of the samples tested through which the cracking or debonding of the fillers could be observed. Additionally, no AE signal was above 60 dB, thus the AE signals after being filtered have not been presented.

From Figures 7.9 (a) to (i), it is apparent that the threshold for the thermoplastic coatings F-4001x should be set at 45 dB similar to that for the coating F-4001B; because there were almost no AE events for F-4001A compared with F-4001B, however, too many events were picked up for F-4001C possibly as a result of the inclusion of unwanted noise caused by friction under the applied load. Figure 7.9 (f) shows that one sensor detected a much larger cumulative energy than the other. This supports the above conclusion and indicates unbalanced/non-uniform friction between the two supporting rollers and the specimens.

Figures 7.9 (j) and (k) show the visual examination of thermoplastic coatings F-4001A and F-4001B after testing. As the coating F-4001C appeared to be the same as the other two coating samples it is not shown here. As previously stated, no cracks and delaminations can be seen on the surface of the coatings or from their side views.

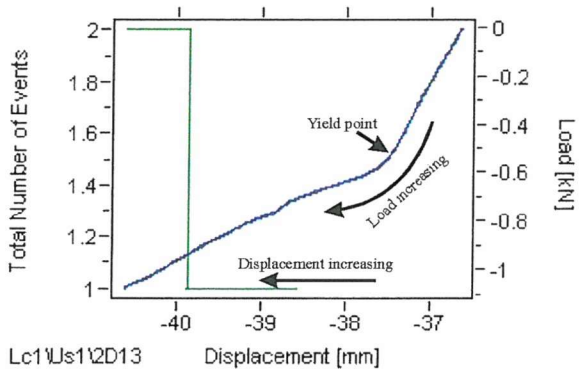

(a) Load and total number of AE events as a function of displacement for sample F-4001A.

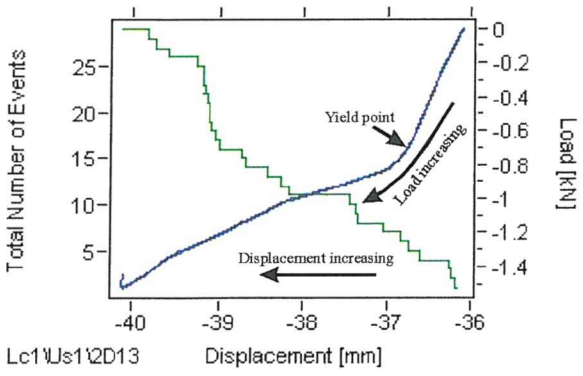

(b) Load and total number of AE events as a function of displacement for sample F-4001B.

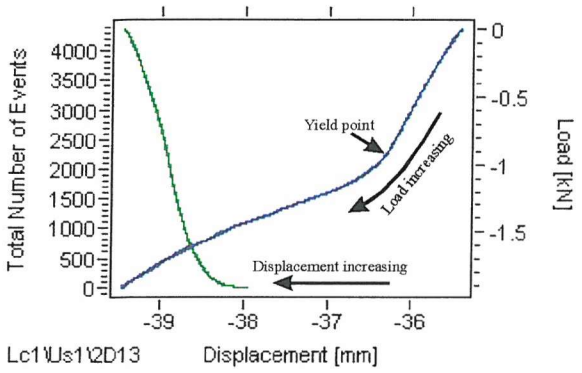

(c) Load and total number of AE events as a function of displacement for sample F-4001C.

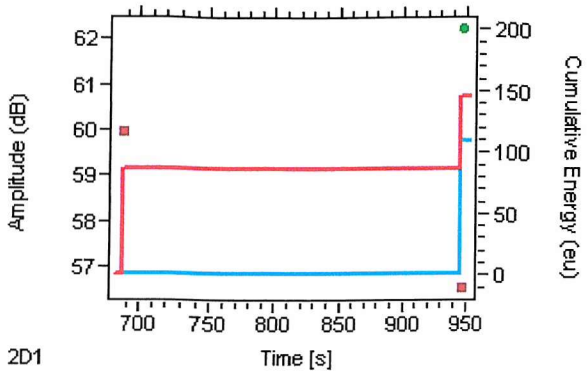

(d) Amplitude distribution and cumulative energy of AE signals for the coating F-4001A in a four point bend test.

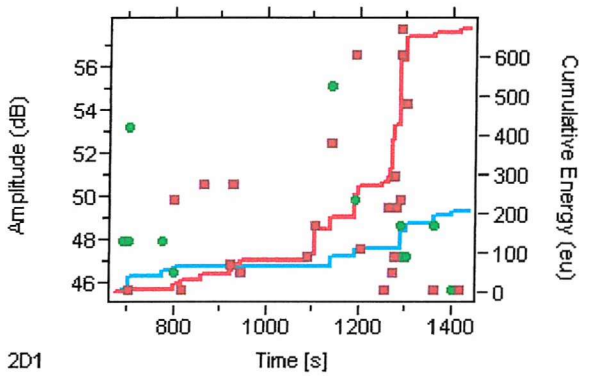

(e) Amplitude distribution and cumulative energy of AE signals for the coating F-4001B in a four point bend test.

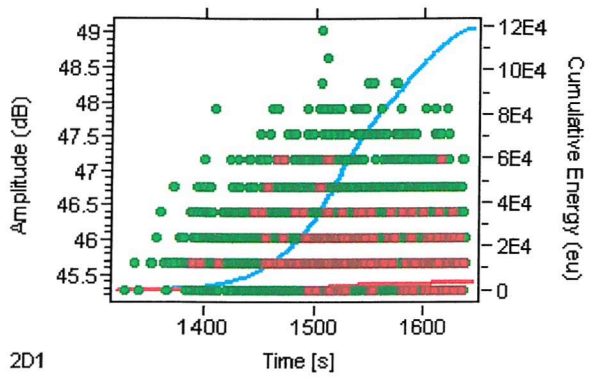

(f) Amplitude distribution and cumulative energy of AE signals for the coating F-4001C in a four point bend test.

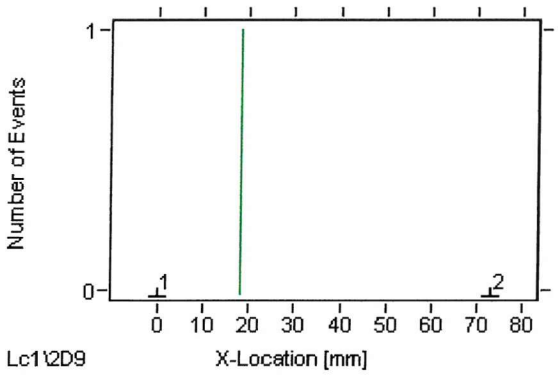

(g) Position distribution of AE signals in a four point bend test for F-4001A.

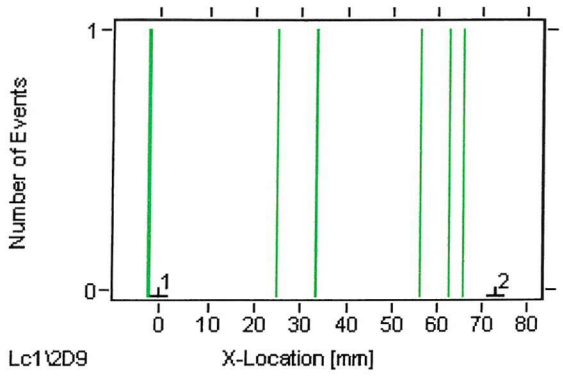

(h) Position distribution of AE signals in a four point bend test for F-4001B.

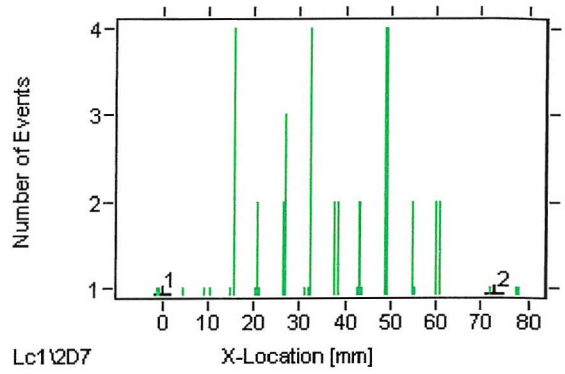

(i) Position distribution of AE signals in a four point bend test for F-4001C.

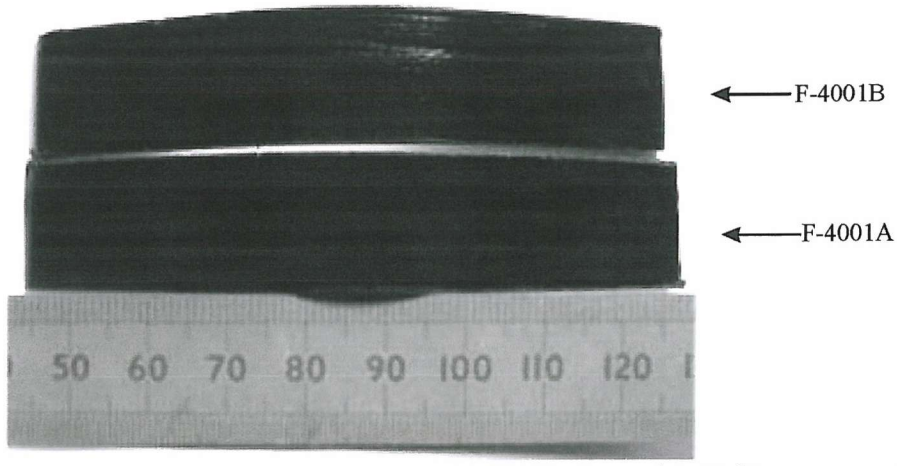

(j) Surface of the coating specimens F-4001A and F-4001B after testing. Neither macrocracks nor microcracks are apparent on their surfaces.

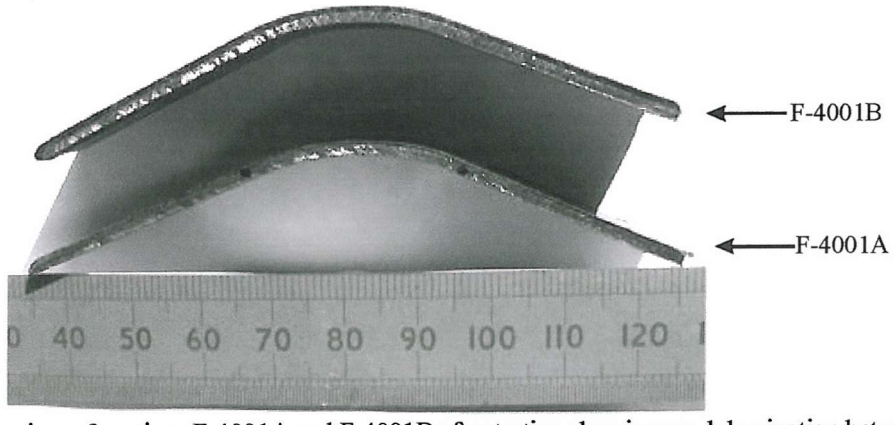

(k) Side view of coatings F-4001A and F-4001B after testing showing no delamination between the coatings and steel substrates.

Fig. 7.9 Experimental results of four point bend tests with AE monitoring for the thermoplastic coatings F-4001A, F-4001B and F-4001C.

7.10 AE Conclusions

Two types of the thermoset coating samples T-15x and T-34x and one type of thermoplastic coating samples F-4001x with various coating thicknesses have been investigated using the four point bend test with AE monitoring. The following conclusions can be drawn from the analysis of the test results contained in Section 7.9:

1. From the positions of the AE signals, the regions around the cracks can be located, although the exact positions are difficult to determine.
2. AE signals obtained during the four point bend tests for the coating samples could be correlated to the phenomena occurring in the coatings: initiation of cracks has the highest AE signals of between 85 – 95 dB; amplitudes of the AE signals due to the propagation of cracks are between 70 – 85 dB; amplitudes resulting from the delamination of the coating are between 60 – 70 dB; debonding or cracking of the embedded fillers in the coating emits AE signals between 52 – 60 dB; the noise caused by the friction between the supporting rollers and the specimen or the background has the lowest AE signals which are below 52 dB. The AE cumulative energy values correlated well with the amount of cracking exhibited, a large difference in AE cumulative energies being shown for samples which cracked and those that did not. Therefore, damage mechanisms can be distinguished from a glance at the cumulative energy values.
3. The different yield loads found for different samples has been partially related to the differences in thicknesses of the coatings present. Other factors which might cause these differences are the yield strengths of the different steels used for some samples and the presence of residual stresses. This will be investigated further.
4. For thermoset coating samples T-15x and T-34x large delaminations were found close to the macrocracks for the thick coatings and small delaminations were found close to the macrocracks of the thin coatings. The larger shear stresses present at the interface for the thicker coating might be responsible for this.

REFERENCES:

[1] M.A. Hamstad, A User's Perspective of Small Computer-Based Acoustic Emission Equipment, Journal of Acoustic Emission Vol. 2 (1983), pp 57-63.

[2] R. J. Boness, S. L. McBride and M. Sobczyk, Wear Studies Using Acoustic Emission Techniques, Tribology International (1990), pp 291-295.

[3] A. G. Beattie, Acoustic Emission, Principles and Instrumentation.

[4] J. T. Dickinson, A Jahan-Latibari and L. C. Jensen, Electron emission and acoustic emission from the fracture of graphite/epoxy composites, Journal of Materials Science Vol. 20 (1985), pp 229-236.

[5] M. A. Hamstad, A Discussion of the Basic Understanding of the Felicity Effect in Fiber Composites, Journal of Acoustic Emission, Vol. 5 (1986), pp 95-102.

[6] C. Scruby, An Introduction to Acoustic Emission, Journal of Physics, E: Science Instrumentation, Vol. 20 (1987), pp 946-953.

[7] L. Jacobs, Characterization of Acoustic Emission Signals From Mode I Crack, Journal of Engineering Mechanics, Vol. 117 (1991), pp 1878-1889.

[8] B. Barna, J. Johnson and R. Allemeier, Determination of Acoustic-Emission Sites Using Digital Nondestructive-Evaluation Workstation, Exp. Mech. (1988), pp 210-213.

[9] K. Buckley, G. Venkatesan, D. West and M. Kaveh, Detection and Characterization of Cracks for Failure Monitoring and Diagnostics, IEEE (1996), pp 2738-2741.

[10] J. Voyer, F. Gitzhofer and M. I. Boulos, Study of the Performance of TBC under Thermal Cycling Conditions using an Acoustic Emission Rig, Journal of Thermal Spray Technology, Vol. 7(2) (1998), pp 181-190.

[11] D. Mitrakovic, I. Grabec and S. Sedmak, Simulation of AE Signals and Signal Analysis Systems, Ultrasonic, Vol. 23 (1985), pp 227-232.

[12] J. T. Dickinson, A. Jahan-Latibari and L. C. Jensen, Electron Emission and Acoustic Emission From the Fracture of Graphite/Epoxy Composites, Journal of Materials Science Vol. 20 (1985), pp 229-236.

[13] Q. Fang, P. S. Sidky and G. M. Hocking, Cracking Behaviours and Stresses Release in Titanium Matrix Composites, Materials Science and Engineering, A, Vol. 288, no. 2, pp 142-147.

[14] A. G. Evans and M. Linzer, Failure Prediction in Structural Ceramics Using Acoustic Emission, Journal of The American Ceramic Society (1973), pp 575-581.

[15] M. M. Mayuram and R. Krishnamurthy, Some Studies on Acoustic Emission Application in Assessing Tribological Characteristics of Plasma Sprayed Ceramic Coatings, Proceedings of the International Thermal Spray Conference & Exposition, Orlando (1992), pp 711-715.

[16] K. H. Zum Ghar, Microstructure and Wear of Materials, Tribology Series Vol. 10, Elsevier (1987).

[17] H. Berns and A. Fischer, Abrasive Wear Resistance and Microstructure of Fe-Cr-C-B- Hard Surfacing Weld Deposits, Wear of Materials, ASME (1985), pp 625-633.

[18] J. Larsen-Badse and K. G. Mathew, Influence of Structure on the Abrasion Resistance of 1040 Steel, Wear 14 (1969), pp 199-206.

[19] H. E. Hintermann, Adhesion, Friction and Wear of Thin Coatings, Wear 100 (1984), pp 381-397.

[20] H. A. Crostack, V. Beckmann and H. J. Strop, Testing of Coatings by Means of Acoustic Emission, Proceeding of 3rd International Symposium on Non-destructive Characterization of Materials, Berlin (1988), pp 825-831.

[21] F. Bordeaux, C. Moreau and R. G. Saint Jacques, Acoustic Emission Study of Failure Mechanisms in TiC Thermal Barrier Coatings, Surface and Coating Technology, 54/55 (1992), pp 70-76.

[22] A. Arora, M. Kendig and F. Mansfeld, Characterisation of Polymer Coatings by Acoustic Emission, Rev. Progress in Quantitative Nondestructive Evaluation, Vol. 3B, 1983, Plenum Press, pp 745-751.

[23] D. Dalmas, S. Benmedakhene, C. Richard and A. Laksimi, Characterization of Cracking Within WC-Co Coated Materials by an Acoustic Emission Method During Four Points Bending Tests, Thermal Spray, Surface Engineering Via Applied Research, ASM International (2000), pp 1335-1340.

[24] U. Senturk, R. S. Lima, C. C. Berndt, C. K. Lin and C. R. C. Lima, Processing and Mechanical Properties of Plasma Sprayed Thermal Barrier Coatings, United Thermal Spray Conference (1999), pp 815-819.

[25] C. Richard, G. Beranger, J. Lu and F. Flavenot et T. Gregoire, Four Point Bending Tests of Thermally Produced WC-Co Coatings, Surface Coating Technology 78 (1996), pp 284-294.

[26] K. Akita, G. Zhang, S. Takahashi, H. Misawa and S. Tobe, In-Situ Observation and AE Analysis of Microscopic Fracture Process of Thermal Spray Coatings, Proceedings of the 15th International Thermal Spray Conference (1998), pp 837-842.

[27] C. K. Lin, C.C. Berndt, S. H. Leigh, and K. Murakami, Acoustic Emission Studies of Alumina-13% Titania Free-Standing Forms During Four-Point Bend Tests, Journal of American Ceramic Society, Vol. 80 [9] (1997), pp 2382-2394.

[28] J. von Stebut, F.Lapostelle, M. Bucsa, H. Vallen, Acoustic Emission Monitoring of Single Cracking Events and Associated Damage Mechanism Analysis in Indentation and Scratch Testing, Surface and Coatings Technology, Vol. 160 (1999), pp 116-119 (1999).

CHAPTER 8 CONCLUSIONS AND FUTURE WORK

In the present work, the wireline wear and impact resistance of polymeric coatings used on the bore of downhole tubulars have been investigated by carrying out abrasive wear, wireline wear, falling-weight impact and four point bend tests on these polymeric coatings. Comparative work has been conducted on thermoplastic and thermoset coatings with various microstructural characteristics, i.e. different coating thicknesses or different fillers and filler contents. The damage mechanisms of the polymeric coatings have been studied and compared under different experimental conditions.

8.1 Conclusions

8.1.1 Improved experimental techniques

- A new pin-on-disc (POD) apparatus was designed and manufactured for the present research work. Rigidity was the main concern in the design of the new POD apparatus so that edge-loading during the wear test can be eliminated. The high flexibility of the new apparatus enables wear tests to be carried out under a wide range of experimental conditions.

- The falling-weight impact test rig was modified to ascertain the best position for the signal transducer. The nearest place to the impact contact point was found to be the most ideal position since it gives the clearest impact signal.

- The four point bend test was adopted in the present research work to investigate the mechanical properties of the polymeric coatings.

8.1.2 Wear conclusions

- The unfilled nylon coating T-99A had the best wear resistance in both abrasive wear and wireline wear tests. By contrast, the silica and dolomite filled polymeric coating I-1100A was found to have the worst abrasive wear resistance. In general, the weak bond between the filler and a thermoplastic polymer matrix leads to the filler particles detaching from the matrix causing enhanced wear.

- The unfilled PVDF coating P-A had a worse abrasive wear resistance than coating T-99A because the presence of many voids and unmelted powder particles reduced the cohesive strength and aided fracture of the ploughed furrows. The presence of voids and unmelted powder particles in coating P-A were the main reasons for its poor wireline wear resistance.

- In wireline wear tests microcutting and microploughing were the main mechanisms causing wear of the thermoplastic coatings. Microcracking was the dominant wear mechanism for the thermoset coatings because the cracks on the wear scar propagated detaching segments of the matrix resulting in material loss.

- The fillers in the thermoset coating T-15 had good bonding to the matrix and supported the load from the slickline wire under moderate applied loads. However, the fillers in the coating T-34 detached very easily due to their poor bonding with the matrix. The cavities produced by filler detachment acted as a stress concentrations causing more cracking and material removal. Image analysis on X-ray maps of the wear tracks was found to be a useful tool in analysing the break up and detachment of fillers in wireline wear.

8.1.3 Impact conclusions

- Through FFT analysis, dominant frequencies can be distinguished from the original impact response. High frequency signals approximately at 3~5 kHz, 6~10 kHz, 13~19 kHz and 19~25 kHz have been recognised to be associated with the impact system used in the present study. Therefore, during the analysis of the impact results these high frequencies can be removed for ease of analysis.

- The size of the plastic indent for F-4001 and the radius of the circumferential cracks formed on T-15 and T-34 showed no marked influence of coating thickness nor substrate thickness.

- The radius of the circumferential cracks formed was considered to be in good agreement with that predicted by the Hertzian approach.

- The fact that Young's modulii of T-15 and T-34 appear to be similar from Hertzian analysis of impact suggests that the fibre efficiency parameter for T-34 is less than that for T-15 as T-34 has 2.2 times more fillers than T-15. This implies that the fillers in T-34 have poorer bonding to the matrix than the fillers in T-15, which is in a good agreement with the wear studies for the two coatings.

- Wavelet analysis is an efficient method of decomposing a signal into a frequency-time representation. It allows the dominant frequencies and how these frequencies vary with time to be determined. Through wavelet analysis, the impact processes and the contact status between the impactor and the sample can be distinguished.

- The variation of dominant frequencies may reflect the contact status between the impactor and any plastic deformation occurring on the sample tested, and thus produce useful information about the impact processes and the damage mechanisms taking place within the sample.

8.1.4 Acoustic Emission (AE) conclusions

- From the positions of the AE signals, the regions around the cracks can be located, although the exact positions are difficult to determine. AE signals obtained during the four point bend tests for the coating samples could be correlated to the phenomena occurring in the coatings.

- The different yield loads found for different samples have been partially related to the differences in thicknesses of the coatings present. Other factors which might cause these differences are the yield strengths of the different steels used for some samples and the presence of residual stresses.

- For thermoset coating samples T-15x and T-34x large delaminations were found close to the macrocracks for the thick coatings and small delaminations were found close to the macrocracks of the thin coatings. The larger shear stresses present at the interface for the thicker coating might be responsible for this.

8.2 Future Work

8.2.1 Future work for wear test

Nylon coating T-99 has been proven to have better wear resistance than the thermoset coatings. There were no fillers embedded in the coating layer for T-99. Although fillers sometimes cause low wear resistance for the thermoset coatings due to weak bonding or being detached during the wear test, they could support a part of load during the wear test. Therefore, it is worth testing the wear resistance of the Nylon coatings embedded with hard fillers. Surface modification agents could also be added in an attempt to improve adhesion between fillers and matrix.

Wear tests for various coatings with different matrix materials and different types of fillers have been carried and their wear mechanisms have been compared. In future work, it is worth testing the wear resistance of the coatings with identical matrix material but different filler contents in order to investigate further the influence of the fillers on wear resistance.

8.2.2 Future work for impact

The present impact rig needs to be improved in a way to make the transducer directly connected with the test sample. This could help to reduce the unwanted "noise" signal caused by parts of the test rig. Thus the signal collected may truly reflect the behaviour of the sample damage during the impact test.

The signal analysis method needs to be improved in order to obtain more accurate information of frequency change during the impact test. This could help to obtain more detailed damage information from the test sample, i.e. the time when different types of cracks take place. Modelling of the impact test by using the Finite Element (FE) analysis method could provide a useful comparison with the practical impact test. Different sample geometries could be tested under different impact conditions and modelled. Through FE analysis the vibration frequencies could be obtained. By comparing the FE modelling result of the impact test and the real signal obtained during the test, the influence of vibration of the sample on the damage mechanisms could be explained in detail.

8.2.3 Future work for AE

In the AE experimental work, it was of interest to find different cracking behaviour for the coating as a function of coating thicknesses during the four point bend test. This phenomenon was thought to be related to the mechanical properties of the material tested, i.e. Young's modulus and residual stress of the coating material. FE modelling is thought to be a useful approach to explain this interesting experimental result during the four

point bend test. By carrying out FE analysis, the distribution of residual stress and mechanical properties of the coating material could be considered and analysed properly, thus the reason for the different cracking behaviour for the same coating material with different coating thicknesses could be discussed further and explained. However, in order to do this analysis the Young's modulus of the coating must be found. Instrumented hardness testing would be a useful approach to adopt. By analysing the unloading curve, the Young's modulus can be ascertained.

APPENDIX A: ENGINEERING DRAWING OF THE NEW POD RIG

The general assembling engineering drawing of the new POD rig and the main parts of the rig inclusive of the main frame, sample holder and sample clamp are presented from Figures A.1 to A.4.

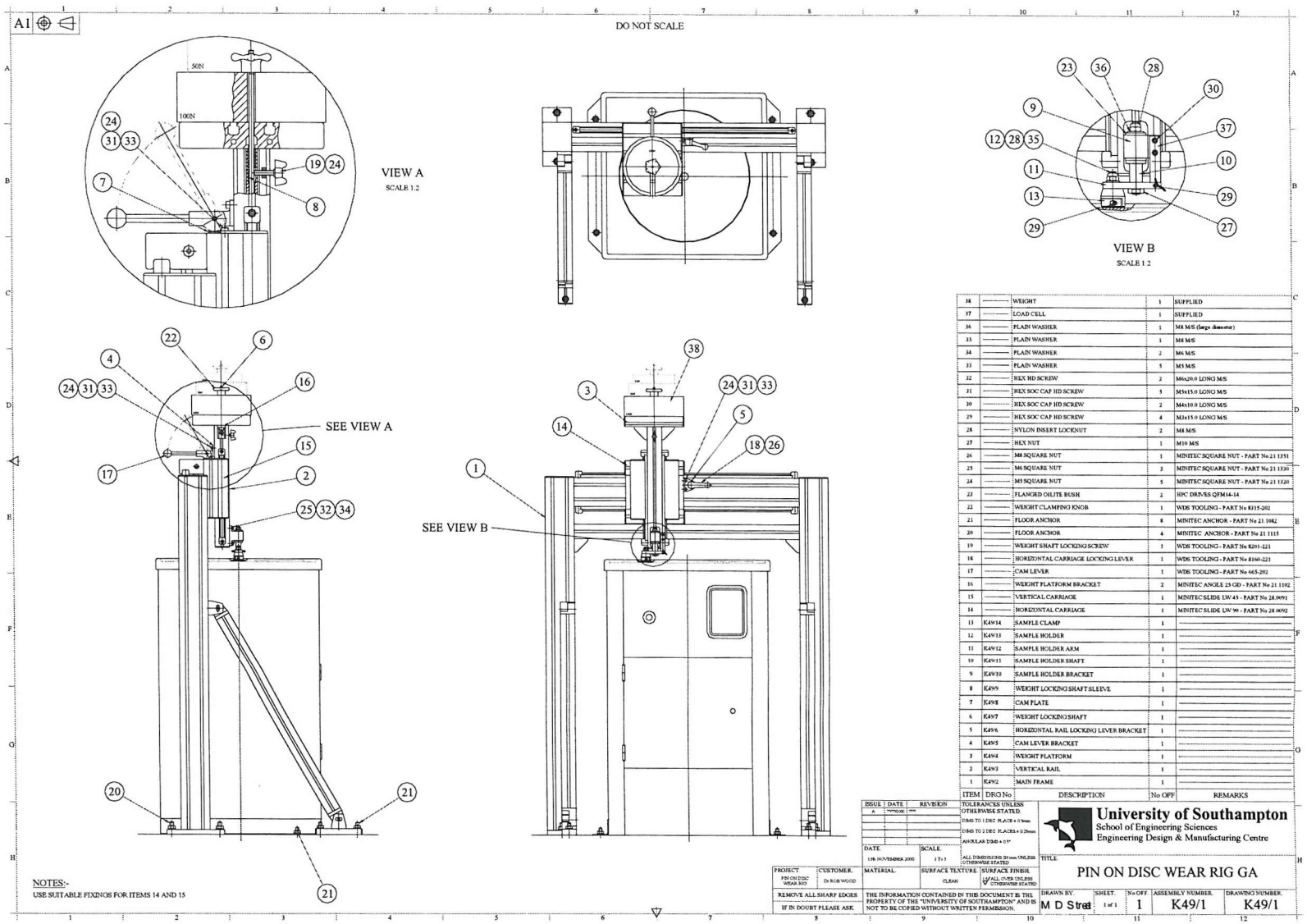

ITEM	DRG No	DESCRIPTION	No OFF	REMARKS
38		WEIGHT	1	SUPPLIED
37		LOAD CELL	1	SUPPLIED
36		PLAIN WASHER	1	M8 M/S (large diameter)
35		PLAIN WASHER	1	M8 M/S
34		PLAIN WASHER	2	M6 M/S
33		PLAIN WASHER	5	M5 M/S
32		HEX HD SCREW	2	M6x20.0 LONG M/S
31		HEX SOC CAP HD SCREW	5	M5x15.0 LONG M/S
30		HEX SOC CAP HD SCREW	2	M4x10.0 LONG M/S
29		HEX SOC CAP HD SCREW	4	M3x15.0 LONG M/S
28		NYLON INSERT LOCKNUT	2	M8 M/S
27		HEX NUT	1	M10 M/S
26		M8 SQUARE NUT	1	MINITEC SQUARE NUT - PART No 21 1351
25		M6 SQUARE NUT	3	MINITEC SQUARE NUT - PART No 21 1330
24		M5 SQUARE NUT	5	MINITEC SQUARE NUT - PART No 21 1320
23		FLANGED OILITE BUSH	2	HPC DRIVES QFM14-14
22		WEIGHT CLAMPING KNOB	1	WDS TOOLING - PART No KJ15-202
21		FLOOR ANCHOR	8	MINITEC ANCHOR - PART No 21 1042
20		FLOOR ANCHOR	4	MINITEC ANCHOR - PART No 21 1115
19		WEIGHT SHAFT LOCKING SCREW	1	WDS TOOLING - PART No K201-221
18		HORIZONTAL CARRIAGE LOCKING LEVER	1	WDS TOOLING - PART No K160-221
17		CAM LEVER	1	WDS TOOLING - PART No 665-202
16		WEIGHT PLATFORM BRACKET	2	MINITEC ANGLE 25 GD - PART No 21 1102
15		VERTICAL CARRIAGE	1	MINITEC SLIDE LW 45 - PART No 28.0091
14		HORIZONTAL CARRIAGE	1	MINITEC SLIDE LW 90 - PART No 28.0092
13	K49/14	SAMPLE CLAMP	1	
12	K49/13	SAMPLE HOLDER	1	
11	K49/12	SAMPLE HOLDER ARM	1	
10	K49/11	SAMPLE HOLDER SHAFT	1	
9	K49/10	SAMPLE HOLDER BRACKET	1	
8	K49/9	WEIGHT LOCKING SHAFT SLEEVE	1	
7	K49/8	CAM PLATE	1	
6	K49/7	WEIGHT LOCKING SHAFT	1	
5	K49/6	HORIZONTAL RAIL LOCKING LEVER BRACKET	1	
4	K49/5	CAM LEVER BRACKET	1	
3	K49/4	WEIGHT PLATFORM	1	
2	K49/3	VERTICAL RAIL	1	
1	K49/2	MAIN FRAME	1	

Fig. A.1 Assembling engineering drawing of the new POD rig.

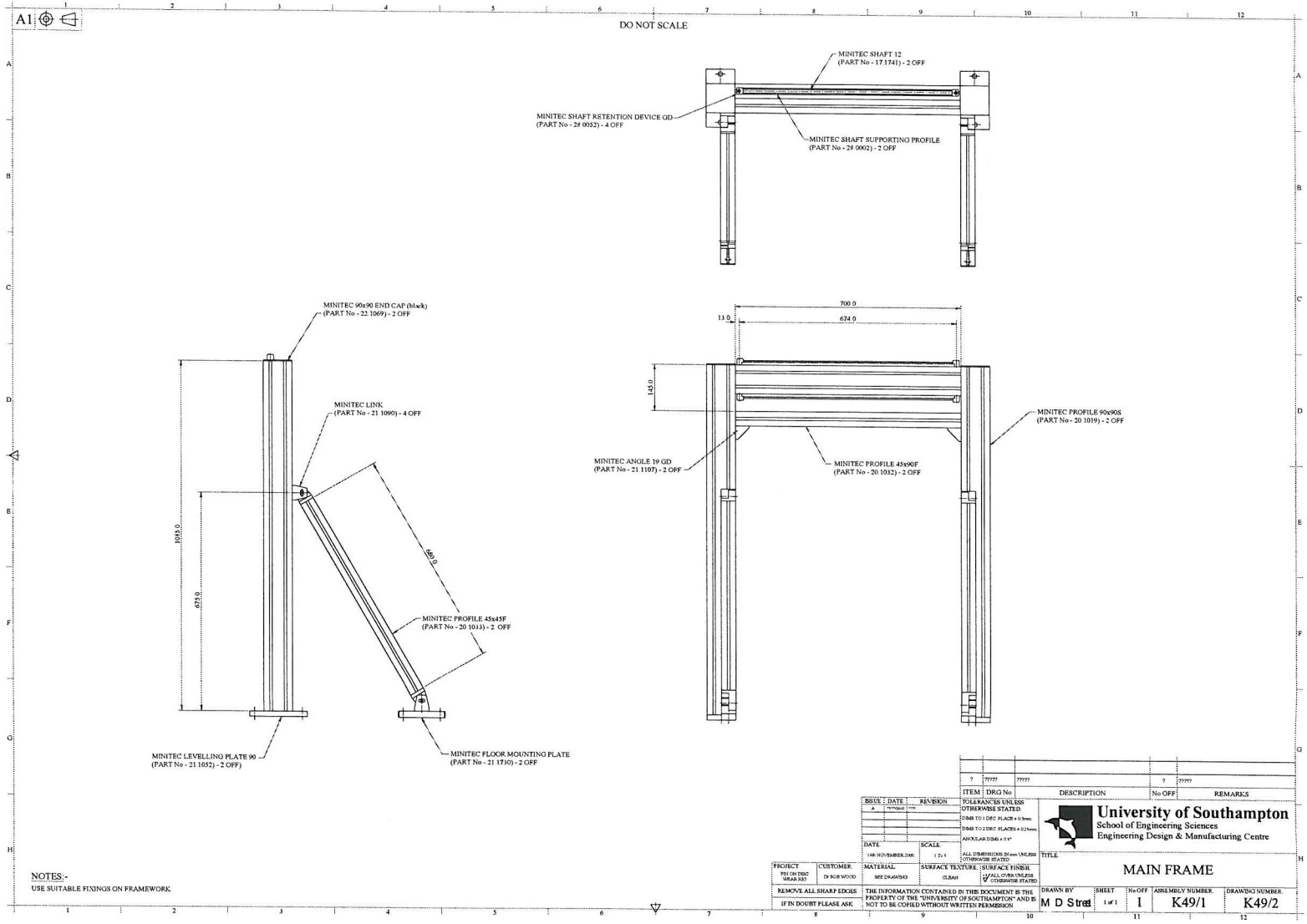

Fig. A.2 Engineering drawing of the main frame of the new POD rig.

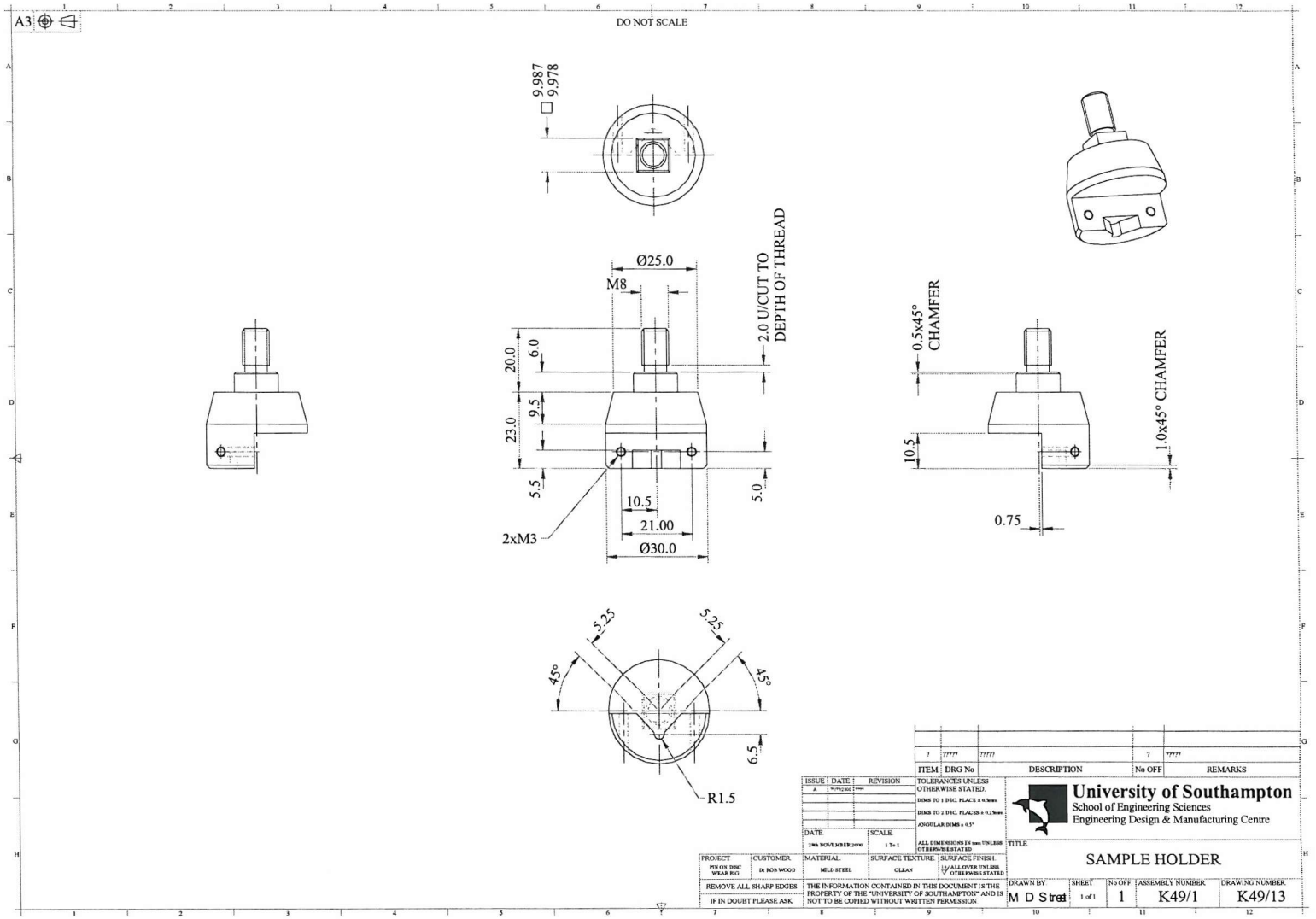

Fig. A.3 Engineering drawing of the sample holder.

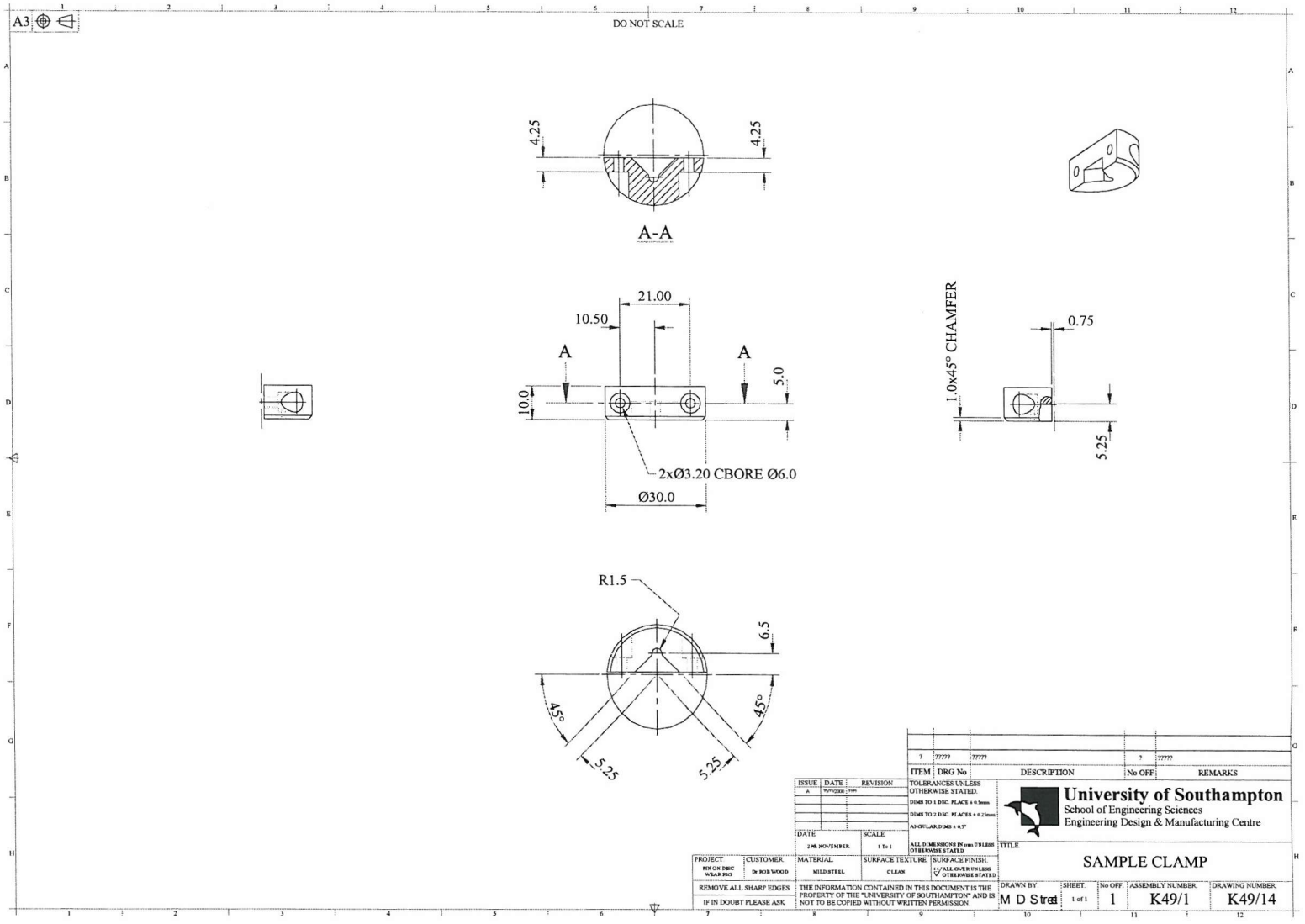

Fig. A.4 Engineering drawing of the sample clamp.

APPENDIX B: MEASUREMENT OF YOUNG'S MODULUS OF COATING MATERIALS

1. Introduction

The Young's modulus (E) of the polymeric coating materials tested is a very important parameter in the present study. For the impact tests, the Young's modulus of the coating material is needed to calculate the impact force obtained during the impact tests, see Chapter 6. For the AE tests, the Young's modulus of the coating material is necessary to calculate the stress on the coating material under the load applied at different positions, so that the cracking mechanism of the coating tested during the four point bending test could be analysed.

As the material properties were not provided by the manufacturer, the following methods were utilised by the present author to measure E values: four point bend test, Dynamic Mechanical Thermal Analysis (DMTA) and tensile test.

2. Four point bend test

The three-point and four-point bend tests for the determination of E can be called a macro-evaluation process. Thus, they can be used to determine the properties of the bulk coating with all the considerable variables, which can typically influence Young's modulus [1].

Three- and four-point bend tests were conducted by Li et. al. [1] for the determination of Young's modulus (E) of high velocity oxy-fuel (HVOF) sprayed coatings. The results obtained from the three-point bend test correspond well to those obtained from the four-point bend tests. In Li's study, the four-point bend test was conducted on a one-sided coating sample with strain gauges attached on the substrate and the coating surface. The size of the specimen and the set-up of the experiment are similar to the present study during four-point bend test in the AE experiment, see Figures 7.4 and 7.5. However, the

HVOF coatings has much higher E values (about 20~30 GPa) than the polymeric coatings used in the present study (about 6 GPa). The E value of the coating materials tested was measured from the following formula:

$$Ec = EsR\frac{KR + 2K - R}{2R - K + 1} \qquad (1)$$

where the subscripts c and s represent coating and substrate materials, and $R = \frac{ls}{lc}$ is defined as the relative thickness. K is the relative strain of the substrate and coating defined as:

$$K = \frac{\varepsilon_s}{\varepsilon_c} \qquad (2)$$

In Li's study, the E value for one type of HVOF coatings was obtained as 29 GPa with an error of ± 2 GPa, indicating an error of ± 0.54% in the strain ratio K during the measurement.

In the present experimental tests, the known parameters of the polymeric coatings are shown in Table B.1.

Table B.1 Parameters of the polymeric coating materials

	T-15B	T-34B	F-4001C
E of steel substrate, GPa	207	207	207
E of coating, GPa	?	?	?
Thickness of coating lc, mm	0.35	0.25	1.5
Thickness of substrate ls, mm	1.5	1.5	1.5
R (ls/lc)	4.3	6	1

With the current geometry of the four point bend test for the coating T-34B, the relationship between the strain ratio K and the E value of the coating can be obtained based on Eqns (1) and (2), and is plotted in Figure B.1.

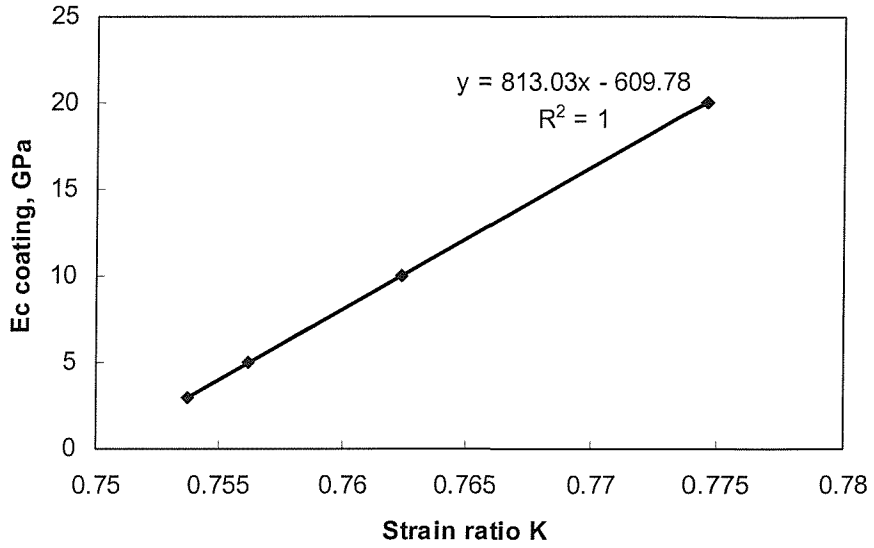

Fig. B.1 Relationship between the E value and the strain ratio of the coating T-34B as the given specimen size shown in Table B.1.

It can be seen from Figure B.1 that the E value of the coating measured is very sensitive to the strain ratio with the present geometry of the specimen, i.e. with a small change of the strain ratio there would be a large variation of the E value.

Assuming a similar error of ± 0.54% for the strain ratio K, could be obtained for the present study as in Li's study [1], if the E value of the coating is given by the reference value of 6 GPa (see Chapter 6), the error in E value would be ± 3.3 GPa which is too large to be accepted. Therefore, using the four point bend test to measure the E value of the polymeric coatings used in the present study is not an ideal method.

3. Dynamic Mechanical Thermal Analysis (DMTA)

The Dynamic Mechanical Thermal Analysis (DMTA) method was also utilised in an attempt to measure E of the polymeric coatings of the present study. DMTA (model RSA II) involves the application of an oscillatory strain to a sample. The resulting sinusoidal stress is measured and correlated against the input strain, and the viscous and elastic properties of the sample are simultaneously measured. During the DMTA testing, the RSA II control computer makes a digital cross-correlation of measured strain and force by comparing the amplitude and phase shift between the imposed motion (strain) and the force (stress).

Figure B.2 shows the Parallel Plate Fixture utilised in the RSA II testing rig. Figure B.3 is the Sample Testing Limit graph showing the Recommended Range, which is the instrument operating range where useful data can be expected. The plot is graphed according to sample dimension as a function of modulus E*. The geometry-modulus relationship shown in the Sample Testing Limit graph can be used to make adjustments to the sample dimensions. Note that the recommended range is surrounded by a grey region where test results may be affected by instrument limits. Testing is not recommended under conditions defined by an area outside of the recommended range and grey region. The E values of the polymeric coatings used in the present study are between 5 to 15 GPa, therefore, in order to satisfy the sample dimensions recommended by Figure B.3 the surface area of the coating tested should be made as small as possible and the length of the sample should be made as large as possible. Because the thicknesses of the polymeric coating T-15 and T-34 are between 0.25 to 0.35 mm, thus at least 10 to 20 samples were needed based upon the smallest surface area that could be cut by the present author.

It was not possible to determine the Young's Modulus of the coatings by means of the DMTA for the following reasons:

1. The coating material cut from the original coating block is not uniform in terms of surface area and the thickness, thus the ratio of sample Radius^2/Length cannot be controlled properly.
2. It was extremely difficult to pile up the 10 to 20 pieces of sample between the two parallel plates of the testing fixture.

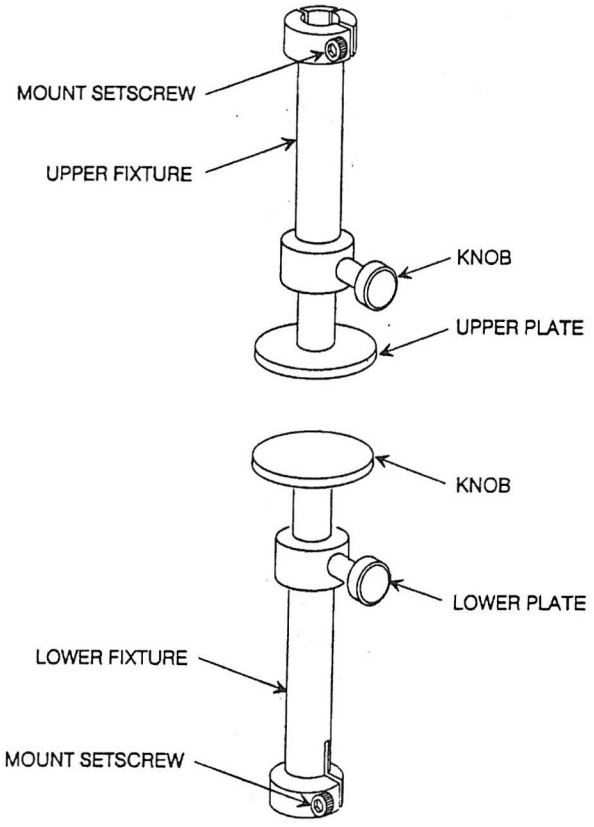

Fig. B.2 Parallel Plate Fixture.

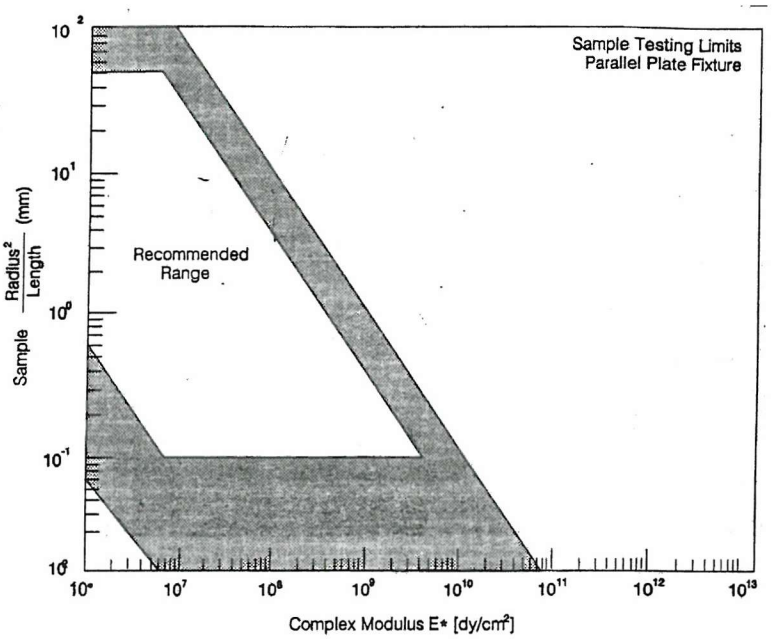

Fig. B.3 Sample testing limits for Parallel Plate Fixture.

4. Tensile test

Tensile tests on polymeric coating materials were attempted using the Instron tensile testing machine. However, none of available machining methods in the workshop could successfully separate the coating layer from the substrate steel. Therefore, a tensile test on the polymeric coatings was unable to be conducted by the present author.

References:

[1] H. Li, K.A. Khor and P. Cheang, Young's modulus and fracture toughness determination of high velocity oxy-fuel-sprayed bioceramic coatings, Surface and Coatings Technology 155 (2002), pp 21-32.